Eigenmode Projection Techniques for Magnetic Polarisabilities in Lattice QCD

Ryan Bignell

Supervisors:
Waseem Kamleh
Derek Leinweber

A thesis submitted towards the degree of Doctor of Philosophy

The Faculty of Sciences
The University of Adelaide

July 16, 2020

Abstract

The magnetic polarisability of a selection of octet baryons and the pion are calculated using lattice QCD and the background field method. Results are from $32^3 \times 64$ dynamical QCD gauge fields with $2 + 1$ flavours provided by the PACS-CS collaboration through the International Lattice Data Grid (ILDG) . These use a clover fermion action and an Iwasaki gauge action with $\beta = 1.9$ providing a physical lattice spacing of $a = 0.0907(13)$ fm.

As the application of a uniform background magnetic field renders standard gauge covariant Gaussian smeared quark operators inefficient at isolating ground state hadron energy eigenstates at non-trivial field strengths, Landau level quark propagator projection techniques are created and utilised.

First the two-dimensional $U(1)$ Laplacian eigenmodes are considered. These describe the Landau levels of a charged particle on a finite periodic lattice. Using this eigenmode projection technique, the neutron ground state energy eigenstate is isolated and hence the magnetic polarisability of the neutron calculated. These results are used to inform a chiral effective field theory analysis to produce a prediction for the magnetic polarisability of the neutron at the physical point. The chiral analysis incorporates both finite-volume effects and sea-quark-loop contributions.

Wilson-like fermion actions are exposed to additive mass renormalisations; when a background magnetic field is introduced, the Wilson term causes a field-dependent renormalisation to the quark mass. This quark mass renormalisation is studied using the neutral pion mass. Herein, the clover fermion action is investigated to determine the extent to which the $\mathcal{O}(a)$ removal of errors suppresses the field-dependent quark mass changes. We demonstrate how a careful treatment of the

nonperturbative-improvement of the clover term is required to resolve this artefact of the Wilson term.

Motivated by the success of the $U(1)$ eigenmode-projected quark-propagator technique, a new technique utilising eigenmodes of the $SU(3) \times U(1)$ Laplacian is considered. Here both QCD and background magnetic field effects are included in the quark propagator projection. This technique is used to calculate proton, neutron, Σ^+ and Ξ^0 two-point correlation functions in a background magnetic field. From these, the magnetic polarisability is calculated at several quark masses enabling a chiral effective field theory analysis. The chiral effective field theory techniques established for the neutron's magnetic polarisability are extended to the other baryons considered herein and the results are compared.

Finally, using the analysis and methods of the $SU(3) \times U(1)$ quark propagator projection technique and improved clover-fermion action, the pion sector is investigated. Results for the magnetic polarisability of both the charged and neutral pions are presented. For the first time, the relativistic energy shift is used to determine the magnetic polarisabilities.

Declaration

I certify that this work contains no material which has been accepted for the award of any other degree or diploma in my name, in any university or other tertiary institution and, to the best of my knowledge and belief, contains no material previously published or written by another person, except where due reference has been made in the text. In addition, I certify that no part of this work will, in the future, be used in a submission in my name, for any other degree or diploma in any university or other tertiary institution without the prior approval of the University of Adelaide and where applicable, any partner institution responsible for the joint-award of this degree. I give consent to this copy of my thesis when deposited in the University Library, being made available for loan and photocopying, subject to the provisions of the Copyright Act 1968. I acknowledge that copyright of published works contained within this thesis resides with the copyright holder(s) of those works. I also give permission for the digital version of my thesis to be made available on the web, via the University's digital research repository, the Library Search and also through web search engines, unless permission has been granted by the University to restrict access for a period of time. I acknowledge the support I have received for my research through the provision of an Australian Government Research Training Program Scholarship.

Ryan Bignell

Acknowledgements

I'd like to thank my supervisors, Waseem Kamleh and Derek Leinweber for their inspiration and guidance throughout these last few years. This would have been a poorer experience and piece of work without you both. The support of the university is also much appreciated.

The last few years have been spent in the company of many wonderful people at the university; you have all made it a pleasure and joy to come into work each day. From physics to cricket to Star Wars, your companionship and banter have been key to an enjoyable PhD experience. Special acknowledgement must go to the 2015 physics honours group for being there throughout my postgraduate journey at the University of Adelaide. Thanks must also go to Finn Stokes and Alex Chambers who were extremely welcoming to a new PhD and taught me much about lattice QCD besides. I greatly enjoyed the opportunity to learn from my fellow students about their research at our weekly student-led meetings during the course of my PhD, so thanks must go to the organisers and all presenters.

My non-Physics friends, whether at cricket, games or elsewhere have been an invaluable opportunity to break away from the Physics bubble for a time and recharge. Thank you.

My family; Meredith, Kevin and Hayden have been a source of unceasing support, tolerance and love throughout the course of my studies. They have given me the gift of an environment where I could focus on my studies as well as listened (with varying amounts of interest) to me describing what I do. Thank you Mum, Dad and Hayden.

Contents

List of figures **xi**

List of tables **xix**

1. Introduction **1**

2. Quantum Chromodynamics **3**

2.1. Hadronic spectrum . . . 3

2.1.1. Quark model . . . 3

2.2. Quantum Chromodynamics . . . 9

2.2.1. Observables in the path integral formalism . . . 11

3. Lattice QCD **15**

3.1. Discretisation . . . 15

3.2. Gluonic Action . . . 18

3.3. Fermion Action . . . 21

3.3.1. Improved Fermion Action . . . 22

3.4. Expectation Values . . . 27

3.4.1. Fourier Projection . . . 30

3.4.2. Hadronic level interpretation of correlation function . . . 30

3.4.3. Boundary conditions . . . 34

3.4.4. Effective Energy . . . 37

3.5. Smearing . . . 39

3.5.1. Link Smearing . . . 40

3.6. Background Field Method . . . 40

3.6.1. Formulation . . . 41

3.6.2. Hadron Energy . . . 47

3.7. Simulation Details . . . 48

4. $U(1)$ Landau mode projection **53**
4.1. Quark operators 54
4.1.1. Gaussian smeared source 55
4.1.2. $U(1)$ Landau mode quark sink 55
4.2. Magnetic Polarisability 60
4.2.1. Formalism 60
4.2.2. Simulation Details 64
4.2.3. Fitting 65
4.3. Chiral Extrapolation 69
4.3.1. Formalism 70
4.3.2. Analysis 72
4.4. Summary 75

5. Background field corrected clover action **77**
5.1. Free-field limit 78
5.1.1. Clover correction 83
5.2. Full QCD 85
5.2.1. Energy shifts for Wilson fermions 86
5.2.2. Nonperturbatively-Improved clover fermions 89
5.2.3. Expected mass renormalisation 91
5.3. Background field corrected clover fermion action 93
5.3.1. Additive mass renormalisation 93
5.3.2. Comparison to Bali *et al.* 97
5.3.3. Magnetic polarisability 98
5.4. Summary 99

6. $SU(3) \times U(1)$ eigenmode projection **101**
6.1. Quark operators 101
6.1.1. $SU(3) \times U(1)$ eigenmode quark projection 101
6.1.2. Gaussian smeared source 105
6.1.3. $U(1)$ hadronic projection 108
6.2. Lattice Results 113
6.2.1. Magnetic polarisability formalism refresher 113
6.2.2. Neutron 114
6.2.3. Proton 121
6.2.4. Hyperons 128
6.2.5. Lattice Magnetic Polarisability Summary 137

6.3. Chiral effective field theory 138
6.3.1. Formalism 139
6.3.2. Results 145
6.4. Summary 156

7. Pion polarisabilities 161
7.1. Interpolating operators 161
7.2. Magnetic polarisability 162
7.2.1. Charged pion 163
7.2.2. Neutral pion 171
7.3. Summary 180

8. Conclusions & Future Work 183

A. Gamma Matrices 187
A.1. Pauli Matrices 187
A.2. Gamma Matrices 187
A.3. Gell-Mann matrices 189
A.4. Useful Identities 189

B. Lattice Appendix 191
B.1. Link variable gauge transformation 191
B.2. The plaquette 192
B.3. Naive Fermion Action 194
B.3.1. Wilson Fermion Action 195
B.4. Baryon Wick contractions 196
B.5. Baryon correlation function spin structure 197
B.6. Least squares fitting 198
B.7. Magnetic section of clover term 199
B.8. Chiral effective field theory coefficients 200
B.8.1. Numerical coupling coefficient values 200
B.9. Baryon masses 206

C. Landau levels 207
C.1. Continuum, infinite volume formulation 207
C.2. Discretised, finite volume formulation 210

Bibliography 213

List of figures

2.1. Pseudoscalar meson nonet with $J^P = 0^-$. 5

2.2. Baryon octet with $J^P = \frac{1}{2}^+$. 6

2.3. Baryon decuplet with $J^P = \frac{3}{2}^+$. 7

3.1. Link variable U_μ on a two-dimensional representation of space-time. . . . 16

3.2. The simplest closed loop of link variables, the plaquette $P_{\mu\nu}(x)$. 18

3.3. Link variables for construction of $R^{1\times 2}_{\mu\nu}$. 20

3.4. Link variables for construction of $\mathcal{C}_{\mu\nu}(x)$. 26

3.5. Meson and baryon quark flow diagrams. 29

3.6. π^+ projected two-point correlation function with (Anti) Periodic boundary conditions in the time dimension. 33

3.7. Σ^+ projected two-point correlation function with fixed boundary conditions in the time dimension. 33

3.8. The background field plaquette away from the boundary of the lattice. . 43

3.9. The background field plaquette at the corner of the lattice, $y = a\,N_y$. . . 44

3.10. The background field plaquette at the corner of the lattice, $y = a\,N_y$, correcting for the discontinuity. 45

3.11. The background field plaquette at the corner of the lattice, $y = a\,N_y$, $x = a\,N_x$. 46

3.12. Kaon mass plotted against m_π^2 on the PACS-CS ensembles using $\kappa_s^{\mathrm{val}} =$ 0.13640. 49

3.13. Kaon mass plotted against m_π^2 on the PACS-CS ensembles using $\kappa_s^{\mathrm{val}} =$ 0.13665. 50

4.1. Neutron effective mass for varied source smearings to point sink correlation function. 54

4.2. $U(1)$ eigenmode probability densities for two magnetic field strengths. . . 56

4.3. $U(1)$ Landau projected sink neutron anti-aligned effective energy for $|k_d| = 3$ on $m_\pi = 411$ MeV ensemble. 58

4.4. $U(1)$ Landau projected sink neutron aligned effective energy for $|k_d| = 1$ on $m_\pi = 296$ MeV ensemble. 59

4.5. Neutron aligned and anti-aligned effective energies with a $\sigma = 1.0$ $U(1)$ Landau mode projected sink. 60

4.6. Magnetic polarisability energy shift for a point sink and a $U(1)$ Landau eigenmode quark sink. 62

4.7. The neutron magnetic polarisability effective energy shift for $m_\pi = 411$ MeV with truncated $(n = 1)$ projection operator of Eq. (4.3). 63

4.8. The neutron magnetic polarisability effective energy shift for $m_\pi = 411$ MeV with untruncated $(n = |3\, q_f\, k_d|)$ projection operator of Eq. (4.3). . . 64

4.9. $m_\pi = 411$ MeV neutron magnetic polarisability energy shift with a $\sigma = 1.0$ $U(1)$ Landau mode projected quark sink. 65

4.10. $m_\pi = 702$ MeV neutron magnetic polarisability energy shift with a $\sigma = 1.0$ $U(1)$ Landau mode projected quark sink. 66

4.11. Quadratic fits of the energy shift to the field quanta at each quark mass for the neutron for a single σ value each. 69

4.12. The leading-order pion-loop contribution to the magnetic polarisability of the neutron. 70

4.13. Pion-loop contributions to the magnetic polarisability of the neutron, allowing transitions to the nearby and strongly coupled Delta baryons. . 70

4.14. Finite volume extrapolations of $\beta^n\,(m_\pi^2)$ for a range of volumes. 73

4.15. Comparison of βn predicted herein with experimental results. 74

5.1. Pion energies from Wilson fermion correlation functions as a function of background magnetic field strength. 81

5.2. Pion zero-field correlator using (anti) periodic boundary conditions. . . . 81

5.3. Pion energies from clover fermion correlation functions as a function of background magnetic field strength. 82

5.4. Neutral pion effective energy shift $E_{[\pi^0]}\,(B) - m_{\pi^0}$ from Eq. (5.24) using a nonperturbatively-improved clover fermion action on the $m_\pi = 296$ MeV ensemble. 90

5.5. As described in Figure 5.4 but for the $E_{[\pi^0]}\,(B) + m_{\pi^0}$ energy shift produced by Eq. (5.25). 91

5.6. Fits of the magnetic-field induced energy shift to the magnetic-field quanta for the nonperturbatively-improved clover fermion action. 92

5.7. Neutral pion effective energy shift $E_{\pi^0}\,(B) - m_{\pi^0}$ from Eq. (5.24) using the BFCC fermion action on the $m_\pi = 296$ MeV ensemble. 94

5.8. As described in Figure 5.7 but for the $E_{\pi^0}\,(B) + m_{\pi^0}$ energy shift produced by Eq. (5.24). 94

5.9. Fits of the magnetic-field induced energy shift to the magnetic-field quanta for the BFCC fermion action. 95

5.10. Fits of the magnetic-field induced energy shift to the magnetic-field quanta for the BFCC fermion action. 96

6.1. Proton energy shift $E\,(B) - m$ of Eq. (4.11) using 64 and 96 eigenmodes in the projection operator of Eq. (6.5) on the $m_\pi = 702$ MeV ensemble. . 104

6.2. Nucleon effective masses for three source smearings to $SU(3) \times U(1)$ eigenmode projected sink correlation functions on the $m_\pi = 702$ MeV ensemble. 105

6.3. Nucleon effective masses for three source smearings to $SU(3) \times U(1)$ eigenmode projected sink correlation functions on the $m_\pi = 296$ MeV ensemble. 106

6.4. Proton $k_d = 2$ effective energies for three source smearings to $SU(3) \times U(1)$ eigenmode projected sink correlation functions on the $m_\pi = 702$ 296 ensemble. 107

6.5. $U(1)$ eigenmode probability densities for $k_d = -6$. 109

6.6. A comparison of the three different hadronic projections for the charged pion on the $\kappa_{ud} = 0.13770$ ensemble. 111

6.7. A comparison of the three different hadronic projections for the charged pion on the $\kappa_{ud} = 0.13700$ ensemble. 112

6.8. Neutron $E\,(B) + M$ energy shift for the $m_\pi = 570$ MeV ensemble. 114

6.9. Neutron effective energy shift for the $m_\pi = 702$ MeV ensemble. 115

6.10. Neutron effective energy shift for the $m_\pi = 570$ MeV ensemble. 116

6.11. Neutron effective energy shift for the $m_\pi = 411$ MeV ensemble. 116

6.12. Neutron effective energy shift for the $m_\pi = 296$ MeV ensemble. 117

6.13. Quadratic only fit to the magnetic polarisability energy shift for the neutron on the $m_\pi = 702$ MeV ensemble. 118

6.14. Quadratic only fit to the magnetic polarisability energy shift for the neutron on the $m_\pi = 570$ MeV ensemble. 119

6.15. Quadratic only fit to the magnetic polarisability energy shift for the neutron on the $m_\pi = 411$ MeV ensemble. 120

6.16. Quadratic only fit to the magnetic polarisability energy shift for the neutron on the $m_\pi = 296$ MeV ensemble. 121

6.17. Proton effective energy shift for the $m_\pi = 702$ MeV ensemble. 122

6.18. Proton effective energy shift for the $m_\pi = 570$ MeV ensemble. 123

6.19. Proton effective energy shift for the $m_\pi = 411$ MeV ensemble. 123

6.20. Proton effective energy shift for the $m_\pi = 296$ MeV ensemble. 124

6.21. Constrained quadratic fit to the proton $E\,(B) - m$ energy shift on the $m_\pi = 702$ MeV ensemble. 125

6.22. Constrained quadratic fit to the proton $E(B) - m$ energy shift on the $m_\pi = 570$ MeV ensemble. 126

6.23. Constrained quadratic fit to the proton $E(B) - m$ energy shift on the $m_\pi = 411$ MeV ensemble. 127

6.24. Constrained quadratic fit to the proton $E(B) - m$ energy shift on the $m_\pi = 296$ MeV ensemble. 127

6.25. Σ^+ effective energy shift for the $m_\pi = 702$ MeV ensemble. 129

6.26. Σ^+ effective energy shift for the $m_\pi = 411$ MeV ensemble. 130

6.27. Σ^+ effective energy shift for the $m_\pi = 296$ MeV ensemble. 130

6.28. Constrained quadratic fit to the Σ^+ $E(B) - m$ energy shifts of Figure 6.25 on the $m_\pi = 702$ MeV ensemble. 131

6.29. Constrained quadratic fit to the Σ^+ $E(B) - m$ energy shifts of Figure 6.26 on the $m_\pi = 411$ MeV ensemble. 132

6.30. Constrained quadratic fit to the Σ^+ $E(B) - m$ energy shifts of Figure 6.27 on the $m_\pi = 296$ MeV ensemble. 133

6.31. Ξ^0 effective energy shift for the $m_\pi = 702$ MeV ensemble. 134

6.32. Ξ^0 effective energy shift for the $m_\pi = 411$ MeV ensemble. 134

6.33. Ξ^0 effective energy shift for the $m_\pi = 296$ MeV ensemble. 135

6.34. Quadratic only fit of the magnetic-field induced energy shift in Figure 6.31 for the Ξ^0. 135

6.35. Quadratic only fit of the magnetic-field induced energy shift in Figure 6.32 for the Ξ^0. 136

6.36. Quadratic only fit of the magnetic-field induced energy shift in Figure 6.33 for the Ξ^0. 136

6.37. The leading order meson, M, loop contributions to the magnetic polarisability of the baryon B. These contributions have no baryon mass-splitting effects. 138

6.38. Leading-order meson, loop contributions to the magnetic polarisability of the baryon B; allowing transitions to nearby and strongly coupled octet or decuplet baryons, B' and octet-meson, M, pairs. 139

6.39. One-loop quark-flow diagrams for $p \to p\,\pi^0$. 141

6.40. The magnetic polarisability of the neutron, β^n from our chiral effective field analysis and lattice results is compared with experimental measurements. 146

6.41. Finite volume extrapolations of β^n with valence-valence coefficients appropriate for electroquenched lattice QCD simulations. 147

6.42. Finite volume extrapolations of β^n with total full QCD coefficients appropriate for fully dynamical background field lattice QCD simulations. . . . 148

6.43. The magnetic polarisability of the proton, β^p, from chiral effective field analysis and lattice results is compared with experimental measurements. 149

6.44. Finite volume extrapolations of β^p with valence-valence coefficients appropriate for electroquenched lattice QCD simulations. 150

6.45. Finite volume extrapolations of β^p with total full QCD coefficients appropriate for fully dynamical background field lattice QCD simulations. . . . 150

6.46. The magnetic polarisability of the Σ^+, β^{Σ^+}, from chiral effective field analysis and lattice results is compared with literature results. 151

6.47. Finite volume extrapolations of β^{Σ^+} with valence-valence coefficients appropriate for electroquenched lattice QCD simulations. 152

6.48. Finite volume extrapolations of β^{Σ^+} with total full QCD coefficients appropriate for fully dynamical background field lattice QCD simulations. 153

6.49. The magnetic polarisability of the Ξ^0, β^{Ξ^0}, from chiral effective field analysis and lattice results is compared with literature results. 154

6.50. Finite volume extrapolations of β^{Ξ^0} with valence-valence coefficients appropriate for electroquenched lattice QCD simulations. 155

6.51. Finite volume extrapolations of β^{Ξ^0} with total full QCD coefficients appropriate for fully dynamical background field lattice QCD simulations. . 155

6.52. Comparisons of β and β^{Σ^+} with total full QCD coefficients at each quark mass and the extrapolated, physical point. 157

6.53. Comparisons of β^n and β^{Ξ^0} with total full QCD coefficients at each quark mass and the extrapolated, physical point. 158

7.1. Charged pion effective energy shift $(E(B) + m_{\pi^+})$ from Eq. (5.24) on the $m_\pi = 702$ MeV ensemble. 163

7.2. Charged pion effective energy shift $(E(B) - m_{\pi^+})$ from Eq. (5.25) on the $m_\pi = 702$ MeV ensemble. 164

7.3. Charged pion effective energy shift $(E(B) + m_{\pi^+})$ from Eq. (5.24) on the $m_\pi = 570$ MeV ensemble. 164

7.4. Charged pion effective energy shift $(E(B) - m_{\pi^+})$ from Eq. (5.25) on the $m_\pi = 570$ MeV ensemble. 165

7.5. Charged pion effective energy shift $(E(B) + m_{\pi^+})$ from Eq. (5.24) on the $m_\pi = 411$ MeV ensemble. 165

7.6. Charged pion effective energy shift $(E(B) - m_{\pi^+})$ from Eq. (5.25) on the $m_\pi = 411$ MeV ensemble. 166

7.7. Charged pion effective energy shift $(E(B) + m_{\pi^+})$ from Eq. (5.24) on the $m_\pi = 296$ MeV ensemble. 166

7.8. Charged pion effective energy shift $(E(B) - m_{\pi^+})$ from Eq. (5.25) on the $m_\pi = 296$ MeV ensemble. 167

7.9. Constrained quadratic fit to the $m_\pi = 702$ MeV $\left(E^2(B) - m_{\pi^+}^2\right)$ energy shift formed from Figures 7.1 and 7.2. 168

7.10. Constrained quadratic fit to the $m_\pi = 570$ MeV $\left(E^2(B) - m_{\pi^+}^2\right)$ energy shift formed from Figures 7.3 and 7.4. 169

7.11. Constrained quadratic fit to the $m_\pi = 411$ MeV $\left(E^2(B) - m_{\pi^+}^2\right)$ energy shift formed from Figures 7.5 and 7.6. 169

7.12. Constrained quadratic fit to the $m_\pi = 296$ MeV $E^2(B) - m_{\pi^+}^2$ energy shift formed from Figures 7.7 and 7.8. 170

7.13. Neutral pion effective energy shift $\left(E(B)+m_{\pi_d^0}\right)$ on the $m_\pi = 702$ MeV ensemble. . . . 172

7.14. Neutral pion effective energy shift $\left(E(B)-m_{\pi_d^0}\right)$ on the $m_\pi = 702$ MeV ensemble. . . . 172

7.15. Neutral pion effective energy shift $\left(E(B)+m_{\pi_d^0}\right)$ on the $m_\pi = 570$ MeV ensemble. . . . 173

7.16. Neutral pion effective energy shift $\left(E(B)-m_{\pi_d^0}\right)$ on the $m_\pi = 570$ MeV ensemble. . . . 173

7.17. Neutral pion effective energy shift $\left(E(B)+m_{\pi_d^0}\right)$ on the $m_\pi = 411$ MeV ensemble. . . . 174

7.18. Neutral pion effective energy shift $\left(E(B)-m_{\pi_d^0}\right)$ on the $m_\pi = 411$ MeV ensemble. . . . 174

7.19. Neutral pion effective energy shift $\left(E(B)+m_{\pi_d^0}\right)$ on the $m_\pi = 296$ MeV ensemble. . . . 175

7.20. Neutral pion effective energy shift $\left(E(B)-m_{\pi_d^0}\right)$ on the $m_\pi = 296$ MeV ensemble. . . . 175

7.21. Quadratic only fit to the π_d^0 $m_\pi = 702$ MeV $\left(E^2(B)-m^2_{\pi_d^0}\right)$ energy shift formed from Figures 7.13 and 7.14. . . . 176

7.22. Quadratic only fit to the π_d^0 $m_\pi = 570$ MeV $\left(E^2(B)-m^2_{\pi_d^0}\right)$ energy shift formed from Figures 7.15 and 7.16. . . . 176

7.23. Quadratic only fit to the π_d^0 $m_\pi = 411$ MeV $\left(E^2(B)-m^2_{\pi_d^0}\right)$ energy shift formed from Figures 7.17 and 7.18. . . . 177

7.24. Quadratic only fit to the π_d^0 $m_\pi = 296$ MeV $\left(E^2(B)-m^2_{\pi_d^0}\right)$ energy shift formed from Figures 7.19 and 7.20. . . . 177

7.25. Magnetic polarisability of the pion as a function of m_π^2. . . . 180

List of tables

2.1. Light quark properties. Masses from the Particle Data Group 2019 and are defined in the $\overline{\text{MS}}$ scheme at $\mu = 2$ GeV. 4

2.2. Properties of the scalar meson nonet depicted in Figure 2.1 from the Particle Data Group. 4

2.3. Properties of the baryon octet depicted in Figure 2.2 from the Particle Data Group. 8

2.4. Properties of the baryon decuplet depicted in Figure 2.3 from the Particle Data Group. 8

2.5. Summary of indexing conventions. 10

3.1. Details of the PACS-CS ensembles used in this work. 51

4.1. Magnetic polarisability values for the neutron at each quark mass. 69

5.1. Magnetic polarisability of the neutral pion from the $\mathcal{O}(a)$-improved BFCC-fermion-action. 99

6.1. The number of sources per configuration used for each hadron type and ensemble. 113

6.2. Magnetic polarisability values for the neutron at each pion mass. 119

6.3. Magnetic polarisability values for the proton at each quark mass. 126

6.4. Magnetic polarisability values for the Σ^+ at each quark mass. 132

6.5. Magnetic polarisability values for the Ξ^0 at each quark mass. 137

6.6. Lattice magnetic polarisability values for the baryons considered at each quark mass. 137

6.7. Predicted magnetic polarisability values for the octet baryons considered herein. 156

7.1. Magnetic polarisability values for the charged pion π^+ at each quark mass. 170

7.2. Magnetic polarisability values for the neutral pion π^0 at each quark mass. 178

B.1. $SU(3)$ flavour coupling coefficients for the chiral effective field theory analysis. The header row indicates the intermediate baryon species in the meson-baryon loop dressing. Through conservation of quark flavour, one can identify the baryon which is being dressed. 201

B.2. Chiral coefficients for the leading-order loop integral contributions for the neutron. 202

B.3. Chiral coefficients for the leading-order loop integral contributions for the proton. 203

B.4. Chiral coefficients for the leading-order loop integral contributions for the Σ^+. 204

B.5. Chiral coefficients for the leading-order loop integral contributions for the Ξ^0. 205

B.6. Zero-field baryon effective masses. 206

Chapter 1.

Introduction

An understanding of the universe at the sub-nuclear scale is provided by the Standard Model (SM) of particle physics. The three fundamental types of interactions described by the SM are the strong, electromagnetic (EM) and weak (WI) interactions. The fourth interaction that governs particle behaviour is the gravitational interaction which is not addressed herein.

The forces governed by the SM are all formulated in terms of gauge field theories. The strong interaction is felt by particles with colour charge such as the quarks and gluons. The EM force is experienced by electrically charged particles while the weak force acts upon the weak isospin of particles. Each force is mediated by a force carrier, an exchange of gluons for the strong, the exchange of photons for the EM, and the $W^{\pm}$ and Z^{0} bosons for the WI.

The interactions of the standard model divide the elementary particles into two categories: matter particles and force carriers. The matter particles are further divided into the quarks which have colour charge and hence interact via the strong force and the leptons which do not possess colour charge. The force carriers are the gluon for the strong force, photon for the EM force and the $W^{\pm}$ and Z^{0} bosons for the WI. The gluon also self-interacts via the strong force. This gives rise to interesting features such as confinement, a property where only colour neutral bound states can be observed at low to moderate energies. An additionary elementary particle of the SM is the Higgs boson. The Higgs boson is a scalar particle, related to electroweak symmetry breaking and mass generation of the otherwise massless elementary particles [1–3].

Quantum Chromodynamics (QCD) is the gauge field theory which describes the strong force. This is a non-Abelian theory and as such, self-interactions of the gluon arise which lead to the non-perturbative nature of QCD at low energies. This non-perturbative nature prompts two main approaches to calculations. The first is a continuum approach where QCD is studied at high energies. The second, used in this thesis, is to formulate an ab-initio non-continuum theory in which nonperturbative calculations are made and then related to the physical, continuum limit.

This latter approach is lattice QCD where the path integral approach to QCD is formulated on a finite, discretised lattice of space-time. The calculations involved are computationally expensive requiring the use of supercomputing resources.

We present here lattice QCD calculations of hadron energies and electromagnetic properties when a uniform, external magnetic field is applied to the simulation. This grants access to the magnetic polarisabilities of octet baryons and mesons. Techniques to improve the efficacy of extraction of these properties and improve the signal of the lattice calculations are investigated. Ratios of two-point correlation functions are taken to form energy shifts from which quantities such as the magnetic polarisability can be extracted.

A brief introduction to the essential components of QCD is presented in Chapter 2. Chapter 3 introduces lattice QCD and the background field method. The magnetic polarisability of the neutron is calculated using a novel technique which improves the signal quality in Chapter 4. An inexpensive solution to a problem of additive mass renormalisation in Wilson fermions introduced through the introduction of the background field method is proposed and shown in Chapter 5. This solution is used in Chapter 6 where an extension of the techniques and method in Chapter 4 for the neutron is used to calculate the magnetic polarisability of the neutron, proton and a selection of hyperons. The magnetic polarisability of the neutral and charged pions is considered in Chapter 7. Finally in Chapter 8 conclusions and proposals for future work are presented.

Chapter 2.

Quantum Chromodynamics

2.1. Hadronic spectrum

Hadrons are strongly interacting composite particles [4]. While it is the elementary quarks and gluons which strongly interact, it is more practical to consider the hadrons due to the aforementioned confinement of quarks. A brief overview of the low-lying spectrum of hadrons [5] will be a useful primer for this thesis.

This overview is not exhaustive and intended merely to familiarise the reader with the low-lying hadronic spectrum considered in this work.

2.1.1. Quark model

A portion of the light hadronic spectrum can be characterised by a set of quantum numbers

- Baryon number B,
- Charge Q,
- Strangeness S,

where light means that only hadrons composed of the three lightest quarks; the up, down and strange are considered. A full characterisation of the light hadronic spectrum requires the additional spin, parity and (where applicable) $G-$parity quantum numbers [3, 7].

Table 2.1. Light quark properties. Masses from the Particle Data Group 2019 [3] and are defined in the $\overline{\text{MS}}$ [6] scheme at $\mu = 2$ GeV.

Flavour	Q	S	B	I	I_3	Y	Mass (MeV)
up	$\frac{2}{3}\,e$	0	$\frac{1}{3}$	$\frac{1}{2}$	$\frac{1}{2}$	$\frac{1}{3}$	$2.16\,\left(^{+49}_{-26}\right)$
down	$-\frac{1}{3}\,e$	0	$\frac{1}{3}$	$\frac{1}{2}$	$-\frac{1}{2}$	$\frac{1}{3}$	$4.67\,\left(^{+48}_{-17}\right)$
strange	$-\frac{1}{3}\,e$	-1	$\frac{1}{3}$	0	0	$-\frac{2}{3}$	$93\,\left(^{+11}_{-\ 5}\right)$

Table 2.2. Properties of the scalar meson nonet depicted in Figure 2.1 from the Particle Data Group [3].

Quark Content	Meson	Mass (MeV)	I_3	I	S
$d\,\overline{s}$	K^0	497.611 ± 0.013	$-\frac{1}{2}$	$\frac{1}{2}$	1
$u\,\overline{s}$	K^+	493.677 ± 0.016	$\frac{1}{2}$	$\frac{1}{2}$	1
$u\,\overline{d}$	π^+	139.57061 ± 0.0002	1	1	0
$\frac{d\,\overline{d} - u\,\overline{u}}{\sqrt{2}}$	π^0	134.9770 ± 0.0005	1	0	0
$\frac{u\,\overline{u} + d\,d - 2\,s\,\overline{s}}{\sqrt{6}}$	η	547.862 ± 0.017	0	0	0
$\frac{u\,\overline{u} + d\,\overline{d} + s\,\overline{s}}{\sqrt{3}}$	η'	957.78 ± 0.06	0	0	0
$d\,\overline{u}$	π^-	139.57061 ± 0.0002	-1	-1	0
$s\,\overline{u}$	K^-	493.677 ± 0.016	$\frac{1}{2}$	$\frac{1}{2}$	-1

The properties and quantum numbers of these three light quark species are described in Table 2.1. Baryons have baryon number $B = 1$, the strangeness S describes the number of strange valence quarks in the hadron. The label I defines the isospin of the quark which is conserved during strong decay processes and associated with the up and down quarks. The composite quantum numbers, isospin projection I_3

$$I_3 = \frac{Q}{e} - \left(\frac{S+B}{2}\right), \tag{2.1}$$

where e is the magnitude of the electrons charge, $|e| = 1.602\,176\,634 \times 10^{-19}$ C [8], and hypercharge Y

$$Y = S + B, \tag{2.2}$$

are introduced to aid in the classification of hadrons.

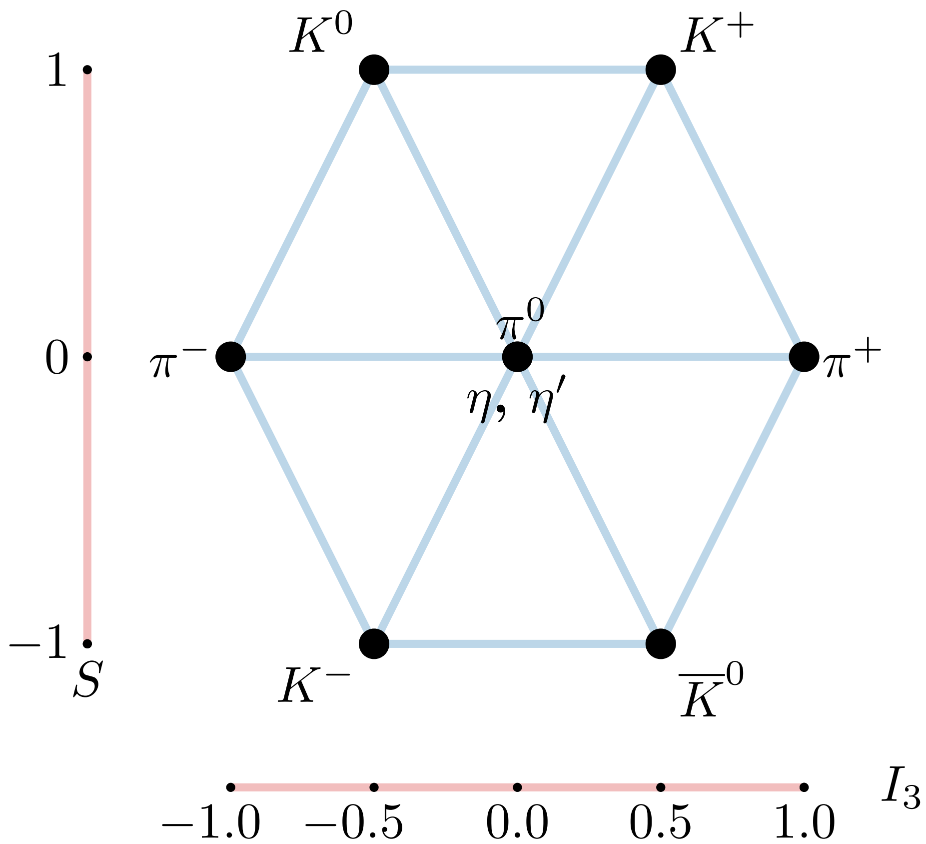

Figure 2.1. Pseudoscalar meson nonet with $J^P = 0^-$.

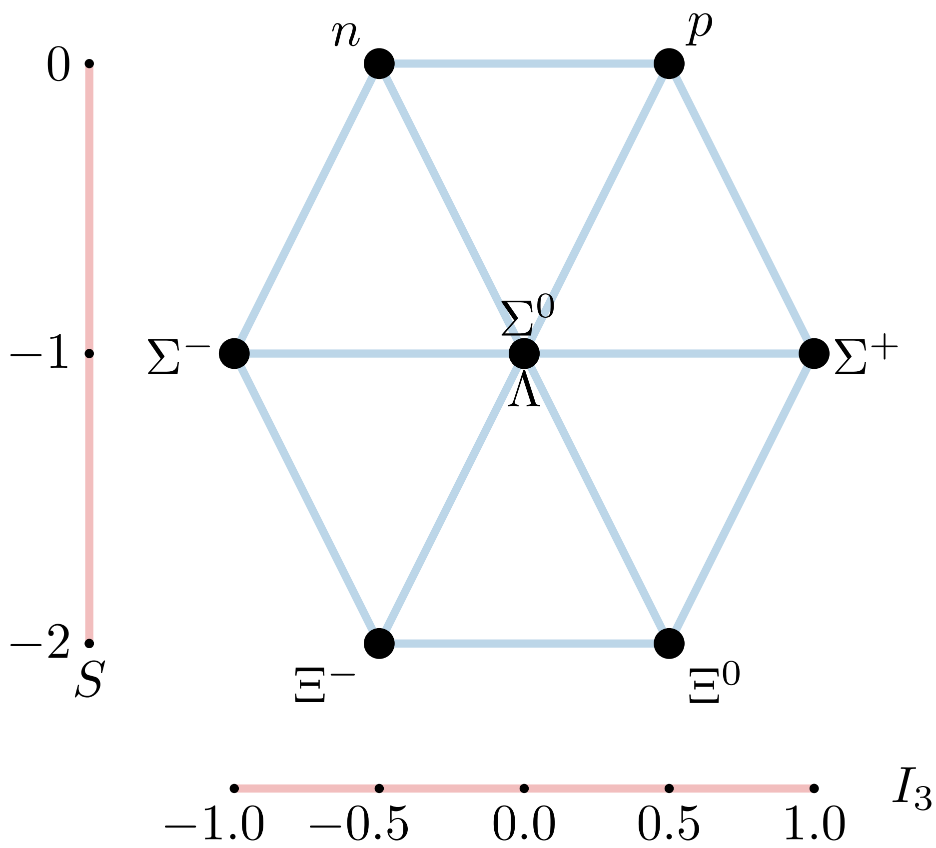

Figure 2.2. Baryon octet with $J^P = \frac{1}{2}^+$.

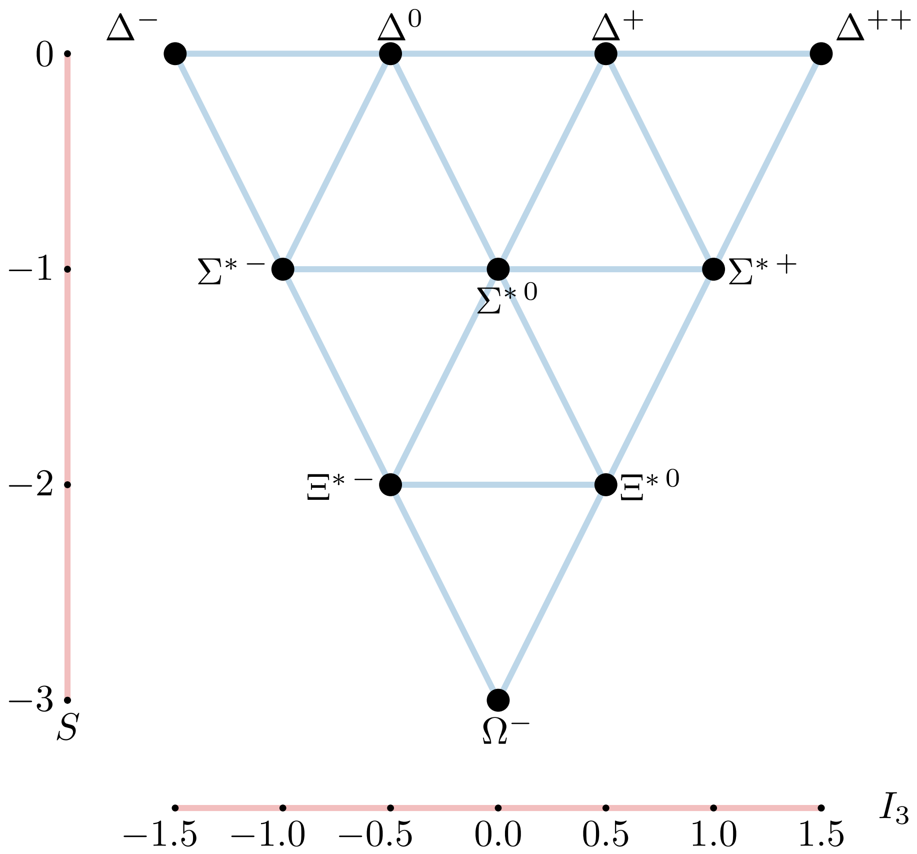

Figure 2.3. Baryon decuplet with $J^P = \frac{3}{2}^+$.

Table 2.3. Properties of the baryon octet depicted in Figure 2.2 from the Particle Data Group [3].

Quark Content	Baryon	Mass (MeV)	I_3	I	S
$u\,d\,d$	n	$939.5654133 \pm 0.0000058$	$-\frac{1}{2}$	$\frac{1}{2}$	0
$u\,u\,d$	p	$938.2720813 \pm 0.0000058$	$\frac{1}{2}$	$\frac{1}{2}$	0
$d\,d\,s$	Σ^-	1197.45 ± 0.04	-1	1	-1
$u\,d\,s$	Λ	1115.683 ± 0.006	0	0	-1
$u\,d\,s$	Σ^0	1192.642 ± 0.024	0	1	-1
$u\,u\,s$	Σ^+	1189.37 ± 0.06	1	1	-1
$d\,s\,s$	Ξ^-	1321.71 ± 0.07	$-\frac{1}{2}$	$\frac{1}{2}$	-2
$u\,s\,s$	Ξ^0	1314.86 ± 0.20	$\frac{1}{2}$	$\frac{1}{2}$	-2

Table 2.4. Properties of the baryon decuplet depicted in Figure 2.3 from the Particle Data Group [3].

Quark Content	Baryon	Mass (MeV)	I_3	I	S
$d\,d\,d$	Δ^-	1232 ± 2	$-\frac{3}{2}$	$\frac{3}{2}$	0
$u\,d\,d$	Δ^0	1232 ± 2	$-\frac{1}{2}$	$\frac{3}{2}$	0
$u\,u\,d$	Δ^+	1232 ± 2	$\frac{1}{2}$	$\frac{3}{2}$	0
$u\,u\,u$	Δ^{++}	1232 ± 2	$\frac{3}{2}$	$\frac{3}{2}$	0
$d\,d\,s$	$\Sigma^{*\,-}$	1387.2 ± 0.5	-1	1	-1
$u\,d\,s$	$\Sigma^{*\,0}$	1383.7 ± 1.0	0	1	-1
$u\,u\,s$	$\Sigma^{*\,+}$	1382.80 ± 0.35	1	1	-1
$d\,s\,s$	$\Xi^{*\,-}$	1535.2 ± 0.8	$-\frac{1}{2}$	$\frac{1}{2}$	-2
$u\,s\,s$	$\Xi^{*\,0}$	1531.78 ± 0.34	$-\frac{1}{2}$	$\frac{1}{2}$	-2
$s\,s\,s$	Ω^-	1672.43 ± 0.32	0	0	-3

The *eight-fold* way was introduced by Gell-Mann [9] and Ne'eman [10] and organised these hadrons based upon their charge and strangeness. The strangeness S and isospin projection I_3 form the two axes of the hadron spectrum diagrams in Figures 2.1, 2.2 and 2.3. The *valence* quark content in the hadrons depicted herein is shown in Tables 2.2, 2.3 and 2.4 along with their masses.

A meson is a quark-anti quark pair $q\,\overline{q}$, corresponding to baryon number $B = 0$. The pseudoscalar nonet depicted in Figure 2.1 have net spin zero as the quark and anti-quark are spin anti-aligned. These meson states also have a zero angular momentum state making total angular momentum $J = 0$ and are of negative parity.

Baryons are hadrons which have baryon number $B = 1$; that is in this quark model, they are bound states of three quarks $q\,q\,q$. The baryon octet in Figure 2.2 have positive parity and $J^P = \frac{1}{2}^+$ while the decuplet of Figure 2.3 has $J^P = \frac{3}{2}^+$, where P represents the parity. The quark spins are coupled such that the baryon is in the lowest energy state, resulting in a net overall spin of $\frac{1}{2}$.

The baryons discussed thus far can be further divided into those with and without strange valence quarks. Baryons with non-zero strangeness and no heavy quarks are known as *hyperons*. Hyperons are investigated in Chapter 6.

2.2. Quantum Chromodynamics

Here we follow the discussion and notation of Refs. [11], [12], [13] and [14].

The Quantum Chromodynamics (QCD) Lagrangian density which describes the dynamics of strongly interacting particles and provides a natural starting point for investigations into the particle spectrum is

$$\mathcal{L}_{QCD}(x) = \left(\overline{\psi}_f\right)^i_\alpha (x)\, \delta_{fg} \left[i\, (\gamma^\mu)_{\alpha\beta}\, (D_\mu)^{ij}(x) - m_g \delta_{\alpha\beta}\, \delta^{ij}\right] (\psi_g)^j_\beta (x) \\ - \frac{1}{4}\, (G_{\mu\nu})^a (x)\, (G^{\mu\nu})^a (x). \tag{2.3}$$

Here $(\psi_f)^i_\alpha$ are four-component spinor fields representing the quarks with flavour f, colour i and Dirac index α, m is the diagonal bare mass matrix, the gamma matrices γ^μ are in the Dirac representation and $(D_\mu)^{ij}$ is the covariant derivative

$$(D_\mu)^{ij}(x) = \delta^{ij}\partial_\mu - i\,g\,\,(t^a)^{ij} A^a_\mu(x). \tag{2.4}$$

The QCD coupling constant is g and t^a are the eight 3×3 Gell-Mann matrices which are the generators of $SU(3)$, displayed in Eq. (A.7). This can be written more compactly by setting

$$D_\mu(x) = \partial_\mu - i\,g\,A_\mu(x), \tag{2.5}$$

Table 2.5. Summary of indexing conventions.

Index	Span	Description
i, j, k, l	$1, 2, 3$	colour index in fundamental representation of $SU(3)$
a, b, c	$1, \ldots, 8$	colour index in adjoint representation of $SU(3)$
f, g, h	$1, \ldots, n_f$ or u, d, s, c, b, t	flavour index
α, β, ζ	$1, \ldots, 4$	Dirac index
μ, ν	$1, \ldots, 4$	Lorentz index

for $A_\mu(x) = (t^a)\, A^a_\mu(x)$ where colour indices have been suppressed. This will be useful in later sections. The field strength tensor is

$$G^{(a)}_{\mu\nu}(x) = \partial_\mu A^a_\nu(x) - \partial_\nu A^a_\mu + g f^{abc} A^b_\mu(x) A^c_\nu(x), \tag{2.6}$$

where f^{abc} are the totally antisymmetric structure constants of $SU(3)$ and A^a_μ are Lorentz vector fields representing the gluons. The indices in each of these equations are described in Table 2.5.

The QCD Lagrangian, Eq. (2.3), is required to be invariant under local $SU(3)$ gauge transformations of the form

$$(\psi_f)^i_\alpha(x) \to \left(\psi'_f\right)^i_\alpha(x) \quad = \Omega^{ij}(x)\,(\psi_f)^j_\alpha(x), \tag{2.7}$$

$$\left(\overline{\psi}_f\right)^i_\alpha(x) \to \left(\overline{\psi'}_f\right)^i_\alpha(x) \quad = \left(\overline{\psi}_f\right)^j_\alpha \Omega^{*,ji}(x), \tag{2.8}$$

$$(t^a)^{ij} A^a_\mu(x) \to (t^a)^{ij} A'^a_\mu(x) = \Omega^{ik}(x)\,(t^a)^{kl} A_\mu(x)\left(\Omega^{-1}\right)^{lj}(x) + \frac{i}{g}\left(\partial_\mu \Omega^{ik}(x)\right)\left(\Omega^{-1}\right)^{kj}(x), \tag{2.9}$$

where $\Omega^{ij}(x) = \mathrm{e}^{\left(i\omega^a(x)\lambda^{ij}_a\right)}$ is an element of $SU(3)$, with $\omega^a(x)$ a phase factor at each point in space-time. Henceforth we will suppress flavour, Dirac, colour and adjoint-colour indices such that Eq. (2.3) may be written

$$\mathcal{L}_{QCD}(x) = \overline{\psi}(x)\,\left[i\gamma^\mu D_\mu(x) - m\right]\psi(x) - \frac{1}{4}\,\mathrm{Tr}\left(G_{\mu\nu}(x)\,G^{\mu\nu}(x)\right). \tag{2.10}$$

This may be written in terms of the fermionic and gluonic contributions

$$\mathcal{L}_{QCD}(x) = \mathcal{L}_F(x) + \mathcal{L}_G(x), \tag{2.11}$$

for

$$\mathcal{L}_F(x) = \overline{\psi}(x)\, \left[i\gamma^\mu\, D_\mu(x) - m\right]\, \psi(x), \tag{2.12}$$

$$\mathcal{L}_G(x) = -\frac{1}{4}\,\mathrm{Tr}\left(G_{\mu\nu}(x)\, G^{\mu\nu}(x)\right). \tag{2.13}$$

2.2.1. Observables in the path integral formalism

QCD is a quantum field theory and so observables can be calculated from vacuum expectation values using the Feynman path integral formalism. In this formalism, a path integral over all possible field configurations, $\psi, \overline{\psi}$ and all possible gauge field configurations A_μ gives the vacuum expectation value of a time ordered operator $\langle\Omega|T\,\hat{\mathcal{O}}|\Omega\rangle$

$$\langle\Omega|T\,\hat{\mathcal{O}}\left[\psi, \overline{\psi}, A_\mu\right]|\Omega\rangle = \frac{1}{\mathcal{Z}}\int \mathcal{D}\psi(x)\,\mathcal{D}\overline{\psi}(x)\,\mathcal{D}A_\mu(x)\,\hat{\mathcal{O}}\,\mathrm{e}^{iS_{QCD}\left[\psi,\overline{\psi},A_\mu\right]}, \tag{2.14}$$

where Ω denotes the vacuum state and the QCD action is

$$S_{QCD}\left[\psi, \overline{\psi}, A_\mu\right] \;=\; \int d^4x\,\mathcal{L}_{QCD}(x) \;\equiv\; S_F\left[\psi, \overline{\psi}, A_\mu\right] + S_G\left[\psi, \overline{\psi}, A_\mu\right], \tag{2.15}$$

for appropriately defined S_F and S_G. The partition function $\mathcal{Z}$ is

$$\mathcal{Z} \equiv \int \mathcal{D}\psi(x)\,\mathcal{D}\overline{\psi}(x)\,\mathcal{D}A_\mu(x)\,\mathrm{e}^{iS_{QCD}\left[\psi,\overline{\psi},A_\mu\right]}. \tag{2.16}$$

As a relevant example, consider the operator $\hat{\mathcal{O}}$ to be the time ordered product of (single flavour) quark field creation and annihilation operators, then

$$\begin{aligned}&\langle\Omega|T\,\psi(x_1)\;\psi(x_2)\;\overline{\psi}(x_1')\;\overline{\psi}(x_2')\,|\Omega\rangle = \\ &\qquad \frac{1}{\mathcal{Z}}\int \mathcal{D}\psi(x)\,\mathcal{D}\overline{\psi}(x)\,\mathcal{D}A_\mu(x)\,\psi(x_1)\;\psi(x_2)\;\overline{\psi}(x_1')\;\overline{\psi}(x_2')\;\mathrm{e}^{iS_{QCD}\left[\psi,\overline{\psi},A_\mu\right]}.\end{aligned} \tag{2.17}$$

As the fermion fields obey Grassman algebra [15], the Grassmanian integration over the fermion fields produces a sum over all possible contractions of $\psi(x_i)\;\overline{\psi}\left(x_j'\right)$. Here, for simplicity only four possible spatial locations are considered. These contractions each produce a quark propagator $S\left(x_i, x'_j\right)$

$$M^{ki}_{\alpha'\alpha}\left(z, x_i\right) \, S^{ij}_{\alpha\beta}\left(x_i, x'_j\right) = \delta^{kj} \, \delta_{\alpha'\beta} \, \delta\left(z - x_i\right). \tag{2.18}$$

The fermion matrix has form $iM = [i\gamma^\mu \, D_\mu(x) - m]$. Then Grassman integration produces

$$\begin{aligned}\int \mathcal{D}\psi(x) \, \mathcal{D}\overline{\psi}(x) \, \psi\left(x_1\right) \, \psi\left(x_2\right) \, \overline{\psi}\left(x'_1\right) \, \overline{\psi}\left(x'_2\right) \, \mathrm{e}^{iS_F} &= \det M\left(A_\mu\right) \\ &\times \left[M^{-1}\left(x_1, x'_1\right) \, M^{-1}\left(x_2, x'_2\right) + M^{-1}\left(x_1, x'_2\right) \, M^{-1}\left(x_2, x'_1\right)\right]\end{aligned} \tag{2.19}$$

and so Eq. (2.17) may be written

$$\begin{aligned}\langle\Omega| T \, \psi\left(x_1\right) \, \psi\left(x_2\right) \, \overline{\psi}\left(x'_1\right) \, \overline{\psi}\left(x'_2\right) |\Omega\rangle &= \frac{1}{\mathcal{Z}} \int \mathcal{D}A_\mu(x) \, \det M\left(A_\mu\right) \mathrm{e}^{iS_G} \\ &\times \left[M^{-1}\left(x_1, x'_1\right) \, M^{-1}\left(x_2, x'_2\right) + M^{-1}\left(x_1, x'_2\right) \, M^{-1}\left(x_2, x'_1\right)\right].\end{aligned} \tag{2.20}$$

This expression, and that of the partition function $\mathcal{Z}$ are reminiscent of the partition function of statistical mechanics [16]. Here though the exponent is imaginary rather than negative, rendering statistical mechanics methods ineffectual. The solution is to formulate the theory in Euclidean (rather than Minkowski) space-time where

$$\vec{x} \to \vec{x} \tag{2.21}$$

$$x^0 \to -ix_4 \tag{2.22}$$

$$A^0 \to iA_4 \tag{2.23}$$

$$S_{QCD} \to iS^{EUCL}_{QCD}, \tag{2.24}$$

and the gamma matrices are now in the Sakurai representation of Eqs. (A.5) and (A.6). This formulation has metric $\delta_{\mu\nu} = \mathrm{diag}\,(+1, \, +1, \, +1, \, +1)$ and so no distinction between contravariant (upper) and covariant (lower) indices is required [17].

The expectation value is then

$$\begin{aligned}\langle\Omega| T \, \psi\left(x_1\right) \, \psi\left(x_2\right) \, \overline{\psi}\left(x'_1\right) \, \overline{\psi}\left(x'_2\right) |\Omega\rangle &= \frac{1}{\mathcal{Z}} \int \mathcal{D}\, A_\mu(x) \, \det M\left(A_\mu\right) \mathrm{e}^{-S_G} \\ &\times \left[M^{-1}\left(x_1, x'_1\right) \, M^{-1}\left(x_2, x'_2\right) + M^{-1}\left(x_1, x'_2\right) \, M^{-1}\left(x_2, x'_1\right)\right].\end{aligned} \tag{2.25}$$

The formulation of the path integral in Euclidean time allows the vacuum expectation value of Eq. (2.14) to be interpreted as a weighted average across all possible field configurations of the operator. This set of field configurations are distributed with probability [11]

$$\mathcal{P}\left[\psi^i, \overline{\psi^i}, A_\mu^i\right] \propto \exp\left(-S_{QCD}^{EUCL}\left[\psi^i, \overline{\psi^i}, A_\mu^i\right]\right) \tag{2.26}$$

and the vacuum expectation value is then the average value across this sub-ensemble

$$\langle\Omega| T\, \hat{\mathcal{O}}\left[\psi, \overline{\psi}, A_\mu\right] |\Omega\rangle \approx \frac{1}{N}\sum_{i=1}^{N} \hat{\mathcal{O}}\left[\left(M^{-1}\right)^i, A_\mu^i\right]. \tag{2.27}$$

This expression can now be evaluated using a discretised, non-perturbative method known as lattice QCD which will be discussed in the following chapter.

Chapter 3.

Lattice QCD

Lattice QCD is the ab-initio method by which QCD can be studied at low energies non-perturbatively. Here QCD is formulated on a finite, discretised lattice in Euclidean space time. As alluded to earlier, the QCD Lagrangian can be separated into fermionic and gluonic contributions. The discretisation of each of these components will be considered separately.

The path integral on the lattice, quark propagators and the construction and properties of two-point correlation functions are discussed in order to provide an introduction for the concepts and calculations used in following chapters. More detailed overviews of lattice QCD can be found in Refs. [15], [17] and [11] which inspired the treatment herein.

The background field method, a technique that can be used within lattice QCD which is the foundation of this thesis, is also discussed in this chapter.

3.1. Discretisation

The continuous space-time of the physical world x^μ, is replaced with a four-dimensional grid of points in space-time known as a "lattice". The transformation used is

$$x^\mu \to x^\mu = a\, n^\mu, \tag{3.1}$$

where n^μ is a vector of integers and a is the minimum distance between points on the lattice called the "lattice spacing". The spatial dimensions are typically taken to be $\mu = 1, 2, 3$ and time to be $\mu = 4$. The vector n^μ has takes values in each dimension of

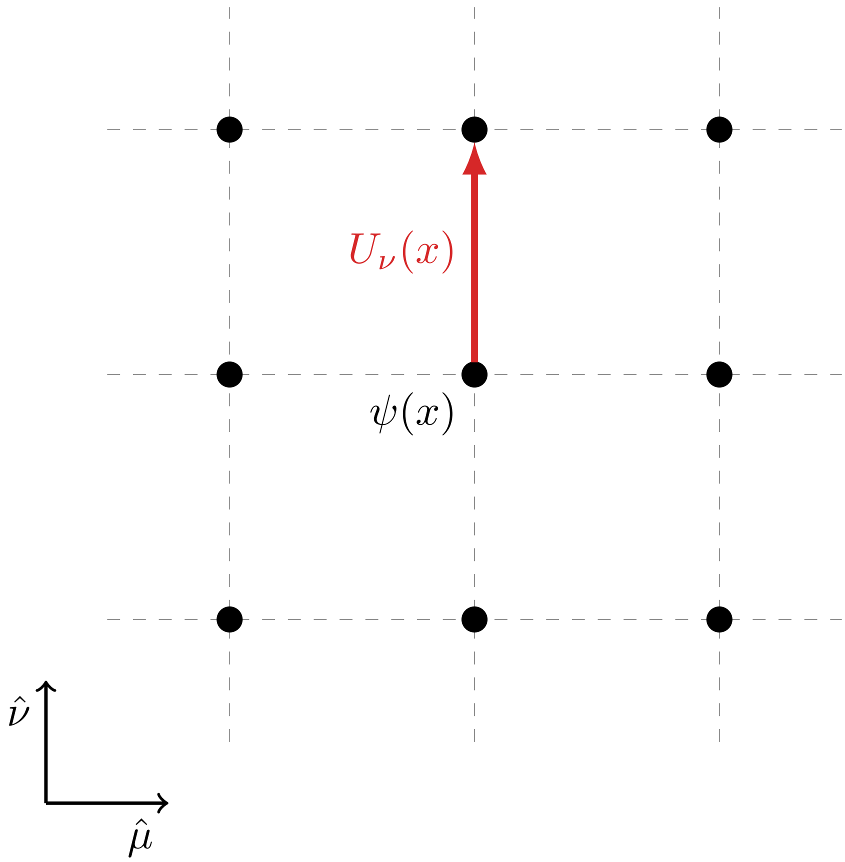

Figure 3.1. Two-dimensional representation of the discretised segment of space-time. Link variables U_μ lie in between lattice sites x while fermion fields ψ are on the lattice sites.

one to N_x, N_y, N_z, N_t for $\mu = 1,2,3,4$ respectively. Typically the spatial dimensions are chosen to have the same extent, labelled N_s.

In the discretised theory, derivatives are replaced by finite differences

$$\partial_\mu \psi(x) \to \frac{1}{2\,a} \left(\psi\left(x + a\,\hat{\mu}\right) - \psi\left(x - a\,\hat{\mu}\right)\right), \tag{3.2}$$

where $\hat{\mu}$ is a unit-vector in direction of μ and integrals over Euclidean space-time are replaced by sums over the lattice volume

$$\int d^4x \to a^4 \sum_{n^\mu} = \sum_{x^\mu} \tag{3.3}$$

Then, recalling the transformation properties of fermion fields in QCD in Eqs. (2.7) and (2.8) where $\Omega\,(x)$ is now an element of $SU(3)$ for each lattice site x, consider the discretised derivative $\overline{\psi}(x)\,\partial_\mu\,\psi(x)$

$$
\begin{aligned}
\overline{\psi}(x)\,\frac{1}{2\,a}\,\left(\psi\,(x+a\,\hat{\mu})-\psi\,(x-a\,\hat{\mu})\right) \xrightarrow{\Omega}& \\
&\frac{1}{2\,a}\,\big[\overline{\psi}(x)\,\Omega^\dagger\,(x)\;\Omega\,(x+a\,\hat{\mu})\;\psi\,(x+a\,\hat{\mu}) \\
&-\overline{\psi}(x)\,\Omega^\dagger\,(x)\;\Omega\,(x-a\,\hat{\mu})\,\psi\,(x-a\,\hat{\mu})\big]\,.
\end{aligned}
\tag{3.4}
$$

This is not gauge invariant. Hence we introduce the gluon fields, represented by link variables: parallel transport operators along the path from one lattice site to the next

$$
U_\mu(x) = P\;\exp\left[-i\,g\int_x^{x+a\,\hat{\mu}} dz_\mu A_\mu(z)\right], \tag{3.5}
$$

where P denotes the path ordering. A two-dimensional representation of this discretised space is shown in Figure 3.1 where the link variable $U_\nu(x)$ in the $\mu-\nu$ plane and a fermion field ψ on a lattice site x are shown.

Under a local gauge transformation Ω, these transform as

$$
U_\mu(x) \xrightarrow{\Omega} \Omega\,(x)\;U_\mu(x)\,\Omega^\dagger(x+a\,\hat{\mu}), \tag{3.6}
$$

$$
U^\dagger_\mu(x) \xrightarrow{\Omega} \Omega(x+a\,\hat{\mu})\,U^\dagger_\mu(x)\,\Omega^\dagger(x). \tag{3.7}
$$

This is shown in Appendix B.1. The covariant derivative is then discretised as the covariant finite difference operator

$$
\nabla_\mu(x)\,\psi(x) = \frac{1}{2\,a}\,\left(U_\mu(x)\,\psi\,(x+a\,\hat{\mu}) - U^\dagger_\mu(x-a\,\hat{\mu})\,\psi\,(x-a\,\hat{\mu})\right), \tag{3.8}
$$

which transforms appropriately to produce the gauge invariant term required for the fermion action as shown below

$$
\begin{aligned}
\overline{\psi}(x)\,\nabla_\mu(x)\,\psi(x) \xrightarrow{\Omega}& \\
&\frac{\overline{\psi}(x)\,\Omega^\dagger\,(x)}{2\,a}\,\big[\Omega\,(x)\;U_\mu(x)\,\Omega^\dagger\,(x+a\,\hat{\mu})\;\Omega\,(x+a\,\hat{\mu})\;\psi\,(x+a\,\hat{\mu}) \\
&\qquad -\Omega\,(x)\;U^\dagger_\mu\,(x-a\,\hat{\mu})\;\Omega^\dagger\,(x-a\,\hat{\mu})\,\Omega\,(x-a\,\hat{\mu})\;\psi\,(x-a\,\hat{\mu})\big] \\
&=\frac{\overline{\psi}(x)}{2\,a}\,\big[U_\mu(x)\,\psi\,(x+a\,\hat{\mu}) - U^\dagger_\mu\,(x-a\,\hat{\mu})\;\psi\,(x-a\,\hat{\mu})\big]\,.
\end{aligned}
\tag{3.9}
$$

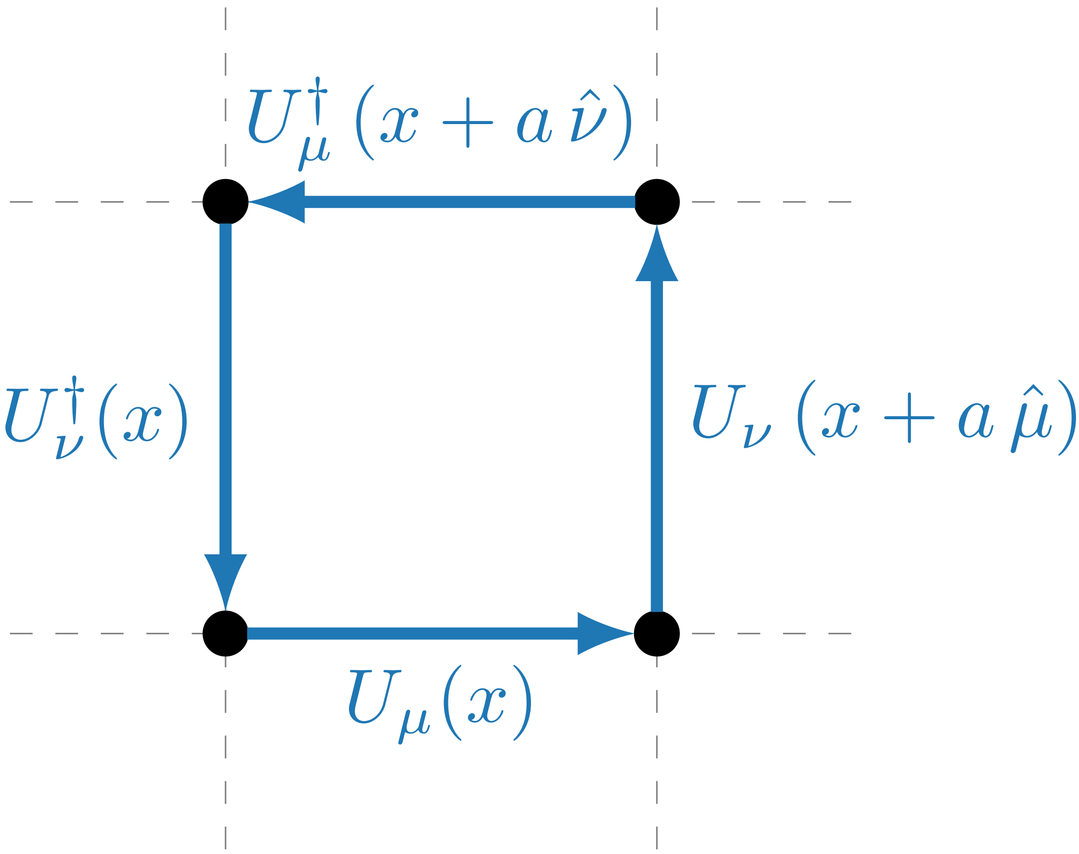

Figure 3.2. The simplest closed loop of link variables, the plaquette $P_{\mu\nu}(x)$.

3.2. Gluonic Action

The gluonic term of the QCD action density in Euclidean metric is

$$S_G\,(x) = -\frac{1}{4}\,\mathrm{Tr}\,(G_{\mu\nu}\,(x)\;G_{\mu\nu}\,(x))\,, \tag{3.10}$$

and recalling the link variable formulation of Eq. (3.5) we seek a gauge invariant expression which in the continuum limit takes this form. We hence consider a closed loop of link variables, as illustrated in Figure 3.2 for the 1×1 closed loop known as a plaquette

$$P_{\mu\nu}(x) = U_\mu(x)\,U_\nu(x + a\,\hat{\mu})\,U_\mu^\dagger(x + a\,\hat{\nu})\,U_\nu^\dagger(x). \tag{3.11}$$

This plaquette has the value

$$P_{\mu\nu}(x) = \exp\left(i\,g\,a^{\,2}G_{\mu\nu}(x) + \mathcal{O}\left(a^3\right)\right)\,, \tag{3.12}$$

as shown in Appendix B.2. A simple Taylor expansion of $P_{\mu\nu}$ produces

$$P_{\mu\nu}(x) = \mathbb{I} + i\, g\, a^{2} G_{\mu\nu}(x) - \frac{1}{2} g^2 a^4 G_{\mu\nu}(x) G_{\mu\nu}(x) + \mathcal{O}\left(a^3\right) \tag{3.13}$$

We recognise now the gluonic action in the real part of the plaquette and take the trace to obtain

$$\begin{aligned} \frac{1}{2} \mathrm{Tr}\left(P_{\mu\nu}(x) + P^{\dagger}_{\mu\nu}(x)\right) &= \mathrm{Tr}\left(\mathbb{1} - \frac{1}{2} g^2 a^4 G_{\mu\nu}(x)\, G_{\mu\nu}(x)\right) \\ &= 3 - \frac{1}{2} g^2 a^4\, \mathrm{Tr}\left(G_{\mu\nu}(x)\, G_{\mu\nu}(x)\right) + \mathcal{O}\left(a^6\right), \end{aligned} \tag{3.14}$$

which has $\mathcal{O}\left(a^2\right)$ errors [18, 19]. The Wilson gauge action [20] is hence

$$S_G^W\left[U_\mu\right] = \beta \sum_x \sum_{\mu>\nu} \left[1 - \frac{1}{3}\frac{1}{2} \mathrm{Tr}\left(P_{\mu\nu}(x) + P^{\dagger}_{\mu\nu}(x)\right)\right]. \tag{3.15}$$

Here $\beta \equiv 6/g^2$ is the inverse lattice coupling, chosen such that in the continuum limit $a \to 0$, the continuum action is obtained. The sum over $\mu > \nu$ is taken in order to avoid double-counting of plaquettes.

In practice, improved lattice gauge actions with additional irrelevant terms are used; the process of determining additional, irrelevant terms is known as Symanzik improvement [21, 22]. Additional terms are generated by introducing Wilson loops of larger dimension, such as the 1×2 loop shown in Figure 3.3 with some relative coefficient on the additional Wilson loops.

The approach used by the Iwasaki gauge action [23] is to formulate the renormalisation group equations [24] on the lattice and hence set the coefficients of the irrelevant operators such that they are as close as possible to the renormalised trajectory. The set of field configurations, known as gauge field configurations which are relevant to this thesis are supplied by the PACS-CS collaboration [25] and use an Iwasaki gauge action of the form

$$S_G^{Iwasaki}\left[U_\mu\right] = \beta \sum_x \sum_{\mu>\nu} \left[c_0 \mathrm{Tr}\left(R^{1\times1}_{\mu\nu}(x) + \left(R^{1\times1}_{\mu\nu}\right)^{\dagger}(x)\right) + c_1 \mathrm{Tr}\left(R^{1\times2}_{\mu\nu}(x) + \left(R^{1\times2}_{\mu\nu}\right)^{\dagger}(x)\right)\right] \tag{3.16}$$

where $R^{1\times1}_{\mu\nu}$ is just the plaquette of Eq. (3.11) and $R^{1\times2}_{\mu\nu}$ is the 1×2 loop illustrated in Figure 3.3. The coefficients c_0 and c_1 are $c_0 = 3.648$ and $c_1 = -0.331$ respectively [25].

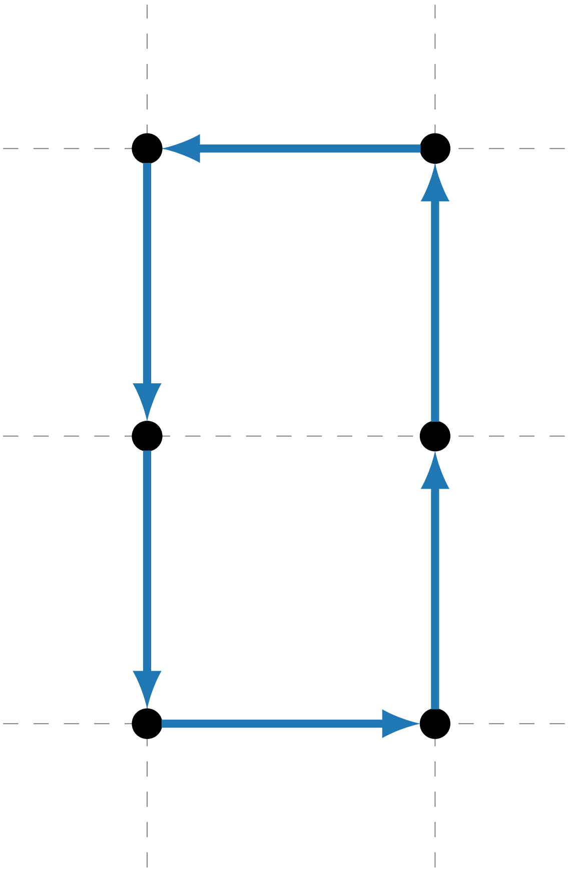

Figure 3.3. Link variables for construction of $R_{\mu\nu}^{1\times 2}$.

3.3. Fermion Action

The fermionic term of the (Euclidean) QCD action is

$$S_F = \overline{\psi}(x)\, [\gamma^\mu\, D_\mu(x) + m]\, \psi(x). \tag{3.17}$$

Using the definition of the covariant finite difference operator defined in Eq. (3.8) this may be written

$$\begin{aligned} S_F &= a^4 \sum_x \overline{\psi}(x)\, [\gamma^\mu\, \nabla_\mu(x) + m]\, \psi(x) \\ &= a^4 \sum_x \overline{\psi}(x)\, \left[i\, g\, \not{A} + \not{\partial} + \mathcal{O}\left(a^2\right) + m\right]\, \psi(x), \end{aligned} \tag{3.18}$$

where the second line is shown in Appendix B.3. Hence it is clear that while this discretisation process recovers the continuum case in the limit $a \to 0$, it also introduces $\mathcal{O}\left(a^2\right)$ errors into the fermion action. An unfortunate side effect of the naive fermion action above is the fermion doubling problem, where in the continuum limit, this action gives rise to $2^4 = 16$ species of fermions rather than one.

The existence of fermion “doublers” can be observed through examination of the free, massless fermion propagator. Suppose the fermion action is written

$$S_F = a^4 \sum_{x,y} \overline{\psi}(x)\, D\,(x, y)\, \psi(x), \tag{3.19}$$

where

$$D\,(x, y) = \sum_{\mu=1}^{4} \gamma^\mu\, \frac{1}{2\,a}\, \left[U_\mu(x)\delta_{x+a\,\hat{\mu},y} - U_\mu^\dagger(x - a\,\hat{\mu})\, \delta_{x-a\,\hat{\mu},y}\right] + m \tag{3.20}$$

is the naive Dirac operator discussed above, in Eq. (3.18).

Consider the Fourier transform for the free ($U_\mu = \mathbb{I}$), massless fermion case . The transform is applied separately to the two space-time indices x and y where the second index y is transformed using the complex conjugate phase. Thus the Fourier transform of the free, massless version of Eq. (3.20) is

$$\begin{aligned}
D\,(p,q) &= \frac{1}{|\Lambda|}\sum_{x,y} \mathrm{e}^{-i\,p\,\cdot\,x}\,D\,(x,y)\;\mathrm{e}^{i\,q\,\cdot\,y} \\
&= \frac{1}{|\Lambda|}\sum_{x} \mathrm{e}^{-i\,p\,\cdot\,x}\left(\sum_{\mu=1}^{4}\gamma^{\mu}\,\frac{1}{2\,a}\,\left(\mathrm{e}^{+i\,q\,\cdot\,(x+a\,\hat{\mu})}-\mathrm{e}^{-i\,q\,\cdot\,(x-a\,\hat{\mu})}\right)\right) \\
&= \frac{1}{|\Lambda|}\sum_{x} \mathrm{e}^{-i(p-q)\,\cdot\,x}\left(\sum_{\mu=1}^{4}\gamma^{\mu}\,\frac{1}{2\,a}\,\left(\mathrm{e}^{+i\,q_{\mu}}-\mathrm{e}^{-i\,q_{\mu}}\right)\right) \\
&= \delta_{p\,q}\,D\,(p)\,,
\end{aligned} \tag{3.21}$$

where $|\Lambda|$ is the total number of lattice sites and

$$\sum_{\vec{x}} \mathrm{e}^{i\,\left(\vec{p}-\vec{p}\,'\right)\,\cdot\,\vec{x}} = \delta_{\vec{p}\,\vec{p}\,'}, \tag{3.22}$$

$$D\,(p) = \frac{i}{a}\sum_{\mu=1}^{4}\gamma^{\mu}\,\sin\left(p_{\mu}\right). \tag{3.23}$$

From Eq. (3.21) it is clear, that in this basis, that the Dirac operator $D\,(p,q)$ is diagonal in momenta. Hence the inverse of the Dirac operator in position space can be found by calculating the inverse of the 4×4 matrix $D\,(p)$ and then taking the inverse Fourier transform.

To show the existence of the fermion doubling problem, it is sufficient to take the inverse of this matrix using Eq. (A.10)

$$D^{-1}\,(p) = \frac{-i\,a\,\sum_{\mu=1}^{4}\gamma^{\mu}\,\sin\left(p_{\mu}\right)}{\sum_{\mu=1}^{4}\sin^{2}\left(p_{\mu}\right)}. \tag{3.24}$$

This has poles when $\sin^2\left(p_\mu\right)=0$, i.e. when $p_\mu = 0$ or π. In the zone $-\pi \leq p_\mu \leq \pi$ of momenta available on the lattice, there exist $2^4 = 16$ poles, of which all but the pole corresponding to $p_\mu = (0,0,0,0)$ are unphysical. These unphysical poles give rise to the unphysical quark species of the doubling problem.

3.3.1. Improved Fermion Action

It is clear that the naive fermion action of Eq. (3.18) isn't fit for purpose. It doesn't accurately reproduce continuum physics when the continuum limit is taken. The first step to resolve this is to remove the fermion doubling problem. There are a number of methods [26–30] through which to do this, the one used in this work and covered below is the Wilson fermion action [20].

Wilson Action

The Wilson fermion action removes the unphysical "doublers" by introduction of an irrelevant term into the action. This term vanishes in the continuum limit and works by forcing the unphysical quark species to have extremely large energies, such that they are suppressed.

Wilson proposed to remove the unphysical poles at $p_\mu = \pi$ by adding an extra term to the (massive) momentum space Dirac operator

$$D\,(p) = m + \frac{i}{a} \sum_{\mu=1}^{4} \gamma^\mu \, \sin\,(p_\mu) + \frac{1}{a} \sum_{\mu=1}^{4} \left(1 - \cos\,(p_\mu)\right). \tag{3.25}$$

Eq. (A.10) can now be used to find the inverse Dirac operator

$$D^{-1}\,(p) = \frac{\left(m + \frac{1}{a}\sum_{\mu=1}^{4} \left(1 - \cos\,(p_\mu)\right)\right) - \frac{i}{a}\sum_{\mu=1}^{4} \gamma^\mu \, \sin\,(p_\mu)}{\left(m + \frac{1}{a}\sum_{\mu=1}^{4} \left(1 - \cos\,(p_\mu)\right)\right)^2 + \frac{1}{a^2}\sum_{\mu=1}^{4} \sin^2\,(p_\mu)}, \tag{3.26}$$

where the physical pole $(m \to 0, p_\mu = 0)$ is maintained but the unphysical poles at $p_\mu = \pi$ are removed. The unphysical quark species acquire a mass

$$m \to m + \frac{2\,n}{a}, \tag{3.27}$$

where n is the number of components where $p_\mu = \pi$. In the continuum limit, these masses become large and the "doublers" hence decouple from the theory

The Wilson term in position space is hence

$$-a \sum_{\mu=1}^{4} \frac{1}{2\,a^2} \left(U_\mu(x)\,\delta_{x+a\,\hat{\mu},y} - 2\,\delta_{x,y} + U_\mu^\dagger\,(x - a\,\hat{\mu})\;\delta_{x-a\,\hat{\mu},y}\right). \tag{3.28}$$

This can be obtained from the free-field case ($U_\mu = \mathbb{I}$) by taking the inverse Fourier transform of the additional term in Eq. (3.25) as shown in Appendix B.3.1. This position space representation of the Wilson term can be seen to be the negative discretisation of the Laplace operator [31]

$$-\frac{a}{2}\,\partial_\mu\,\partial_\mu. \tag{3.29}$$

In removing the "doublers", the discretisation error has increased from $\mathcal{O}\left(a^2\right)$ to $\mathcal{O}\left(a\right)$ as shown in Appendix B.3.1. As such, the Wilson term introduces an $\mathcal{O}\left(a\right)$ discretisation error into the fermion action.

The full Wilson fermion action is the sum of Eq. (3.18) and r times Eq. (3.28) and may be written

$$\begin{aligned} D_F^W(x,y) = {} & m\,\delta_{x,y} + \sum_{\mu=1}^{4} \gamma^\mu\,\frac{1}{2\,a}\,\left(U_\mu(x)\,\delta_{x+a\,\hat{\mu},y} - U_\mu^\dagger\left(x - a\,\hat{\mu}\right)\,\delta_{x-a\,\hat{\mu},y}\right) \\ & - \sum_{\mu=1}^{4} \frac{r}{2\,a}\,\left(U_\mu(x)\delta_{x+a\,\hat{\mu},y} - 2\,\delta_{x,y} + U_\mu^\dagger\left(x - a\,\hat{\mu}\right)\,\delta_{x-a\,\hat{\mu},y}\right) \\ = {} & \frac{r}{2\,a}\sum_{\mu=1}^{4}\left[\left(\gamma^\mu - 1\right)\,U_\mu(x)\,\delta_{x+a\,\hat{\mu},y} - \left(\gamma^\mu + 1\right)\,U_\mu^\dagger\left(x - a\,\hat{\mu}\right)\,\delta_{x-a\,\hat{\mu},y}\right] \\ & + \left(m + \frac{4\,r}{a}\right)\,\delta_{x,y}. \end{aligned} \tag{3.30}$$

where r is the Wilson parameter, commonly set to $r = 1$.

The fermion fields are rescaled according to

$$\psi \to \frac{\psi}{\sqrt{2\,\kappa}}, \tag{3.31}$$

for

$$\kappa = \frac{1}{2\,m\,a + 8\,r}. \tag{3.32}$$

The Wilson fermion action can then be written

$$S_F^W\left[\psi,\overline{\psi},U\right] = a^4\sum_x \overline{\psi}(x)\,\mathcal{M}(x,y)\,\psi(y), \tag{3.33}$$

where $\mathcal{M}$ is the Wilson fermion matrix

$$\mathcal{M}(x,y) = \delta_{x,y} - \kappa \sum_{\mu=1}^{4} \left[(r - \gamma^{\mu})\, U_{\mu}(x)\, \delta_{x+a\,\hat{\mu},y} + (r + \gamma^{\mu})\, U_{\mu}^{\dagger}(x - a\,\hat{\mu})\, \delta_{x-a\,\hat{\mu},y} \right] . \tag{3.34}$$

The Wilson fermion action of Eq. (3.33) successfully removes the unphysical doublers of the naive fermion action. The cost of this fix however is to increase the discretisation errors to $\mathcal{O}(a)$ and to explicitly break chiral symmetry as Eq. (3.30) does not anti-commute with γ_5.

The *Nielsen-Ninomiya No-Go theorem* [32–35] forbids the formulation of a discretised Dirac operator D_a which simultaneously satisfies

- D_a has the correct continuum limit, $\lim_{a\to 0} D_a = \not{D}$ for D_μ the continuum covariant derivative,
- No fermion doublers; the non-continuum modes of D_a decouple in the continuum limit,
- D_a is exponentially local; the norm of D_a's matrix elements decays exponentially as $|x-y|$ increases,
- D_a does not explicitly break chiral symmetry, i.e. $\{D_a,\, \gamma_5\} = 0$.

The No-Go theorem can be partially avoided using Domain Wall fermions [36–40] or the overlap [26, 27] quark formulation which impose a lattice deformed version of chiral symmetry at the cost of increased computational expense.

Here however we use a numerically cheaper fermion action and thus we seek a further improved fermion action which reduces the $\mathcal{O}(a)$ errors.

Clover Fermion Action

In order to provide $\mathcal{O}(a)$ improvement of the Wilson fermion action Sheikholeslami and Wohlert [41] considered all scalar dimension five operators which obey gauge-invariance and are also invariant under, parity and charge conjugation and the discrete rotations

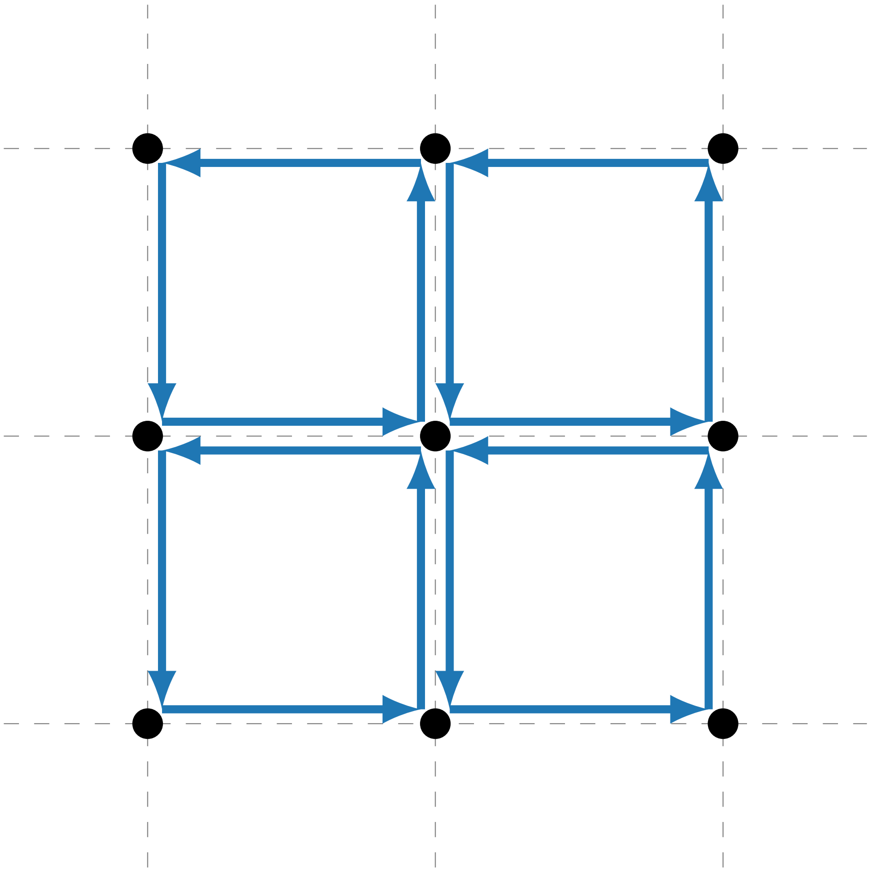

Figure 3.4. Link variables for construction of $\mathcal{C}_{\mu\nu}(x)$.

available on the lattice. In particular the clover fermion term

$$\mathcal{O}_1 = \frac{i\, g\, a\, C_{SW}\, \kappa\, r}{4} \overline{\psi}\, \sigma_{\mu\nu}\, G_{\mu\nu}\, \psi, \tag{3.35}$$

is found to be the only dimension-five operator required to obtain $\mathcal{O}\,(a)$ improvement. The clover fermion action is then

$$S_F^{SW} = S_F^{W} - \frac{i\, g\, a\, C_{SW}\, \kappa\, r}{4} \overline{\psi}\, \sigma_{\mu\nu}\, G_{\mu\nu}\, \psi, \tag{3.36}$$

where C_{SW} is the clover coefficient, a tunable parameter for removal of $\mathcal{O}\,(a)$ errors to all orders in the gauge coupling g.

The lattice discretisation of the field strength tensor is encoded in the plaquette as shown in Eq. ($B.14$). Hence an expression for $G_{\mu\nu}$ can be produced from the sum of the four 1×1 plaquettes in the $\mu - \nu$ plane around any lattice site shown in Figure 3.4

$$G_{\mu\nu}(x) = \frac{1}{8\,i\,g\,a^2}\left[\mathcal{C}_{\mu\nu}(x) - \mathcal{C}^{\dagger}_{\mu\nu}(x) - \frac{1}{3}\,\mathrm{Tr}\left(\mathcal{C}_{\mu\nu}(x) - \mathcal{C}^{\dagger}_{\mu\nu}(x)\right)\right], \tag{3.37}$$

where

$$\begin{aligned}\mathcal{C}_{\mu\nu}(x) = {} & U_\mu(x)\,U_\nu\,(x + a\,\hat{\mu})\;U^{\dagger}_\mu\,(x + a\,\hat{\nu})\;U^{\dagger}_\nu(x) \\ & + U_\nu(x)\,U^{\dagger}_\mu\,(x + a\,\hat{\nu} - a\,\hat{\mu})\;U^{\dagger}_\nu\,(x - a\,\hat{\nu})\;U_\mu\,(x - a\,\hat{\mu}) \\ & + U^{\dagger}_\mu\,(x - a\,\hat{\mu})\;U^{\dagger}_\nu\,(x - a\,\hat{\mu} - a\,\hat{\nu})\;U_\mu\,(x - a\,\hat{\mu} - a\,\hat{\nu})\;U_\nu\,(x - a\,\hat{\nu}) \\ & + U^{\dagger}_\nu\,(x - a\,\hat{\nu})\;U_\mu\,(x - a\,\hat{\nu})\;U_\nu\,(x + a\,\hat{\mu} - a\,\hat{\nu})\;U^{\dagger}_\mu(x).\end{aligned} \tag{3.38}$$

$G_{\mu\nu}$ is made traceless by subtracting 1/3 of the trace from the diagonal elements. This is an improved lattice definition of the field strength tensor which removes the $\mathcal{O}\,(a)$ lattice artefacts from the definition of the plaquette.

3.4. Expectation Values

We return now to the path-integral approach to expectation values considered in Chapter 2. As the fermion and gluonic terms of the QCD action in Euclidean space have been discretised this path-integral is now calculable.

Considering first the quark propagator of Eq. (2.18) and returning to the fermion correlation function of Eq. (2.14) for an appropriate quark bilinear operator $\hat{\mathcal{O}}$ we write

$$\langle\Omega|\hat{\mathcal{O}}\left(x_i, x'_j\right)|\Omega\rangle = \frac{1}{\mathcal{Z}}\int \mathcal{D}\psi(x)\,\mathcal{D}\overline{\psi}(x)\,\mathcal{D}U\,\hat{\mathcal{O}}\left(x_i, x'_j\right)\,\mathrm{e}^{-\left(S_G[U] + S_F^{SW}[U]\right)} \tag{3.39}$$

$$= \frac{1}{\mathcal{Z}}\int \mathcal{D}U\;\det M\,[U]\,\mathrm{e}^{-S_G[U]}\,\hat{\mathcal{M}}, \tag{3.40}$$

where M is associated with Eq. (3.36) and $\hat{\mathcal{M}}$ is the set of fully contracted quark propagators $S\left(x_i, x'_j\right)$. $\hat{\mathcal{M}}$ is the i.e. traces discussed below, i.e. Eq. (3.50) as in Eq. (2.25).

Appropriate gauge invariant meson (M) and baryon $\left(\mathcal{B},\, \overline{\mathcal{B}}\right)$ fields will take the form (temporarily resuming colour, spin and flavour indices)

$$M^{\alpha\, f}_{\beta\, g}\,(x) = \delta_{ij}\ \left(\psi_f\right)^i_\alpha(x)\ \left(\overline{\psi}_g\right)^j_\beta(x) \tag{3.41}$$

$$\mathcal{B}^{\alpha\, f,\, \beta\, g,\, \zeta\, h}\,(x) = \epsilon_{ijk}\ \left(\psi_f\right)^i_\alpha(x)\ \left(\psi_g\right)^j_\beta(x)\ \left(\psi_h\right)^k_\zeta(x) \tag{3.42}$$

$$\overline{\mathcal{B}}^{\alpha\, f,\, \beta\, g,\, \zeta\, h}\,(x) = \epsilon_{ijk}\ \left(\overline{\psi}_f\right)^i_\alpha(x)\ \left(\overline{\psi}_g\right)^j_\beta(x)\ \left(\overline{\psi}_h\right)^k_\zeta(x)\,. \tag{3.43}$$

From these fields we construct appropriate meson and baryon operators which have the correct quantum numbers to produce the desired states. We consider operators

$$M^{\alpha\, f}_{\beta\, g}\,(x,\Phi) = \delta_{ij}\ \left(\psi_f\right)^i_\alpha(x)\ \Phi^{\alpha\,\beta}\ \left(\overline{\psi}_g\right)^j_\beta(x) \tag{3.44}$$

$$\mathcal{B}^{f,\,g,\,h}\,(x,\Phi) = \epsilon_{ijk}\ \left(\psi_f\right)^i_\alpha(x)\ \Phi_1^{\alpha\,\beta}\ \left(\psi_g\right)^j_\beta(x)\ \Phi_2^{\beta\,\zeta}\ \left(\psi_h\right)^k_\zeta(x) \tag{3.45}$$

$$\overline{\mathcal{B}}^{f,\,g,\,h}\,(x,\Phi) = \epsilon_{ijk}\ \left(\overline{\psi}_f\right)^i_\alpha(x)\ \Phi_1^{\alpha\,\beta}\ \left(\overline{\psi}_g\right)^j_\beta(x)\ \Phi_2^{\beta\,\zeta}\ \left(\overline{\psi}_h\right)^k_\zeta(x)\,, \tag{3.46}$$

where Φ_1 and Φ_2 specify the spin-flavour structure to give the physical states of interest. An example of a mesonic operator is

$$M^u_d\,(x,\Phi) = \overline{d}\,(x)\ i\,\gamma_5\,u\,(x)\,, \tag{3.47}$$

where flavour has been made explicit through

$$\psi_u\,(x) = u\,(x)\,,\quad \psi_d\,(x) = d\,(x) \tag{3.48}$$

and $\Phi = i\,\gamma_5$. Eq. (3.47) is a π^+ operator. Similarly for the neutron, we can write

$$\mathcal{B}^{u,\,d,\,d}\,(x,\Phi) = u\,(x)\ C\,\gamma_5\,d\,(x)\ \mathbb{I}\,d\,(x)\,, \tag{3.49}$$

where $\Phi_1 = C\,\gamma_5$ and $\Phi_2 = \mathbb{I}$. C is the charge conjugation matrix and $\mathbb{I}$ the identity matrix. An extensive list of possible spin-flavour operators Φ can be found in Refs. [42] and [43].

From these operators a gauge-invariant meson correlator can be written as

$$\begin{aligned}\langle M\,(x,\Phi)\ M\,(x',\Phi')\rangle = &- \langle \mathrm{Tr}\,(\Phi\, S\,(x,x')\ \Phi'\, S\,(x',x))\rangle_U \\ &+ \langle \mathrm{Tr}\,(\Phi\, S\,(x,x))\ \mathrm{Tr}\,(\Phi'\, S\,(x',x'))\rangle_U\,. \end{aligned} \tag{3.50}$$

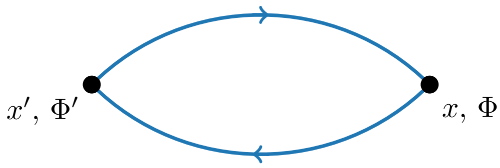

(a) Meson operator connected term.

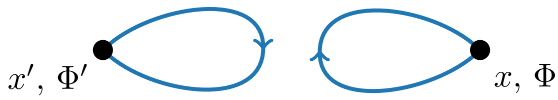

(b) Meson operator disconnected term.

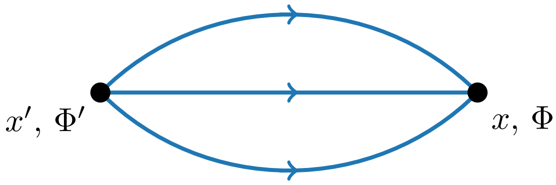

(c) Baryon operator.

Figure 3.5. Meson and baryon quark flow diagrams.

The first term of this is illustrated in Figure 3.5a and the second in Figure 3.5b. The subscript U signifies that this operator is constructed on a specified configuration of link variables $U_\mu(x)$. Similarly the baryon operator

$$\langle \mathcal{B}\,(x,\Phi)\;\overline{\mathcal{B}}\,(x',\Phi')\rangle = \overline{\Phi}_{\alpha\beta\zeta}\sum_{Wick}\langle S^{\alpha}_{\alpha'}\,(x,x')\;S^{\beta}_{\beta'}\,(x,x')\;S^{\zeta}_{\zeta'}\,(x,x')\rangle_U\;\Phi'_{\alpha'\beta'\zeta'}, \tag{3.51}$$

where flavour indices have been suppressed and the Φ tensors describe the contractions of the Dirac indices and hence specify the spin-flavour structure. The quark flow is illustrated in Figure 3.5c. The sum over $Wick$ represents the six possible sets of Wick contractions of the quark fields $\psi_{f/g/h}$ and $\overline{\psi}_{f'/g'/h'}$. These are expanded generally in Appendix B.4. The Wick contractions contribute a non-zero term only when ψ and $\overline{\psi}$ are the same flavour. An explicit example of this for the neutron is

$$\begin{aligned}\langle \mathcal{N}\,(x,\Phi)\;\overline{\mathcal{N}}\,(x',\Phi')\rangle = \epsilon^{abc}\epsilon^{a'b'c'}\Big[&-S^{bb'}_{d}\,(x,x')\;C\,\gamma_5\,S^{aa'T}_{u}\,(x,x')\;C\,\gamma_5\,S^{cc'}_{d}\,(x,x')\\ &-S^{cc'}_{d}\,(x,x')\;\mathrm{Tr}\left(C\,\gamma_5\,S^{bb'}_{d}\,(x,x')\;C\,\gamma_5\,S^{aa'T}_{a}\,(x,x')\right)\Big]_U,\end{aligned} \tag{3.52}$$

for the baryon interpolator of Eq. (3.49) and where S_u and S_d represent up and down quark propagators respectively.

As these operators are dependent now only on the quark propagator, they are calculated by constructing a set of N gauge fields $\{U_i\}$ which are distributed according to Eq. (2.26). The continuous integral of Eq. (3.51) according to Eq. (3.40) is then replaced by an average of the operator on each gauge field in the set in an analogous way to Eq. (2.27)

$$\langle \Omega | \mathcal{B}\left(x,\Phi\right)\, \overline{\mathcal{B}}\left(x',\Phi'\right) |\Omega\rangle \approx \frac{1}{N}\sum_{i=1}^{N} \overline{\Phi}_{\alpha\beta\zeta} \sum_{Wick} \left\langle S^{\alpha}_{\alpha'}\left(x,x'\right)\, S^{\beta}_{\beta'}\left(x,x'\right)\, S^{\zeta}_{\zeta'}\left(x,x'\right)\right\rangle_{U_i} \Phi'_{\alpha'\beta'\zeta'} . \tag{3.53}$$

3.4.1. Fourier Projection

The hadron states constructed by the two-point correlation function must be states of definite spatial momentum $\vec{p}$. Thus the Fourier projection of the spatial correlation function of Eq. (3.53) is taken

$$G\left(\vec{p},t\right) = \sum_{\vec{x}} \mathrm{e}^{-i\,\vec{p}\,\cdot\,\vec{x}}\, \langle \Omega | \mathcal{B}\left(x,\Phi\right)\, \overline{\mathcal{B}}\left(x',\Phi'\right) |\Omega\rangle\,. \tag{3.54}$$

Note that the Fourier projection is over the spatial momenta $\vec{p}$ and that this projection has been performed only for the annihilation operator $\mathcal{B}\left(x,\Phi\right)$ while the creation operator $\overline{\mathcal{B}}\left(x',\Phi'\right)$ remains in real space [11].

3.4.2. Hadronic level interpretation of correlation function

Inserting a complete set of states over energy, momentum and spin $|\alpha,\tilde{p},s\rangle$

$$\mathbb{I} = \sum_{\alpha,\tilde{p},s} |\alpha,\tilde{p},s\rangle\, \langle\alpha,\tilde{p},s| \tag{3.55}$$

into the two point correlation function $G\left(\vec{p},t\right)$ yields

$$G\left(\vec{p},t\right) = \sum_{\alpha,\tilde{p},s}\sum_{\vec{x}} \mathrm{e}^{-i\,\vec{p}\,\cdot\,\vec{x}}\, \langle \Omega | \mathcal{B}\left(x,\Phi\right) |\alpha,\tilde{p},s\rangle\, \langle\alpha,\tilde{p},s| \overline{\mathcal{B}}\left(0,\Phi'\right) |\Omega\rangle\,. \tag{3.56}$$

Here α describes the state with mass M_α and energy $E_\alpha = \sqrt{M_\alpha^2 + \vec{p}^{\,2}}$. The sum over α, is the sum over all possible states α with quantum numbers described by $\mathcal{B}$, $\overline{\mathcal{B}}$.

Operator translation in Euclidean time allows us to write

$$\mathcal{B}\left(x,\Phi\right) = \mathrm{e}^{\hat{H}\,t}\, \mathrm{e}^{-i\,\hat{\vec{p}}\,'\,\cdot\,\vec{x}} \mathcal{B}\left(0,\Phi\right)\, \mathrm{e}^{-\hat{H}\,t}\, \mathrm{e}^{+i\,\hat{\vec{p}}\,'\,\cdot\,\vec{x}}. \tag{3.57}$$

$\hat{H}$ is the Hamiltonian operator which has the properties

$$\hat{H}\ |\Omega\rangle = 0, \tag{3.58}$$

$$\hat{p}\ |\Omega\rangle = 0, \tag{3.59}$$

$$\hat{H}\ |\alpha, \tilde{p}, s\rangle = E_{\alpha,\tilde{p},s}\ |\alpha, \tilde{p}, s\rangle\,, \tag{3.60}$$

$$\hat{p}\ |\alpha, \tilde{p}, s\rangle = \tilde{p}\ |\alpha, \tilde{p}, s\rangle\,. \tag{3.61}$$

The identity

$$\sum_{\vec{x}} \mathrm{e}^{i\,(\vec{p}-\vec{p}\,')\cdot\vec{x}} = \delta_{\vec{p}\,\vec{p}\,'} \tag{3.62}$$

can be used together with operator translation in Eq. (3.57) to simplify Eq. (3.56).

$$\begin{aligned} G(\vec{p}, t) &= \sum_{\alpha,\tilde{p},s} \sum_{\vec{x}} \mathrm{e}^{-i\,\vec{p}\cdot\vec{x}}\ \langle\Omega|\mathcal{B}(0,\Phi)\,|\alpha,\tilde{p},s\rangle\ \mathrm{e}^{-E_\alpha\,t}\,\mathrm{e}^{i\,\vec{\tilde{p}}\cdot\vec{x}}\ \langle\alpha,\tilde{p},s|\overline{\mathcal{B}}(0,\Phi')\,|\Omega\rangle \\ &= \sum_{\alpha,\tilde{p},s} \mathrm{e}^{-E_\alpha\,t} \sum_{\vec{x}} \mathrm{e}^{i\left(\vec{\tilde{p}}-\vec{p}\right)\cdot\vec{x}}\ \langle\Omega|\mathcal{B}(0,\Phi)\,|\alpha,\tilde{p},s\rangle\ \langle\alpha,\tilde{p},s|\overline{\mathcal{B}}(0,\Phi')\,|\Omega\rangle \\ &= \sum_{\alpha,s} \mathrm{e}^{-E_{\alpha,\vec{p}}\,t}\ \langle\Omega|\mathcal{B}(0,\Phi)\,|\alpha,p,s\rangle\ \langle\alpha,p,s|\overline{\mathcal{B}}(0,\Phi')\,|\Omega\rangle\,. \end{aligned} \tag{3.63}$$

It is clear that this expression offers access to the energy of state α as it is proportional to $\exp\left(-E_{\alpha,\vec{p}}\,t\right)$.

If the states are specified, i.e. as positive parity nucleons, the matrix elements describing the overlap of the interpolating fields $\mathcal{B}$ and $\overline{\mathcal{B}}$ can be expressed as [44]

$$\langle\Omega|\mathcal{B}(0,\Phi)\,|N_{1/2+},\vec{p},s\rangle = Z^{\alpha}_{N_{1/2+}} \sqrt{\frac{M_{N_{1/2+}}}{E_{N_{1/2+}}}}\,\psi(p,s)\,, \tag{3.64}$$

$$\langle N_{1/2+},\vec{p},s|\overline{\mathcal{B}}(0,\Phi')\,|\Omega\rangle = \overline{Z'}^{\alpha}_{N_{1/2+}} \sqrt{\frac{M_{N_{1/2+}}}{E_{N_{1/2+}}}}\,\overline{\psi}(p,s)\,, \tag{3.65}$$

where $Z^{\alpha}_{N_{1/2+}}$, $\overline{Z'}^{\alpha}_{N_{1/2+}}$ are the couplings of the interpolators $\mathcal{B}$ and $\overline{\mathcal{B}}$ to the baryon states and $\psi(p,s)$ and $\overline{\psi}(p,s)$ are Dirac spinors. If the operators at the source and sink are not identical, i.e. differing levels of smearing have been performed, than $Z^{\alpha}_{N_{1/2+}}$ and $\overline{Z'}^{\alpha}_{N_{1/2+}}$ are not the adjoint of each other. As $p_{N_{1/2+}}$ is on-shell, $p_4 = \sqrt{\vec{p}^{\,2} + M^2_{N_{1/2+}}}$ and the normalisation $\sqrt{\frac{M_{N_{1/2+}}}{E_{N_{1/2+}}}}$ here produces

$$\overline{\psi}\,(p,s)\;\psi\,(p,s) = 1.$$

The identity

$$\sum_{s} \psi\,(p,s)\;\overline{\psi}\,(p,s) = \frac{\gamma \cdot p + M}{2M} \tag{3.66}$$

along with Eqs. (3.64) and (3.65) will be useful for simplifying Eq. (3.63) to

$$G\,(\vec{p}\,,t) = \sum_{\alpha,\vec{p},s} \mathrm{e}^{-E_\alpha\, t} \sum_{\vec{x}} \mathrm{e}^{-i\,\vec{p}\,\cdot\,\vec{x}}\, Z^{\alpha}_{N_{1/2+}}\, \overline{Z'}^{\alpha}_{N_{1/2+}} \left(\frac{\gamma \cdot p + M^{\alpha}_{N_{1/2+}}}{2\,E^{\alpha}_{N_{1/2+}}} \right). \tag{3.67}$$

For zero momentum $\left(\vec{p} = \vec{0}\right)$ it is shown in Appendix B.5 that the positive parity signal considered here is contained within the $(1,1)$ and $(2,2)$ spinor components of the correlation function.

The interpolating fields $\mathcal{B}$ and $\overline{\mathcal{B}}$ also have overlap with negative parity states [12,44,45]. Following a similar process to the positive parity sector, reveals that negative parity states contribute in the $(3,3)$ and $(4,4)$ components of the correlation function [12].

Hence, in order to access a spin averaged positive parity baryon state, the spinor trace of the correlation function with the positive parity projection operator

$$\Gamma_+ = \frac{1}{2}\,(\mathbb{I} + \gamma_4)\,, \tag{3.68}$$

is used

$$\begin{aligned} G\left(\vec{0},t\right) =& \mathrm{Tr}\left(\Gamma_+\, G\left(\vec{0},t\right)\right)_{spinor} \\ =& \sum_{\alpha} \mathrm{e}^{-E_\alpha\, t}\, Z^{\alpha}_{N_{1/2+}}\, \overline{Z'}^{\alpha}_{N_{1/2+}}. \end{aligned} \tag{3.69}$$

Similar arguments can be made for meson spectroscopy [43].

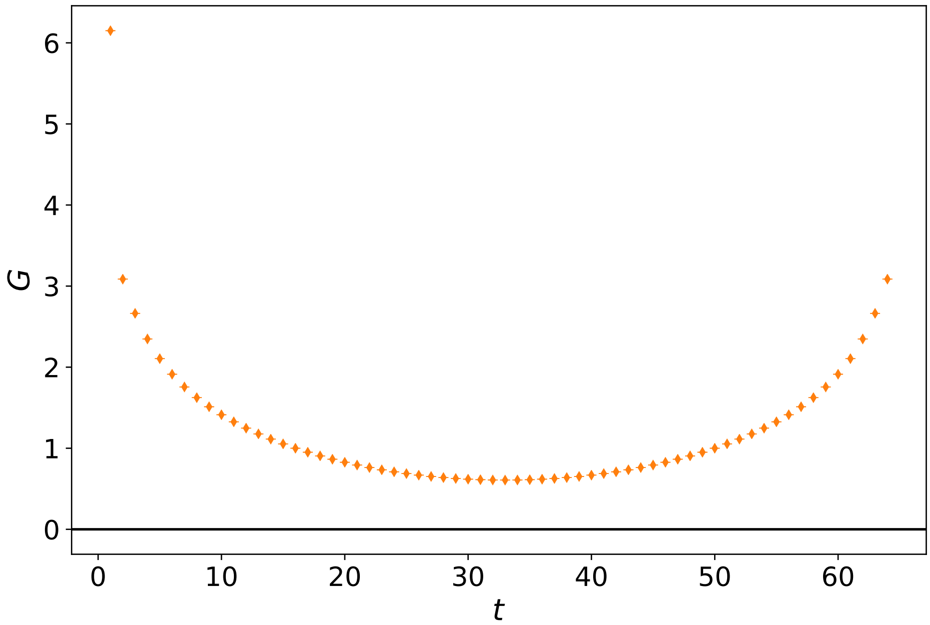

Figure 3.6. π^+ projected two-point correlation function with (Anti) Periodic boundary conditions in the time dimension. The source is at $t_s = 1$.

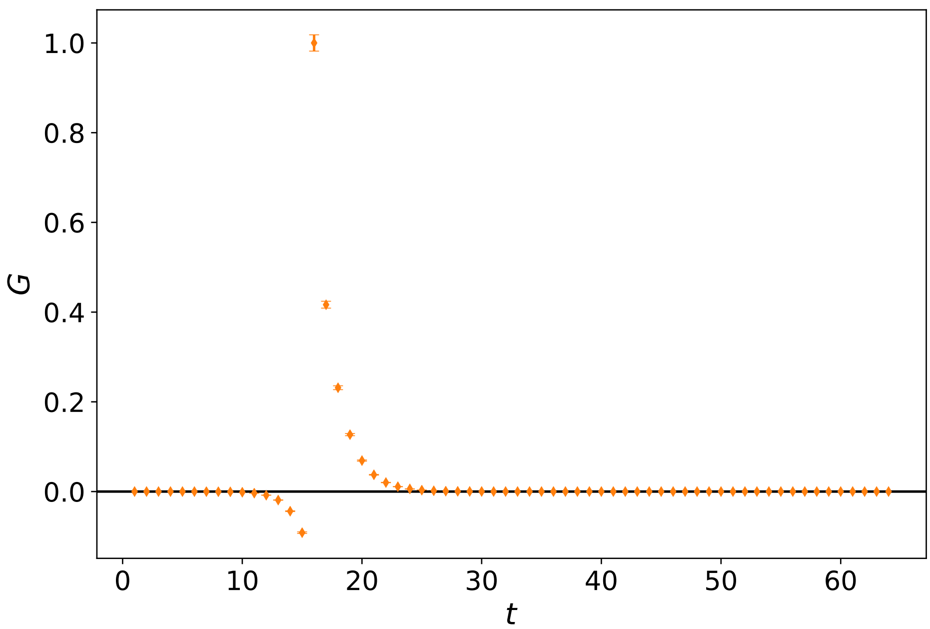

Figure 3.7. Σ^+ projected two-point correlation function with fixed boundary conditions in the time dimension. The source location is at $t_s = 16$.

3.4.3. Boundary conditions

We consider the convention where lattice sites are labelled from 1 to N.

Periodic boundary conditions are used in the spatial dimensions, i.e.

$$\begin{aligned} U_\mu\left(N_x+1,\, n_2,\, n_3,\, n_4\right) &= U_\mu\left(1,\, n_2,\, n_3,\, n_4\right) \\ U_\mu\left(n_1,\, N_y+1,\, n_3,\, n_4\right) &= U_\mu\left(n_1,\, 1,\, n_3,\, n_4\right) \\ U_\mu\left(n_1,\, n_2,\, N_z+1,\, n_4\right) &= U_\mu\left(n_1,\, n_2,\, 1,\, n_4\right). \end{aligned} \tag{3.70}$$

This preserves the discrete translation symmetry of the lattice. Gauge field generation typically uses the same periodic boundary conditions in the temporal dimension as the spatial [11, 15, 25]

$$U_\mu\left(n_1,\, n_2,\, n_3,\, N_t+1\right) = U_\mu\left(n_1,\, n_2,\, n_3,\, 1\right). \tag{3.71}$$

The interpolating operators in Eq. (3.63) couple to states propagating both forward and backwards in time. This means that the fermionic temporal boundary conditions have a significant effect on the correlation function. The three most commonly used options are described below.

- **Periodic boundary conditions**

  When periodic boundary conditions are used, backwards propagating states travel through the temporal edges of the lattice and have the potential to contaminate the forward running signal. These backwards running states appear in the sum of exponentials with opposite time dependence and, in the case of baryons, with opposite parity, i.e. with exponential contributions

  $$G_{\text{back}}\left(\vec{p}, t\right) \propto \sum_{\alpha^*} \mathrm{e}^{-E_{\alpha^*}\,(T-t)}, \tag{3.72}$$

  where α^* now represents states with opposite parity to states labelled by α and $T = (N_t + t_s)$ where t_s is the source location. This interference can be problematic if the states under investigation are particularly light such as (near) physical mass pions, or if the lattice has a short temporal extent.

- **Anti-Periodic boundary conditions**

The backwards running state interacts here in a similar manner to when periodic boundary conditions are used. However, this time the propagator changes sign at the boundary. For mesons with two propagators, the effect cancels and generates a correlator similar to that for periodic boundary conditions.

In this case the interference term can be isolated by simultaneously fitting to both the backwards and forwards propagating states. An example of a simple suitable fit is

$$G_{\text{fit}}\left(\vec{0}, t\right) = c_e \left(\mathrm{e}^{-E\,t} + \mathrm{e}^{-E\,(T-t)}\right), \tag{3.73}$$

where c_e and E are fit parameters and it is assumed that only a single energy state with energy E contributes to the correlation function. An example of a two-point correlation function using anti-periodic boundary conditions is shown in Figure 3.6. As this correlator is a meson it is also an example of periodic boundary conditions for a meson.

- **Fixed boundary conditions**

  The final of the three most commonly used boundary conditions is fixed boundary conditions. Here the links in the time dimension at the boundary are set to zero, i.e. set

$$U_4\left(\vec{x}, N_t\right) = 0. \tag{3.74}$$

  Hence correlators do not travel around the temporal edges of the lattice to contaminate with the forward propagating signal. However boundary effects do extend from the boundary and can contaminate the correlator. A solution to this is to place the source location of the correlator at some finite time separation from the temporal edge of the lattice. Such a solution is displayed in Figure 3.7 where the source is located $\frac{1}{4}\,N_t = 16$ time slices away from the lattice boundary. This approach is successful in preventing contamination provided that the state is sufficiently heavy. As the lightest hadron with the longest correlation length, the pion is the natural choice with which to investigate boundary condition effects.

  Previous studies [45–47] have shown that the effects of a fixed temporal boundary condition are only significant for the pion in approximately the first and last quarter of time slices on the lattice. This region can be avoided by placing the source this distance or more from the boundary. A nucleon or other baryon will have decayed to noise by the time the correlator reaches this region.

- **Open boundary conditions**

  Open boundary conditions are proposed as a method with which the critical slow-down [48–50] typical to generation of gauge fields with extremely fine lattice spacings can be avoided [51, 52]. These boundary conditions describe both gluonic and fermionic terms and can offer improved stability and efficiency for gauge field generation but slightly complicate the physics analysis of the correlation functions which are the focus of this thesis.

Fixed boundary conditions for the valence sector are used in this thesis unless otherwise stated. As the fixed boundary conditions apply only to the valence sector and were not used for gauge field generation, the result is a non-unitary mixed action theory. The effects of this can be avoided by considering only the time regions far from the boundary.

3.4.4. Effective Energy

From the parity projected two point correlation function of Eq. (3.69) the energy of the ground state can be extracted in the infinite time limit. The decaying exponential nature of $\sum_\alpha \mathrm{e}^{-E_\alpha\, t}$ produces

$$G\left(\vec{0}, t\right) = \mathrm{e}^{-E_0\, t}\, Z^0_{N_{1/2+}}\, \overline{Z'}^0_{N_{1/2+}} + \mathrm{e}^{-E_1\, t}\, Z^1_{N_{1/2+}}\, \overline{Z'}^1_{N_{1/2+}} + \dots \tag{3.75}$$

$$\overset{t\to\infty}{=} \mathrm{e}^{-E_0\, t}\, Z^0_{N_{1/2+}}\, \overline{Z'}^0_{N_{1/2+}}, \tag{3.76}$$

where E_0 corresponds to the state with the smallest energy.

In this infinite time limit, the ground state energy can be accessed through the effective energy, defined as

$$E_{eff}(t) = \frac{1}{\delta\, t} \log\left(\frac{G\left(\vec{0}, t\right)}{G\left(\vec{0},\, t + \delta\, t\right)}\right) \tag{3.77}$$

$$\begin{aligned} t \gg 1 &= \frac{1}{\delta\, t} \log\left(\frac{\mathrm{e}^{-E_0\, t}\, Z^0_{N_{1/2+}}\, \overline{Z'}^0_{N_{1/2+}}}{\mathrm{e}^{-E_0\,(t+\delta\, t)}\, Z^0_{N_{1/2+}}\, \overline{Z'}^0_{N_{1/2+}}}\right) \\ &= \frac{1}{\delta\, t}\left[\log\left(\mathrm{e}^{-E_0\, t}\right) - \log\left(\mathrm{e}^{-E_0\,(t+\delta\, t)}\right)\right] \\ &= \frac{1}{\delta\, t}\, E_0\, \delta\, t \\ &= E_0 \end{aligned} \tag{3.78}$$

As the data is produced by Monte Carlo processes, the effective energy as a function of lattice time will not be exactly equal at all times. Hence a correlated fit across a range of time slices is performed. The method with which fits are performed is described in Appendix B.6. For this work we require that the covariance-matrix χ^2_{dof} of these *plateau* fits is ≤ 1.2. This aids in ensuring that the long-time limit has been reached and that the ground state energy has been isolated.

It follows from Eq. (3.69) that if the long-time limit has not been reached that there will be remaining excited states with energies $E_n > E_{n-1} > \cdots > E_1 > E_0$. There are a number of methods through which the ground and excited state energies can be extracted [11,53] of which a few will be discussed briefly herein. Particular attention will be on their applicability to the studies in this thesis.

A naive approach would be to fit two or more exponentials to the two point correlation function. This would enable a determination of excited state energies as well as improve the ground state signal by removing higher order contaminations. This approach however has been demonstrated to produce unreliable determination of energies and matrix elements [11, 54, 55], particularly for quantities which are highly sensitive to excited state effects [55].

This difficulty prompted the use of the variational method [56–59] wherein the source and sink operators are systematically varied to alter the couplings $Z^{\alpha}_{N_{1/2+}}$ and $\overline{Z'}^{\alpha}_{N_{1/2+}}$ to each state. The resulting matrix of source and sink varied correlation functions is then diagonalised in order to produce a new set of operators by solving the generalised eigenvalue problems [60]

$$G_{ij}\left(\vec{p}\,, t_0 + \Delta\, t\right)\, u_{\alpha,j}\left(\vec{p}\,\right) = \mathrm{e}^{-E_\alpha(\vec{p}\,)\,\Delta\,t}\, G_{ij}\left(\vec{p}\,, t_0\right)\, u_{\alpha,j}\left(\vec{p}\,\right), \tag{3.79}$$
$$v_{\alpha,i}\left(\vec{p}\,\right)\, G_{ij}\left(\vec{p}\,, t_0 + \Delta\, t\right) = \mathrm{e}^{-E_\alpha(\vec{p}\,)\,\Delta\,t}\, v_{\alpha,i}\left(\vec{p}\,\right)\, G_{ij}\left(\vec{p}\,, t_0\right). \tag{3.80}$$

Here G_{ij} is an element of the correlation function matrix with interpolating operators $\mathcal{B}_i\,\overline{\mathcal{B}}_j$; u_α, v_α are the eigenvectors which diagonalise the correlation matrix and provide the weights to produce the new correlation functions which are optimised for a single energy eigenstate

$$G\left(\vec{p}\,, t, \alpha\right) = v_{\alpha,i}\left(\vec{p}\,\right)\, G_{ij}\left(\vec{p}\,, t\right)\, u_{\alpha,j}\left(\vec{p}\,\right). \tag{3.81}$$

The variational analysis method works well [55, 61, 62] but is computationally expensive requiring a separate fermion matrix inversion for each source used in the correlation matrix. Extensions to non-zero momentum exist and are essential for correctly isolating excited states at non-zero momentum [62]. Variational analysis relies upon a basis of operators which couple to the energy eigenstates of interest. For pure QCD calculations, this is usually accomplished by creating source operators of different widths, in analogy to the different particle radii observed in nature and on the finite-volume lattice. These source operators are not necessarily appropriate for calculations involving an external background field. Similarly due to the small differences between the Landau energy levels of a hadron, it is anticipated that the variational method will not prove useful to isolating the lowest lying Landau level state [61].

An alternative approach; the Athens Model Independent Analysis Scheme (AMIAS) [63] uses importance sampling methods to directly determine the number of distinguishable states in Eq. (3.69). An advantage of AMIAS is that it can be applied to the correlation function at any time by allowing any number of states to contribute. This is in contrast to the plateau fitting method where the long time-limit behaviour is required. This freedom allows AMIAS to be performed at smaller times, before the onset of significant amounts of noise in the correlation function. AMIAS has been applied to nucleon excited states using a single operator [64] and a correlation matrix [63] as well as to meson spectroscopy [65].

In this work the plateau fitting method is used through a linear least squares fit [31] as discussed in Appendix B.6. This fit method allows the χ^2_{dof} of the fit to be examined, where it is important to note that the χ^2_{dof} is determined via a consideration of the full covariances matrix between the different Euclidean time slices in the fit region. An upper limit of $\chi^2_{dof} \leq 1.2$ is set on all fits considered; this ensures ground state dominance for successful energy extractions.

3.5. Smearing

In order to increase the overlap of the interpolating operators with a specific state α of interest a number of approaches can be used [66–71]. As the ground state is the desired energy eigenstate, gauge invariant Gaussian smearing [66] is used.

A smeared source or creation operator is created by distributing the fermion fields over multiple lattice sites. The quark propagator is then formed by inverting the fermion matrix against this distributed source rather than a delta function as in Eq. (2.18); i.e.

$$M^{ki}_{\alpha'\alpha}\left(z, x_i\right) \, S^{ij}_{\alpha\beta}\left(x_i, x'_j\right) = \delta^{kj} \, \delta_{\alpha'\beta} \, \delta\left(z - x_j\right) \, \eta\left(z\right) , \tag{3.82}$$

where $\eta\left(z\right)$ is the distributed source called the source vector. This source vector is constructed using an iterative Gaussian smearing process. Starting with the delta function source of Eq. (2.18) a smearing operator $F\left(x, x'\right)$ is iteratively applied

$$\eta\left(z\right)^{(i)} = \sum_{\vec{x}'} F\left(x, x'\right) \, \eta\left(z\right)^{(i-1)} . \tag{3.83}$$

Here the smearing operator is [66, 72]

$$F\left(x, x'\right) = \left(1 - \epsilon\right) \, \delta_{x,x'} + \frac{\epsilon}{6\, u_0} \sum_{\mu=1}^{3} \left[U_\mu(x) \, \delta_{x',x+a\,\hat{\mu}} + U^\dagger_\mu\left(x - a\,\hat{\mu}\right) \, \delta_{x',x-a\,\hat{\mu}}\right] , \tag{3.84}$$

where ϵ is the smearing strength which determines the amount of smearing on each application of the operator. The mean-field improvement factor u_0 [73, 74] represents the average value of the gauge links U_μ and is defined by

$$u_0 \equiv \left\langle \frac{1}{3} \operatorname{Tr}\left(P_{\mu\nu}\right) \right\rangle^{\frac{1}{4}} . \tag{3.85}$$

The width of the smeared source vector depends on both the smearing strength ϵ and the number of applications i.

3.5.1. Link Smearing

The high frequency modes of a gauge field theory such as QCD can contaminate the lower order behaviour responsible for much of the interesting physics [75–79]. This has the effect of increasing the noise even for *simple* quantities such as the effective energy [80, 81]. In particular, this occurs when the operator is concerned with or involves substantial gluonic effects [82]. To remedy this problem, the link variables are averaged or smeared. The approach used in this work is stout link smearing [82]; here the gauge links are replaced with a weighted average of the surrounding gauge links. The replacement process occurs several times in an iterative fashion.

Link variable smearing can also significantly improve the lattice action used. Examples are the Asqtad improved staggered quark action [83–85] and the fat link irrelevant clover action [86, 87].

3.6. Background Field Method

An external electromagnetic field can be applied to the lattice QCD simulation through the background field method [88–90]. Such an approach was used in early lattice QCD studies of nucleon magnetic moments through the calculation of the Zeeman splitting induced by a classical magnetic field [91, 92]. The electric polarisability of a neutral hadron can be accessed through the quadratic Stark effect [93–96] with a background electric field.

In the years since these early studies, the background field method and lattice QCD have been extended to calculations of quantities such as the neutron electric dipole moment [97, 98], baryon magnetic moments [99–102] and other more exotic phenomena [103–105].

This is not a full formulation of Quantum Electrodynamics (QED) on the lattice as a full formulation of QED is signficantly non-trivial due to the problems posed by the long-range interaction nature of QED on the finite volume of the lattice [106]. Instead interactions exist only between the external field and the charged particles; no electromagnetic inter-particle interactions exist.

The magnetic field induced using the background field method is the simplest means through which to access purely magnetic quantities of the hadron on the lattice. It is computationally simple to implement as discussed below.

3.6.1. Formulation

To introduce a background field on the lattice, first consider the continuum case. Here a minimal electromagnetic coupling is added to form the covariant derviative

$$D_\mu = D_\mu^{\mathrm{QCD}} + i\, qe\, A_\mu, \tag{3.86}$$

where qe is the charge on the fermion field and A_μ the electromagnetic four-potential. This additional term is discretised in the same manner as the usual gauge fields in Eq. (3.5). Hence, the equivalent modification on the lattice is to multiply the QCD gauge links by an exponential phase factor [92]

$$U_\mu(x) \to U'_\mu(x) = U_\mu^{(B)}(x)\, U_\mu(x) = \mathrm{e}^{i\, a\, qe\, A_\mu(x)}\, U_\mu(x), \tag{3.87}$$

where $U_\mu^{(B)}(x) = \mathrm{e}^{i\, a\, qe\, A_\mu(x)}$. These modified gauge links are used when performing the lattice QCD calculation. Note that the coordinates in the $U(1)$ gauge links are relevant to the source position, such that the link is the identity at the source position. This does not effect the quantisation discussion which follows.

Quantisation

In the continuum, a uniform magnetic field along the $\hat{z}$ axis can be obtained using Maxwell's equations [107]

$$\vec{B} = \vec{\nabla} \times \vec{A}. \tag{3.88}$$

$$\tag{3.89}$$

That is

$$B_z = \partial_x A_y - \partial_y A_x. \tag{3.90}$$

To give a constant magnetic field of magnitude B in the $+\hat{z}$ axis, a potential

$$A_x = -B\, y, \tag{3.91}$$

is used over the interior of the $N_x \times N_y \times N_z \times N_t$ lattice. It was shown earlier in Eq. (3.12) that the smallest closed loop of gauge links, known as the plaquette encodes the field strength tensor

$$P_{\mu\nu}(x) = \exp\left(i\, qe\, a^2 F_{\mu\nu}(x)\right). \tag{3.92}$$

Here this equation is exact as the higher order terms involve derivatives of at least second order which vanish in the case of a constant background field and we write $F_{\mu\nu}(x)$ to emphasise this equation applies for a constant background field.

We can verify that Eqs. (3.90) and (3.91) produces the desired field strength by examing a general plaquette away from the edges of the lattice where periodic boundary conditions are in effect. Such a plaquette is depicted in Figure 3.8 and gives (setting $A_y = A_z = 0$)

$$\mathrm{e}^{-i\, a\, qe\, B\, y}\, \mathrm{e}^{+i\, a\, qe\, B\, (y+a)} = \mathrm{e}^{i\, a^2\, qe\, B}, \tag{3.93}$$

as expected.

The spatial periodic boundary conditions of the lattice require a non-trivial potential to ensure that the field is uniform over the entirety of the lattice. This can be observed by examing a plaquette at the boundary where $y = a\ (N_y)$ as shown in Figure 3.9. This

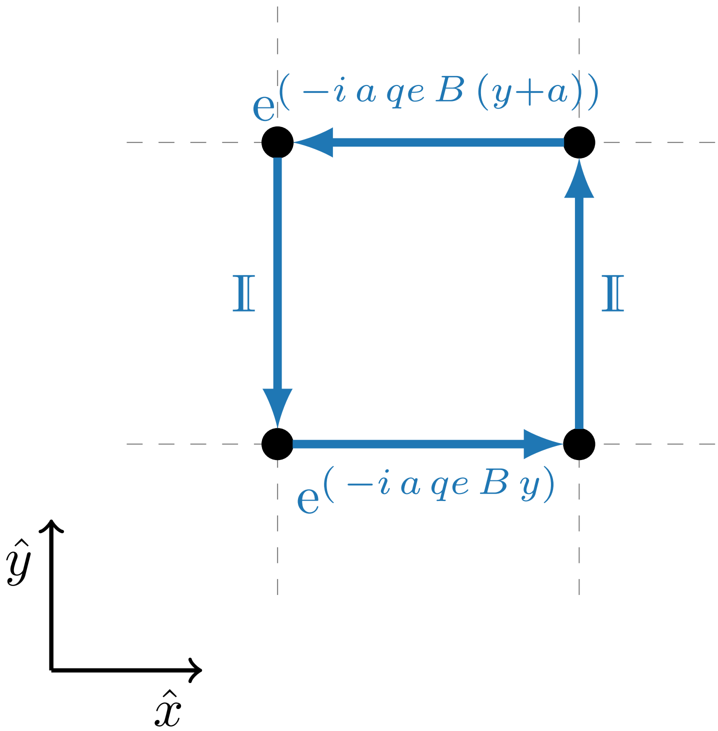

Figure 3.8. The simplest closed loop of link variables, the plaquette $P_{\mu\nu}(x)$ with the values of the background field links $U_{\mu}^{(B)}(x)$ for a general plaquette away from the boundary the lattice.

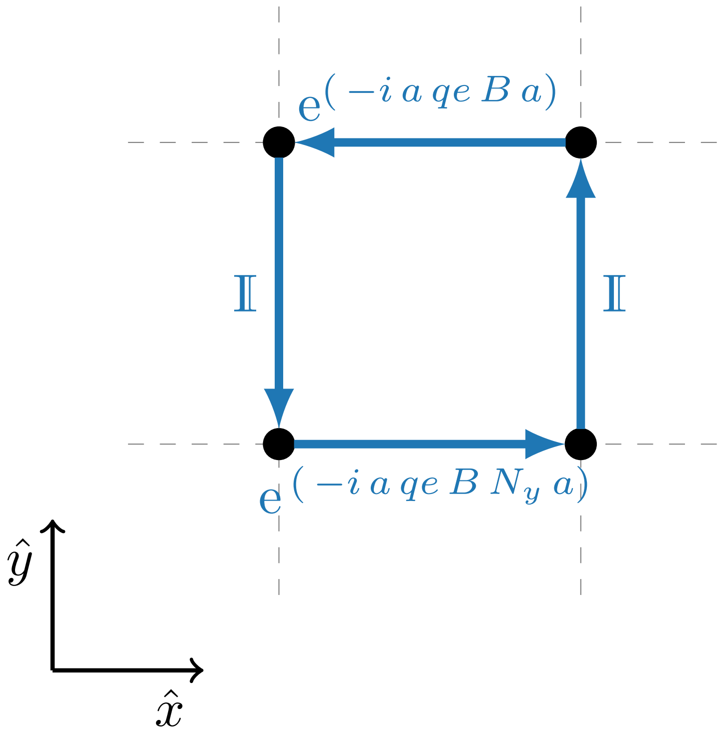

Figure 3.9. The simplest closed loop of link variables, the plaquette $P_{\mu\nu}(x)$ with the values of the background field links $U_\mu^{(B)}(x)$ for a plaquette at the edge of the lattice, $y = a\,N_y$.

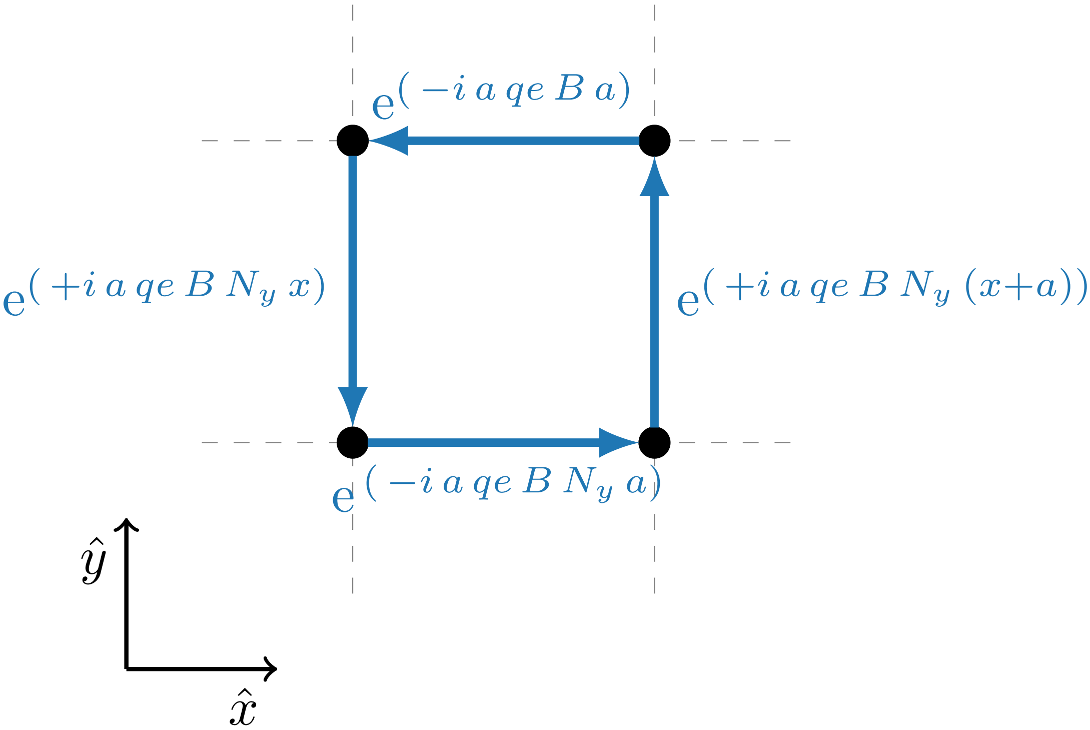

Figure 3.10. The simplest closed loop of link variables, the plaquette $P_{\mu\nu}(x)$ with the values of the background field links $U_\mu^{(B)}(x)$ for a plaquette at the edge of the lattice, $y = a\,N_y$. Here the boundary terms of Eq. (3.95) have been added to correct for the discontinuity.

plaquette gives

$$\mathrm{e}^{-i\,a\,qe\,B\,N_y\,a}\,\mathrm{e}^{i\,a\,qe\,B\,a} = \mathrm{e}^{-i\,a\,qe\,B\,(N_y\,a-a)}, \tag{3.94}$$

which is clearly not the desired field strength. This failure is due to the periodic boundary conditions on this boundary and can be corrected for by using the otherwise unused A_y term in Eq. (3.90). We set

$$A_y = \begin{cases} N_y\,B\,x, & y/a = N_y, \\ 0, & \text{elsewhere.} \end{cases} \tag{3.95}$$

The plaquette at the $y = a\,N_y$ boundary using this additional term is depicted in Figure 3.10 and is

$$\mathrm{e}^{-i\,a\,qe\,B\,N_y\,a}\,\mathrm{e}^{i\,a\,qe\,B\,N_y\,(x+a)}\,\mathrm{e}^{i\,a\,qe\,B\,a}\,\mathrm{e}^{-i\,a\,qe\,B\,N_y\,(x)} = \mathrm{e}^{i\,a^2\,qe\,B}, \tag{3.96}$$

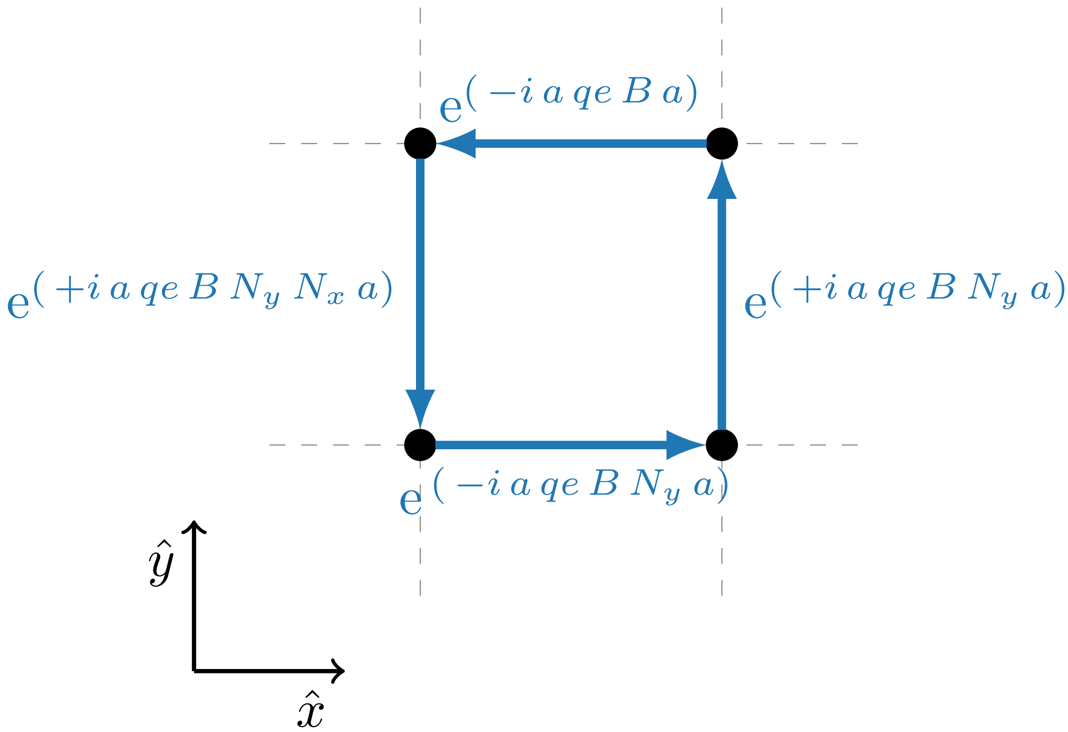

Figure 3.11. The simplest closed loop of link variables, the plaquette $P_{\mu\nu}(x)$ with the values of the background field links $U_{\mu}^{(B)}(x)$ for a plaquette at the corner of the lattice, $y = a\,N_y$ and $x = a\,N_x$. Here the boundary terms of Eq. (3.95) have been added to correct for the discontinuity.

as is required.

The final plaquette considered in Figure 3.11 depicts the double boundary where $x = a\,N_x$ and $y = a\,N_y$. This plaquette has form

$$\mathrm{e}^{-i\,a\,qe\,B\,N_y\,a}\,\mathrm{e}^{i\,a\,qe\,B\,N_y\,a}\,\mathrm{e}^{i\,a\,qe\,B\,a}\,\mathrm{e}^{-i\,a\,qe\,B\,N_y\,N_x\,a} = \mathrm{e}^{i\,a^2\,qe\,B}\,\mathrm{e}^{-i\,a^2\,qe\,B\,N_y\,N_x}, \tag{3.97}$$

which only results in the desired value if

$$\mathrm{e}^{-i\,a^2\,qe\,B\,N_y\,N_x} = 1. \tag{3.98}$$

This requirement produces a quantisation condition on the magnetic field strength [92,101,108] $a^2\,qe\,B\,N_y\,N_x = 2\,\pi\,k$ such that

$$|qe\,B| = \frac{2\,\pi\,k}{N_x\,N_y\,a^2}, \tag{3.99}$$

where k is an integer governing the field strength for a particle of charge qe and a the lattice spacing.

As the down quark is the particle with smallest (non-zero) charge considerered, we consider the charge of the down quark to be $q_d e$. The up quark has corresponding charge $q_u e = -2 \times q_d e$ and a charged hadron such as the proton or π^+ charge $q_{B(k_d)} e = -3 \times q_d e$. The integer governing the field strength of the hadron is then $k_B = -3\, k_d$.

3.6.2. Hadron Energy

The energy of a hadron in an external magnetic field is the foundation of this work. The energy contribution from quantities such as the magnetic moment, Landau levels and the magnetic polarisability are what allows the background field method and lattice QCD two-point correlation functions to calculate these quantities.

The relativistic energy of a hadron H with mass m_H in an external magnetic field B along the $\hat{z}$ axis is [90, 109–112]

$$E_{H;n}^2(B) = m_H^2 + (2\,n+1)\ |qe\,B| + p_z^2 + \vec{\mu}\cdot\vec{B}\ (2\,m_p) - 4\,\pi\,m_H\,\beta_H\ |e\,B|^2 + \mathcal{O}\left(B^3\right), \tag{3.100}$$

where $\vec{\mu}$ is the magnetic moment of H in units of nuclear magnetons, m_p is the proton mass, β_H is the magnetic polarisability and the hadron has momentum p_z along the $\hat{z}$ direction. The momentum available on the lattice is quantised due to the discrete nature of the lattice according to

$$a^2\,p_z^2 = \sin^2\left(\frac{2\,\pi\,n_z}{N_z}\right),$$

where n_z is an integer and N_z the number of lattice sites in the $\hat{z}$ direction [11]. The Landau energy term proportional to $|qe\,B|$ is discussed in more detail in Appendix C.

It is often sufficient to use the non-relativistic Taylor expansion of Eq. (3.100) [89, 91, 92, 101, 104, 113]

$$E_H(B) = m_H + \vec{\mu}\cdot\vec{B}\,\frac{m_p}{m_H} + \frac{|qe\,B|}{2\,m_H} - \frac{4\,\pi}{2}\,\beta_H\ |e\,B|^2 + \mathcal{O}\left(B^3\right) \tag{3.101}$$

where the lowest lying Landau approximation ($n = 0$) has also been taken. This non-relativistic expansion is directly accessible using lattice QCD and the background field method, in contrast to Eq. (3.100).

The validity of this Taylor expansion can be checked by considering

$$E_H^2(B) = (E + m_H)\ (E - m_H) + m_H^2, \tag{3.102}$$

and taking the (positive) square root

$$\begin{aligned}\sqrt{E_H^2(B)} = E_H(B) &= \sqrt{(E_H + m_H)\ (E_H - m_H) + m_H^2} \\ &= m_H \sqrt{1 + \frac{(E_H + m_H)\ (E_H - m_H)}{m_H^2}} \\ &= m + \frac{(E_H + m_H)\ (E_H - m_H)}{2\, m_H} + \ldots \end{aligned} \tag{3.103}$$

where a first order Taylor expansion of the square root has been used. Eq. (3.103) is only true, and thus the Taylor expansion valid if $E_H + m_H \approxeq 2\, m_H$. This is the check on the validity of the Taylor expansion. An alternate formulation of this condition is that

$$\frac{2\, m_H}{E_H + m_H} \approxeq 1. \tag{3.104}$$

At the higher field strengths considered herein, one might be concerned about the validity of the energy-field expansion of Eq. (3.101). Checking the condition of Eq. (3.104), quantity is found to be typically within a few percent of one for all but the largest field strength. At the lightest quark mass considered herein, the deviation from one can approach 10%; this is however small in the context of the current statistical uncertainities at this lightest quark mass as well as the other systematic uncertainties discussed in this thesis. This will be an important issue to consider as one moves toward the precision era of background field method calculations in lattice QCD.

3.7. Simulation Details

The aforementioned PACS-CS $2 + 1$ flavour dynamical gauge configurations [25] are used throughout this thesis. These configurations span a variety of light quark masses,

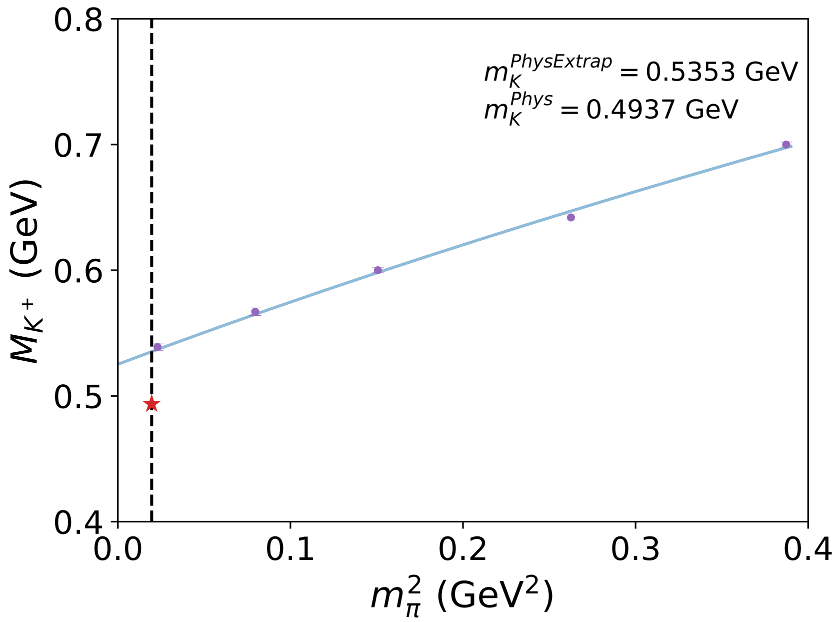

Figure 3.12. Kaon mass plotted against m_π^2 on the PACS-CS ensembles using $\kappa_s^{\mathrm{val}} = 0.13640$. Kaon masses are from Ref. [25] and the dashed vertical line represents the physical pion mass. The red star indicates the physical kaon mass. The Sommer parameter has been used to set the scale on each ensemble to convert to physical units. The model $M_{K^+} = \sqrt{c_0 + c_2\, m_\pi^2}$ used to fit the kaon mass yields $c_0 \approx 0.276$ and $c_2 \approx 0.544$. Uncertainties are plotted on each point.

allowing chiral extrapolations to be performed. The *strange* quark is fixed at its physical mass, allowing the difference between *strange* and *down* quarks to be investigated.

The clover fermion action of Section 3.3.1 is used with $C_{SW} = 1.715$ while the gauge fields are represented using the Iwasaki gauge action of Eq. (3.16). There are $N_S = 32$ points in each spatial dimension and $N_t = 64$ in the temporal direction and the inverse lattice coupling is $\beta = 1.90$. The physical extrapolated lattice spacing is $a = 0.0907\,(13)$ fm, set via an extrapolation of the Sommer parameter [114] to the physical quark mass. Each ensemble considered can have the scale set independently by considering the Sommer parameter for that ensemble only; this approach is used in this work.

The *strange* quark hopping parameter of the PACS-CS ensembles is $\kappa_s = 0.13640$ which does not accurately reproduce the physical kaon mass [115, 116]. This can be observed in Figure 3.12 where the kaon masses from Ref. [25] are extrapolated to the

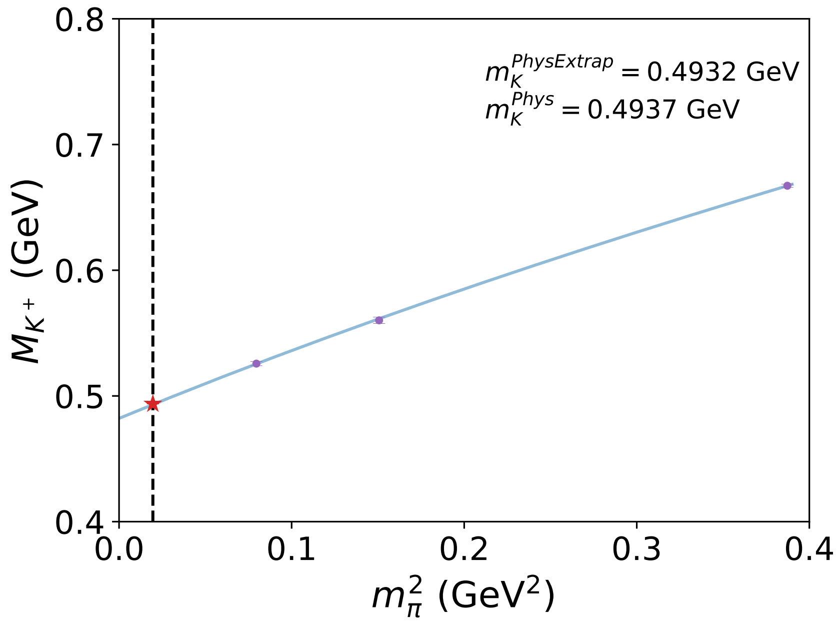

Figure 3.13. Kaon mass plotted against m_π^2 on the PACS-CS ensembles using $\kappa_s^{\mathrm{val}} = 0.13665$. Details as in Figure 3.12 with $c_0 \approx 0.232$ and $c_2 \approx 0.549$.

physical pion mass using a fit function of form

$$M_{K^+} = \sqrt{c_0 + c_2\, m_\pi^2}, \tag{3.105}$$

which contains the leading terms of chiral perturbation theory.

The extrapolated kaon mass is too high by ≈ 42 MeV compared to the physical value. The *strange* quark hopping parameter can be recalculated to reproduce a physical mass kaon by requiring the correct kaon mass at the lightest available quark mass through the Gell-Mann-Oakes-Renner [117] relation. This process was performed in Ref. [116] and the hopping parameter for valence *strange* quarks found to be $\kappa_s^{\mathrm{val}} = 0.13665$. This value accurately reproduces the physical kaon mass for a physical light quark mass as evident in Figure 3.13.

This change of hopping parameter for valence strange quarks causes the masses of the strange valence and sea quarks to differ. This is an effect known as partial quenching [118–122] and is formally a non-unitary theory [122]. Partial quenching effects could be avoided by using quark mass reweighting [123, 124] to set the strange sea quark hopping parameter, κ_s^{sea} to match that use for valence strange quarks.

Table 3.1. Details of the PACS-CS ensembles [25] used in this work where $m_\pi^{\rm phys}$ the is pion mass with the scale set in the physical limit while m_π is the same but with the scale set on each ensemble individually. Values for m_π are from Ref. [13].

κ_{ud}	$\kappa_s^{\rm sea}$	$\kappa_s^{\rm val}$	$m_\pi^{\rm phys}$ (GeV)	m_π (MeV)	a (fm)	Number of configurations
0.13700	0.13640	0.13665	701.0(100)	623.2(91)	0.1022(15)	399
0.13727	0.13640	0.13665	569.8(83)	515.2(80)	0.1009(15)	400
0.13754	0.13640	0.13665	411.3(61)	390.5(55)	0.0961(13)	450
0.13770	0.13640	0.13665	295.7(52)	280.0(45)	0.0951(13)	400

The details of the ensembles used, including the number of gauge field configurations in each ensemble, can be found in Table 3.1.

An important consideration is that the configurations used are electro-quenched; the background field exists only for the valence quarks of the hadron. It is possible to include the background field at configuration generation time [93] but this requires a separate Monte Carlo simulation for each field strength and is hence prohibitively expensive. The advantageous correlation between field strengths used when constructing correlation function ratios in later chapters is also destroyed by separate Monte Carlo simulations. An alternative is to use a reweighting procedure on the gauge-field configurations [95] for the different field strengths B, but this is not performed here. Instead, we draw on chiral effective field theory [125] to calculate these corrections. Drawing on the techniques of partially quenched chiral perturbation theory, previous analyses have shown that electroquenching effects are small for the magnetic polarisability [104, 125].

The smearing parameters used are $\epsilon = 0.7$ for the Gaussian smearing of Eq. (3.84). The stout link smearing uses 10 sweeps at smearing fraction $\alpha = 0.1$. Time orientated links are not smeared.

Chapter 4.

$U(1)$ Landau mode projection

The magnetic polarisability of a system of charged particles describes the response of the system to an external magnetic field. The magnetic polarisability of the neutron is of intense experimental and theoretical interest. Experimentally, measurement of this quantity remains challenging with considerable uncertainties [126–128] although progress has been made in recent years [129, 130]. Lattice QCD can be used to make important predictions in this area.

In this chapter, lattice QCD with a uniform background field will be used to determine the magnetic polarisability of the neutron. A uniform background magnetic field is introduced to the lattice QCD simulation as discussed in Section 3.6. This causes an energy shift from which the magnetic polarisability can be determined using the energy-field relation of Eq. (3.101)

$$E\,(B) = m + \hat{\mu}\cdot\vec{B} + \frac{|qe\,B|}{2m} - \frac{4\,\pi}{2}\,\beta\,\,|e\,B|^2 + \mathcal{O}\left(B^3\right) \tag{4.1}$$

The $|qe\,B|\,/2m$ term is the lowest Landau energy level for a charged hadron. There is in principle an infinite tower of Landau levels as described in Eq. (C.14).

Naively it is simple to extract the magnetic polarisability by fitting the linear and quadratic coefficients of the energy of the hadron in a uniform background magnetic field [91, 113]. This is difficult in practice however as baryon correlation functions exhibit a rapidly decaying signal-to-noise problem [131]. As such the extraction of the magnetic polarisability using standard neutron operators is considerably challenging as demonstrated by previous studies [89, 92, 104, 113] as it appears at second order in the energy-field relation.

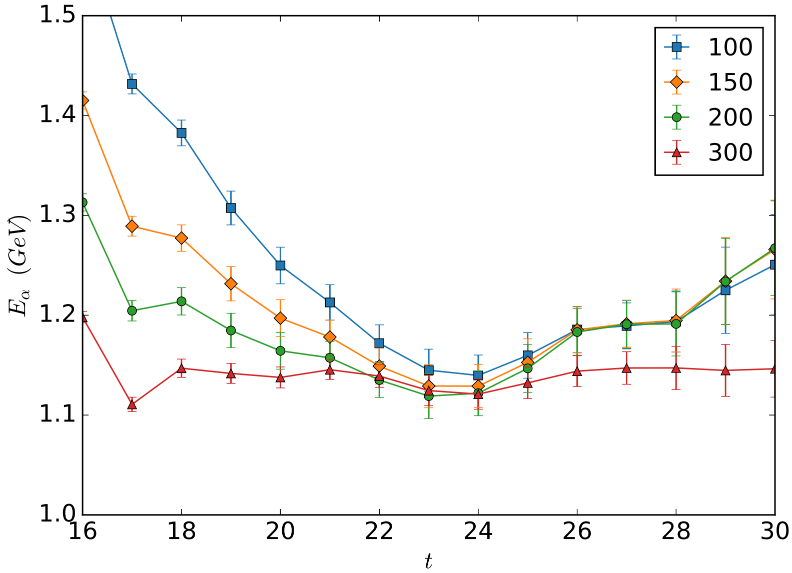

Figure 4.1. Neutron zero-field effective mass from smeared source to point sink correlators for various levels of covariant Gaussian smearing at the source on the $m_\pi = 411$ MeV ensemble. The source is at $t = 16$.

In pure QCD calculations, three-dimensional gauge-covariant Gaussian smearing on the quark fields at the source and/or sink, as discussed in Section 3.5, is highly effective at isolating the nucleon ground state [72]. The addition of a uniform background magnetic field fundamentally alters the physics, breaking three-dimensional spatial symmetry and introducing electromagnetic perturbations into the dynamics of the charged quarks.

To accommodate this altered physics, the quark level $U(1)$ eigenmode projection method sink is introduced.

4.1. Quark operators

Asymmetric source and sink operators are used to construct zero-momentum projected correlation functions which have greater overlap with the energy eigenstates of the neutron in a background magnetic field. The asymmetry allows the dominant QCD and magnetic effects to be emulated separately.

4.1.1. Gaussian smeared source

As Gaussian smeared sources are highly effective in pure QCD calculations, we use such a source here to provide a representation of the QCD interactions. The physics associated with the external magnetic field are captured at the sink.

In order to isolate the QCD nucleon ground state, the amount of source smearing is varied at $B = 0$ with a point sink. We find that for $m_\pi = 411$ MeV that 300 sweeps of standard Gaussian smearing with a smearing fraction $\epsilon = 0.7$ is optimal as illustrated in Figure 4.1. As a point sink is used in Figure 4.1, the source and sink operators are different. This allows some states in the sum of Eq. (3.69) to have a negative weight, this is responsible for the upward trend visible in Figure 4.1 for the smaller smearings. As we choose to use 300 sweeps of covariant Gaussian smearing which has an early onset of plateau behaviour, this is not an issue.

At each of the other quark masses considered; an identical process is followed producing optimal smearings of $N_{sm} = 150, 175, 300, 350$ for masses $m_\pi = 702, 570, 411, 296$ MeV respectively.

4.1.2. $U(1)$ Landau mode quark sink

When QCD interactions are present, the quarks will hadronise (in the confining phase) such that the Landau energy corresponds to that of the composite particle. A relevant example, the neutron has zero charge and thus the *udd* quarks must combine so that the overall Landau energy vanishes.

This highlights that the QCD and magnetic interactions compete with each other in the confining phase. Indeed, there is evidence that residual Landau mode effects remain even at the quark level when the QCD interaction is turned on [101, 105]. This physics is captured using a quark level $U(1)$ Landau mode projection at the sink. In Appendix C the relevant Landau mode physics is discussed.

The Landau levels of a charged scalar particle correspond to the eigenmodes of the 2D lattice Laplacian as discussed in Appendix C.2

$$\Delta_{\vec{x},\vec{x}'} = 4\,\delta_{\vec{x},\vec{x}'} - \sum_{\mu=1,2} U^B_\mu(\vec{x})\ \delta_{\vec{x}+\hat{\mu},\vec{x}'} + U^{B\dagger}_\mu(\vec{x}-\hat{\mu})\ \delta_{\vec{x}-\hat{\mu},\vec{x}'}\,. \tag{4.2}$$

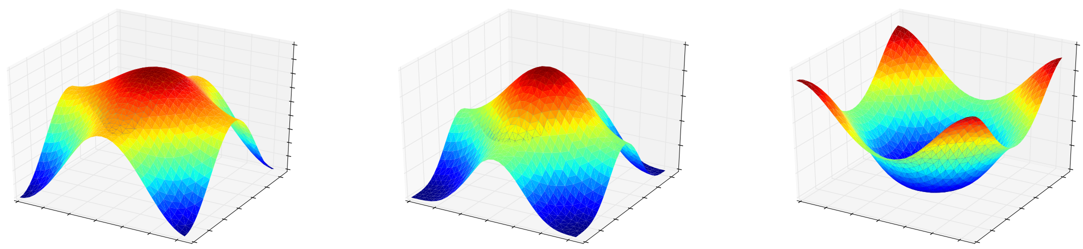

Figure 4.2. $U(1)$ eigenmode probability densities at two different field strengths. The origin is the centre of the $x - y$ plane. **Left:** The eigenmode for the smallest field strength. **Middle and right:** The two degenerate eigenmodes for the second smallest field strength.

In the infinite volume limit, the degeneracy of the Landau eigenmodes is infinite; in contrast the lattice Landau modes have a finite degeneracy dependent on the magnetic field strength. Of particular relevance is the lowest Landau level which has a degeneracy equal to the magnetic flux quanta $|k|$ [105].

The eigenmodes of a particle on a three-dimensional lattice with a $U(1)$ background magnetic field are calculated. This lattice has the same dimension as the gauge fields which are used in the lattice QCD calculations but there are no QCD effects present. These eigenmodes are calculated at multiple field strengths as they are relevant to both the field strength felt by the hadron as well as the individual quarks. We note again that the magnetic field experienced by the hadron is related to that of the down quark by $k_B = -3\, k_d$.

The lowest lying Landau mode in the continuum, infinite volume takes a Gaussian form, $\psi_{\vec{B}}\,(x, y) \sim e^{-|qe\,B|\left(x^2+y^2\right)/4}$. In the finite volume of the lattice, the periodicity of the lattice causes the form of the wave function to alter [113, 132]. Depicted in Figure 4.2 are the probability densities of the lowest lying Landau levels on a finite lattice at two different magnetic field strengths. These probability densities have been shifted such that the origin is at the centre of the $x - y$ plane. It is clear that the periodic boundary conditions distorts the probability density away from the symmetric form seen in the infinite-volume continuum limit. In particular there is very little overlap between the right-most probability density in Figure 4.2 and the standard spherically symmetric Gaussian commonly used in Lattice QCD calculations.

This difference between the Landau eigenmode structure and the typical lattice QCD source or sink structure reinforces the need for the U(1) Landau projection method.

Using the U(1) Landau eigenmodes the individual quarks are projected at the sink. This aids in isolating the ground state of the hadron.

We define a projection operator onto the lowest n eigenmodes $|\psi_{i,\vec{B}}\rangle$ of the 2D Laplacian as

$$P_n = \sum_{i=1}^{n} |\psi_{i,\vec{B}}\rangle \, \langle\psi_{i,\vec{B}}| \, , \tag{4.3}$$

where $n = |3\, q_f\, k_d|$ for the lowest Landau level. To project at the quark level, a coordinate-space representation of this two dimensional projection operator is applied to the quark propagators at the sink

$$S_n\left(\vec{x}, t; \vec{0}, 0\right) = \sum_{\vec{x}'} P_n\left(\vec{x}, \vec{x}'\right) \, S\left(\vec{x}', t; \vec{0}, 0\right) . \tag{4.4}$$

As the U(1) Laplacian is not QCD gauge covariant, the gluon field is fixed to Landau gauge [133, 134] and the appropriate gauge rotation applied to the quark propagator before projecting. Using a gauge fixed sink operator can only affect the overlap with the ground state, not the ground state energy as this is gauge invariant.

One dimensional spatial modulation

The eigenmodes of the two-dimensional $U(1)$ Laplacian have no dependence on the z coordinate. This freedom allows a functional form which varies the spatial extent of the $U(1)$ Landau projection in the $\hat{z}$ axis to be applied, an idea analogous to standard Gaussian smearing.

The z dependence of the projected quark propagator is modulated using a normalised Gaussian

$$\phi_\sigma\left(z\right) = \frac{1}{\sigma\,\sqrt{2\pi}} \exp\left(-\frac{z^2}{2\,\sigma^2}\right) , \tag{4.5}$$

where σ is the width parameter controlling the spatial extent in the $\hat{z}$ direction. The gauge-fixed, U(1) Landau projected quark propagator is averaged over the z direction

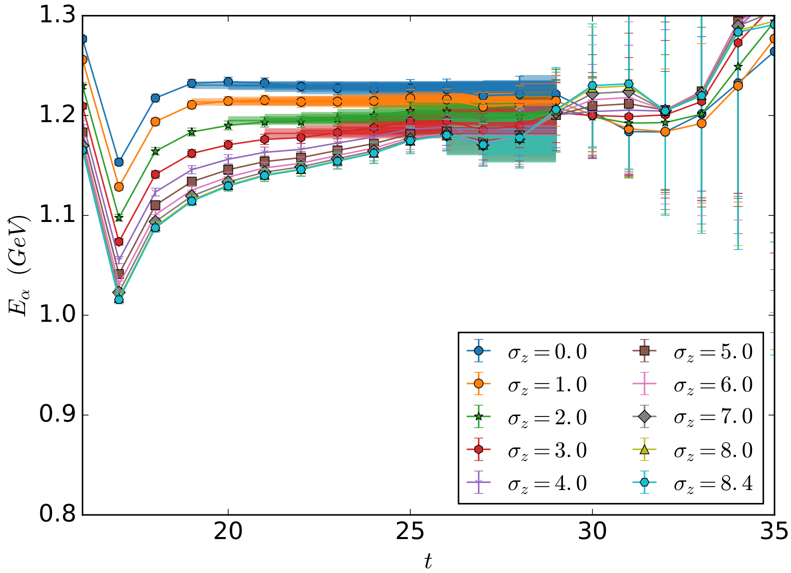

Figure 4.3. Anti-aligned effective energy of the neutron in the largest field strength, $|k_d| = 3$, for $U(1)$ Landau projected sinks at $m_\pi = 411$ MeV. Consecutive fits ending at $t = 29$ where all effective masses agreed with $\chi^2_{dof} \leq 1.2$ are shown.

using the modulation function as a weighting

$$S_{n,\sigma}\left(x, y, z, t; \vec{0}, 0\right) = \sum_{z'} \phi_\sigma\left(z - z'\right) S_n\left(x, y, z', t; \vec{0}, 0\right), \tag{4.6}$$

where $\sigma = 0$ is defined as the case where no z modulation is applied. This is equivalent to defining that $\phi_{\sigma=0}(z) = \delta\left(z' - z\right)$, such that $S_{n,0} \equiv S_n$.

The coupling to each of the energy eigenstates present is dependent upon the spatial modulation used. The desired lowest lying level is dominant in the long Euclidean time limit. Many choices of σ are investigated simultaneously in order to determine which has the greatest overlap with the lowest lying energy level [46].

The neutron spin polarisation and the magnetic-field orientation may be chosen independently to be in the positive z or negative z directions. To efficiently extract the magnetic polarisability, combinations of correlation functions with differing magnetic-field and spin-polarisation alignments are used to create spin and magnetic field aligned and anti-aligned correlation functions. As these are the correlation functions used to extract the magnetic polarisability, these correlation function's effective energies will be examined in order to optimise the quark sink.

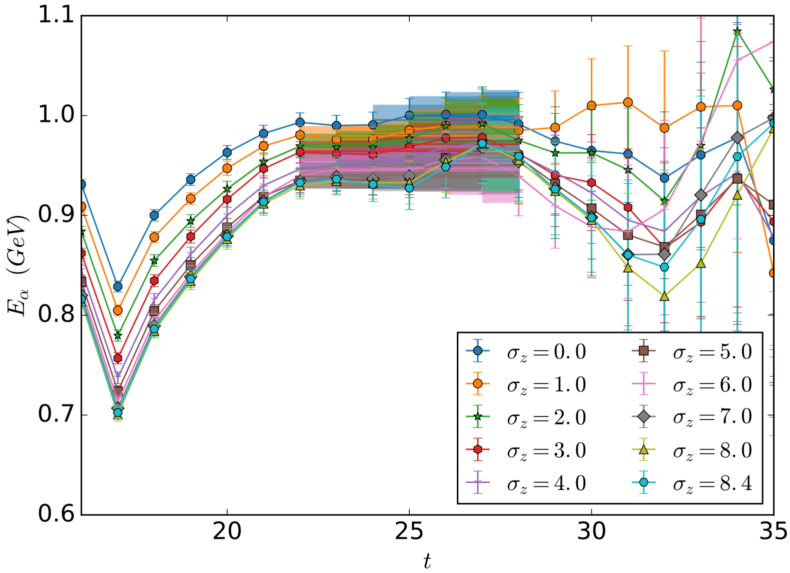

Figure 4.4. Aligned effective energy of the neutron in the smallest field strength, $|k_d| = 1$, for $U(1)$ Landau projected sinks at $m_\pi = 296$ MeV. Consecutive fits ending at $t = 28$ where all effective masses agree with $\chi^2_{dof} \leq 1.2$ are shown.

The optimal quark sink has the longest plateau when fitting backward in Euclidean time from the point at which all correlators agree. In evaluating this extent, the χ^2_{dof} is determined via a consideration of the full matrix of covariances between different time slices under consideration and an upper limit of 1.2 is employed. The spatially-modulated, sink projected correlator that has converged the earliest is chosen. The systematic error associated with the choice of σ is minimised by this process, which is performed for each combination of field strength and aligned or anti-aligned energies. Figure 4.3 shows an example of this process for the $m_\pi = 411$ MeV neutron in the largest magnetic field considered with $|k_d| = 3$. All of the sink projections here agree by $t = 29$ and $\sigma = 0.0, 1.0$ both produce excellent fits which plateau early. This is in contrast to Figure 4.4 which shows the aligned energies for the $m_\pi = 296$ MeV neutron in the smallest field strength where no clear longest plateau is seen. In such a case where multiple spatial modulations are allowed by both length and χ^2_{dof}, the full process for calculating the magnetic polarisability is performed for each value of σ. The resulting magnetic polarisability values are averaged to give a combined statistical error as well as a systematic error associated with the range of allowed σ. This systematic error is determined by taking half the difference between the polarisability values produced by the allowed σ values.

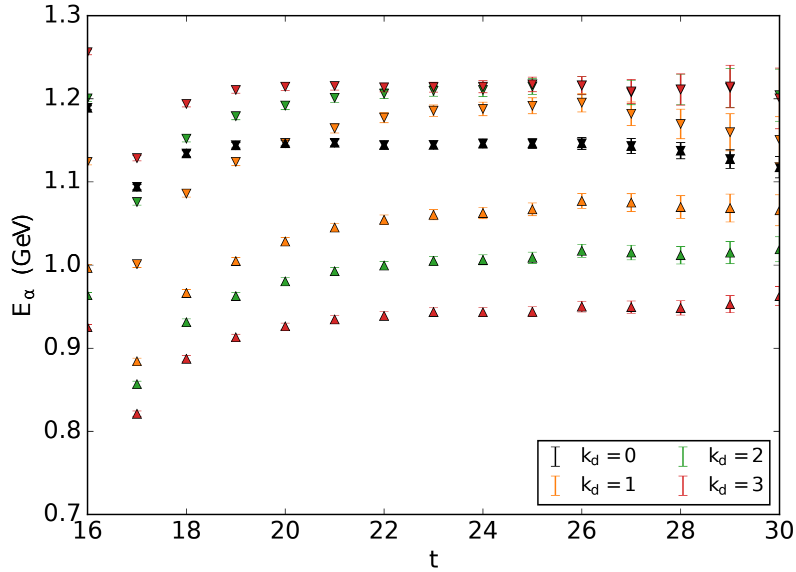

Figure 4.5. Aligned (up arrows) and anti-aligned (down arrows) effective energies of the $m_\pi = 411$ MeV neutron using a $U(1)$, $\sigma = 1.0$ Landau mode sink projection. Three non-zero field strength energies and the zero-field mass are illustrated.

In general, small σ values, $\sigma = 0.0, 1.0, 2.0$ are preferred across multiple pion masses, field strengths and aligned or anti-aligned combinations. These sink projections provide a good representation of the neutron ground state in a background magnetic field. This is evident in the clear plateau behaviour in the neutron energy shown in Figure 4.5. Through consideration of a broad range of σ values, we have minimised the systematic error associated with the choice of fit window by selecting a σ value which has the best overlap with the ground-state.

For the first time, clear plateaus have been identified, a direct result of the consideration of Landau modes at the quark level. This result is a significant advance in the determination of magnetic polarisabilities.

4.2. Magnetic Polarisability

4.2.1. Formalism

Recalling the energy-field relation of Eq. (4.1), note that a combination of energies at different field strengths and spin orientations can be used to isolate the magnetic polarisability term $\propto \beta$

$$\begin{aligned}\delta E(B) &= \frac{1}{2}\left[\left(E_{\uparrow}(B) - E_{\uparrow}(0)\right) + \left(E_{\downarrow}(B) - E_{\downarrow}(0)\right)\right] \\ &= -\frac{4\,\pi}{2}\,\beta\,\left|e\,B\right|^2 + \mathcal{O}\left(B^4\right) \end{aligned} \tag{4.7}$$

where as the neutron has overall charge $qe = 0$ the hadronic Landau energy term vanishes. Here, the arrows denote the neutron spin polarisation along the $\hat{z}$ axis.

While this method of isolating the polarisability term is valid, it is much more effective in practice to take ratios of appropriate spin-up $(+s)$ and spin-down $(-s)$ correlators due to the cancellation of correlated fluctuations on a common ensemble of lattice gauge configurations. An improved unbiased estimator is provided by averaging over both positive $(+B)$ and negative $(-B)$ magnetic-field orientations. Thus the spin-field aligned correlator is defined by

$$G_{\uparrow\uparrow}(B) = G(+s, +B) + G(-s, -B) \tag{4.8}$$

and the spin-field anti-aligned correlator by

$$G_{\uparrow\downarrow}(B) = G(+s, -B) + G(-s, +B) \tag{4.9}$$

The spin-field aligned and anti-aligned correlators, along with the spin-averaged zero-field correlator, are used to form the ratio

$$R(B, t) = \frac{G_{\uparrow\uparrow}(B, t)\, G_{\uparrow\downarrow}(B, t)}{G(0, t)^2}. \tag{4.10}$$

The product of the spin-field aligned and anti-aligned correlators yields an exponent that is the sum of the respective energies $\sim E_{\uparrow\uparrow} + E_{\uparrow\downarrow}$, removing the contribution from the magnetic moment term. Upon taking the effective energy, in an analogous way to the effective mass of Eq. (3.78), the desired energy shift

$$\begin{aligned}\delta E(B, t) &= \frac{1}{2}\,\frac{1}{\delta\,t}\,\log\left(\frac{R(B, t)}{R(B, t + \delta\,t)}\right) \\ t \gg 1 &= -\frac{4\,\pi}{2}\,\beta\,\left|e\,B\right|^2 + \mathcal{O}\left(B^4\right), \end{aligned} \tag{4.11}$$

is obtained. The magnetic field $\pm B$ is that which is experienced by the neutron and is hence related to the down quark magnetic field by a factor of -3.

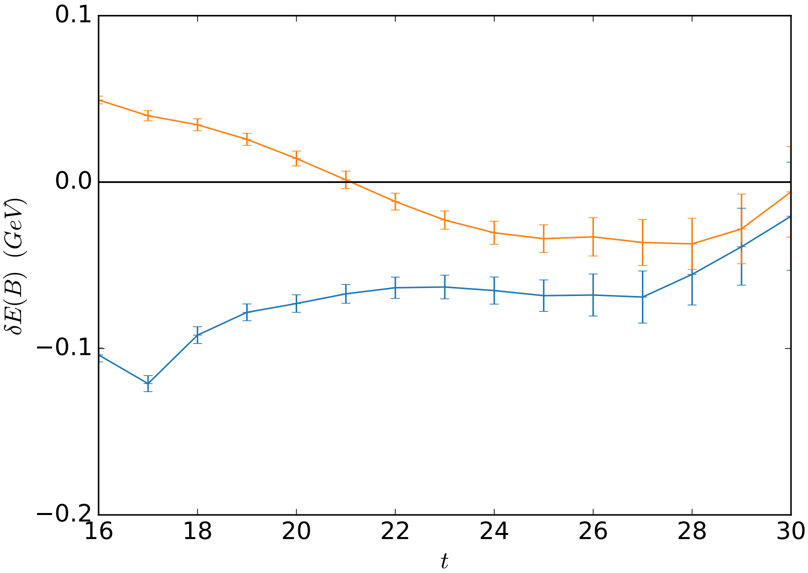

Figure 4.6. The magnetic polarisability effective energy shift at the largest field strength for the neutron as a function of Euclidean time (in lattice units), using a smeared source. A point sink (orange) and a $U(1)$ Landau eigenmode quark sink (blue) are illustrated.

Correlated QCD fluctuations between the finite field strength and zero-field energies are significantly reduced by taking the ratio in Eq. (4.10). As Landau levels do not exist at zero-field, the $U(1)$ eigenmode projection technique is not applied for the zero-field correlator. Instead a standard point sink is used, thus motivating the source tuning process outlined in Section 4.1.1. By using a source optimised for the zero-field neutron in the denominator of Eq. (4.10), the onset of plateau behaviour in the effective energies occurs at an early Euclidean time. This improved method is particularly important to the determination of the magnetic polarisability as it is at second order in B and hence at these small field strengths, its contribution to Eq. (4.1) is small relative to the overall energy and easily hidden by the statistical noise at large Euclidean time.

It is vital to have a precise determination of the polarisability energy shift. The efficiency of the $U(1)$ Landau eigenmode quark sink projection technique can be in seen in Figure 4.6 where a comparison of the energy shift for a standard point sink and a $U(1)$ Landau mode sink projection is presented; the latter is seen to display better plateau behaviour.

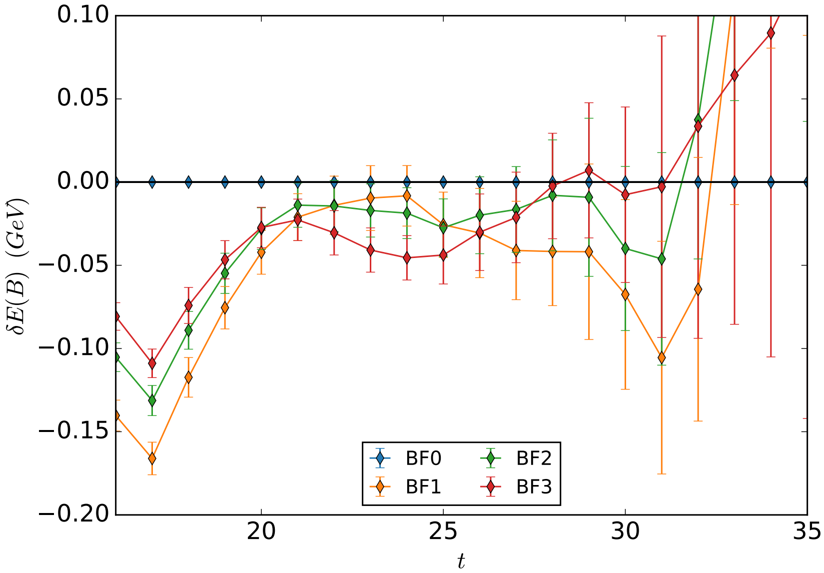

Figure 4.7. The neutron magnetic polarisability effective energy shift for $m_\pi = 411$ MeV with truncated $(n = 1)$ projection operator of Eq. (4.3).

Projection operator eigenmode number

The projection operator of Eq. (4.3) raises the natural question of how many of the lowest n eigenmodes are required. This is particularly relevant as the eigenmodes are such that the $i = 1$ eigenmode most closely resembles the continuum Gaussian form and smeared source considered herein.

To investigate this query, a truncated form of the projection operator in Eq. (4.3) where $n = 1$ is examined. New correlation functions are calculated and the magnetic polarisability energy shift of Eq. (4.11) compared with that of the untruncated projection operator. This quantity is examined as it highlights the difference between the two projection operators in an effective manner. This effectiveness is because the zero-field mass term has already been removed using a point sink correlator; leaving only the contributions from magnetic field dependent quantities.

The magnetic polarisability energy shift for the neutron with $\sigma = 1.0$ spatial projection at $m_\pi = 411$ MeV and the two different projection operators is shown in Figures 4.7 and 4.8. It is clear that the untruncated projection operator in Figure 4.8 provides superior access to the magnetic polarisability energy shift as the energy shifts display better plateau behaviour.

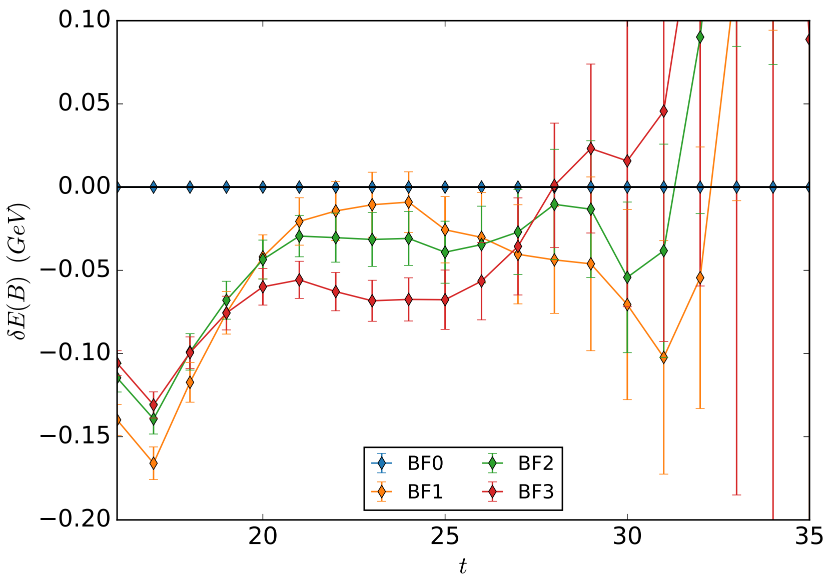

Figure 4.8. The neutron magnetic polarisability effective energy shift for $m_\pi = 411$ MeV with untruncated ($n = |3\,q_f\,k_d|$) projection operator of Eq. (4.3).

It is for this reason that all further calculations using a U(1) Landau projected sink use the untruncated projection operator of Eq. (4.3).

4.2.2. Simulation Details

The $2+1$ flavour dynamical gauge configurations provided by the PACS-CS [25] group through the ILDG [135] are used. These have degenerate *up* and *down* quark masses and a physical *strange* quark mass, hence $2+1$ flavour. The details are summarised in Section 3.7.

Source locations were systematically varied to produce large distances between adjacent source locations. An initial source location of $(\vec{x}, t) = \left(\vec{0}, 16\right)$ was varied three times using additive shifts of $\left(\vec{0}, 16\right)$ for a total of four source locations. A further set of four sources were produced using an initial source location of $\left(\vec{16}, 8\right)$ in an identical manner. As such, a total of eight sources were used for each configuration in each ensemble. By doing this, the effective number of configurations is increased while minimising the correlations between simulations on the same gauge field.

Correlation functions at four distinct hadronic magnetic-field strengths are calculated. Quark propagators at ten non-zero field strengths, $eB = \pm 0.087$, ± 0.174, ± 0.261,

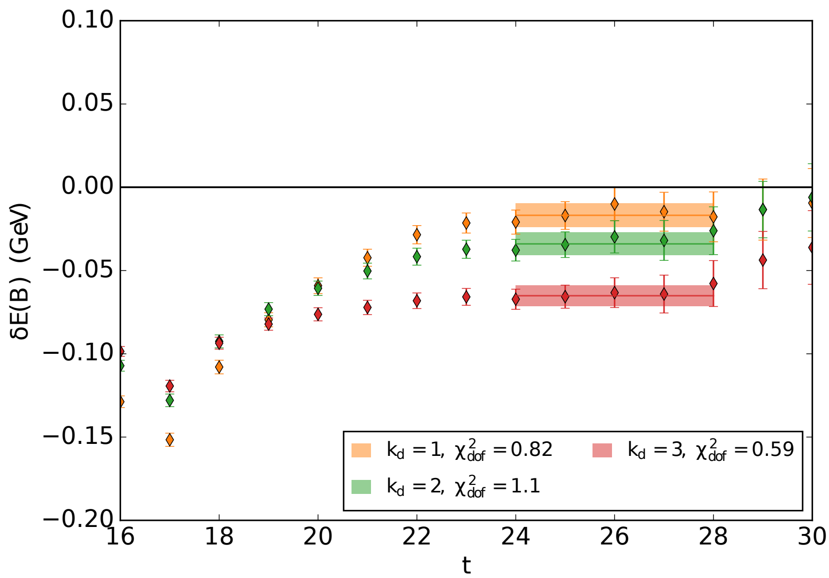

Figure 4.9. The $m_\pi = 411$ MeV neutron magnetic polarisability effective energy shift as a function of Euclidean time (in lattice units), using a smeared source and $\sigma = 1.0$ $U(1)$ Landau eigenmode quark sink projection. Results for field strengths $k_d = 1, 2, 3$ are shown with the magnetic field strength increasing away from zero. The selected fits and χ^2_{dof} are also illustrated.

± 0.348, ± 0.522 GeV^2 , are required in order to achieve this. These correspond to $k_d = \pm 1, \pm 2, \pm 3, \pm 4, \pm 6$ in Eq. (3.99). The zero-momentum projected correlation functions calculated contain spin-up and spin-down components.

4.2.3. Fitting

Each field strength produces an energy shift of the form specified by Eq. (4.11) and as such a quadratic fit is used. These neutron energy shifts for the magnetic polarisability are illustrated in Figures 4.9 and 4.10 with a smeared source and $U(1)$ Landau mode quark sink projections. Clear plateaus are visible, a first for this difficult-to-obtain quantity. In order to consider fitting further, a plateau must be present at each of the non-zero field strengths.

For the $m_\pi = 411$ MeV neutron in Figure 4.9 the plateau does not occur until eight time-slices after the source at $t = 24$; this region is a common starting point at the heavier quark masses. The primary cause of this late onset is the zero-field correlator used in Eq. (4.10) as it has fundamentally different physics. As such any potential excited state

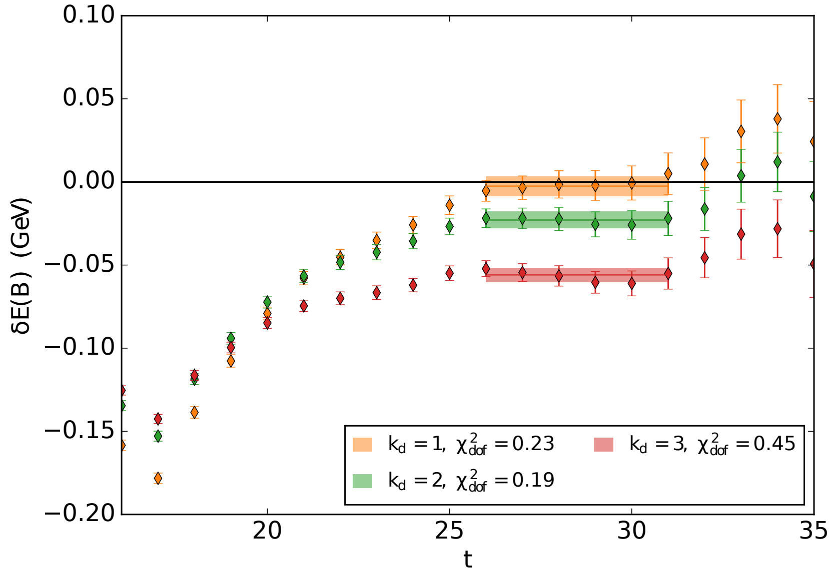

Figure 4.10. The $m_\pi = 702$ MeV neutron magnetic polarisability effective energy shift as a function of Euclidean time (in lattice units), using a smeared source and $\sigma = 01.0$ $U(1)$ Landau eigenmode quark sink projection. Details are as in Figure 4.9.

behaviour of the zero-field correlator differs from that of the background field correlators. Plateau onset is only evident once the ground state has been isolated for both correlators.

These results represent a breakthrough in the ability to construct ground state neutron correlation functions in an external background field which display good plateau behaviour at non-zero background field. This is evident with comparison to Refs. [101] and [136] where a variety of source smearings were investigated in an attempt to produce plateau behaviour for neutron and proton magnetic polarisability energy shifts, however plateau behaviour was not evident. The lattice results presented in this chapter using the $U(1)$ Landau eigenmode projected quark sink technique typically display good plateau behaviour in the region $t \in [24, 31]$, and represent a significant improvement on the results of Refs. [101] and [136].

The fit is performed as a function of k_d, the magnetic field experienced by the neutron which is related to integer magnetic flux quanta in Eq. (3.99)

$$\delta E(k_d) \equiv c_2\, k_d^2. \tag{4.12}$$

Here c_2 is the fit parameter and has the units of $\delta E(k_d)$. As a further check as to the validity of Eq. (4.1) and hence the energy shift in Eq. (4.11); a quadratic + quartic fit, $c_2\, k_d^2 + c_4\, k_d^4$ is also performed. The size of the quartic term provides an estimate of the higher order corrections to Eq. (4.11). For the two heavier masses, $m_\pi = 702, 570$ MeV, it is found that the quartic term is indistinguishable from zero. For the next mass, $m_\pi = 411$ MeV the quadratic + quartic fit is disfavoured by the χ^2_{dof} of the fit while the fit for the lightest mass $m_\pi = 296$ MeV allows a quartic term. The uncertainties for the fit at this lightest mass are extremely large, suggesting that the fit is only possible due to the larger uncertainties associated with lighter quark mass.

If the energy-field Taylor expansion were not valid, a remnant term proportional to B should be evident in the fit to Eq. (4.11). Since it is possible to fit a purely quadratic term as in Eq. (4.12) no such term is found to be present. As the higher order terms have been considered and found to be negligible, the validity of Eq. (4.1) for the neutron is confirmed for the field strengths considered.

This fit parameter c_2 is converted to the physical units of magnetic polarisability, fm^3 , by use of the background field quantisation condition, Eq. (3.99). The resulting transformation is

$$\begin{aligned} q_d\, e\, |B| &= \frac{2\,\pi\, k_d}{N_x\, N_y\, a^2}, \\ |e\, B| &= \frac{1}{q_d}\, \frac{2\,\pi\, k_d}{N_x\, N_y\, a^2}, \end{aligned} \tag{4.13}$$

where $q_d\, e = (-1/3)\; e$ is the charge of the down quark. Hence consider

$$\begin{aligned} c_2\, k_d^2 &= -\frac{4\,\pi}{2}\, \beta\; |e\, B|^2 \\ &= -\frac{4\,\pi}{e^2}\, \frac{1}{2}\, \frac{\beta}{q_d^2} \left(\frac{2\,\pi}{N_x\, N_y\, a^2} \right)^2 k_d^2, \\ c_2 &= -\frac{1}{2}\, \frac{1}{\alpha}\, \frac{\beta}{q_d^2} \left(\frac{2\,\pi}{N_x\, N_y\, a^2} \right)^2, \end{aligned} \tag{4.14}$$

where $\alpha = e^2/\,(4\,\pi) = 1/137\ldots$ is the fine structure constant. For c_2 with units of GeV and a with units of fm, the magnetic polarisability in the physical units of fm^3 is

$$\beta = -2\, c_2\, \alpha\, q_d^2\, a^4 \left(\frac{N_x\, N_y}{2\,\pi} \right)^2 \frac{1}{0.1973 \text{ GeV fm}}. \tag{4.15}$$

The energy shifts used for the quadratic fitting process all used the same spatial modulation of Eq. (4.5), parameterised by σ. As discussed earlier using Figures 4.3 and 4.4, the spatial extent modulation changes the coupling to the mix of energy eigenstates in a background magnetic field. It is hence important that the σ value chosen is the optimal choice. This was achieved using a simultaneous investigation of the spatial extent, proportional to σ and field strength. The selected spatial modulations must provide early isolation of the eigenstate at each field strength. This early isolation is visible in the long plateaus of Figures 4.3 and 4.4.

The sink projection choice is already significantly constrained but in order to determine where energy shifts for the quadratic fit in k_d can be fitted, a further constraint is needed. This constraint is produced by considering the constant Euclidean time plateau fits to the energy shift at each non-zero field strength. By considering all possible fit windows, fit windows where good plateau behaviour exists for all non-zero field strengths simultaneously are selected. Good plateau behaviour is characterised by a $\chi^2_{dof} \leq 1.2$. This constraint dramatically reduces the number of possible fit windows. In particular it is often difficult to obtain acceptable energy shift plateau fits for the largest field strength considered.

The final constraint on the chosen fit comes from the quadratic fit itself. This fit must also be acceptable, having a $\chi^2_{dof} \leq 1.2$. In the case where multiple possible fit windows remain after this process, the fit window with the longer time extent and χ^2_{dof}'s closest to one are preferred. Once the specific quadratic fit has been chosen, the magnetic polarisability, β, is extracted from the quadratic coefficient of the fit using Eq. (4.15).

Using the $U(1)$ sink eigenmode projection technique at each quark mass, it is possible to extract magnetic polarisabilities from the fits to the constant energy shift plateaus as a function of field strength which are illustrated in Figure 4.11. Results for the magnetic polarisability of the neutron at each quark mass are presented in Table 4.1. Note that for the $m_\pi = 570$ MeV ensemble only $\sigma = 0.0$ provided good access to the ground state across all field strengths and hence no systematic error associated with the variation of σ is reported.

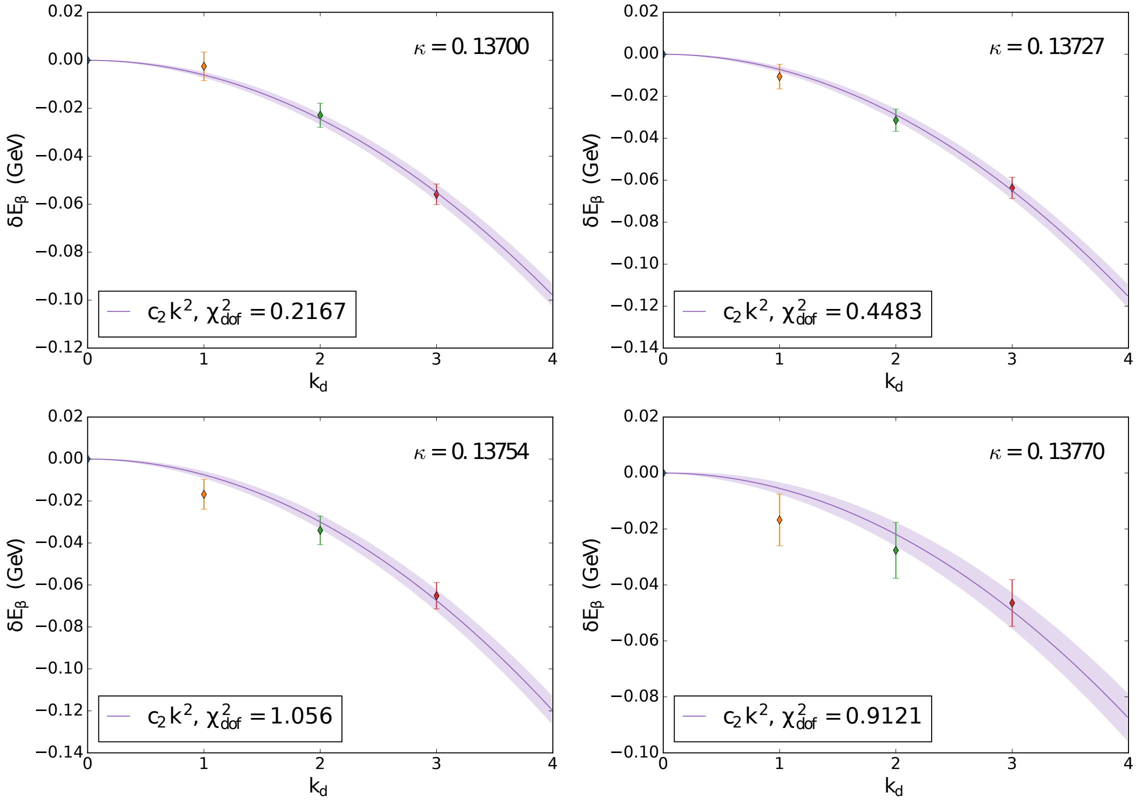

Figure 4.11. Quadratic fits of the energy shift to the field quanta at each quark mass for the neutron for a single σ value each.

Table 4.1. Magnetic polarisability values for the neutron at each quark mass. Eight sources are used for each quark mass. The numbers in parentheses describe statistical and systematic uncertainties respectively.

κ	m_π (MeV)	$\beta\left(\mathrm{fm}^3 \times 10^{-4}\right)$	χ^2_{dof}
0.13700	702	1.51(21)(6)	0.21
0.13727	570	1.63(16)	0.44
0.13754	411	1.29(20)(11)	1.06
0.13770	296	1.14(25)(17)	0.91

4.3. Chiral Extrapolation

To connect lattice QCD results to the physical regime, chiral effective-field theory (χEFT) is considered. This topic is revisited in Chapter 6 in more detail as is required there. The analysis used here follows that of Ref. [125] and is summarised below.

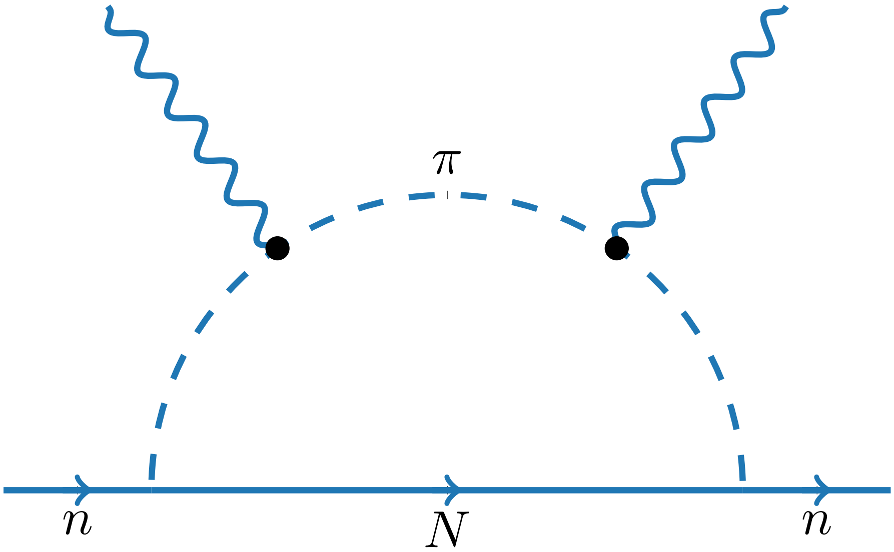

Figure 4.12. The leading-order pion-loop contribution to the magnetic polarisability of the neutron.

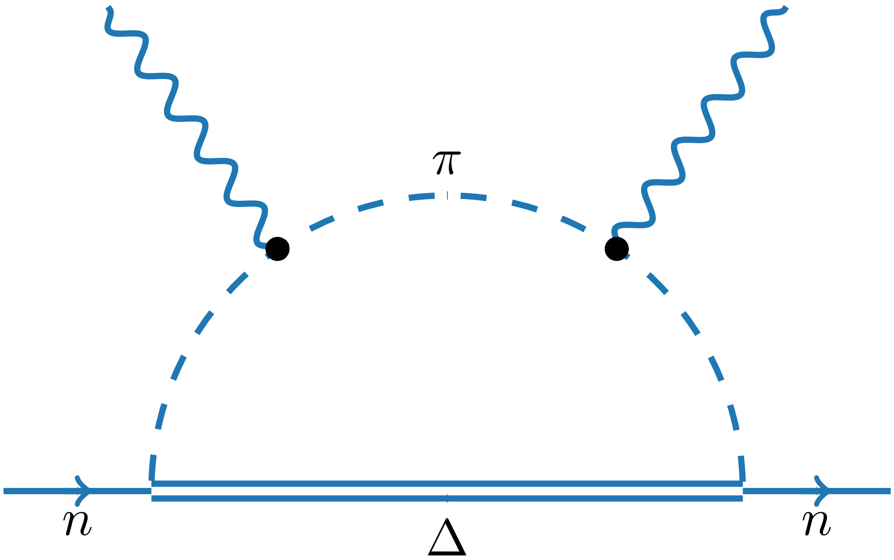

Figure 4.13. Pion-loop contributions to the magnetic polarisability of the neutron, allowing transitions to the nearby and strongly coupled Delta baryons.

4.3.1. Formalism

The chiral expansion considered is

$$\beta\left(m_\pi^2\right) = \beta^{\pi N}\left(m_\pi^2\right) + \beta^{\pi \Delta}\left(m_\pi^2\right) + a_0 + a_2\, m_\pi^2. \tag{4.16}$$

The leading order loop contributions $\beta^{\pi\, N}\,(m_\pi^2)$ and $\beta^{\pi\, \Delta}\,(m_\pi^2)$ are depicted in Figures 4.12 and 4.13. These loop-integral contributions are evaluated in the heavy-baryon limit [137] appropriate to a low energy expansion. The three-dimensional integral forms are [125]

$$\beta^{\pi\, N}\left(m_\pi^2\right) = \frac{e^2}{4\,\pi}\,\frac{1}{288\,\pi^3\,f_\pi^2}\,\chi_N \int d^3k\,\frac{\vec{k}^2\,u^2\,(k,\,\Lambda)}{\left(\vec{k}^2+m_\pi^2\right)^3}, \tag{4.17}$$

$$\beta^{\pi\, \Delta}\left(m_\pi^2\right) = \frac{e^2}{4\,\pi}\,\frac{1}{288\,\pi^3\,f_\pi^2}\,\chi_\Delta \int d^3k\,u^2\,(k,\,\Lambda) \times \frac{\omega_{\vec{k}}^2\,\Delta\,\left(3\,\omega_{\vec{k}}+\Delta\right)+\vec{k}^2\,\left(8\,\omega_{\vec{k}}^2+9\,\omega_{\vec{k}}\,\Delta+3\,\Delta^2\right)}{8\,\omega_{\vec{k}}^5\,\left(\omega_{\vec{k}}+\Delta\right)^3}, \tag{4.18}$$

where $\omega_{\vec{k}} = \sqrt{\vec{k}^2+m_\pi^2}$ is the energy carried by a pion with three-momentum $\vec{k}$, Δ is the mass splitting between the Delta baryon and the nucleon, $\Delta \equiv M_\Delta - M_N = 292$ MeV, and the pion decay constant is taken as $f_\pi = 92.4$ MeV. Here Λ is a renormalisation scale introduced through the dipole regulator

$$u\,(k,\,\Lambda) = \frac{1}{\left(1+\vec{k}^2/\Lambda^2\right)^2}, \tag{4.19}$$

which ensures that only soft momenta flow through the effective-field theory degrees of freedom.

The loop integral of Eq. (4.17) for $\beta^{\pi\, N}\,(m_\pi^2)$ contains the leading non-analytic contribution to the chiral expansion proportional to $1/m_\pi$ [138], while the loop integral of Eq. (4.18) accounts for transitions to a Delta baryon and contributes a non-analytic logarithmic contribution proportional to $(-1/\Delta)\log\,(m_\pi/\Lambda)$ to the expansion.

The coefficients a_0 and a_2 are residual series coefficients which are constrained by the lattice QCD results after they are corrected to infinite volume. This process is detailed in Chapter 6. These are combined with the analytic contributions contained within the loop integrals [139] to form the renormalised low-energy coefficients of the chiral expansion. Complete details of the renormalisation procedure are provided in the Appendix of Ref. [139].

It is noteworthy that the lattice QCD results do not incorporate contributions from photons coupling to the disconnected sea-quark loops of the vacuum which form the full meson dressings of the χEFT - they are electroquenched. It is hence necessary to model the corrections associated with these effects. This is done using partially quenched χEFT. In this case, the standard coefficients for full QCD,

$$\chi_N = 2\, g_A^2, \tag{4.20}$$
$$\chi_\Delta = \frac{16}{9}\, \mathcal{C}^2, \tag{4.21}$$

are modified to account for partial quenching effects [140] as explained in Ref. [125]. Thus when the lattice QCD results are fitted the coefficients used reflect the absence of disconnected sea-quark-loop contributions

$$\chi_N \to \chi_N^{pQ} = 2\, g_A^2 - (D-F)^2 - \frac{7}{27}\,(D+3F)^2\,, \tag{4.22}$$
$$\chi_\Delta \to \chi_\Delta^{pQ} = \frac{16}{9}\,\mathcal{C}^2 - \frac{2}{9}\,\mathcal{C}^2. \tag{4.23}$$

The standard values of $g_A = 1.267$ and $\mathcal{C} = -1.52$ with $g_A = D + F$ and the $SU(6)$ symmetry relation $F = \frac{2}{3}\, D$ are used [141–143].

The value $\Lambda = 0.80$ GeV is adopted in preparation for accounting for the missing disconnected sea-quark-loop contributions in the lattice QCD calculations [144–148]. This regulator mass defines a pion cloud contribution to masses [145], magnetic moments [146], and charge radii [144], which enables corrections to the pion cloud contributions associated with missing disconnected sea-quark-loop contributions. This choice of regulator mass defines a neutron core contribution which is insensitive to sea-quark-loop contributions [149].

Finite-volume effects are considered by replacing the continuum integrals of the chiral expansion with sums over the momenta available on the periodic lattice. Recalling our use of the Sommer scale, we note that the lattice volume varies slightly across the four lattice data points available but is ≈ 3.0 fm for each lattice data point.

4.3.2. Analysis

The integrals of Eqs. (4.17) and (4.18) are calculated in the finite volume of the periodic lattice by replacing the continuum integrals of the chiral expansion with sums over the momenta available. As the lattice QCD results do not include the contributions of disconnected sea-quark-loop contributions, the coefficients of Eqs. (4.22) and (4.23)

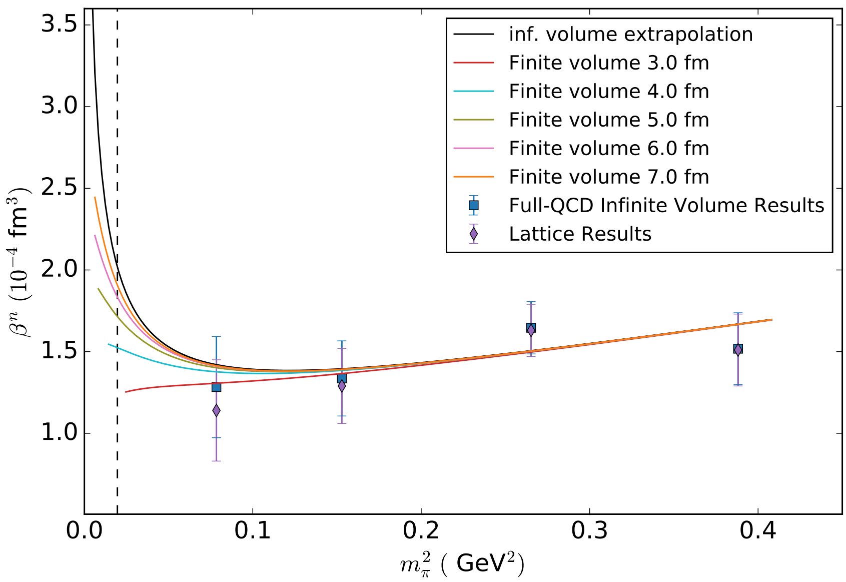

Figure 4.14. Correction of the lattice QCD results (violet diamond) for the neutron magnetic polarisability β^n to infinite volume and full QCD (blue square) as described in the text. Extrapolations of β^n for a variety of spatial lattice volumes provide a guide to future lattice QCD simulations. The infinite-volume case relevant to experiment is also illustrated.

are used in Eqs. (4.17) and (4.18). This calculation is performed for each quark mass considered on the lattice.

The loop-integrals are then numerically integrated in infinite volume and with the full QCD coefficients of Eqs. (4.20) and (4.21). The difference between the finite-volume partially quenched result and this infinite volume full-QCD result at each quark mass is used to correct the lattice QCD results to infinite volume and full QCD. Through this method, both finite-volume and sea-quark loop contribution corrections have been incorporated. These corrections are illustrated in Figure 4.14 by the (blue square) "Full-QCD Infinite-Volume Results" next to the original (violet-diamond) "Lattice Results".

The fit function of Eq. (4.16) is fit to the corrected lattice QCD results by modifying the residual series coefficients, a_0 and a_2. Once these parameters are constrained any volume can be considered. Figure 4.14 shows chiral extrapolations for a range of volumes ranging from near that used in this study to much larger. These extrapolations provide a guide to future lattice QCD simulations. At the physical pion mass, the 7 fm curve still differs the infinite-volume prediction by 6%.

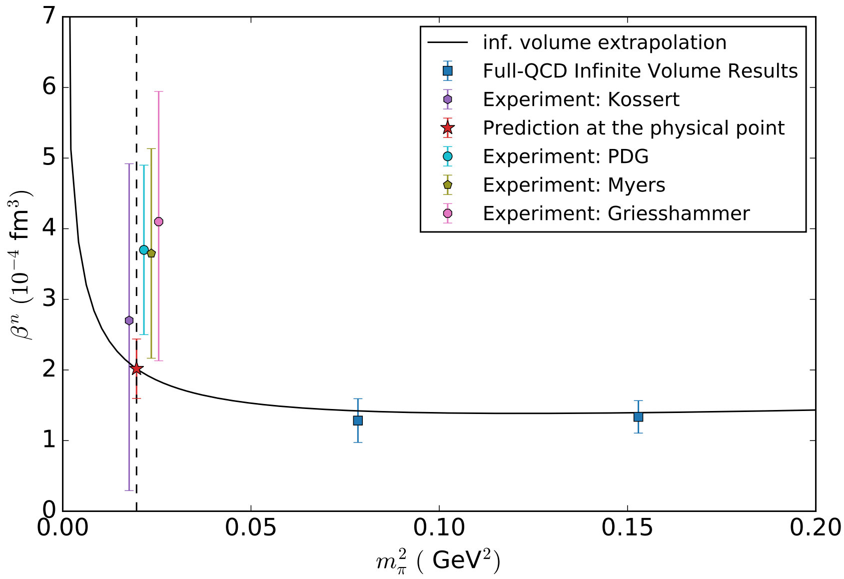

Figure 4.15. The magnetic polarisability of the neutron, β^n obtained herein is compared with experimental results. The uncertainties in the lattice results contain both statistical and systematic errors simply added together. This is a conservative approach to produce a reliable estimation. Experimental results from Kossert *et al.* [126, 127], the PDG [3], Myers *et al.* [129] and Griesshammer *et al.* [128] are offset for clarity.

The physical polarisability is obtained by considering the constrained fit function of Eq. (4.16) with $m_\pi = m_\pi^{phys} = 140$ MeV. While the coefficients of the leading non-analytic terms of the chiral expansion have been determined in a model-independent fashion, the uncertainty in the higher-order terms of the expansion can be examined through a variation of the regulator parameter Λ, which affects the sum of these contributions. The broad range of $0.6 \leq \Lambda \leq 1.0$ GeV considered provides a systematic uncertainty of 0.19×10^{-3} fm^3 at the physical point. Thus the magnetic polarisability of the neutron is found to be, $\beta^n = 2.05(25)(19) \times 10^{-3}$ fm^3 at the physical point. The uncertainties are derived from the statistical errors of the fit parameters and the systematic uncertainty associated with the chiral extrapolation respectively.

Figure 4.15 provides a comparison between this result and recent experimental data. This result is in good agreement with a number of the experimental results, posing an interesting challenge for greater experimental precision. Similarly, further progress in experimental measurements would drive further lattice QCD and chiral effective-field theory work.

As these results use a single lattice spacing it is not possible to quantify an uncertainty associated with taking the continuum limit. However, as a non-perturbatively improved clover action is used, the $\mathcal{O}(a^2)$ corrections are expected to be small relative to the uncertainties already presented. It is anticipated that due to the interaction of the background field with the Wilson term in the fermion action that there is some degree of additive quark mass renormalisation [111]. The extent to which this small effect remains with the clover fermion will be discussed in Chapter 5.

4.4. Summary

Asymmetric operators at the source and the sink have been used to calculate the neutron magnetic polarisability. The dominant QCD dynamics are encapsulated by gauge-invariant Gaussian smearing at the source, while a gauge-fixed $U(1)$ two-dimensional eigenmode quark projection technique is used at the sink to encode the Landau level physics resulting from the presence of the uniform background magnetic field. The parameter space was explored systematically throughout to optimise the operators used such that they couple efficiently to the neutron ground state in a magnetic field. This use of the Landau mode projection at the sink has for the first time enabled the fitting of plateaus in the magnetic polarisability energy shift at light quark masses approaching the physical values.

Calculations at several pion masses have enabled the lattice QCD results to be related to experiment through the use of heavy-baryon chiral effective-field theory. This enabled the theoretical prediction for the neutron magnetic polarisability of $\beta^n = 2.05(25)(19) \times 10^{-3}$ fm^3 . This prediction was founded on *ab initio* lattice QCD simulations, with effective-field theory used to account for the disconnected sea-quark-loop contributions, finite-volume of the lattice and to extrapolate to the light quark masses of nature. The resulting value is in good agreement with current experimental measurements and presents an interesting challenge for greater experimental precision.

To guide future lattice QCD simulations, a range of finite-volume extrapolations, incorporating the contributions of sea-quark-loops, are performed in the framework of chiral effective-field theory. It is found that extremely large box sizes are required in order to produce a result at the physical pion mass which is close to the infinite volume result.

Chapter 5.

Background field corrected clover action

The background-field method is a useful tool with which to investigate magnetic field effects when combined with lattice QCD. Recently, Bali *et al.* demonstrated that unphysical changes in the fermion energy are introduced when the Wilson quark formulation is used with the background field method [111, 150]. This is an important problem with the potential to effect all calculations made with Wilson style fermions (such as clover fermions) and the background field method. The high degree of sensitivity required for magnetic polarisability calculations renders this problem one that must be addressed.

In particular, Bali *et al.* determined the free-field limit of this unphysical change; the mass of a Wilson quark is shifted by an amount $\frac{a}{2}\,|qe\,B|$ to

$$m_{[\mathrm{w}]}\,(B) = m\,(0) + \frac{a}{2}\,|qe\,B|\,, \tag{5.1}$$

where a is the lattice spacing, B the magnetic field strength and the Wilson quark has charge qe and mass $m\,(0)$. The notation introduced here is that subscript labels in square brackets indicate a quantity which is affected by lattice background field artefacts due to the fermion action. This notation will be used throughout this chapter to distinguish quantities, particularly energies, which are and are not affected by the additive background field mass renormalisation. An example would be the pion mass $m_{[\pi]}$ and m_{π} respectively.

An alternative to the Wilson action, the overlap quark formalism [26, 27] was shown not to suffer from this problem of field-dependent mass renormalisation in Refs. [150] and [151]. However the overlap fermion action is many times more computationally expensive than the Wilson action, and thus the Wilson clover fermion action used in Chapter 4 and described in Section 3.3.1 is investigated to determine its suitability with respect to the additive mass renormalisation arising from the background field.

The clover fermion action is designed to remove $\mathcal{O}(a)$ lattice artefacts arising from the Wilson term. The additive mass renormalisation appears at $\mathcal{O}(a)$ in Eq. (5.1) and hence it is interesting to examine the extent to which it survives in the clover fermion formulation. In this chapter, the clover fermion is studied in both the free-field limit appropriate to Eq. (5.1) and full QCD to determine its efficacy in removing the unphysical background field dependent Wilson fermion artefacts.

This study is performed using neutral pion correlation functions which are a natural choice. Neutral pion correlation functions

- are free of hadronic magnetic moment contributions,
- provide precision at low computational expense,
- have no hadronic Landau level energy contribution,
- and offer insight into the difference between neutral and charged pions.

The lack of a hadronic Landau contribution is particularly helpful when investigating the Wilson-term field-dependent additive mass renormalisation.

The free-field limit is investigated first, to begin formulating a solution without the complications of QCD. When QCD interactions are present, the effects of the background field and QCD are in competition, making isolating and understanding the additive mass renormalisation due to the external magnetic field more challenging. Moreover, the full QCD calculations use a non-perturbatively improved clover coefficient, C_{SW}, which further complicates the transition from free-field to full QCD interactions.

5.1. Free-field limit

In the free-field limit, the quarks couple to the external magnetic field through their electric charges but do not experience any QCD interactions. This is done by setting the QCD gauge links U_μ to $U_\mu = \mathbb{I}$. The energy of a charged particle will contain a Landau energy contribution proportional to the charge of the particle. A free quark in a background magnetic field along the $\hat{z}$ axis will have relativistic energy

$$E^2\,(B) = m^2 + (2\,n + 1)\;|qe\,B| + p_z^2 + 2\,\vec{s}\cdot qe\vec{B}, \tag{5.2}$$

where p_z is the quark's momentum in the $\hat{z}$ direction, $|\vec{s}\,| = 1/2$ and the quark has charge qe. A Wilson fermion will have an additional energy contribution to the quark mass according to Eq. (5.1), and thus a free-field energy

$$E_{[\mathrm{w}]}^2\,(B) = \left(m + \frac{a}{2}\;|qe\,B|\right)^2 + (2\,n + 1)\;|qe\,B| + p_z^2 + 2\,\vec{s}\cdot qe\vec{B}, \tag{5.3}$$

as the mass renormalisation of Eq. (5.1) is the discretised lattice Laplacian, the mass renormalisation term is the lowest lying Landau level as discussed in Appendix C.2. This additional term vanishes in the continuum limit as a is the lattice spacing and it is hence identified with field-strength dependent additive quark mass renormalisation.

The presence of this additive mass term is demonstrated using the free-field pion mass. Both the charged pion energy, $E_{\pi^{\pm}}$ and neutral, connected pion energy $E_{\pi^0_{u/d}}$ are considered. The neutral-connected pion contains only the wick contractions of Figure 3.5a rather than the disconnected loops of Figure 3.5b. Nonetheless, it is a useful tool in this situation. The standard pseudoscalar interpolating operator

$$\chi = \overline{q}\,\gamma_5\,q \tag{5.4}$$

is considered, where the quark flavours are $\overline{u}u$, $\overline{d}d$ or $\overline{d}u$, corresponding to π^0_u, π^0_d and π^+ respectively.

To determine the expected energies of each of these three pions, it is necessary to consider the quark energies for each quark within the hadron. Consider first the $\overline{u}u$ pseudoscalar. As this is a spin-zero state composed of two quarks with spin magnitude $|\vec{s}| = 1/2$, the two quarks must have opposite spin orientations. Similarly the quark and anti-quark have opposite charges. Hence the lowest energy states for the u and $\overline{u}$ quarks in the $\overline{u}u$ pseudoscalar have energies

$$
\begin{aligned}
E^2_{[u]}\left(B,\downarrow\right) &= \left(m_u + \frac{a}{2}\,\left|q_u e\,B\right|\right)^2 + \left(2\,n+1\right)\,\left|q_u e\,B\right| + p^2_{z,u} - 2\,\frac{1}{2}\,q_u e\,B, \\
&= \left(m_u + \frac{a}{2}\,\left|q_u e\,B\right|\right)^2 + p^2_{z,u}, \qquad (5.5)\\
E^2_{[\overline{u}]}\left(B,\uparrow\right) &= \left(m_{\overline{u}} + \frac{a}{2}\,\left|q_{\overline{u}} e\,B\right|\right)^2 + \left(2\,n+1\right)\,\left|q_{\overline{u}} e\,B\right| + p^2_{z,\overline{u}} + 2\,\frac{1}{2}\,q_{\overline{u}} e\,B, \\
&= \left(m_{\overline{u}} + \frac{a}{2}\,\left|q_{\overline{u}} e\,B\right|\right)^2 + p^2_{z,\overline{u}}, \qquad (5.6)
\end{aligned}
$$

where the lowest lying Landau level $n = 0$ assumption has been made and $\uparrow$ / $\downarrow$ represents the spin orientation with respect to the orientation of the magnetic field, $\vec{B}$. The zero momentum, $p_z = 0$, $\overline{u}u$ pseudoscalar will then have energy

$$
\begin{aligned}
E_{[\pi^0_u]}\left(B\right) &= E_{[u]}\left(B,\downarrow\right) + E_{[\overline{u}]}\left(B,\uparrow\right), \\
&= m_u + \frac{a}{2}\,\left|q_u e\,B\right| + m_{\overline{u}} + \frac{a}{2}\,\left|q_{\overline{u}} e\,B\right|, \\
&= m_{\pi^0} + a\,\left|q_u e\,B\right|. \qquad (5.7)
\end{aligned}
$$

The lowest energy state is realised when the Landau level and quark spin-dependent terms cancel. An identical argument can be made for the $\overline{d}d$ pseudoscalar meson.

For a charged pion the spin-dependent term does not cancel the Landau term for both quark and anti-quark sectors. The lowest energy state of the charged pion is realised when the terms cancel for the quark flavour with the largest magnitude of electric charge.

For the charged π^+ meson comprised of $\overline{d}u$, the lowest energy state occurs when the u quark is spin down, enabling the cancellation of the spin-dependent and Landau terms as in Eq. (5.5). For $p_z = 0$, the charged pion will hence have energy

$$
\begin{aligned}
E_{[\pi^+]}\left(B\right) &= E_{[u]}\left(B,\downarrow\right) + E_{[\overline{d}]}\left(B,\uparrow\right), \\
&= m_u + \frac{a}{2}\,\left|q_u e\,B\right| + \sqrt{\left(m_{\overline{d}} + \frac{a}{2}\,\left|q_{\overline{d}} e\,B\right|\right)^2 + 2\,\left|q_{\overline{d}} e\,B\right|} \qquad (5.8)
\end{aligned}
$$

As QCD interactions are not present, no energy is required to displace the quarks from each other and thus the magnetic polarisability, β contribution to the energy is absent.

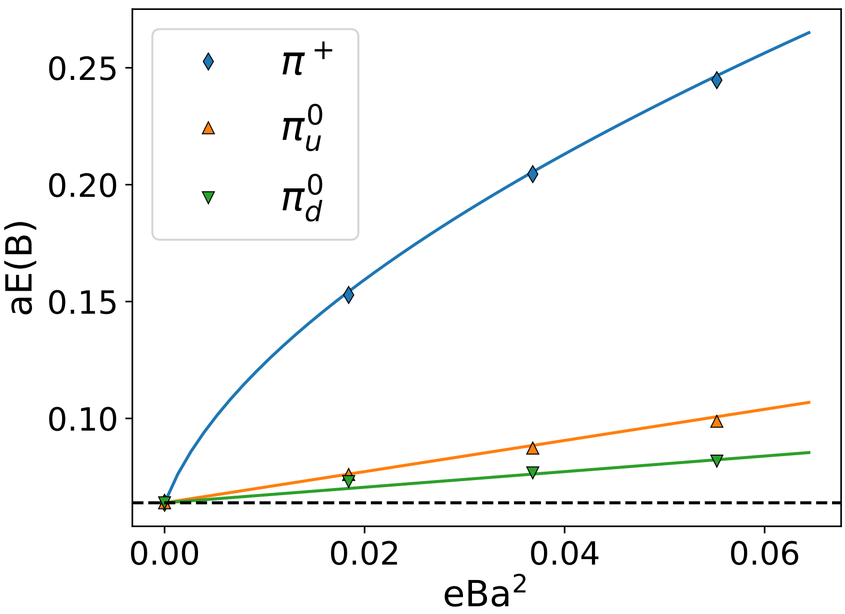

Figure 5.1. Pion energies from Wilson fermion correlation functions as a function of background magnetic field strength. The coloured curves are the expected energies for Wilson fermions based on Eqs. (5.7) and (5.8).

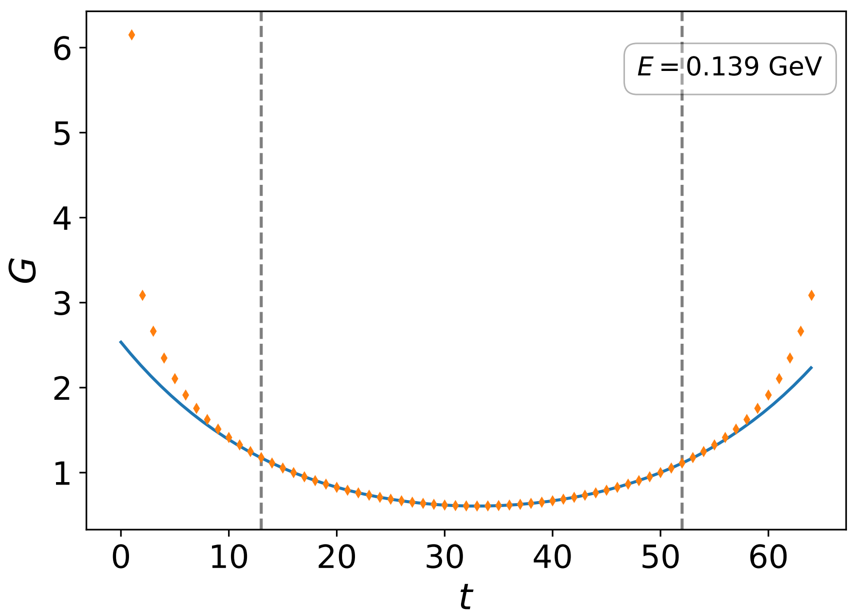

Figure 5.2. Pion zero-field correlator using (anti) periodic boundary conditions. The fit region, fit using Eq. (3.73) and resultant energy fit parameter are also shown.

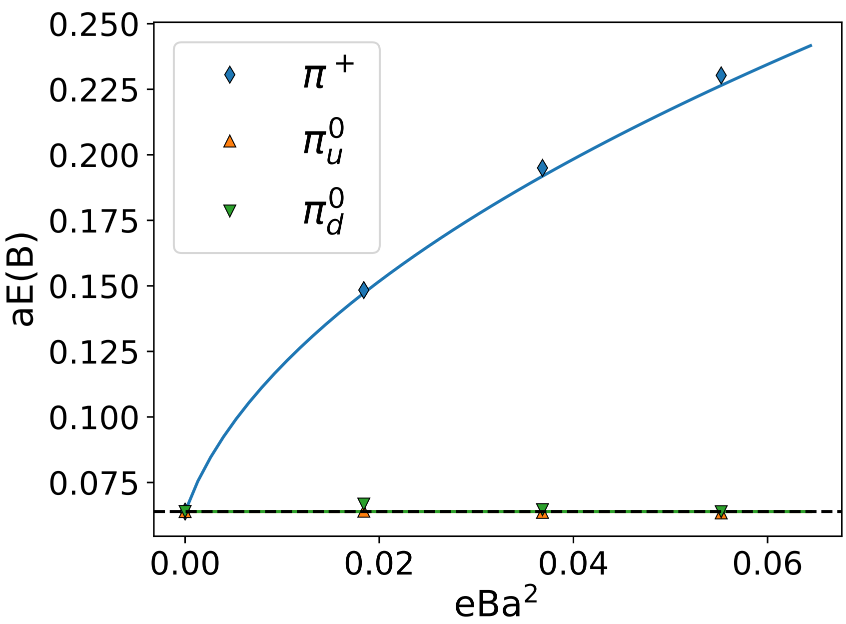

Figure 5.3. Pion energies from clover fermion correlation functions as a function of background magnetic field strength. The coloured lines are the expected energies in the absence of the Wilson background-field additive mass renormalisation, constant for the neutral pions and Eq. (5.9) for the charged pion.

It is useful to consider the absence of the Wilson background-field additive mass renormalisation where the charged pion energy is given by

$$\begin{aligned} E_{\pi^+}(B) &= E_u(B, \downarrow) + E_{\bar{d}}(B, \uparrow) \\ &= m_u + \sqrt{m_{\bar{d}}^2 + 2\,|q_{\bar{d}} e\, B|} \end{aligned} \tag{5.9}$$

Free-field numerical results for the charged and neutral pion energies in three non-zero background magnetic fields are shown in Figure 5.1 for Wilson fermions. Here the hopping parameter κ of Eq. (3.32) has been set to $\kappa = 0.12400$, relative to the bare critical hopping parameter of $\kappa_{cr} = 1/(8\,r)$, where $r = 1$. This is done in anticipation of exploring full QCD where the PACS-CS Sommer scale provides $a = 0.0951$ fm where this kappa value corresponds to a physical pion mass of approximately 140 MeV in the free-field limit.

Due to the lack of QCD interactions, the pion correlator is free to *wrap* or *reflect* around the temporal dimension of the lattice with only a gradual loss of signal. This poses an issue for the fixed boundary conditions used in Chapter 4; the reflected state interferes with the standard forward propagating state used to extract the pion energy. To remedy this, (anti) periodic boundary conditions are used in the time direction and the fits accommodate both the forward and backward propagating states. The fit function used is that of Eq. (3.73) and the corresponding fit displayed in Figure 5.2.

It is clear from the Wilson fermion energies in Figure 5.1 that the neutral pion energy closely follows that described by Eq. (5.7), showing that the additive mass renormalisation due to the Wilson term is correctly described by Eqs. (5.1) and (5.7). The charged π^+ energy further validates the additive mass renormalisation of Eq. (5.1) as it agrees with the analytic expectation of Eq. (5.8).

5.1.1. Clover correction

The aforementioned clover fermion action removes the $\mathcal{O}(a)$ artefacts from the Wilson action for QCD. The focus of this chapter is to determine the efficacy of clover fermions in removing the $\mathcal{O}(a)$ field strength dependent term of Eq. (5.1) due to the Wilson action.

Recalling Section 3.3.1; the clover fermion matrix may be written

$$D_{cl} = \nabla\!\!\!\!/ + \frac{a}{2}\,\Delta - a\,c_{cl} \sum_{\mu<\nu} \sigma_{\mu\nu}\,F_{\mu\nu} + m, \tag{5.10}$$

for m the bare quark mass, a the lattice spacing, ∇ the covariant finite difference operator of Eq. (3.8) and Δ the Wilson term of Eq. (3.28). The clover coefficient is c_{cl} and the clover term is

$$\sum_{\mu<\nu} \sigma_{\mu\nu}\,F_{\mu\nu}, \tag{5.11}$$

where the sum is restricted to avoid double counting and $F_{\mu\nu}$ is the clover discretisation of the lattice field strength tensor shown in Eq. (3.37) and Figure 3.4.

It is often useful in QCD+QED calculations to consider the electromagnetic and chromodynamic contributions to the field strength tensor separately [152]

$$F_{\mu\nu} = F_{\mu\nu}^{QCD} + F_{\mu\nu}^{EM}. \tag{5.12}$$

Here, as all the QCD links are set to unity in the free-field limit, the QCD field strength vanishes, $F_{\mu\nu}^{QCD} = 0$. As such we consider only the electromagnetic field strength in order to determine the appropriate value for the clover coefficient c_{cl}. Using the definition of the clover field strength tensor in Eq. (3.37) it is shown in Appendix B.7 that

$$\begin{aligned} F_{\mu\nu}^{EM} &= \frac{1}{2\,i}\left(\mathcal{C}_{\mu\nu} - \mathcal{C}_{\mu\nu}^{\dagger}\right), \\ \Longrightarrow\ F_{12} &= \frac{1}{2\,i}\left(\mathrm{e}^{i\,a^2\,qe\,B} - \mathrm{e}^{-i\,a^2\,qe\,B}\right) \\ &= \sin\left(a^2\,qe\,B\right). \end{aligned} \tag{5.13}$$

For the background field only along the $\hat{z}$ axis the field strength tensor has only one non-zero entry at $F_{12} = \sin\left(a^2\,qe\,B\right)$. As such the clover term is diagonal with

$$-c_{cl}\sum_{\mu<\nu}\sigma_{\mu\nu}F_{\mu\nu} = -\frac{c_{cl}}{2}\begin{pmatrix} +\sin(a^2\,qe\,B) & 0 & 0 & 0 \\ 0 & -\sin(a^2\,qe\,B) & 0 & 0 \\ 0 & 0 & +\sin(a^2\,qe\,B) & 0 \\ 0 & 0 & 0 & -\sin(a^2\,qe\,B) \end{pmatrix}. \tag{5.14}$$

This operator commutes with the lattice Laplacian of the Wilson term which is diagonal in Dirac space. Hence, as both operators are Hermitian, it is possible to write a shared eigenvector basis. In a uniform background magnetic field along the $\hat{z}$ axis, the minimum eigenvalue of this clover term is

$$\begin{aligned} \lambda_{\min} &= -\frac{c_{cl}}{2}\left|\sin\left(a^2\,qe\,B\right)\right| \\ &\approx -\frac{c_{cl}}{2}\,a^2\,qe\,B. \end{aligned} \tag{5.15}$$

For small field strengths where the Taylor expansion in the last line of Eq. (5.15) is valid; it is clear that if the clover coefficient is set to $c_{cl} = 1$, the tree-level value, that the clover term will cancel the Landau shift induced by the Wilson term which is described in Eq. (5.1).

This cancellation is evident in Figure 5.3 for the clover improved π_u^0 and π_d^0 neutral pions which do not show this additive mass renormalisation. The neutral pion energies do not change as a function of field strength. Similarly, the charged pion results agree with Eq. (5.9) for the charged pion energy in the absence of the Wilson background-field additive mass renormalisation. The tree level clover term has removed the $\mathcal{O}(a)$ additive mass renormalisation due to the Wilson term in a background magnetic field.

5.2. Full QCD

The removal caused by the clover term in the free-field limit is highly encouraging and necessitates a move to full QCD to understand the efficacy when QCD interactions are present. There are a number of complications to be considered in this transfer; namely the non-perturbatively improved clover coefficient, C_{SW} used with full QCD and the additional energy terms which make isolating the additive mass renormalisation difficult.

To study the possible adjustments to the clover coefficient required to obtain the correction observed in the free-field limit, the QCD and electromagnetic field strengths are allowed to posses different clover coefficients

$$c_{cl} \to C_{SW}\, F_{\mu\nu}^{QCD} + c_{EM}\, F_{\mu\nu}^{EM} . \tag{5.16}$$

Here C_{SW} is the coefficient of the clover improvement term discussed in Section 3.3.1 for the QCD gauge field interactions and c_{EM} the coefficient of the clover term which is generated by the $U(1)$ electromagnetic gauge field.

The QCD clover coefficient C_{SW} is renormalised by QCD and hence a non-perturbatively improved coefficient C_{SW}^{NP} is used. In order to determine the appropriate value for the electromagnetic clover coefficient c_{EM}, the "naive" approach where $c_{EM} = C_{SW}^{NP}$ is considered. Here the clover terms for the electromagnetic and QCD field strengths are treated in a uniform manner. Using this set up, the pion energy is investigated for the presence of magnetic field strength dependent artefacts as was done in the QCD free-field case.

When QCD interactions are present, there is a complex interplay between the background field and QCD effects [105, 132]. The pion has gained an internal structure and a mass which is dependent on the mass of the quarks in a more subtle way [117, 153] than in Eqs. (5.7) and (5.8).

Returning to the energy of a relativistic particle in a background field as in Eq. (3.100), here note that the pion has no magnetic moment term and thus (additive mass renormalisation free) energy

$$E_{\pi,n}^2\,(B) = m_\pi^2 + (2\,n+1)\;|qe\,B| + p_z^2 - 4\,\pi\, m_\pi\, \beta_\pi\, B^2 + \mathcal{O}\left(B^3\right) . \tag{5.17}$$

The fully relativistic form is used here as the Taylor expansion validity check of Eq. (3.104), $2\,m_H/\,(E_H + m_H)$ differs substantially from one for the largest field strength and lightest pion mass. Indeed at $m_\pi = 296$ MeV, this difference is as much as 22% which is significant in the context of highly precise pion correlation functions.

5.2.1. Energy shifts for Wilson fermions

The method with which to the effect of the nonperturbatively-improved clover coefficient in the full QCD calculations is investigated is with the neutral pion energy. The lowest-lying neutral pion energy in a background magnetic field is

$$E^2_{\pi^0}\,(B) = m^2_{\pi^0} - 4\,\pi\,m_\pi\,\beta_\pi\,B^2 + \mathcal{O}\left(B^3\right). \tag{5.18}$$

The additive quark mass renormalisation will have an effect on the pion mass. In QCD this effect is described by the Gell-Mann-Oakes-Renner relation [11, 117]

$$\begin{aligned} m^2_{\pi^0} &= -\frac{2\,m_{u/d}}{f^2_\pi}\,\langle\Omega\,|\,\overline{u}u\,|\,\Omega\rangle \\ &= m_{u/d}\,E_\Omega. \end{aligned} \tag{5.19}$$

Here $E_\Omega = -2\,\langle\Omega\,|\,\overline{u}u\,|\,\Omega\rangle\,/f^2_\pi$, where f_π is the pion decay constant and $\langle\Omega\,|\,\overline{u}u\,|\,\Omega\rangle$ is the chiral condensate. As $m^2_\pi \propto m_q$, E_Ω has a relatively weak quark mass dependence [154–156].

The background-field dependent pion mass is formed using the Wilson additive mass renormalisation of Eq. (5.1)

$$\begin{aligned} m^2_{[\pi^0]}\,(B) &= m_{[u/d]}\,(B)\;E_\Omega\,(B) \\ &= \left(m_{u/d} + \frac{a\,\xi}{2}\,\left|q_{u/d}e\,B\right|\right)\,E_\Omega\,(B)\,, \end{aligned} \tag{5.20}$$

where the coefficient ξ has been introduced to account for QCD effects modifying Eq. (5.1). ξ can in principle be B-field dependent.

An example of these QCD effects can be seen in Ref. [111]. Bali *et al.* investigated the Wilson fermion quark mass in full QCD by examining the change in the critical hopping parameter, κ_{cr} as a function of background magnetic field strength. The mass shift is an order of magnitude smaller than the free-field case for small external magnetic field strengths; and for their smallest field strengths the sign of the observed mass shift is opposite the free field case. The behaviour of Eq. (5.1) emerges at large magnetic field strengths as QCD effects become relatively small. The nonperturbatively-improved clover fermion results presented in the following section also display this order of magnitude suppression. The magnetic field strengths surveyed herein do not display the Wilson fermion sign change in the mass shift. Thus it is sufficient to treat ξ as a constant to be determined.

As it has been indicated in previous studies [157, 158] that E_Ω changes only slowly in an external magnetic field, the leading order approximation is considered

$$\begin{aligned} m^2_{[\pi^0]}(B) &\simeq \left(m_{u/d} + \frac{a\,\xi}{2}\,\left|q_{u/d} e\,B\right| \right)\,E_\Omega(0) \\ &\simeq m^2_{\pi^0} + \frac{a\,\xi}{2}\,\left|q_{u/d} e\,B\right|\,E_\Omega(0)\,. \end{aligned} \tag{5.21}$$

The zero-momentum neutral pion energy in an external magnetic field using Wilson fermions is thus

$$\begin{aligned} E^2_{[\pi^0]}(B) &= m^2_{[\pi^0]} - 4\,\pi\,m_{[\pi^0]}\,\beta_{\pi^0}\,B^2 + \mathcal{O}\left(B^3\right) \\ &\simeq m^2_{\pi^0} + \frac{a\,\xi}{2}\,E_\Omega(0)\,\left|q_{u/d} e\,B\right| - 4\,\pi\,\beta_{\pi^0}\,B^2\,\sqrt{m^2_{\pi^0} + \frac{a\,\xi}{2}\,E_\Omega\,\left|q_{u/d} e\,B\right|}. \end{aligned} \tag{5.22}$$

If the magnetic field dependence of E_Ω is linear in B, these terms can combined multiplicatively with the linear term $\frac{a\,\xi}{2}\,\left|q_{u/d} e\,B\right|$ due to the Wilson-term additive mass renormalisation to provide a contribution proportional to B^2. This is the same order as the $\mathcal{O}(B^2)$ signal used to extract the magnetic polarisability, $\beta^{\pi^0}_{u/d}$. It is hence important to ensure that this $\mathcal{O}(a)$ term is removed.

In order to determine the presence of additive quark mass renormalisation, consider the quantity

$$E^2_{[\pi^0]}(B) - m^2_{\pi^0} \simeq \frac{a\,\xi}{2}\,E_\Omega\,\left|q_{u/d} e\,B\right| - 4\,\pi\,\beta_{\pi^0}\,B^2\,\sqrt{m^2_{\pi^0} + \frac{a\,\xi}{2}\,E_\Omega\,\left|q_{u/d} e\,B\right|}. \tag{5.23}$$

This energy shift is constructed using a combination of correlator ratios and products

$$R_+(B,t) = G(B,t)\,G(0,t)\,, \tag{5.24}$$

$$R_-(B,t) = \frac{G(B,t)}{G(0,t)}, \tag{5.25}$$

where $G(B,t)$ is the zero-momentum projected two-point correlation function. Taking the effective energy, as defined by Eq. (3.78), of Eq. (5.24) yields

$$R_{+}(B,t) \overset{E_{eff}}{\rightarrow} E_{[\pi^0]}(B,t) + m_{\pi^0}(t)\,, \tag{5.26}$$

and Eq. (5.25)

$$R_{-}(B,t) \overset{E_{eff}}{\rightarrow} E_{[\pi^0]}(B,t) - m_{\pi^0}(t)\,. \tag{5.27}$$

These effective energy shifts are multiplied together to form the $E^2_{[\pi^0]}(B) - m^2_{\pi^0}$ energy shift of Eq. (5.23). Correlated QCD fluctuations largely cancel in the ratio of Eq. (5.25), an effect crucial to the isolation of B-dependent terms.

As Eq. (5.23) has leading order linear and quadratic terms in B, the fit function

$$E^2_{[\pi^0]}(k_d) - m^2_{\pi^0} = c_1\,k_d + c_2\,k_d^2, \tag{5.28}$$

where k_d is the integer describing the field strength experienced by the *down* quark in the pion from the quantisation condition of Eq. (3.99) and c_1, c_2 are fit parameters. The fit parameter c_1 can be estimated using Eq. (5.23)

$$c_1 = \frac{\pi}{a}\left|\frac{q_{u/d}}{q_d}\,\frac{\xi\,E_\Omega(0)}{N_x\,N_y}\right|. \tag{5.29}$$

Recalling the Gell-Mann-Oakes-Renner relation at zero magnetic field provides $E_\Omega(0) = m^2_{\pi^0}/m_q$ and the Wilson quark-mass relation of Eq. (3.32) which may also be written

$$m_q = \frac{1}{2\,a}\left(\frac{1}{\kappa} - \frac{1}{\kappa_{cr}}\right), \tag{5.30}$$

where κ_{cr} is the critical hopping parameter where the zero-field pion mass vanishes. Eq. (5.29) can hence be written

$$c_1 = 2\,\pi\,\left|q_{u/d}\right|\,q_d\,\frac{\xi\,m^2_{\pi^0}}{N_x\,N_y}\left(\frac{1}{\kappa} - \frac{1}{\kappa_{cr}}\right)^{-1}. \tag{5.31}$$

The magnetic polarisability may be related to c_2 using Eq. (5.23) as

$$\beta = -c_2\,\alpha\,\frac{q_d^2\,a^4}{m_{[\pi^0]}}\left(\frac{N_x\,N_y}{2\,\pi}\right)^2, \tag{5.32}$$

where $m_{[\pi^0]}$ is as in Eq. (5.21) and $\alpha = 1/137\ldots$ the fine structure constant. It is vital to remove the $\mathcal{O}(a)$ error due to background field dependent mass renormalisation, as if $c_1 \neq 0$ magnetic field dependence of E_Ω in Eq. (5.29) will induce $\mathcal{O}(B^2)$ contaminations to Eq. (5.32), and hence the magnetic polarisability value extracted will be incorrect.

Mass degeneracy of the zero-field *up* and *down* quark propagators in the lattice simulated allows neutral pion correlation functions with quark content $\overline{u}u$ or $\overline{d}d$ to be considered as magnetic field strength offset versions of each other, i.e. $G_{\overline{u}u}(B) = G_{\overline{d}d}(2\,B)$. As such, neutral pion correlation functions can be evaluated at a larger range of magnetic field strengths than is possible for the π^+, using the same quark propagators.

5.2.2. Nonperturbatively-Improved clover fermions

The nonperturbatively improved clover fermion action used in the full QCD calculations has a different clover coefficient C_{SW} than that used in the free-field calculations. The clover coefficient multiplies the $\mathcal{O}(a)$ clover term of the fermion action

$$\frac{i\,g\,a\,C_{SW}\,\kappa\,r}{4}\,\overline{\psi}\,\sigma_{\mu\nu}\,G_{\mu\nu}\,\psi, \tag{5.33}$$

where we return to $G_{\mu\nu}$ to emphasise the presence of QCD interactions. The clover term is discussed in more detail in Section 3.3.1. The full QCD calculations use the nonperturbatively improved value $C_{SW} = 1.715$ [25, 159] while the free-field simulations use the tree-level value of $C_{SW} = 1$. The energy shift defined in Eq. (5.21) is used to determine the extent which this changes the removal of the additive mass renormalisation seen to occur in Figure 5.3.

The two energy shifts required are $E_{[\pi^0]}(B) - m_{\pi^0}$ and $E_{[\pi^0]}(B) + m_{\pi^0}$. The first of these is displayed in Figure 5.4 where excellent plateau behaviour is readily observed. The second is shown in Figure 5.5 where correlated QCD fluctuations between field strengths compound rather than cancel, hence it is difficult to fit constant plateaus. The difficulty in fitting a constant plateau to Eq. (5.27) is problematic as common plateau fits are required for both $E_{[\pi^0]}(B) - m_{\pi^0}$ and $E_{[\pi^0]}(B) + m_{\pi^0}$. This substantially reduces the fit parameter space available.

Finally, a fit window of $t = [28, 34]$ is chosen. This fit window provides good fits for both energy shifts across each field strength considered, with acceptable $\chi^2_{dof} \leq 1.2$ as

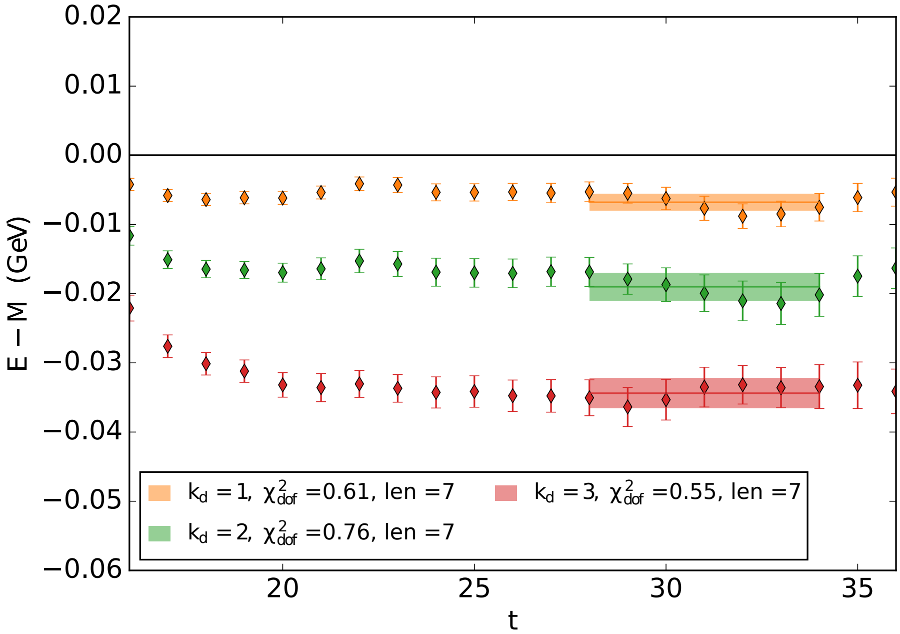

Figure 5.4. Neutral pion effective energy shift $E_{[\pi^0]}(B) - m_{\pi^0}$ from Eq. (5.24) using a nonperturbatively-improved clover fermion action on the $m_\pi = 296$ MeV ensemble. The fit window selected is indicated by the shaded region. The fit window was selected by considering the full covariance-matrix χ^2_{dof}, the extent of the fit window and the desire to select the same fit window for all effective-energy shifts. The three smallest field strengths are illustrated.

elsewhere in this thesis. This process minimises the systematics associated with a change of fit window provided $\chi^2_{dof} \leq 1.2$.

Recalling Eq. (5.23), the fit function of Eq. (5.28) is considered and the energy shifts fit as a function of field strength. First consider fixing $c_1 = 0$ and using a $c_2\, k_d^2$ quadratic-only fit function. This would be applicable to the complete removal of additive quark mass renormalisation by the clover fermion term. However as illustrated in Figure 5.6, the quadratic-only fit does not fit the data well and has an unacceptable χ^2_{dof} of $\chi^2_{dof} = 6.1$.

Using the full fit function, with allowance for a non-trivial c_1 coefficient produces a fit with $\chi^2_{dof} = 0.5$ which describes the lattice simulation results well. The success of this fit with a non-trivial c_1 coefficient indicates that the nonperturbatively-improved clover fermion simulation suffers from the presence of external field strength dependent additive mass renormalisation. The nonperturbatively-improved clover fermion action has not

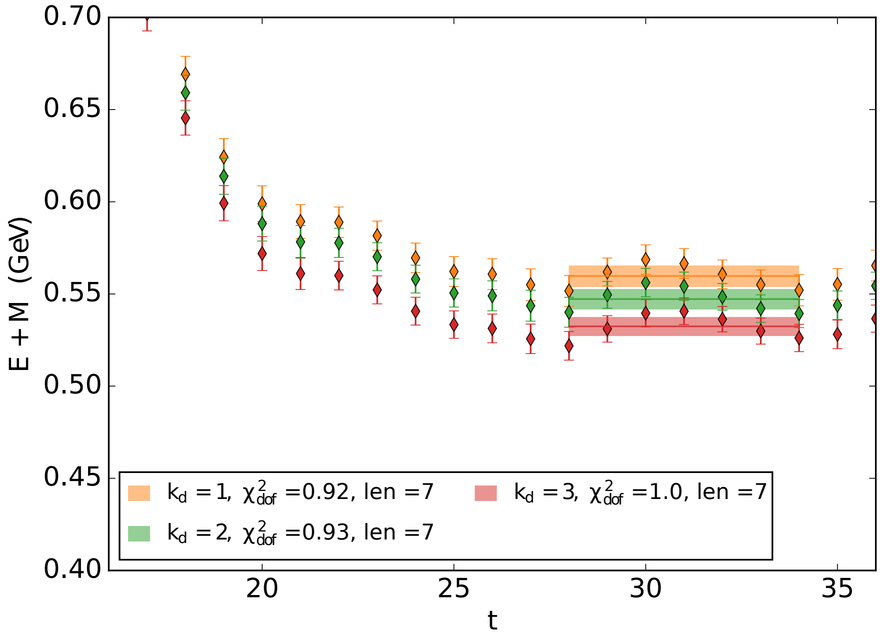

Figure 5.5. As described in Figure 5.4 but for the $E_{[\pi^0]}(B) + m_{\pi^0}$ energy shift produced by Eq. (5.25).

removed the additive mass renormalisation in full QCD as the tree-level clover action did in the free-field case.

A quadratic + cubic, $c_2\, k_d^2 + c_3\, k_d^3$ fit is also considered. Such a fit is applicable to higher order terms and explores the necessity of the $\mathcal{O}(a)$ term linear in the magnetic field strength. However, this model produces unacceptably high χ^2_{dof} values and does not describe the lattice simulation results. Due to the mass degeneracy of *up* and *down* quarks, a fit over four field strengths is able to be considered. Acceptable fits as a function of field quanta to this require linear, quadratic and cubic terms. While a sufficient number of higher order terms will clearly fit perfectly with as many terms as field strengths considered, the addition of a linear term is a simpler model than adding multiple higher order terms. Thus, the demand for an $\mathcal{O}(B)$ linear term associated with the presence of additive mass renormalisation is robust.

5.2.3. Expected mass renormalisation

The results just presented indicate that the naive use and formulation of the clover term is insufficient to removal the Wilson-like additive quark mass renormalisation. With a

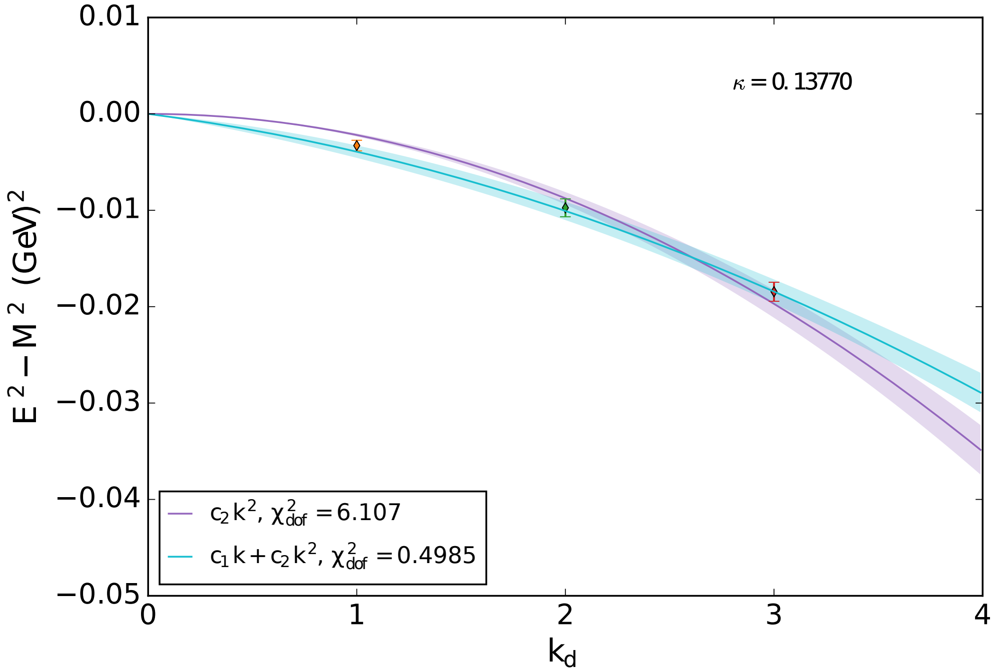

Figure 5.6. Fits of the magnetic-field induced energy shift to the magnetic-field quanta for the nonperturbatively-improved clover fermion action. The full covariance-matrix based χ^2_{dof} provides evidence of a non-trivial value for the fit coefficient c_1, associated with the presence of unphysical Wilson-like additive mass renormalisation in the nonperturbatively-improved clover fermion action.

view to the free-field results, the application of the nonperturbatively-improved clover coefficient $C_{SW}^{NP} = 1.715$ to both the QCD and background field contributions to the clover term has prevented the removal of the magnetic field dependent additive mass renormalisation.

Recalling the discussion of Section 5.1.1, the tree-level value of $C_{SW}^{Tree} = 1$ is the value required for the removal of $\mathcal{O}(a)$ errors. As such the nonperturbative value has over compensated by an amount

$$D^{NP} = C_{SW}^{Tree} - C_{SW}^{NP} = 1.0 - 1.715 = -0.715, \tag{5.34}$$

where this over compensation is relative to the standard Wilson action coefficient of

$$D^{W} = C_{SW}^{Tree} = 1.0. \tag{5.35}$$

In order to produce a prediction for the non-trivial value of c_1 using the nonperturbatively-improved clover fermion action, the over compensation factor of Eq. (5.34) is incorporated into the expectations for Wilson-fermion of Section 5.2.1 through

$$\xi \to \xi^{NP} = \frac{D^{NP}}{D^{W}}\, \xi. \tag{5.36}$$

Hence Eqs. (5.31) and (5.36) can be used with the order of magnitude factor, $\xi = 1/10$ to provide an estimate for the fit parameter c_1.

For the π_d^0 on the $m_\pi = 296$ MeV ensemble, $\kappa_d = 0.13770$ and $\kappa_{cr} = 0.13791$ [25], this produces $c_1 \sim -3 \times 10^{-3}$ GeV^2. The corresponding linear + quadratic, $c_1\, k_d + c_2\, k_d^2$ fit provides $c_1 = -2.8(9) \times 10^{-3}$ GeV^2. These results are close, and the simulation result agrees with the expectation within statistical error.

This result is highly encouraging, and hence in the next section the clover terms for the QCD and background fields are separated, such that C_{SW}^{Tree} can be applied to the background field contributions while the QCD fields use C_{SW}^{NP}.

5.3. Background field corrected clover fermion action

Here a modified fermion action is formulated, where the QCD and background magnetic field contributions to the field strength tensor, $G_{\mu\nu}(x)$ of the $\mathcal{O}(a)$ clover term are treated separately. This enables the nonperturbatively improved value of $C_{SW}^{NP} = 1.715$ to be applied to the QCD contributions and the tree-level value $c_{EM} = 1.0$ to be applied to the background magnetic-field contributions. As the background-magnetic field is known analytically, its contributions are calculated analytically and added to the QCD contributions. The modified fermion action will henceforth be referred to as the Background Field Corrected Clover (BFCC) fermion action.

5.3.1. Additive mass renormalisation

Correlation functions and energy shifts are calculated and formed as described in Section 5.2.1 using the BFCC fermion action. The new effective energy shifts and fits are displayed in Figures 5.7 and 5.8 for the $m_\pi = 296$ MeV ensemble. The $E_{\pi^0}(B) + m_{\pi^0}$ energy shift remains challenging, but possible to fit. This is not-unexpected as no specialised sink is used here as is done in Chapters 4 and 6.

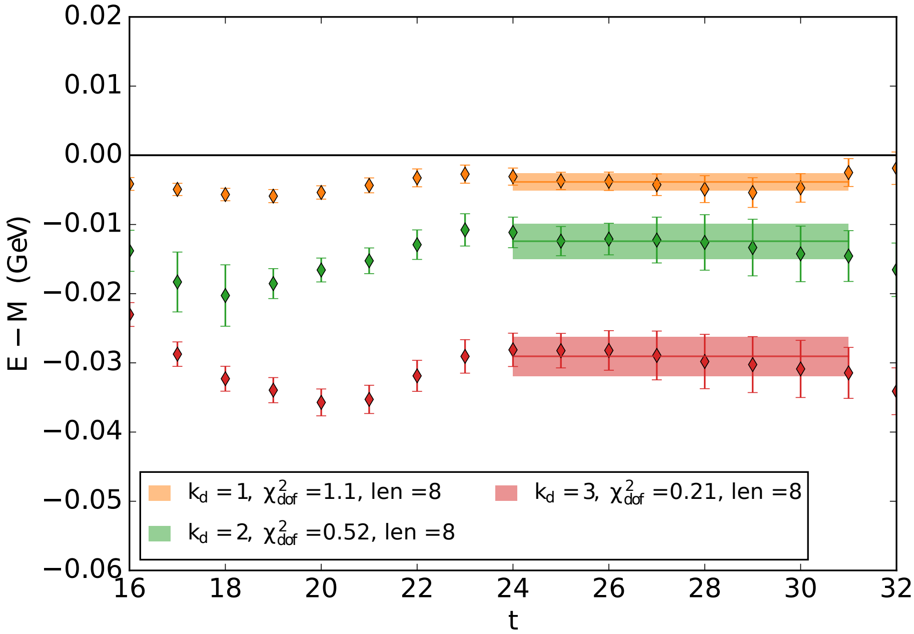

Figure 5.7. Neutral pion effective energy shift $E_{\pi^0}(B) - m_{\pi^0}$ from Eq. (5.24) using the BFCC fermion action on the $m_\pi = 296$ MeV ensemble. The shaded region illustrates the fit window chosen as in Figure 5.4.

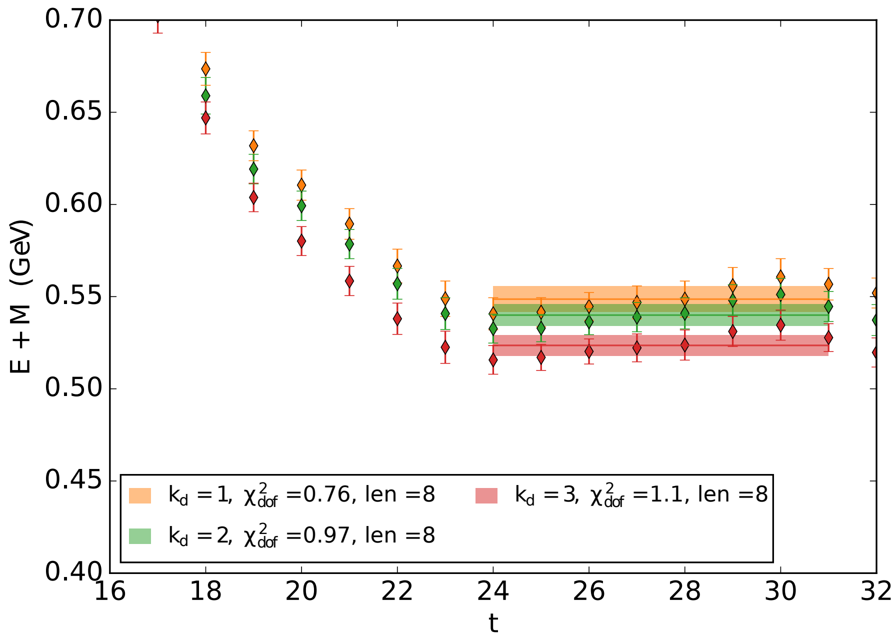

Figure 5.8. As described in Figure 5.7 but for the $E_{\pi^0}(B) + m_{\pi^0}$ energy shift produced by Eq. (5.24).

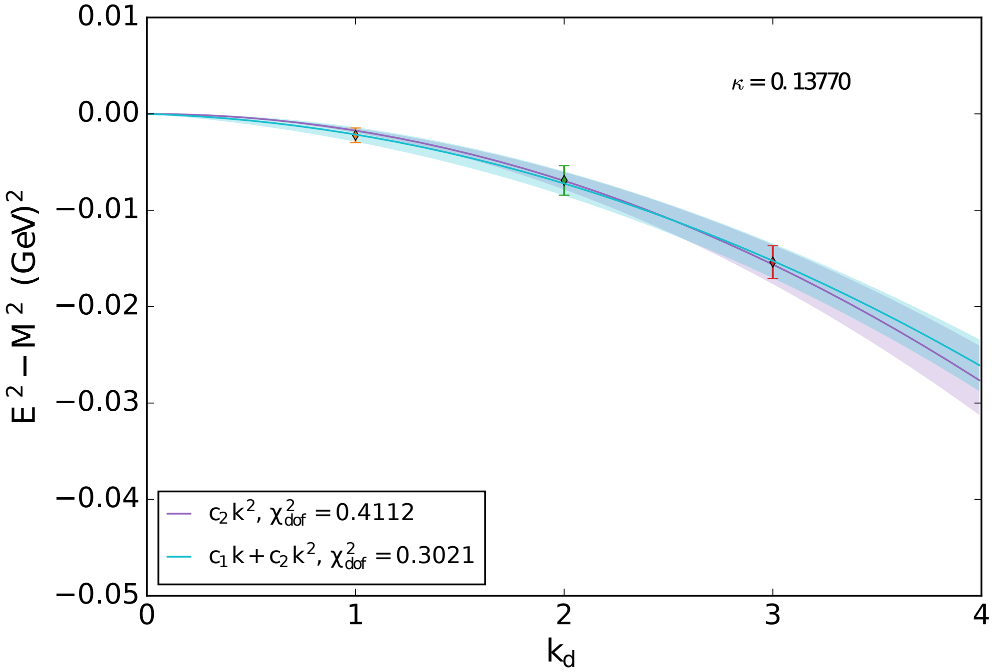

Figure 5.9. Fits of the magnetic-field induced energy shift to the magnetic-field quanta for the BFCC fermion action. The full covariance-matrix based χ^2_{dof} provides evidence of the elimination of unphysical Wilson-like additive mass renormalisation in the nonperturbatively-improved clover fermion action. Allowing for a non-trivial value of c_1 produces a value consistent with zero.

Supposing now the absence of additive mass renormalisation, then Eq. (5.23) simplifies to

$$E^2_{\pi^0}\,(B) - m^2_{\pi^0} = -4\,\pi\,m_{\pi^0}\,\beta_{\pi^0}\,B^2 + \mathcal{O}\left(B^3\right), \tag{5.37}$$

and thus fit functions of the form

$$E^2_{\pi^0}\,(k_d) - m^2_{\pi^0} = c_1\,k_d + c_2\,k_d^2 + c_3\,k_d^3, \tag{5.38}$$

are considered. Wilson-like additive mass renormalisation is allowed for by the linear term proportional to c_1. This term should not be required if the BFCC action has removed the field-dependent additive mass renormalisation.

Fits to the three lowest $E^2_{\pi^0}\,(k_d) - m^2_{\pi^0}$ energy shifts using the fit functions of Eq. (5.38) are displayed in Figure 5.9. Acceptable fits are obtained with the higher order fit coefficient c_3 constrained to zero. The success of the quadratic only $c_2\,k_d^2$ fit reflects the ability of the BFCC action to fully remove the Wilson-like additive quark mass renormalisation

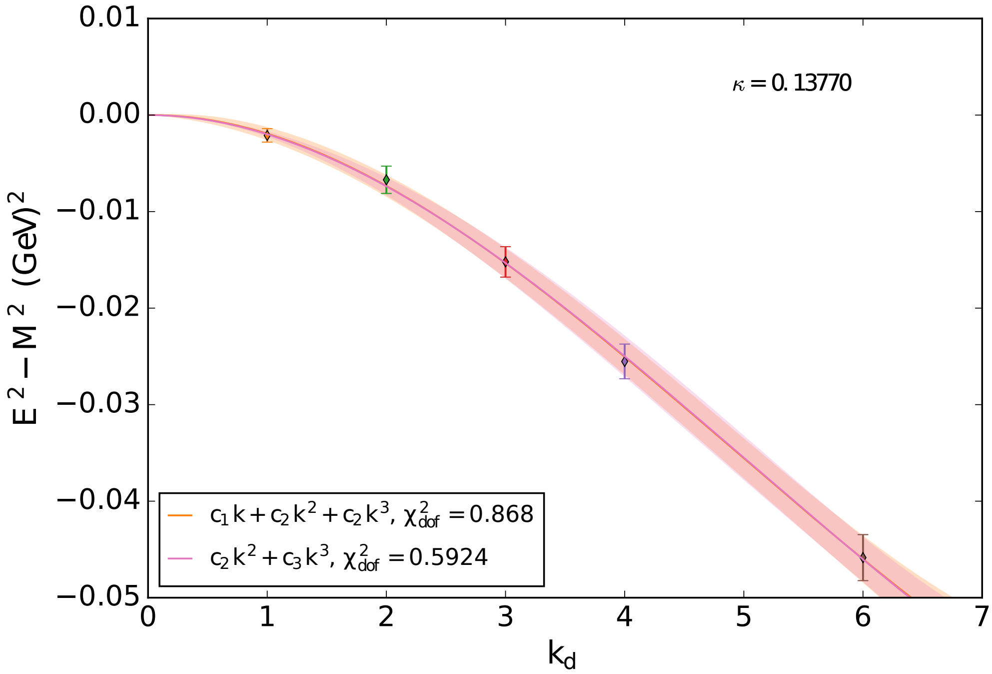

Figure 5.10. Fits of the magnetic-field induced energy shift to the magnetic-field quanta for the BFCC fermion action. The full covariance-matrix based χ^2_{dof} provides evidence of the elimination of unphysical Wilson-like additive mass renormalisation in the nonperturbatively-improved clover fermion action. Allowing for a non-trivial value of c_1 produces a value consistent with zero.

and produce an energy shift matching Eq. (5.37). The $c_1\, k_d + c_2\, k_d^2$ fit, which allows for a non-trivial value of c_1 yields $c_1 = (-5.3 \pm 8.7) \times 10^{-4}$ GeV^2, which is consistent with zero.

Due to the mass degeneracy of *up* and *down* quarks in the lattice simulation, the full range of magnetic field strengths corresponds to $k_d = 1, 2, 3, 4, 6$. This full range is considered in Figure 5.10. Here the fits require $c_3 \neq 0$, indicating the presence of a $\mathcal{O}\left(B^3\right)$ term. The success of the BFCC is reconfirmed as the quadratic + cubic fit provides an excellent description of the results without a non-trivial c_1 term. A linear + quadratic + cubic fit which allows for a non-trivial value for c_1, produces $c_1 = (1.1 \pm 9.0) \times 10^{-4}$ GeV^2, consistent with zero.

Fits to the first four magnetic field strengths produces similar results. The BFCC action lattice results do not require fits with a linear c_1 term and allowing for $c_1 \neq 0$ gives $c_1 = (-6.2 \pm 8.2) \times 10^{-4}$ GeV^2, which is again consistent with zero. With only four field strengths, a cubic term proportional to c_3 is not required, but as the onset of non-trivial $\mathcal{O}\left(B^3\right)$ behaviour is clearly between the field strengths which correspond to

$k_d = 4$ and $k_d = 6$; only the three smallest field strengths will be used when determining the magnetic polarisability.

These results have shown that the BFCC fermion action removes the additive quark mass renormalisation due to the Wilson term. The key modification is to use a tree level value $c_{EM} = 1$ for uniform background-field contributions to the fermion clover term.

5.3.2. Comparison to Bali *et al.*

In Ref. [111], Bali *et al.*demonstrated the existence of a background field dependent additive quark mass renormalisation due to the Wilson term and proposed to account for this effect by a field dependent tuning of the bare quark mass. A summary of this method is presented below, drawn from the full details presented in Ref. [111].

While the neutral pion mass vanishes in the chiral limit, even at finite background magnetic field strengths, electroquenching effects produce chiral logarithms [160, 161] which make it difficult to use the neutral pion mass to determine the bare quark mass at non-trivial field strengths. Instead the current quark mass $\widetilde{m}_f$, obtained from the axial Ward-Takahashi identity (WI) is used. As the neutral WIs are unchanged from their zero-field form, this gives

$$a\,\widetilde{m}_f\,(B) = \frac{\partial_0 \left\langle (J_A)_0^f\,(x_0)\; P^f\,(0)\right\rangle}{2\,\langle P^f\,(x_0)\; P^f\,(0)\rangle}, \tag{5.39}$$

where $x_0 \neq 0$, $(J_A)^f$ is the point-split axial current operator and P^f is the associated pseudoscalar density for fermion fields of flavour f. Eq. (5.39) is considered separately for both the π_d^0 and π_u^0 as earlier in this chapter.

The current quark mass is calculated for several values of the hopping parameter κ for each background field strength considered and a linear fit performed as a function of $1/\kappa - 1/\kappa_{c,f}\,(B=0)$ where $\kappa_{c,f}\,(B=0)$ is the zero-field critical hopping parameter. The bare quark mass in a background field will then vanish at a field and flavour dependent critical hopping parameter $\kappa_{c,f}\,(B)$

$$\frac{1}{\kappa_{c,f}\,(B)} = \left(\frac{1}{\kappa\,(0)} - \frac{1}{\kappa_{c,f} B = 0}\right)\Bigg|_{a\,\widetilde{m}_f(B)=0}^{fit}, \tag{5.40}$$

where $(1/\kappa(0) - 1/\kappa_{c,f}(B=0))\,|^{fit}_{a\,\widetilde{m}_f(B)=0}$ is the value of $1/\kappa - 1/\kappa_{c,f}(B=0)$ where the linear fit crosses $a\,\widetilde{m}_f(B) = 0$. The bare quark mass can then be tuned at each field strength to keep $a\,\widetilde{m}_f(B)$ constant and hence remove the field dependent additive quark mass renormalisation. This process takes the form

$$\frac{1}{\kappa_f(B)} = \frac{1}{\kappa(B=0)} - \left(\frac{1}{\kappa_{c,f}(B)} - \frac{1}{\kappa_{c,f}(B=0)}\right), \tag{5.41}$$

where $\kappa_f(B)$ is the new-field dependent hopping parameter and $\kappa(B=0)$ is the zero-field hopping parameter desired.

While the method described above and in Ref. [111] is successful in removing the field dependent additive quark mass renormalisation due to the Wilson term, it is a theoretically and computationally challenging process. It requires calculations at multiple quark masses (κ values) for each field strength, increasing the computational resources required substantially. The point split axial current operator $(J_A)^f$ is also non-trivial to implement. Furthermore the quark mass retuning will need to be performed again if $\mathcal{O}(a)$ improvement, i.e. from the clover fermion term is implemented.

The BFCC action in contrast includes $\mathcal{O}(a)$ improvement, does not require tuning, is easy to implement and does not incur substantial additional computational expense as it requires only a minor change to the fermion action. The BFCC action modifies the clover term such that QCD contributions use a non-perturbatively improved clover coefficient while the background field contributions to the clover term use a tree level coefficient.

5.3.3. Magnetic polarisability

As the Wilson-like additive quark mass renormalisation has been removed by the BFCC fermion action, the magnetic polarisability can be determined from the B^2 term, now free of the $\mathcal{O}(a)$ contamination discussed in Section 5.2.1.

The fits and energy shifts performed in Section 5.3 are used and the polarisability extracted from the coefficient c_2 of the fit of Eq. (5.38). The magnetic polarisability is then given by the conversion of Eq. (5.32) where $m_{[\pi^0]}$ is now just the mass m_{π^0} rather than the Wilson-mass.

The magnetic polarisability of the neutral pion using the $\mathcal{O}(a)$ improved BFCC fermion action analysis for the three lowest magnetic field strength is reported in Table

Table 5.1. Magnetic polarisability of the neutral pion from the $\mathcal{O}(a)$-improved BFCC-fermion-action analysis of the lowest three magnetic-field strengths. Correlation functions with a smeared source and point sink are considered. Numbers in parentheses represent statistical uncertainties.

κ_{ud}	m_π (MeV)	$\beta_{\pi^0_d}$ ($\times 10^{-4}$ fm^3)
0.13754	411	0.62(4)
0.13770	296	0.54(7)

5.1 on two gauge field ensembles. While the report in this chapter has discussed only the ensemble with light-quark hopping parameter $\kappa_{ud} = 0.013770$ corresponding to $m_\pi = 296$ MeV, results for $\kappa_{ud} = 0.013754$ corresponding to $m_\pi = 411$ MeV are also reported.

Only the three lowest field strengths and a single quadratic fit, $\propto c_2\, k_d^2$ are used in these results. This is to avoid the possibly complications of non-trivial $\mathcal{O}(B^3)$ contributions as discussed in the previous section. The inclusion of a fourth point for the $m_\pi = 296$ MeV ensemble takes the magnetic polarisability from $\beta_{\pi^0_d} = 0.54(7)$ to $0.52(5) \times 10^{-4}$ fm^3. The small improvement in statistical uncertainty may be offset by an increase in the systematic uncertainty associated with non-trivial $\mathcal{O}(B^3)$ contributions and so only the three smallest field strengths are used.

5.4. Summary

In this chapter, the pion in a uniform background field has been investigated. Particular attention has been paid to the possibility of the existence of a field-strength dependent additive quark-mass renormalisation associated with Wilson fermions. This existence was confirmed and clover fermions examined to determine the ability of the clover fermion action to remove these spurious contributions.

In the free-field limit, where no QCD interactions are present, the clover term with a tree level clover coefficient removes the field-strength dependent additive quark-mass renormalisation. To ensure the same when QCD interactions are present, a careful treatment of the clover term of Eqs. (3.35) and (5.33) is required. In order to remove $\mathcal{O}(a)$ errors in QCD, the nonperturbatively-improved clover coefficient $C_{SW}^{NP} = 1.715$ is required; while the background magnetic-field contributions require $c_{EM} = 1.0$. Separating this treatment enables the clover term to remove the $\mathcal{O}(a)$ errors in QCD and also the $\mathcal{O}(a)$

errors associated with the background magnetic field. This modified fermion action is referred to as the Background Field Corrected Clover (BFCC) fermion action.

Once the $\mathcal{O}(a)$ errors associated with the Wilson term of the fermion action have been suppressed by the BFCC fermion action, the neutral pion magnetic polarisability is determined using the fully relativistic energy shift for the first time. Results at two pion masses are summarised in Table 5.1. The magnetic polarisability of the neutral pion, $\beta_{\pi^0_d}$ is positive, hence the energy of a neutral pion in a magnetic field decreases. Such a decrease and its extent is of interest [162, 163] and these results indicate that the $\mathcal{O}(B^3)$ contributions may soften this trend.

Research presented in Chapter 7 will involve an extension to the charged pion, an approach to the physical quark mass regime and an interface with chiral perturbation theory [164, 165]. The lattice simulations for this future work is performed in Chapter 7 using the formalism developed here and in Chapter 6. Sea-quark-loop interactions with the background field are also important and not present in these results. They may be incorporated by producing a separate Monte-Carlo ensemble for each field-strength considered and is as such prohibitively expensive. Separate ensembles also removes the advantageous QCD correlations between different magnetic field strengths.

An alternate approach to multiple Monte-Carlo ensembles is to separate the valence and sea-quark-loops contributions to the magnetic polarisability in effective field theory [125]. This process is discussed in detail in Chapter 6 for a general baryon, with the proton as a specific example. Such separation would enable a calculation of sea-quark-loop contributions to the magnetic polarisability of the pion and hence an accurate extrapolation of current lattice QCD results to the physical regime.

Chapter 6.

$SU(3) \times U(1)$ eigenmode projection

The magnetic polarisabilities of the neutron, proton and a selection of hyperons are calculated using the formalism developed in Chapters 4 and 5. A new eigenmode projected quark sink, which encapsulates both QCD and Landau level physics, is introduced. As demonstrated in Chapter 4 and previous studies [105,166] Landau physics remains relevant even when QCD interactions are present. Thus it is anticipated that this sink will provide good access to the energy shifts required to determine the magnetic polarisability.

6.1. Quark operators

As in Chapter 4, asymmetric source and sink operators are used to construct correlation functions which have greater overlap with the energy eigenstates of the various particles in a background magnetic field.

6.1.1. $SU(3) \times U(1)$ eigenmode quark projection

In a manner similar to the $U(1)$ Landau eigenmode projected quark sink discussed in Section 4.1.2, the low-lying eigenmodes of the two-dimensional lattice Laplacian

$$\Delta_{\vec{x},\vec{x}'} = 4\,\delta_{\vec{x},\vec{x}'} - \sum_{\mu=1,2} U_\mu\left(\vec{x}\right)\,\delta_{\vec{x}+\hat{\mu},\vec{x}'} + U_\mu^\dagger\left(\vec{x}-\hat{\mu}\right)\,\delta_{\vec{x}-\hat{\mu},\vec{x}'}, \tag{6.1}$$

are calculated. Here, the gauge links $U_\mu\left(\vec{x}\right)$ contain the full $SU(3) \times U(1)$ gauge links as applied in the full lattice QCD simulation. When the number of eigenmodes considered is truncated to some selected value, the completeness relation for the mode projection

$$\mathbb{I} = \sum_{i=1} \left|\psi_{i,\vec{B}}\right\rangle \left\langle\psi_{i,\vec{B}}\right| , \tag{6.2}$$

is truncated, giving rise to a finite-size, two-dimensional smearing of the quark propagator sink by filtering out the high frequency modes. This smearing grows in size as more higher order modes are truncated. It is important to quantify the effect of the truncation when choosing an appropriate truncation level.

The factors considered when selecting this truncation value include

- Computational feasibility - Eigenmodes must be able to be calculated and stored. This can be a significant problem with eigenmode files containing ~ 100 eigenmodes being ≈ 10 Gigabytes for a lattice of size $32^3 \times 64$.
- Plateau behaviour - Early onset of plateau behaviour in effective mass shifts is required.
- Statistical uncertainty - The finite-size smearing of the quark propagator sink can increase the statistical noise in the correlation function.
- Consistency with lowest lying Landau level - It is essential to only use the eigenmodes which correspond to the lowest lying Landau level.

In the pure $U(1)$ case considered in Section 4.1.2, the lowest Landau level on the lattice has a degeneracy equal to the magnetic flux quanta $|k|$, which provides a natural truncation level. As Eq. (6.1) introduces QCD interactions into the Laplacian via the $SU(3)$ component of the gauge links, the $U(1)$ modes associated with the different Landau levels become mixed. It is no longer possible to clearly identify the modes which are associated with the lowest Landau level at small field strengths [105, 167]. Instead a number of modes $n > |k|$ are projected. Here we investigate three levels of eigenmode truncation, $n = 32$, 64 and 96. This spread was chosen such that both small and large eigenmode number were considered.

As Eq. (6.1) is a two-dimensional Laplacian, we calculate the low-lying eigenspace independently on each (z, t) slice. This allows us to interpret the four-dimensional coordinate space representation of an eigenmode

$$\left\langle \vec{x}, t \,\middle|\, \psi_{i,\vec{B}} \right\rangle = \psi_{i,\vec{B}}\left(x, y|z, t\right) , \tag{6.3}$$

as selecting the two-dimensional coordinate space representation $\psi_{i,\vec{B}}(x,y)$ from the eigenspace which belongs to the corresponding (z,t) slice of the lattice. The four-dimensional coordinate space representation of the projected operator used to investigate the appropriate eigenmode number is hence

$$P_n(\vec{x},t;\vec{x}',t') = \sum_{i=1}^{n} \left\langle \vec{x},t \,\middle|\, \psi_{i,\vec{B}} \right\rangle \left\langle \psi_{i,\vec{B}} \,\middle|\, \vec{x}',t' \right\rangle \delta_{zz'}\,\delta_{tt'}, \tag{6.4}$$

where the Kronecker delta functions ensure the outer product is only taken between eigenmodes from the subspace (and equivalently, that the projection operator acts trivially on the (z,t) coordinates).

This is the same construction as the projection operator of Eq. (4.3) with the notable difference of the eigenmodes used. As before, this projection operator is applied at the sink to the quark propagator in a coordinate-space representation as

$$S_n\left(\vec{x},t;\vec{0},0\right) = \sum_{\vec{x}'} P_n(\vec{x},t;,\vec{x}',t')\; S\left(\vec{x}',t;\vec{0},0\right), \tag{6.5}$$

where n is the number of eigenmodes and hence is either $n = 32$, 64 or 96.

The appropriate eigenmode number is guided by the properties of the relevant correlation functions. While $n = 32$ eigenmodes is not effective in energy eigenstate isolation due to statistical noise, both 64 and 96 eigenmodes produce qualitatively similar results as is evident in Figure 6.1. A comparison of the magnetic polarisability energy shift of Eq. (4.11) for three non-zero field strengths is presented in Figure 6.1. The projected sink using $n = 96$ eigenmodes fulfils the requirements above with improved signal isolation compared to $n = 64$ eigenmodes. Hence $n = 96$ eigenmodes are used for the remainder of this work.

Distillation

The $SU(3) \times U(1)$ eigenmode projection technique introduced herein shares some similarities with the distillation approach of Refs. [70], [168] and [169]. The distillation approach calculates the low-lying eigenspace of the three-dimensional spatial Laplacian independently on each time (t) slice of the lattice. Distillation enables efficient construction of all-to-all propagators [70, 170, 171] once the *perambulators* have been constructed by inversion of the lattice Dirac operator against each eigenvector in the eigenspace of time

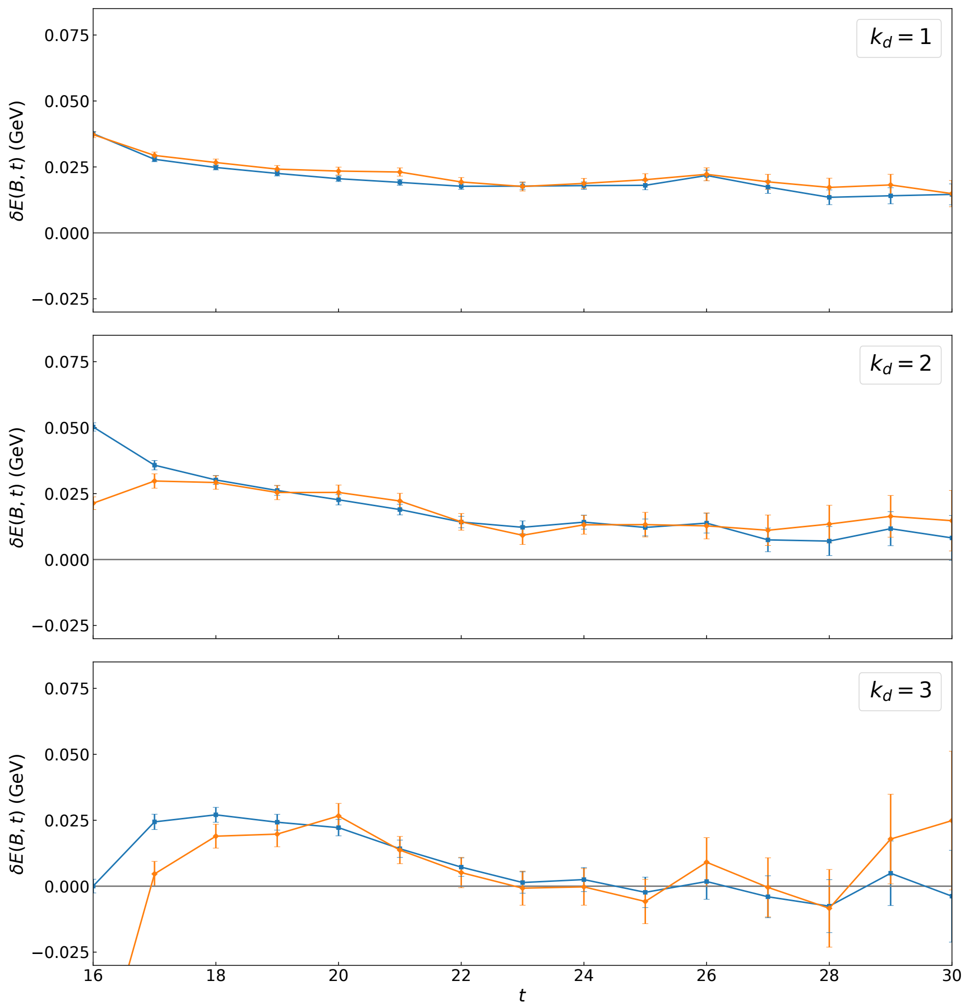

Figure 6.1. Proton energy shift $E(B) - m$ using 64 (orange diamond) and 96 (blue square) eigenmodes in the projection operator of Eq. (6.5) on the $m_\pi = 702$ MeV ensemble.

slice (t). Hence, there is a significant initial overhead in constructing the *perambulators*, but once this overhead has been paid the ability to access the all-to-all nature is a benefit.

In contrast, the approach herein utilises the two-dimensional Laplacian operator defined in Eq. (6.1) which is calculated independently on each (z, t) slice. The three-dimensional nature of the distillation approach is not suitable in the presence of a background magnetic field along the $\hat{z}$-axis that explicitly breaks three-dimensional spatial symmetry. Furthermore the Laplacian projector is applied to a standard point-to-all propagator, avoiding the significant overheard required for the distillation approach. The two-dimensional Laplacian projector used herein can be applied to any all-to-all computational approach, including stochastic estimation such as in Ref. [171] or the

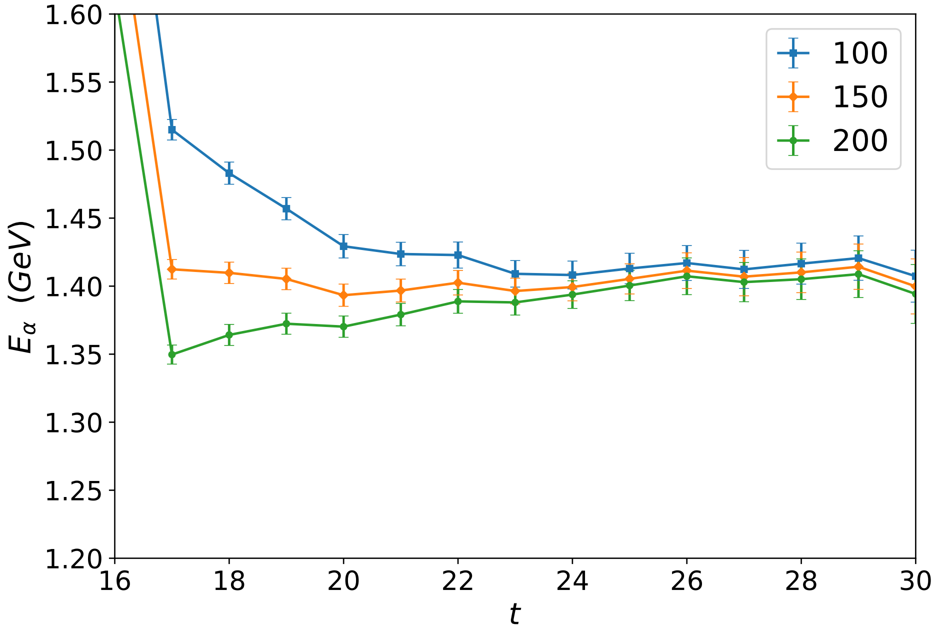

Figure 6.2. Nucleon zero-field effective masses from three different smeared sources to $SU(3)$ $\times U(1)$ eigenmode projected sink correlation functions on the m_π = 702 MeV ensemble. The source is at $t = 16$.

distillation method. Once the eigenmodees have been calculated, the computational cost of including these quark operators is comparable to a typical QCD-only calculation using the same technique.

The scaling behaviour of the required number of eigenmodes for the $SU(3) \times U(1)$ projection technique as a function of lattice volume is worth investigation and may be guided by the approach used in Ref. [70]. The notable difference is that in the presence of a background field, the introduction of the lowest Landau level is likely to affect the number of eigenmodes required.

6.1.2. Gaussian smeared source

The Gaussian smeared source provides a representation of the QCD interactions. The QCD ground state is isolated through examination of a broad range of smearing levels at zero field strength. The effective mass was investigated for each ensemble of gauge fields considered and the smearing which produces the earliest onset of plateau behaviour chosen.

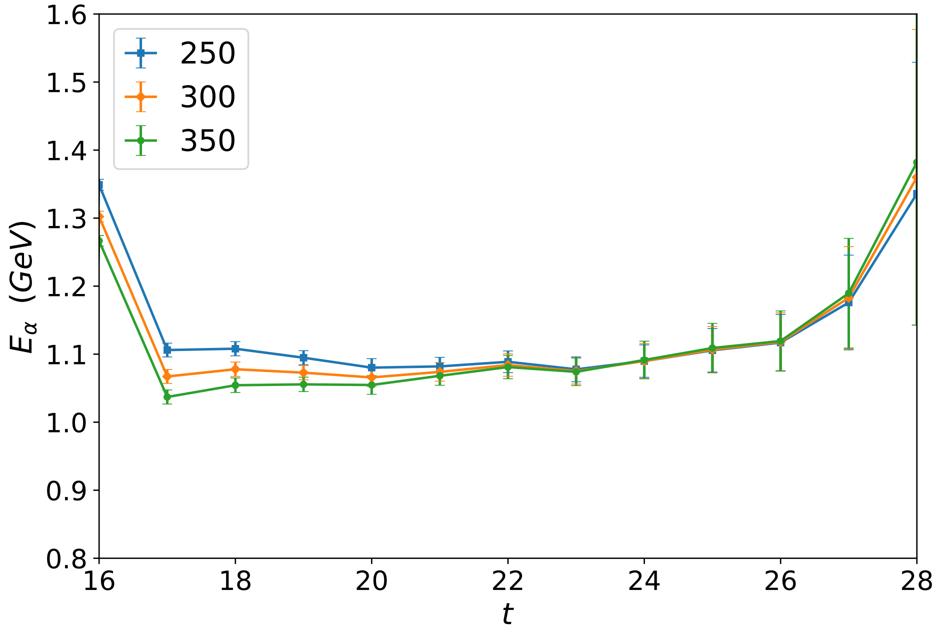

Figure 6.3. Nucleon zero-field effective masses from three different smeared sources to $SU(3)$ $\times U(1)$ eigenmode projected sink correlation functions on the $m_\pi = 296$ MeV ensemble. The source is at $t = 16$.

For the ensemble with the heaviest quark mass considered, $\kappa_{ud} = 0.13700$, corresponding to $m_\pi = 702$ MeV, this choice is quite obvious as shown in Figure 6.2. The optimal smearing of 150 sweeps produces the early onset of plateau behaviour while 100 and 200 sweeps do not plateau as early and approach from above and below respectively.

When the $\kappa_{ud} = 0.13770$ ensemble is examined in Figure 6.3, the choice is not as obvious. The three smearing levels reach agreement earlier and are less different than for the $\kappa_{ud} = 0.13700$ ensemble in Figure 6.2. Hence, to fully understand and determine the optimal smearing, correlation functions are run at each finite field strength to be considered for each smearing and these results are examined. The $k_d = 2$ proton anti-aligned (as in Section 4.2) correlation function is shown in Figure 6.4 where a problem with large amounts of smearing is clearly visible. The anti-aligned energy has spin and magnetic field anti-aligned as in Eq. (4.9). This energy is examined in preparation for its use in the energy shift ratio of Eq. (4.10).

The proton $k_d = 2$ anti-aligned energy with 350 sweeps of smearing differs from that produced by 250 or 300 sweeps. This difference corresponds to the difference between

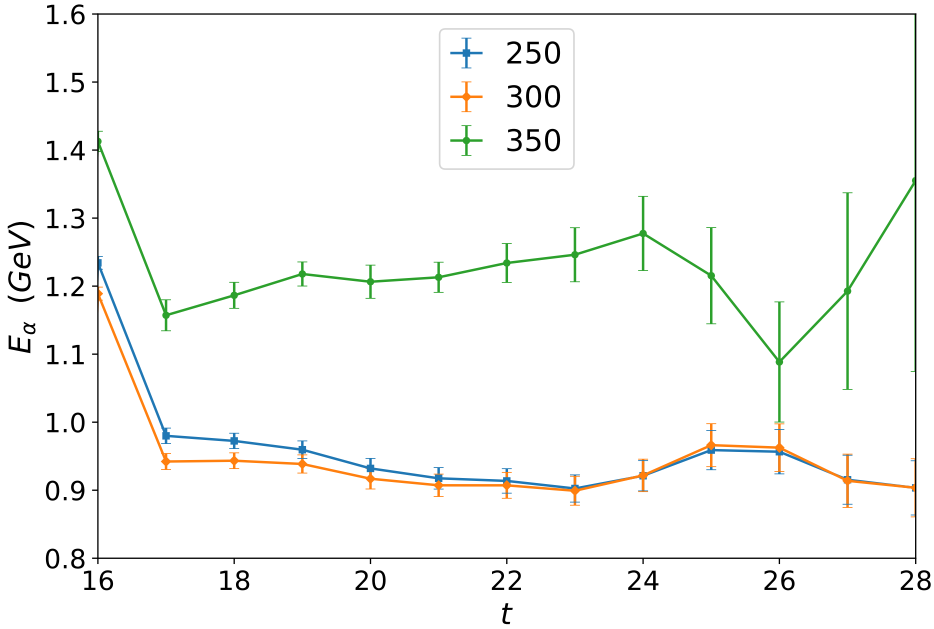

Figure 6.4. Proton $k_d = 2$ anti-aligned effective energy shifts of Eq. (4.9) from three different smeared sources to $SU(3) \times U(1)$ eigenmode projected sink correlation functions on the $m_\pi = 296$ MeV ensemble. The source is at $t = 16$.

Landau levels for the proton, i.e. for

$$E_n^2\,(B) \sim m^2 + |e\,B|\,\left(2\,n + 1 - \alpha\right), \tag{6.6}$$

where $n = 0, 1, 2, 3, \ldots$ and α is the eigenvalue of σ_z which appears in the spin operator as in Appendix C; the difference can be determined by considering the relativistic energy difference

$$\begin{aligned}
E_1^2\,(B) - E_0^2\,(B) &= 2\,|e\,B| \\
\left(E_1\,(B) - E_0\,(B)\right)\,\left(E_1\,(B) + E_0\,(B)\right) &= 2\,|e\,B| \\
\Delta\,E_{10}\,(B)\,\left(E_1\,(B) + E_0\,(B)\right) &= 2\,|e\,B| \\
\Delta\,E_{10}\,(B)\,\left(\Delta\,E_{10}\,(B) + 2\,E_0\,(B)\right) &= 2\,|e\,B|\,, \\
\Delta\,E_{10}^2\,(B) + 2\,E_0\,(B)\,\Delta\,E_{10}\,(B) - 2\,|e\,B| &= 0,
\end{aligned} \tag{6.7}$$

where $\Delta E_{10}(B) = E_1(B) - E_0(B)$ is what must be determined. Using the appropriate values for Figure 6.4 of

$$E_0(k_d = 2) \sim 0.9 \text{ GeV},$$
$$|e\,B(k_d = 2)| \sim 0.522 \text{ GeV}^2,$$

where we recall that the field strength experienced by the proton is related to that of the down quark by $k_B = -3\,k_d$; the energy difference between these two Landau levels is $\Delta E_{10}(k_d = 2) \sim 0.46$ GeV. This is close to the difference between smearings in Figure 6.4.

The proton, with an excessively large source couples to the higher Landau levels rather than the lowest. This is evident in how the effective energy for $N_{sm} = 350$ sweeps differs from the other smearings of Figure 6.4 in both value and slope. Due to this higher Landau level coupling, the optimal smearing level chosen is $N_{sm} = 250$ sweeps of Gaussian smearing.

The source smearing is varied and examined on each of the ensembles considered. The optimal smearings for ensembles with light quark hopping parameters κ_{ud} = 0.13700, 0.13727, 0.13754, 0.13770 and corresponding masses m_π = 702, 570, 411, 296 MeV are chosen to be N_{sm} = 150, 175, 300, 250 sweeps respectively.

6.1.3. $U(1)$ hadronic projection

While the $SU(3) \times U(1)$ eigenmode projection technique is relevant to the quark level Landau effects; charged hadrons, such as the proton and Σ^+ also experience hadronic Landau effects. The hadronic energy eigenstates constructed by the Fourier momentum-projected two-point correlation function of Eq. (3.54) are no longer eigenstates of the p_x and p_y momentum components due to the presence of the uniform background field in the $\hat{z}$ direction. Hence the x, y dependence of the two-point correlation function is projected onto the lowest Landau level explicitly, and a specific value for the z component of momentum chosen

$$G\left(p_z, \vec{B}, t\right) = \sum_r \sum_{i=1}^{n} \psi_{i,\vec{B}}(x,\, y)\; e^{-i\,p_z\,z}\; \langle\Omega|\overline{\chi}(r,t)\;\chi\left(\vec{0},t\right)|\Omega\rangle\,. \tag{6.8}$$

Here a linear combination of the $U(1)$ eigenmodes calculated in Chapter 4 are used at the appropriate field strength for the hadron of charge q_H and $n = n_{\max} = 3\,q_H\,k_d$. The

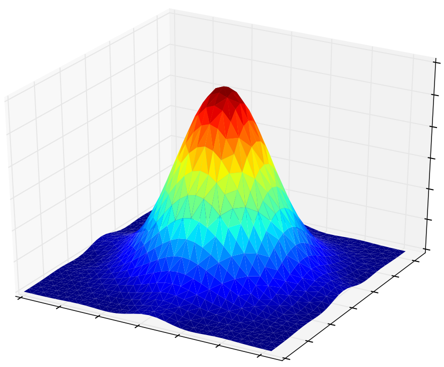

(a) $i = 1$ eigenmode for $k_d = -6$.

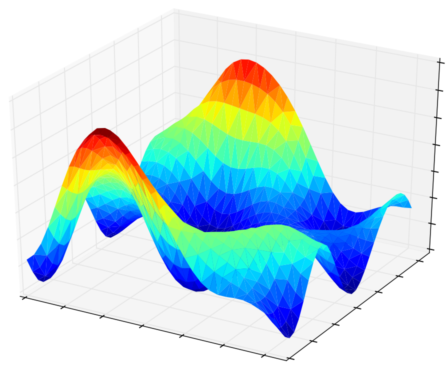

(b) $i = 2$ eigenmode for $k_d = -6$.

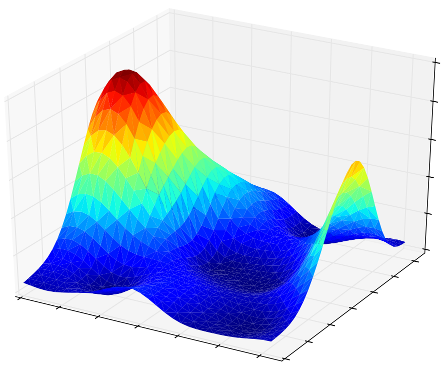

(c) $i = 3$ eigenmode for $k_d = -6$.

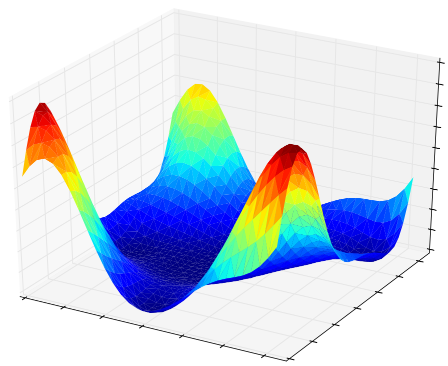

(d) $i = 4$ eigenmode for $k_d = -6$.

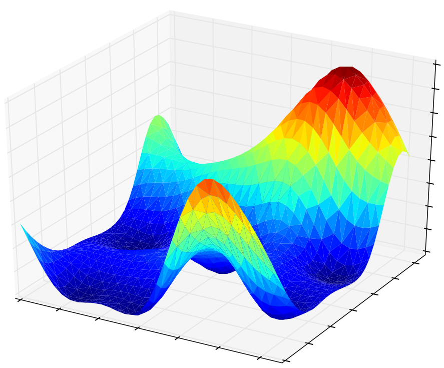

(e) $i = 5$ eigenmode for $k_d = -6$.

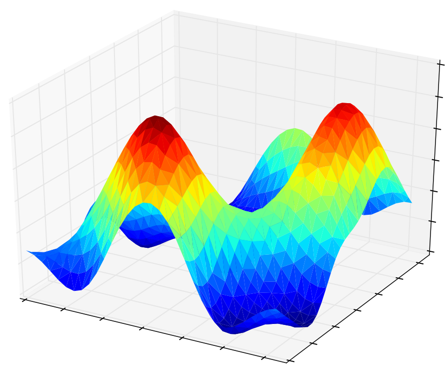

(f) $i = 6$ eigenmode for $k_d = -6$.

Figure 6.5. Lowest lying $U(1)$ eigenmode probability densities of the lattice Laplacian operator in a constant background magnetic field oriented in the $\hat{z}$ direction are plotted as a function of the x, y coordinates. The degenerate eigenmodes for the sixth quantised field strength, relevant to the $k_d = 2$ proton are displayed. The origin is at the centre of the $x - y$ plane.

six degenerate eigenmodes for $k_d = -6$, relevant to the proton with down quark magnetic field quanta $k_d = 2$ are shown in Figure 6.5. Noting that the $n = 1$ eigenmode in Figure 6.5a has the greatest overlap with the smeared source and also the continuum Landau wave function; an eigenmode using just the $n = 1$ single mode is also examined. This overlap is by construction; we perform an optimised rotation of eigenmodes to construct this overlap.

A comparison of the three different types of hadronic projection is shown in Figure 6.6 for the π^+ on the $m_\pi = 296$ MeV ensemble. The π^+ is chosen to investigate this choice due to the greater precision of pion correlation functions. The left column displays the effective energy for each of the three non-zero field strengths and the zero-field correlator while the right is the energy shift $E(B) - m$ of Eq. (4.11) required to access the magnetic polarisability. The zero-field correlator uses the appropriate standard Fourier projection method on each occasion.

It is clear that the single-mode eigenmode projection of Figures 6.6c and 6.6d produce the cleanest plateau behaviour. This distinction is particularly obvious for this choice of hadron and ensemble - the statistical uncertainty is such that a clear difference is seen. For nucleons on this ensemble, the statistical error is greater [131] and distinction between the all and single-mode projection methods is not present. Conversely on ensembles with a heavier quark (hence pion) mass, both eigenmode projection methods converge for the pion, and often for the nucleon. This convergence is evident in the pion energies presented in Figure 6.7.

The single-mode projection is tuned such that it encapsulates the majority of the overlap of the wave function; adding the additional modes of the sum does not change the observed effective energy in the high statistics regime. This is evident in the success of the $n = 1$ eigenmode projection.

The hadronic eigenmode projection is crucially important in isolating the ground Landau state for a charged hadron [113] and hence construction of the energy shifts of Eqs. (4.11) and (5.37) required to extract the magnetic polarisability.

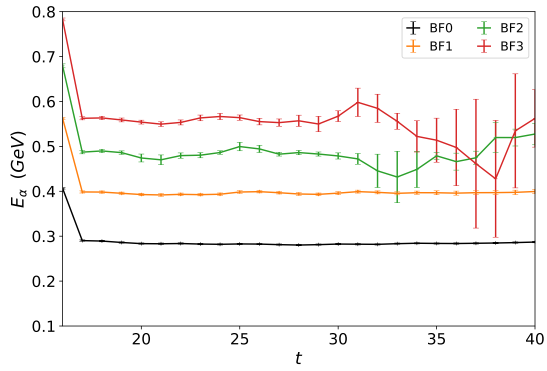

(a) π^+ energy using standard Fourier projection in four field strengths.

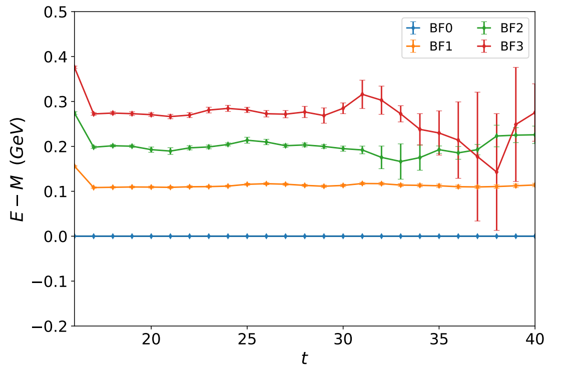

(b) π^+ energy shift from Eq. (4.10) using standard Fourier projection in four field strengths.

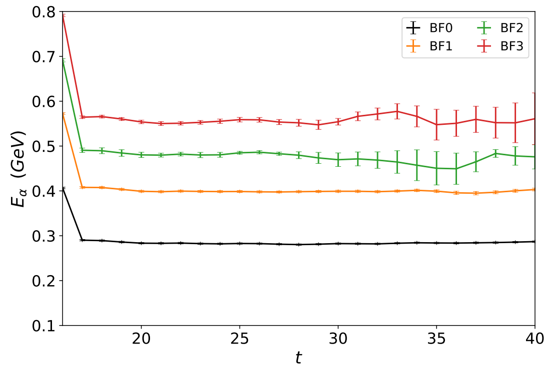

(c) π^+ energy using single eigenmode projection in four field strengths.

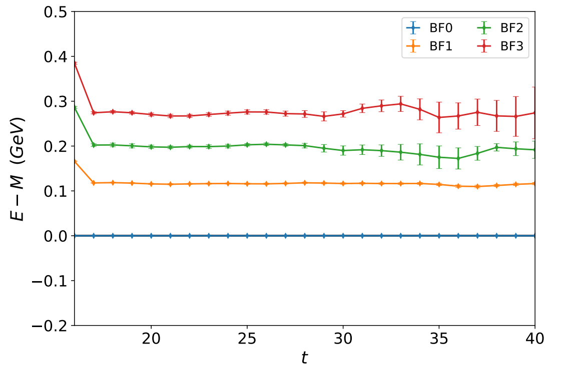

(d) π^+ energy shift from Eq. (4.10) using single eigenmode projection in four field strengths.

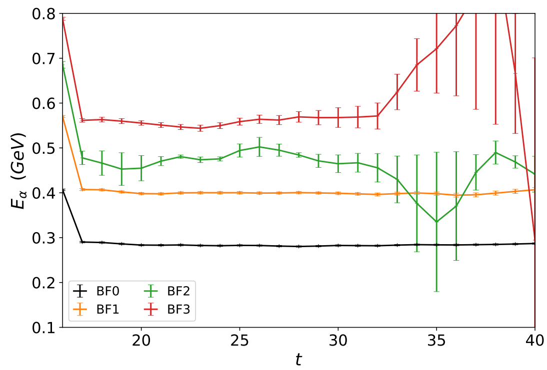

(e) π^+ energy using $n = 3\, q_H\, k_d$ eigenmodes projection in four field strengths.

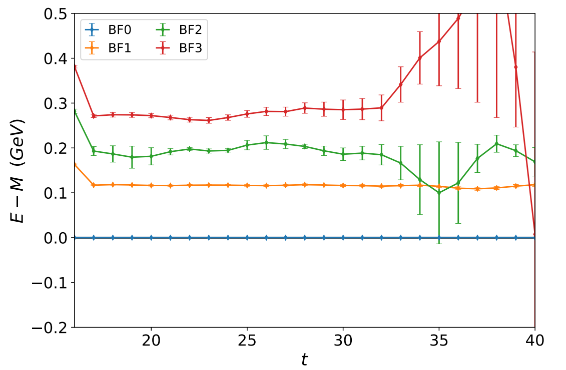

(f) π^+ energy shift from Eq. (4.10) using $n = 3\, q_H\, k_d$ eigenmodes projection in four field strengths.

Figure 6.6. A comparison of the three different hadronic projections for the charged pion on the $\kappa_{ud} = 0.13770$ ensemble with $m_\pi = 296$ MeV. The energy and energy shift as a function of field strength are shown in the left and right columns respectively.

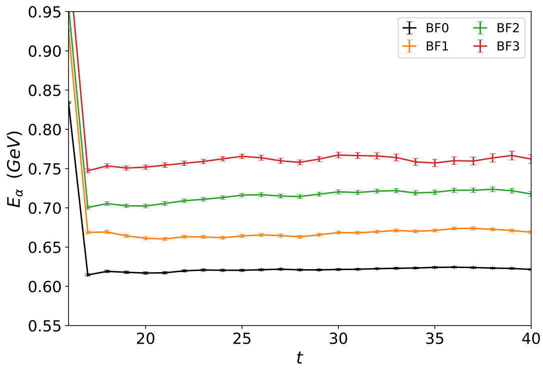

(a) π^+ energy using standard Fourier projection in four field strengths.

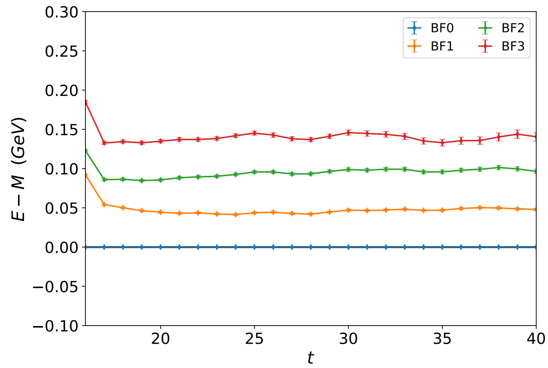

(b) π^+ energy shift from Eq. (4.10) using standard Fourier projection in four field strengths.

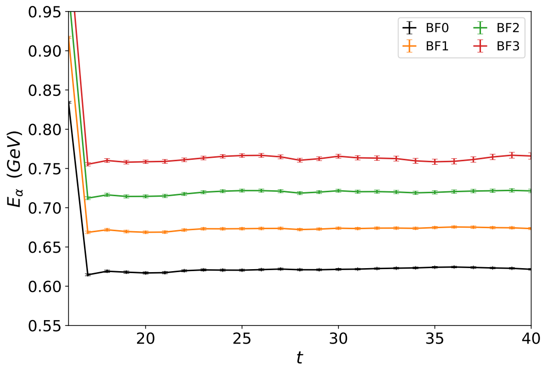

(c) π^+ energy using single eigenmode projection in four field strengths.

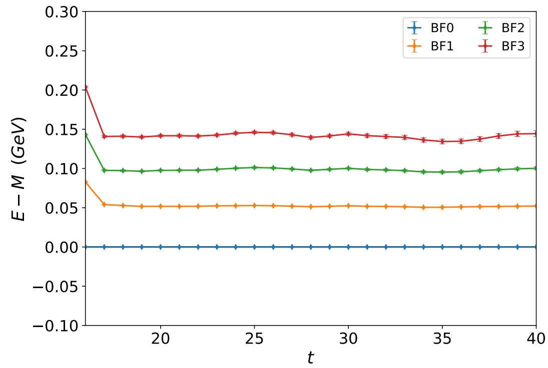

(d) π^+ energy shift from Eq. (4.10) using single eigenmode projection in four field strengths.

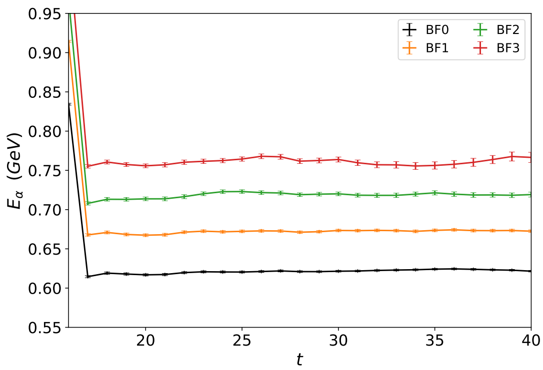

(e) π^+ energy using $n = 3\, q_H\, k_d$ eigenmodes projection in four field strengths.

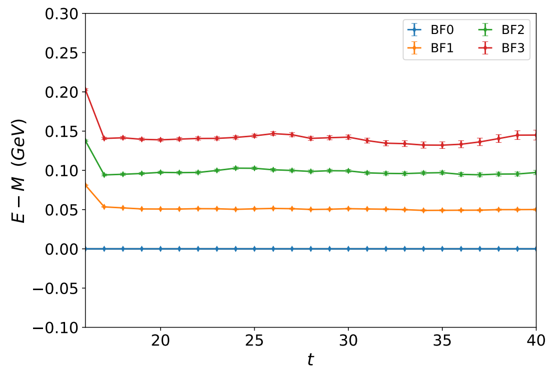

(f) π^+ energy shift from Eq. (4.10) using $n = 3\, q_H\, k_d$ eigenmodes projection in four field strengths.

Figure 6.7. A comparison of the three different hadronic projections for the charged pion on the $\kappa_{ud} = 0.13700$ ensemble with $m_\pi = 702$ MeV. The energy and energy shift as a function of field strength are shown in the left and right columns respectively.

Table 6.1. The number of sources per configuration used for each hadron type and ensemble.

κ_{ud}	m_π (MeV)	Nucleons	Hyperons	Number of configurations
0.13700	702	5	3	399
0.13727	570	4	–	400
0.13754	411	6	6	450
0.13770	296	7	3	400

6.2. Lattice Results

Here the results calculated using the smeared source and $SU(3) \times U(1)$ Laplacian projected sink quark propagators are presented. Here we consider the two nucleon states and a selection of hyperons. Using the source shifting strategy of Section 4.2.2; the number of sources used for each ensemble is described in Table 6.1.

6.2.1. Magnetic polarisability formalism refresher

The magnetic polarisability can be extracted from the energy of a (spin-averaged) hadron in a background magnetic field using the relativistic energy shift analogous to Eq. (5.37) for the neutral pion

$$E^2(B) - m^2 = (E(B) + m)\,(E(B) - m) = |qe\,B| - 4\,\pi\,m\,\beta\,|e\,B|^2 + \mathcal{O}\left(B^3\right), \quad (6.9)$$

or where it is not possible to fit constant plateaus to $E(B)+m$, using the Taylor expanded energy shift, as in Eq. (4.11)

$$\delta E(B,t) = \frac{|qe\,B|}{2\,m} - \frac{4\,\pi}{2}\,\beta\,|e\,B|^2 + \mathcal{O}\left(B^4\right). \quad (6.10)$$

To these energy shifts, an appropriate fit function as a function of field strength is fitted and the quadratic coefficient used to extract the magnetic polarisability according to the parameter relation of Eq. (4.15) or Eq. (5.32). This process is explicitly detailed in Chapter 4.

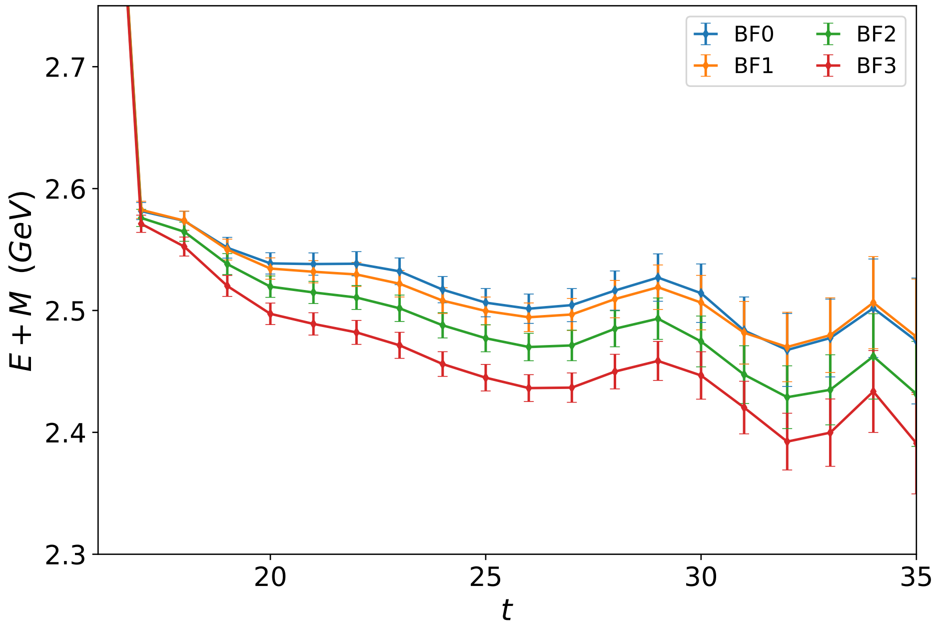

Figure 6.8. Neutron $E(B)+M$ energy shift for $m_\pi = 570$ MeV ensemble constructed using Eq. (5.24).

6.2.2. Neutron

Due to the inherent noisiness of baryon correlation functions, it is not possible to successfully fit plateaus to the $E(B)+m$ energy shifts required to construct the fully relativistic energy shift of Eq. (6.9). This is evident in Figure 6.8 for the neutron on the $\kappa_{ud} = 0.13727$ ensemble with $m_\pi = 570$ MeV. Hence the non-relativistic energy shift of Eq. (6.10) is used. Relativistic corrections to the overall energy are estimated to be less than $\sim 10\%$.

Plateau fitting

As the non-relativistic energy shift is used, it is only necessary to fit Euclidean time plateaus in the single energy shift given by the ratio of Eq. (4.10). This is done for each of the four ensembles considered herein. The selected fits must display good plateau behaviour and are required to have a $\chi^2_{dof} \leq 1.2$. These fits are illustrated in Figures 6.9 through 6.12 for $\kappa_{ud} = 0.13700, 0.13727, 0.13754, 0.13770$ with $m_\pi = 702, 570, 411, 296$ MeV respectively.

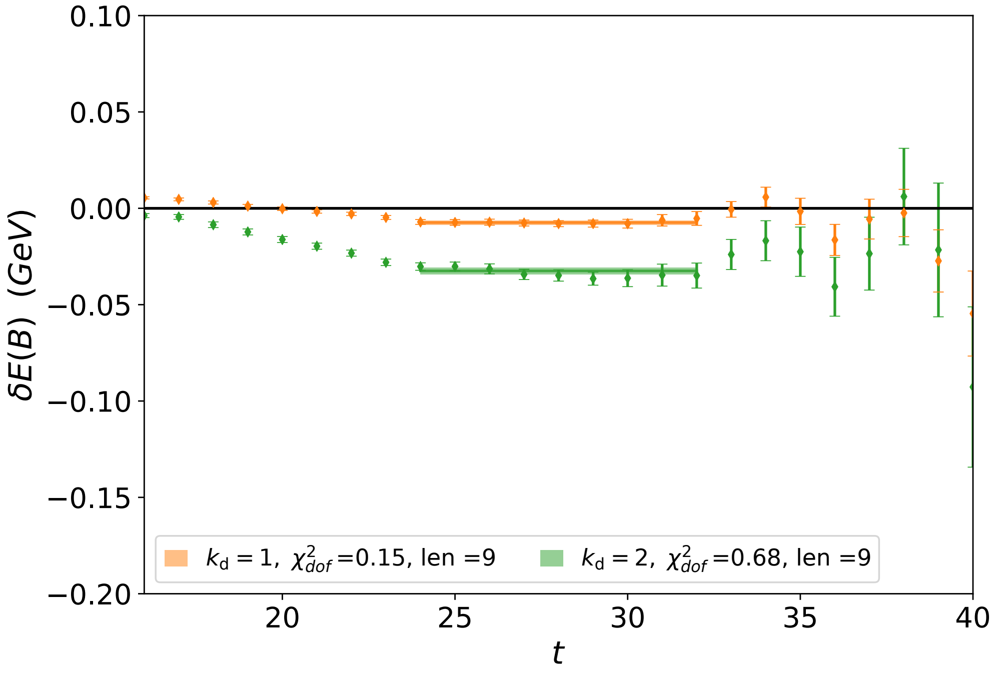

Figure 6.9. Neutron effective energy shift for the $m_\pi = 702$ MeV ensemble. The shaded regions illustrate the fit windows selected through consideration of the full covariance-matrix χ^2_{dof}, the extent of the window and the desire to select the same fit window across all field strengths.

It is apparent in Figures 6.9 through 6.12 that the energy shift required to extract the magnetic polarisability for the neutron is small compared to the mass of the neutron. This necessitates the correlation function ratios developed in Eq. (4.10). The energy shifts for the $m_\pi = 702$ MeV neutron are illustrated in Figure 6.9 where good plateau behaviour for the two smallest background magnetic field strengths is clearly evident. The third energy shift is not shown as it compromises the fit windows required for the first two energy shifts and is not required in order to do a polarisability fit.

The next ensemble considered in Figure 6.10 has light quark hopping parameter $\kappa_{ud} = 0.13727$ and a pion mass of $m_\pi = 570$ MeV. Here the plateau fits at each field strength are allowed to monotonically vary such that they have the same end point. In this way we account for the increased time before plateaus are formed for the larger background magnetic field strengths.

The energy shifts depicted in Figure 6.11 for the $m_\pi = 411$ MeV neutron are substantially harder to fit plateaus to. They descend into noise earlier than in Figures 6.9 and 6.10. The fit windows chosen here are also substantially restricted by the necessity of being able to perform the polarisability fits of Eqs. (6.10) and (6.11).

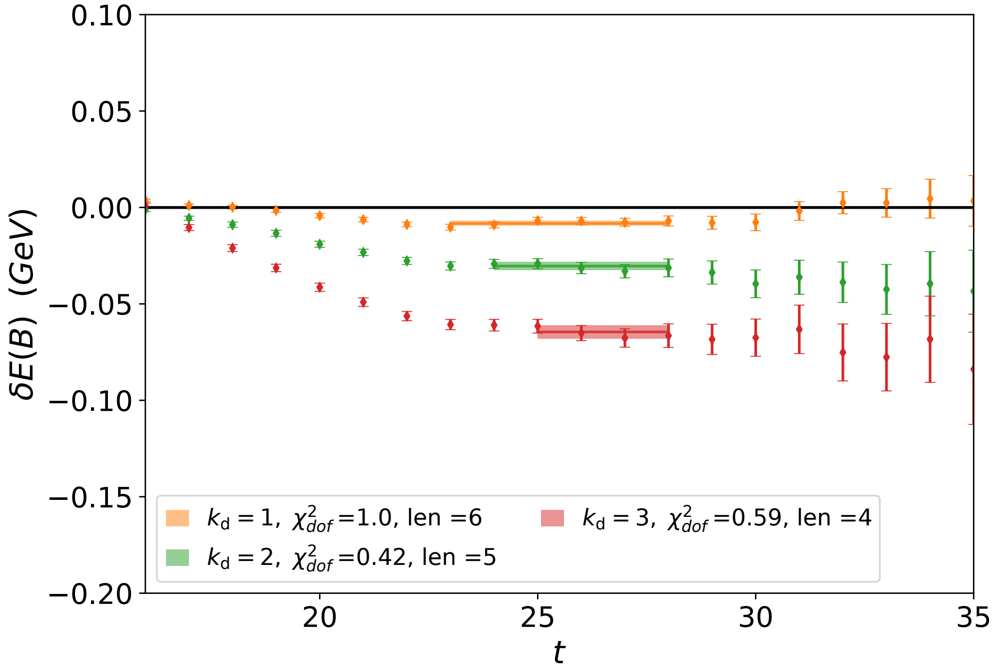

Figure 6.10. Neutron effective energy shift for the $m_\pi = 570$ MeV ensemble. Details are as in the caption of Figure 6.9.

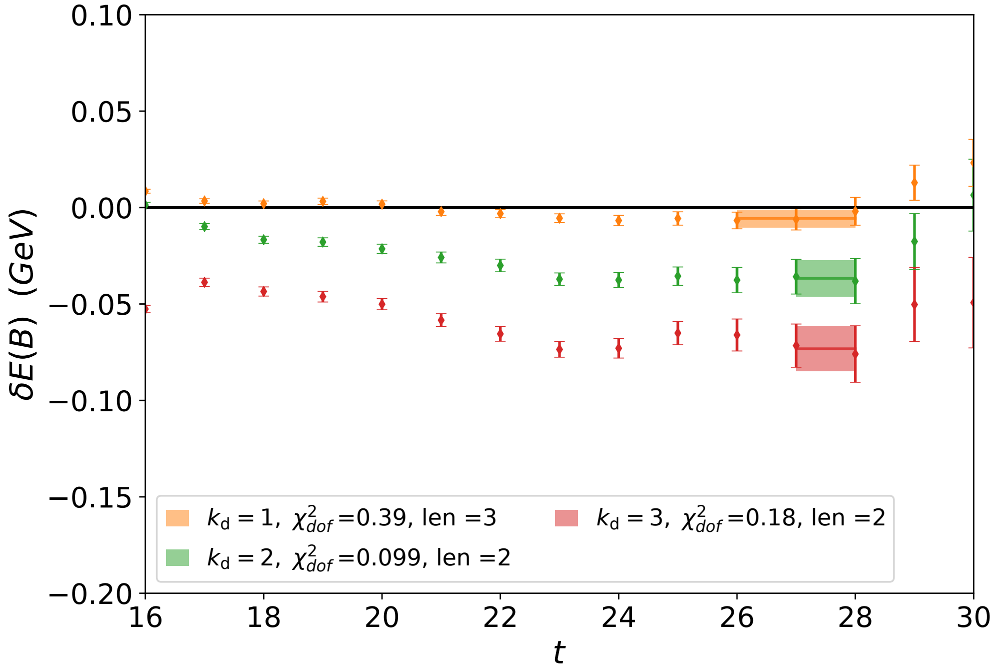

Figure 6.11. Neutron effective energy shift for the $m_\pi = 411$ MeV ensemble. Details are as in the caption of Figure 6.9.

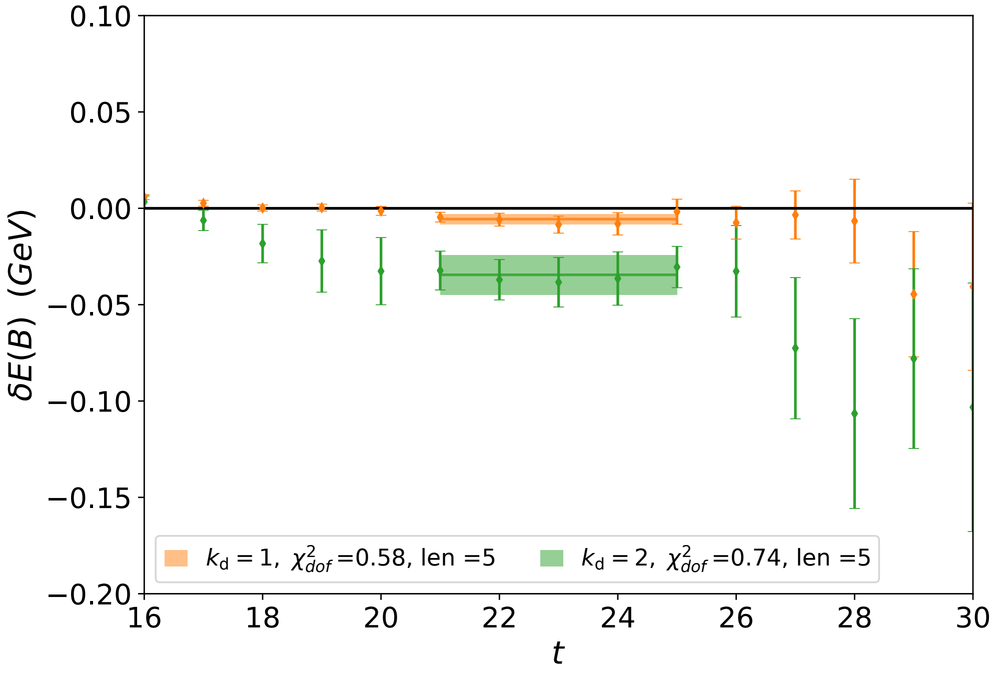

Figure 6.12. Neutron effective energy shift for the $m_\pi = 296$ MeV ensemble. Details are as in the caption of Figure 6.9.

For the remaining energy shifts for the $m_\pi = 296$ MeV neutron depicted in Figure 6.12, only the energy shifts for the two smallest magnetic field strengths are shown. This is as it is not possible to find constant plateau fits to the energy shift of the third field strength.

Overall, the energy shifts and fits displayed in Figures 6.9 through 6.12 typically display good plateau behaviour. This is directly due to the consideration of Landau-type physics at the quark level through the $SU(3) \times U(1)$ eigenmode projection technique of Section 6.1.

The neutron magnetic polarisability energy shifts produced using the $SU(3) \times U(1)$ generally display better plateau behaviour than those presented in Chapter 4 where a $U(1)$ Landau eigenmode quark projection technique is used. The early time behaviour of these two sets of energy shifts is quite different. The energy shifts using the $U(1)$ Landau eigenmode projected quark sink approach their long-time behaviour slowly and from below, while the $SU(3) \times U(1)$ eigenmode projection technique produces neutron energy shifts which approach from above and typically display better plateau behaviour. While the plateau behaviour of the $SU(3) \times U(1)$ eigenmode projected energy shifts only occurs a few time slices earlier than for the $U(1)$ projected energy shifts, this is significant in the

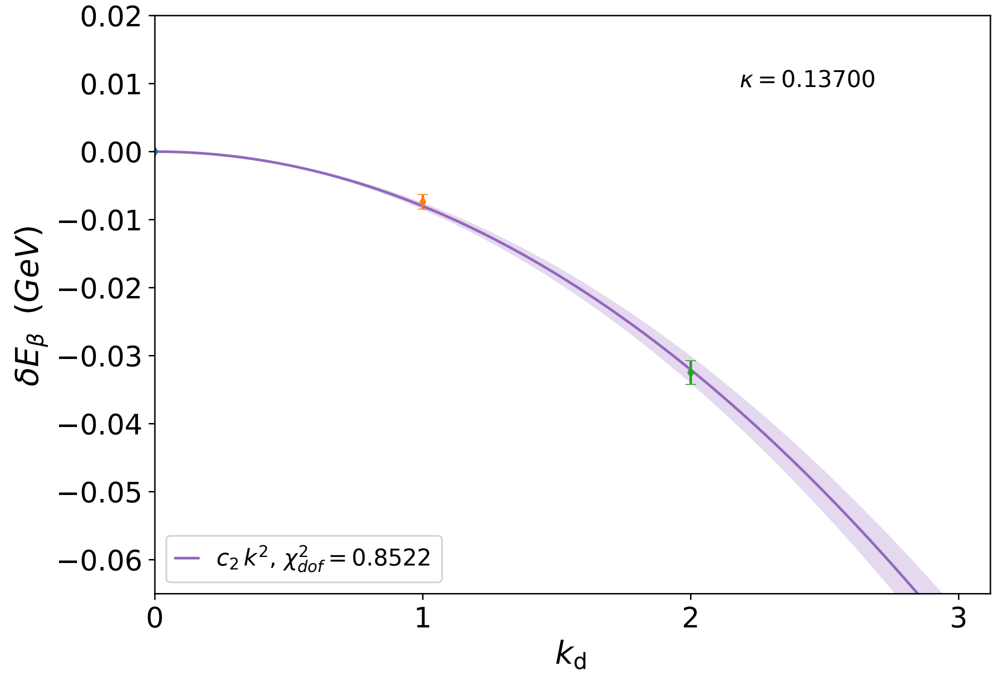

Figure 6.13. Quadratic only fit of the magnetic-field induced energy shift to the magnetic-field quanta for the neutron on the $m_\pi = 702$ MeV ensemble using a smeared source and $SU(3) \times U(1)$ eigenmode projected sink.

context of the onset of noise in our energy shifts. This is another area where the $SU(3)$ $\times U(1)$ eigenmode projection technique is superior, the onset of noise and loss of signal is delayed by up to five time slices or ≈ 0.45 fm in comparison to the results presented in Chapter 4. It should be noted that the results in Chapter 4 used eight sources on each gauge field configuration, compared to the maximum of seven in this chapter as detailed in Table 6.1, making the observed improvement even more significant.

Polarisability fitting

Once the energy shifts have been determined, a field strength dependent fit is performed in order to extract the magnetic polarisability.

As the neutron is a neutral particle, the fit function as a function of field-strength has only a single quadratic term

$$\delta E(k_d) \equiv c_2\, k_d^2. \tag{6.11}$$

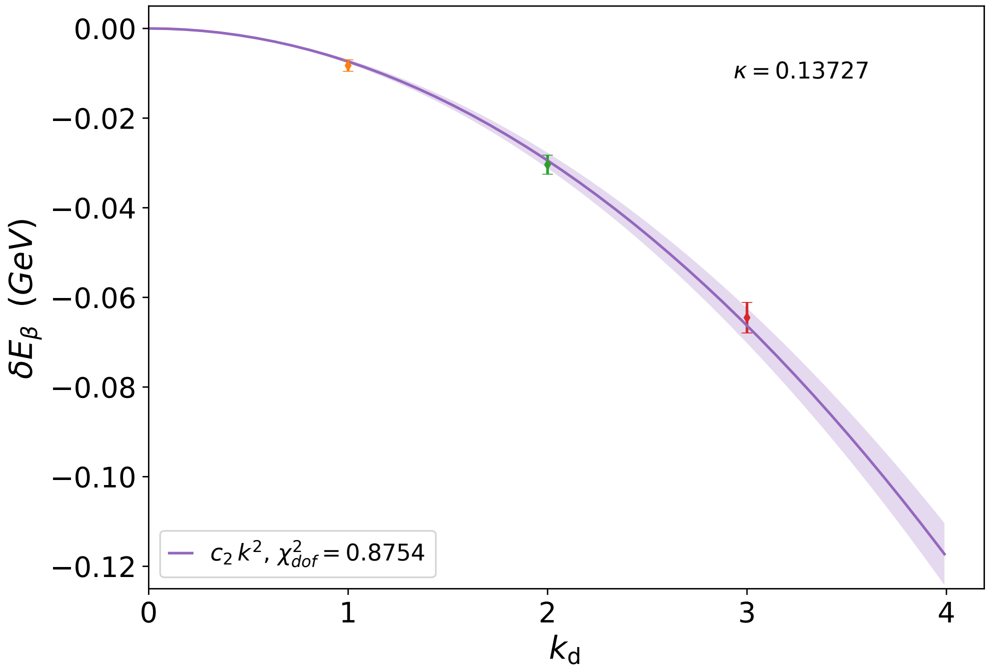

Figure 6.14. Quadratic only fit of the magnetic-field induced energy shift to the magnetic-field quanta for the neutron on the $m_\pi = 570$ MeV ensemble using a smeared source and $SU(3)\ \times U(1)$ eigenmode projected sink.

Table 6.2. Magnetic polarisability values for the neutron at each pion mass considered. The numbers in parentheses describe statistical uncertainties.

m_π (MeV)	κ_{ud}	$\beta\,(\times 10^{-4})$ fm^3
702	0.13700	1.91(12)
570	0.13727	1.61(10)
411	0.13754	1.53(29)
296	0.13770	1.27(37)

The quadratic fits to the energy shift plateaus in Figures 6.13 through 6.16 are then required to meet the same fit criteria as the plateaus. The quadratic fits in Figures 6.13, 6.14, 6.15 and 6.16 all describe the energy shifts well. For the lightest mass neutron considered in Figure 6.16, the statistical uncertainty is larger but the quadratic fit still works well.

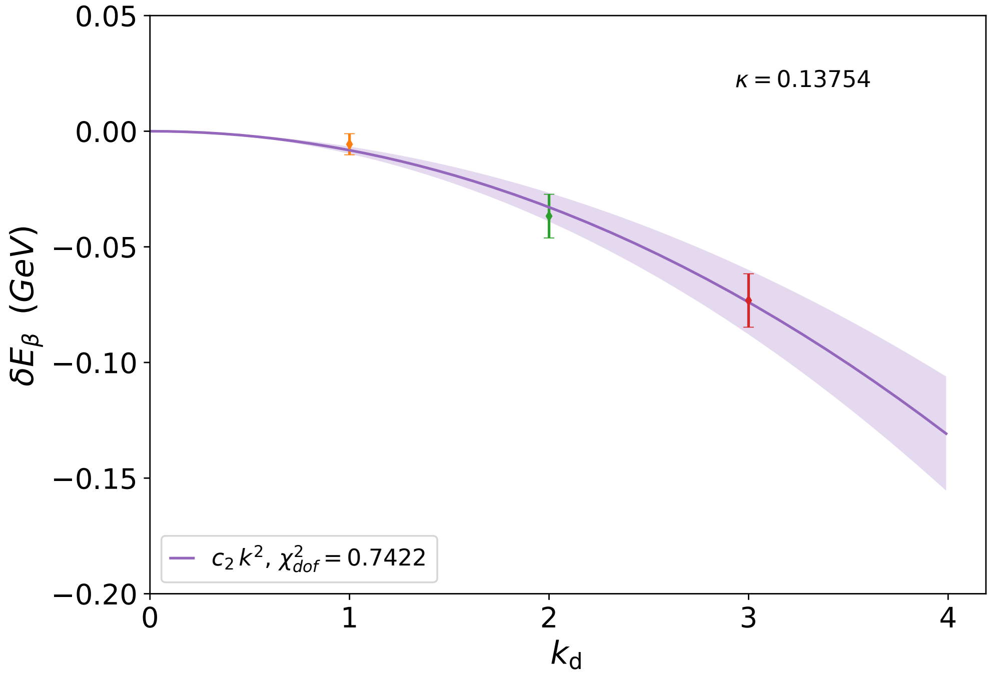

Figure 6.15. Quadratic only fit of the magnetic-field induced energy shift to the magnetic-field quanta for the neutron on the $m_\pi = 411$ MeV ensemble using a smeared source and $SU(3)\ \times U(1)$ eigenmode projected sink.

Neutron lattice summary

The magnetic polarisability of the neutron has been calculated using the $SU(3) \times U(1)$ eigenmode projection technique with an external background field. The resulting polarisability values are presented in Table 6.2.

These results can be used to inform a chiral extrapolation to the physical regime, as touched upon on in Section 4.3 and performed later in this chapter.

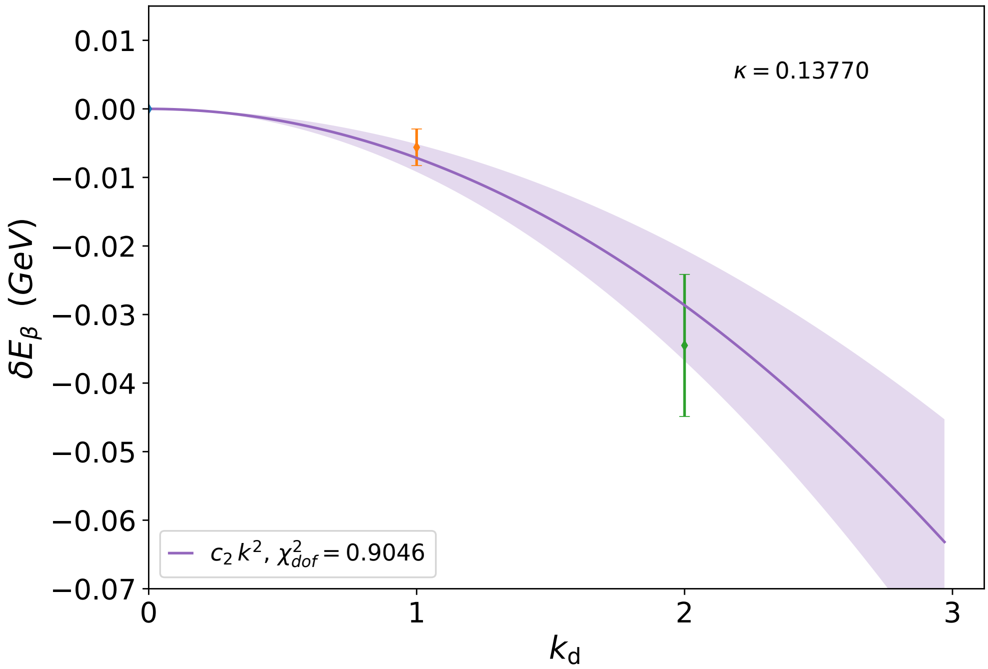

Figure 6.16. Quadratic only fit of the magnetic-field induced energy shift to the magnetic-field quanta for the neutron on the $m_\pi = 296$ MeV ensemble using a smeared source and $SU(3) \times U(1)$ eigenmode projected sink.

6.2.3. Proton

Here again the non-relativistic energy shift of Eq. (6.10) is used. As a charged particle, the proton energy shift will have a Landau level term which is linear in the magnetic field strength. This Landau term and the magnetic polarisability contribute to the energy with opposite sign and as such the clear ordering of neutron energy shifts is not expected here.

As the proton is a charged particle, the $U(1)$ hadronic projection technique of Section 6.1.3 is used. For the heavier masses of $m_\pi = 702, 511$ MeV in Figures 6.17 and 6.18, the increased precision allows the all-mode projection, $n = 3\, q_H\, k_d$, to be used interchangeably with the single mode projection, $n = 1$. Similarly the increased noise at the lightest mass in Figure 6.20 allows either projection to be utilised, and here $n = 3\, q_H\, k_d$. It is at the intermediate mass of $m_\pi = 411$ MeV in Figure 6.20 that the projection operators differ the most. It is found that the single-mode projection works best for the proton at this mass.

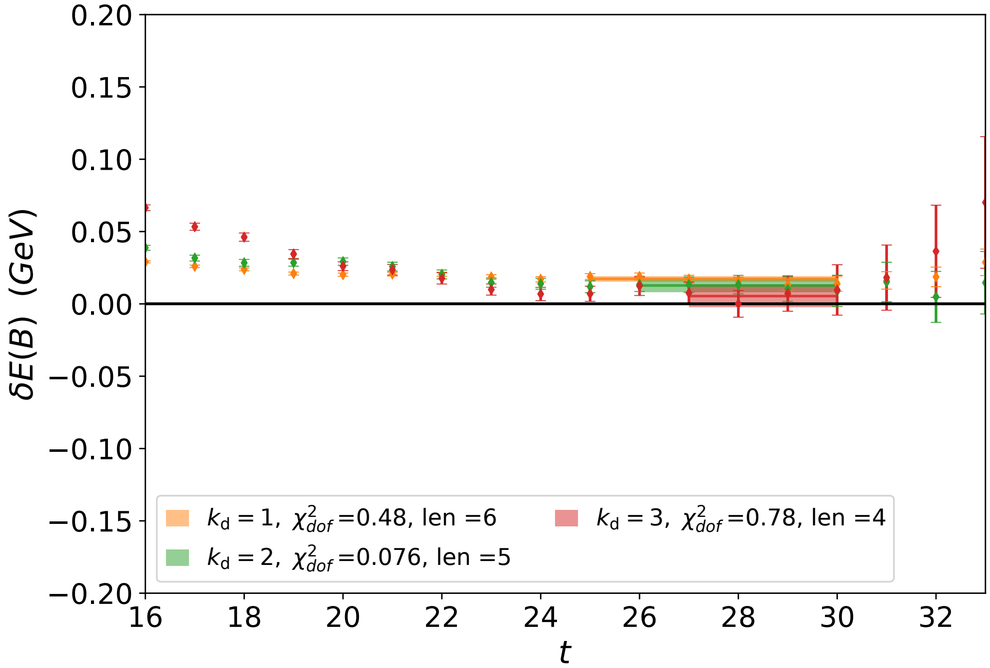

Figure 6.17. Proton effective energy shift for the $m_\pi = 702$ MeV ensemble. Details are as in the caption of Figure 6.9.

Plateau fitting

The proton energy shifts are illustrated in Figures 6.17 through 6.20. These energy shifts are near degenerate across the different magnetic field strengths considered herein. This is due to the competing effects of the magnetic polarisability and the Landau energy term.

The fit region is again allowed to monotonically vary for the energy shifts in Figures 6.17 and 6.19. It should be noted that the fit regions inspected are not necessarily the only monotonic fit regions possible, but are chosen such that the space of possible monotonic fit regions is manageable. The selected fits are chosen in order to maximise plateau length with out χ^2_{dof} requirement of $\chi^2_{dof} \leq 1.2$ in accordance with fits elsewhere in this thesis. These fits correspond to ensembles with $\kappa_{ud} = 0.13700$ and 0.13754 for $m_\pi = 702$ and 411 MeV respectively. The remaining fits in Figures 6.18 and 6.20 do not require this allowance.

As with the neutron, no constant plateau fit is possible to the third magnetic field strength for the proton on the $\kappa_{ud} = 0.13770$ ensemble with $m_\pi = 296$ MeV and as such it is excluded from Figure 6.20.

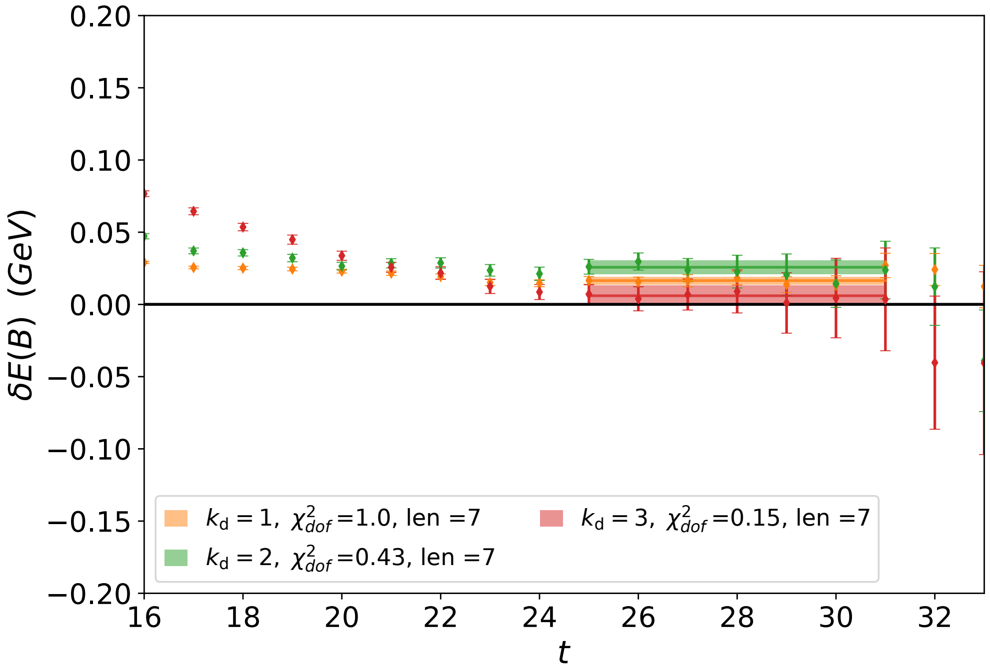

Figure 6.18. Proton effective energy shift for the $m_\pi = 570$ MeV ensemble. Details are as in the caption of Figure 6.9.

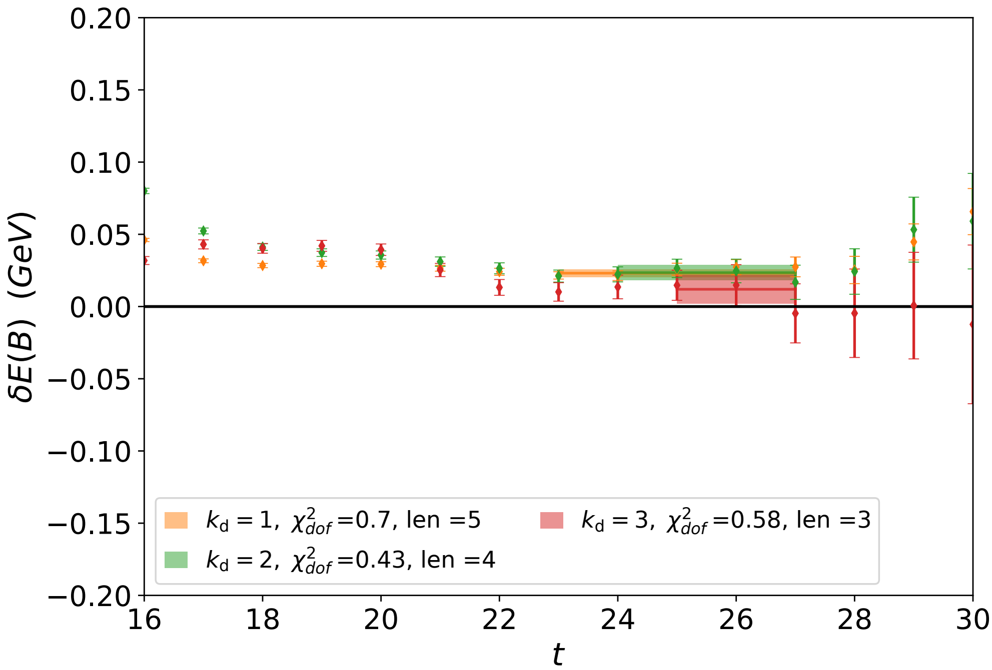

Figure 6.19. Proton effective energy shift for the $m_\pi = 411$ MeV ensemble. Details are as in the caption of Figure 6.9.

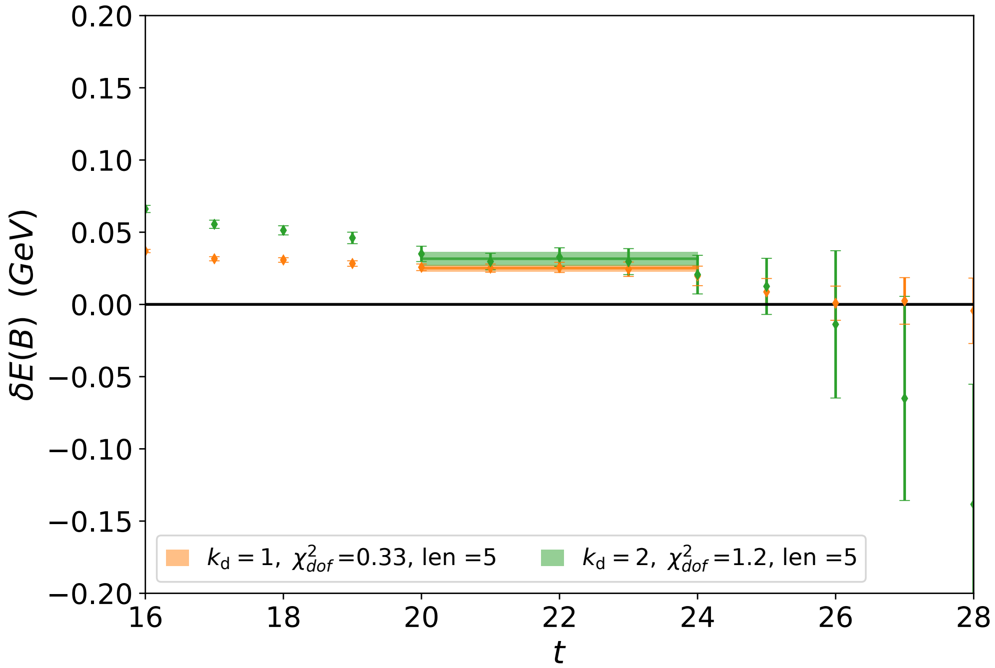

Figure 6.20. Proton effective energy shift for the $m_\pi = 296$ MeV ensemble. Details are as in the caption of Figure 6.9.

The proton energy shifts depicted herein display excellent behaviour, beginning around eight time slices (≈ 0.7 fm) after the source, a point comparable to the neutron results. These results are a first at these quark masses with previous results unable to fit plateaus [101, 136]. The $U(1)$ Landau quark level eigenmode projection technique was also unsuccessful at producing adequate proton energy shift plateaus at all the quark masses required for a chiral extrapolation. Key to the improvement in this chapter is the consideration of background field effects at both the quark and hadronic levels via the $SU(3) \times U(1)$ eigenmode projection technique and the $U(1)$ hadronic projection technique respectively.

Polarisability fitting

As the proton is charged, the fit function of Eq. (6.11) is not appropriate; the Landau term of Eq. (6.10) must be considered. An appropriate fit is

$$\delta E(k_d) \equiv c_1\, k_d + c_2\, k_d^2. \tag{6.12}$$

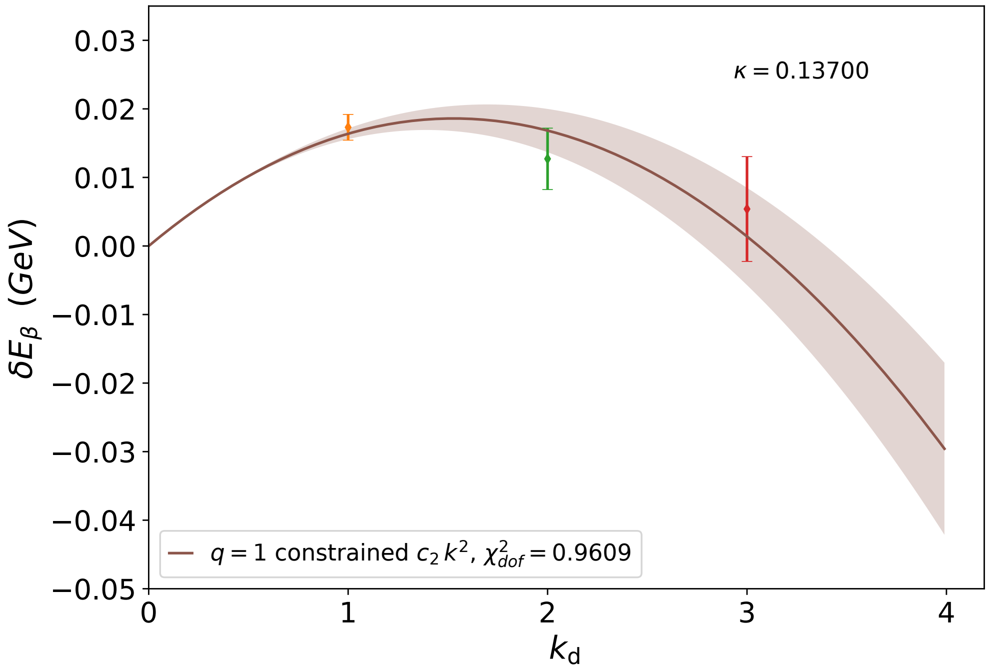

Figure 6.21. Constrained quadratic fit to the proton $E\,(B) - m$ energy shifts of Figure 6.17. The $\kappa_{ud} = 0.13700$ ensemble has a pion mass of $m_\pi = 702$ MeV. The hadronic Landau projection of Eq. (6.8) is used with the $n = 3\,k_d$ lowest eigenmodes.

However the free c_1 parameter allows the charge of the proton to differ from unity. As the mass and charge of the proton are known, these are subtracted from the energy shift to form the linear constrained energy shift

$$\delta E(B) - \frac{|e\,B|}{2\,m} = -\frac{4\,\pi}{2}\,\beta\,|e\,B|^2 + \mathcal{O}\left(B^4\right), \tag{6.13}$$

which is fit using a single quadratic term

$$\delta E(k_d) - \frac{|e\,B|}{2\,m} \equiv c_2\,k_d^2. \tag{6.14}$$

This ensures that the proton has charge $q = 1$ as required.

These fits are shown in Figures 6.21 through 6.24. These fits all provide acceptable χ^2_{dof}, signifying that the fit function of Eq. (6.14) is appropriate.

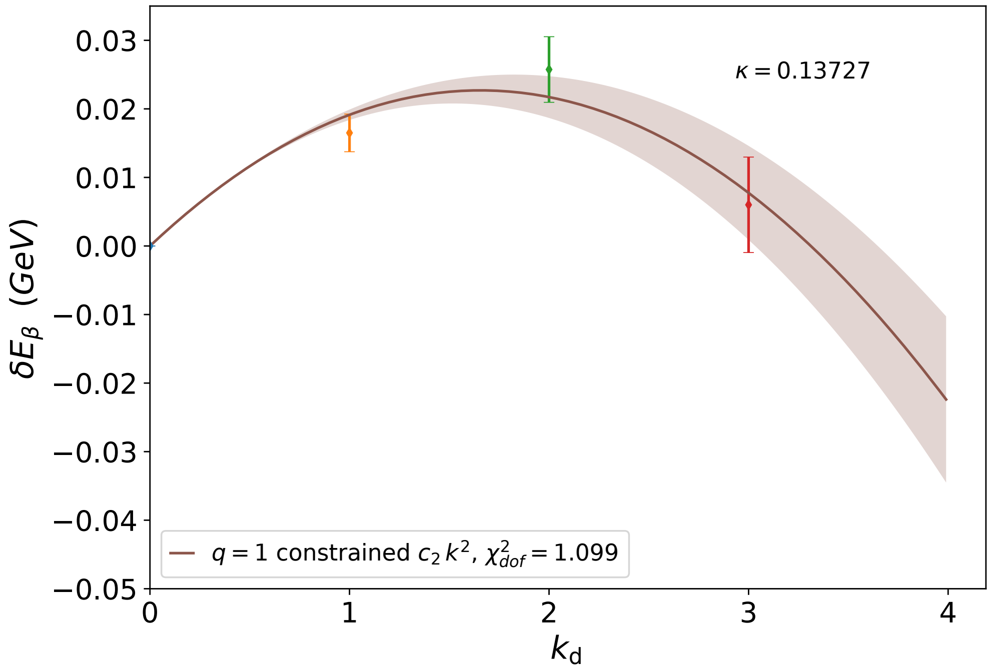

Figure 6.22. Constrained quadratic fit to the proton $E(B) - m$ energy shifts of Figure 6.18. The $\kappa_{ud} = 0.13727$ ensemble has a pion mass of $m_\pi = 570$ MeV. The hadronic Landau projection of Eq. (6.8) is used with the $n = 3\,k_d$ lowest eigenmodes.

Table 6.3. Magnetic polarisability values for the proton at each quark mass. The numbers in parentheses describe statistical uncertainties.

m_π (MeV)	κ_{ud}	$\beta\,(\times 10^{-4})$ fm^3
702	0.13700	1.90(19)
570	0.13727	1.87(18)
411	0.13754	1.98(21)
296	0.13770	1.93(22)

Proton lattice summary

At each pion mass considered, a constrained quadratic fit has been performed and the magnetic polarisability of the proton extracted from the quadratic fit coefficient. These magnetic polarisabilities of the proton at four non-physical pion masses can be found in Table 6.3. These results are made possible by the combination of the consideration of Landau effects at both the quark and hadronic levels.

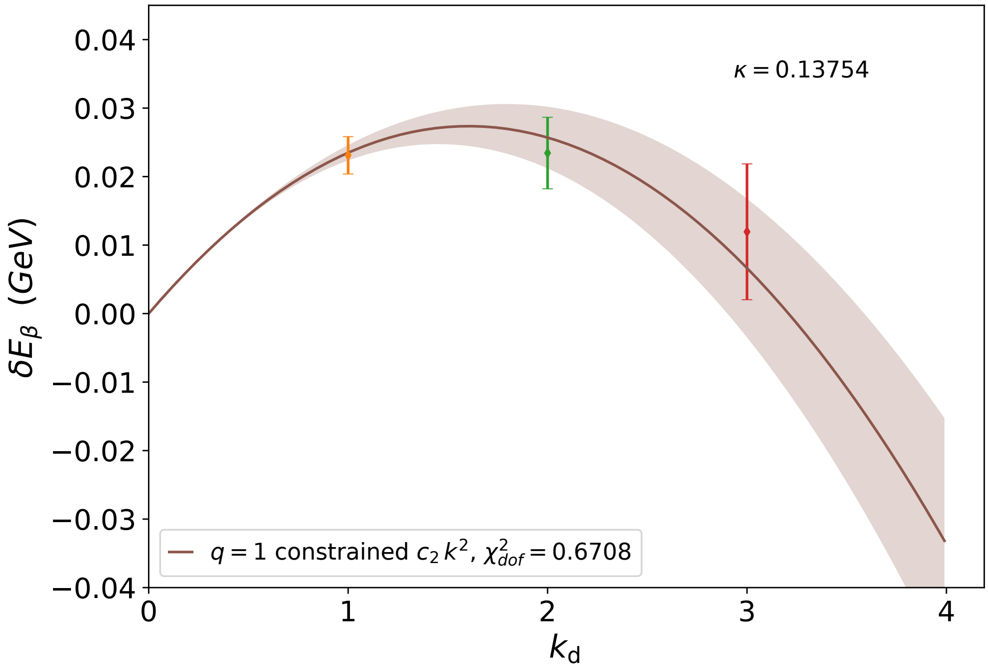

Figure 6.23. Constrained quadratic fit to the proton $E(B) - m$ energy shifts of Figure 6.19. The $\kappa_{ud} = 0.13754$ ensemble has a pion mass of $m_\pi = 411$ MeV. The hadronic Landau projection of Eq. (6.8) is used with only the $n = 1$ lowest eigenmode.

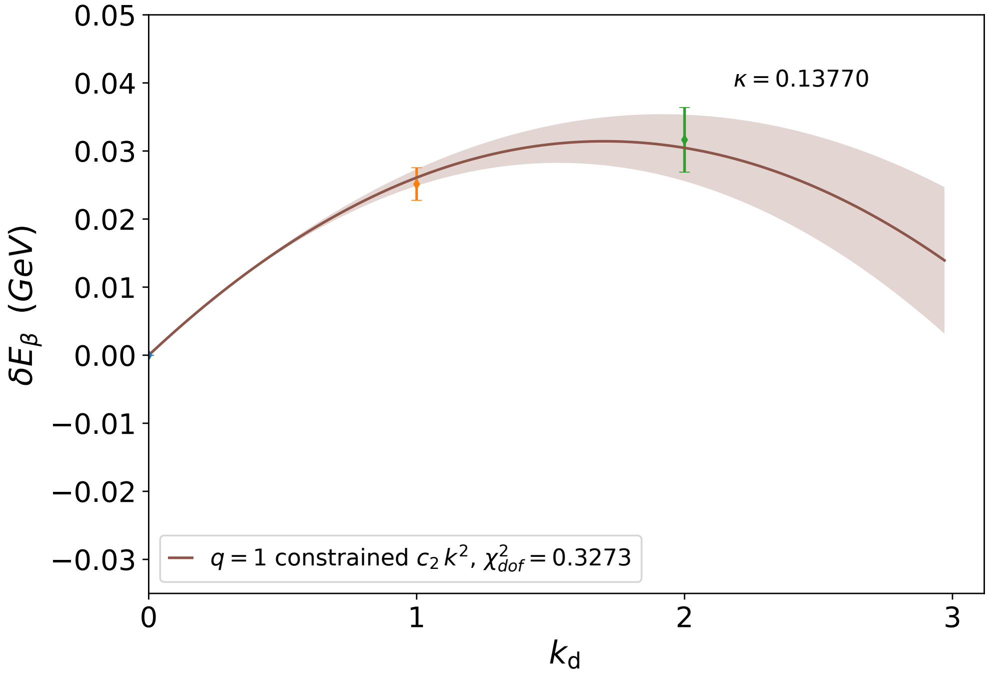

Figure 6.24. Constrained quadratic fit to the proton $E(B) - m$ energy shifts of Figure 6.20. The $\kappa_{ud} = 0.13770$ ensemble has a pion mass of $m_\pi = 296$ MeV. The hadronic Landau projection of Eq. (6.8) is used with the $n = 3\,k_d$ lowest eigenmodes.

6.2.4. Hyperons

Hyperons are baryons which are composed of three valence light quarks with non-zero strangeness, that is hyperons have at least one valence strange quark. There are a number of hyperons which could be investigated, as shown in Figures 2.2 and 2.3 with composition shown in Tables 2.3 and 2.4.

The hyperons selected here to be examined are the Σ^+ and the Ξ^0. The Σ^+ closely resembles a proton with the negative down quark replaced with a negative strange quark. Similarly the Ξ^0 is a neutron with the two down quarks replaced by two strange quarks.

While experimental results for hyperon magnetic polarisabilities are very difficult to obtain [3, 172, 173] calculations in several model approaches [172–175] are beginning to produce similar results. A first principles approach such as lattice QCD has considerable scope to aid in discriminating between these different model approaches and to provide a guide for future experiments.

Previous lattice QCD calculations using the background field method for hyperon polarisabilities [176] used a non-uniform background field, introducing a systematic error into the calculation. Using the field-quantisation condition of Eq. (3.99) we maintain a uniform field. Another improvement herein is our correct treatment of the Wilson-term additive mass renormalisation induced by the background magnetic field, as discussed in Chapter 5. Finally the effects of quenched valence quarks are resolved in chiral extrapolations section.

In this first examination of hyperon polarisabilities the gauge fields with $\kappa_{ud} =$ 0.13700, 0.13754, 0.13770 corresponding to $m_\pi = 702, 411, 296$ MeV are used. The addition of a strange valence quark requires a separate quark propagator inversion, in addition to that of the two light quarks, and the fourth ensemble is not available at the time of writing.

Σ^+ baryon

The Σ^+ is a charged hyperon with valence quark content $(u\,u\,s)$. This resembles the proton with the proton's down quark swapped for a strange quark. Investigating the magnetic polarisability of the Σ^+ will hint towards the sensitivity of the magnetic polarisability to the presence of the heavier strange quarks.

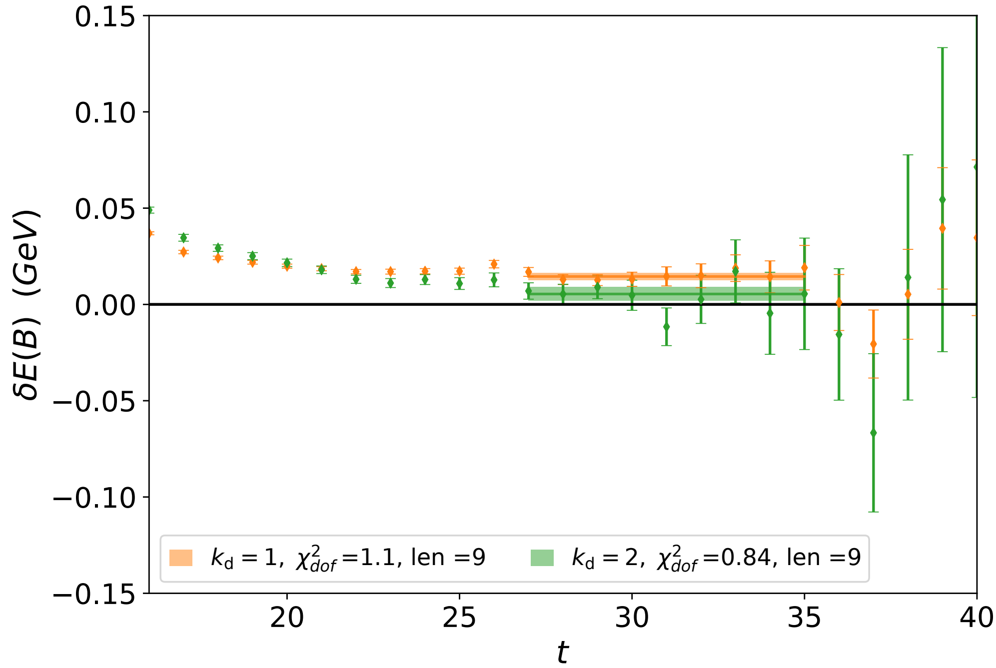

Figure 6.25. Σ^+ effective energy shift for the $m_\pi = 702$ MeV ensemble. Details are as in Figure 6.13.

As a charged baryon, the hadronic Landau level projection of Eq. (6.8) is used. Here only the lowest lying eigenmode $n = 1$ is chosen.

The non-relativistic energy shift is considered for the Σ^+ in Figures 6.25 through 6.27. Only the lowest two energy shifts are considered due to the difficulty in obtaining constant plateau fits at the third field strength. This is a common theme across the hyperons considered herein. It may be that the level of source smearing appropriate for the nucleon, as used here, is not as effective for the larger mass hyperons.

The ordering of the two energy shifts in each of Figures 6.25 through 6.27 is different. In Figure 6.25

$$\delta\, E\, (k_d = 1) > \delta\, E\, (k_d = 2)\,, \tag{6.15}$$

while for Figure 6.26

$$\delta\, E\, (k_d = 1) \approx \delta\, E\, (k_d = 2)\,, \tag{6.16}$$

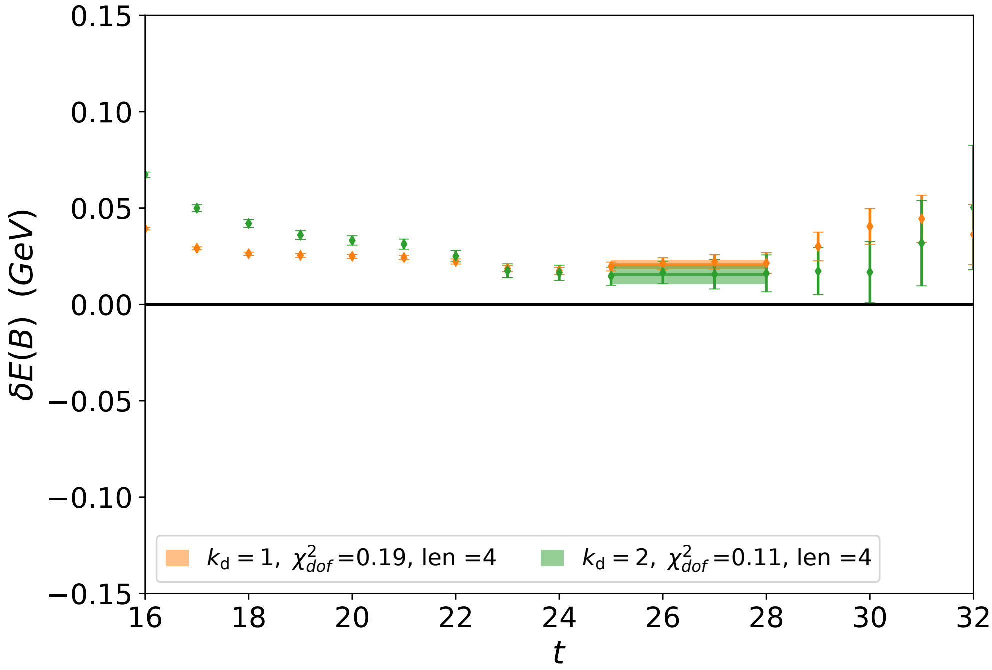

Figure 6.26. Σ^+ effective energy shift for the $m_\pi = 411$ MeV ensemble. Details are as in Figure 6.13.

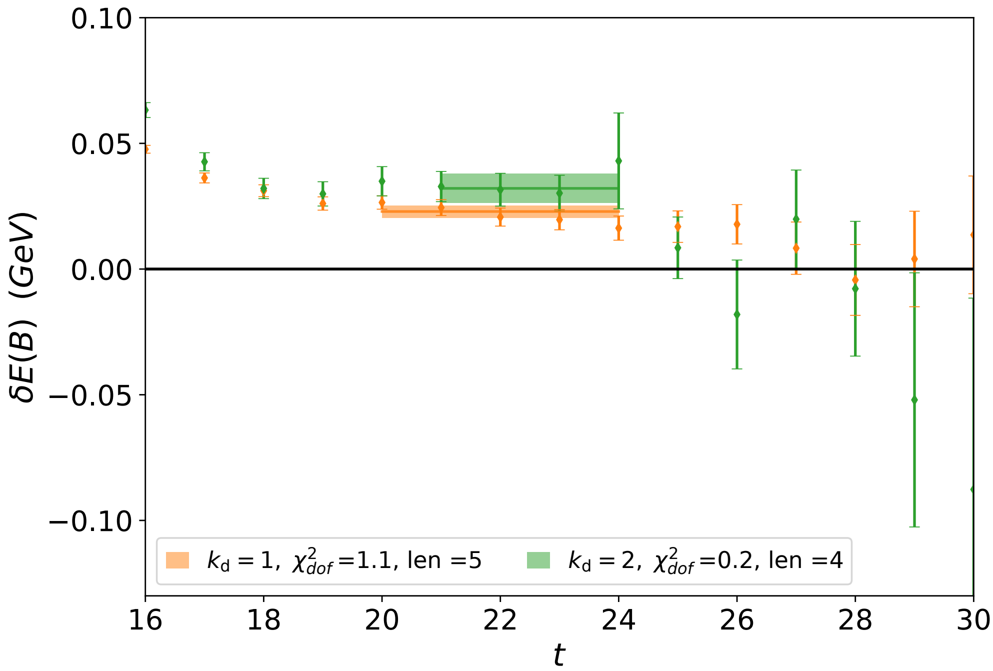

Figure 6.27. Σ^+ effective energy shift for the $m_\pi = 296$ MeV ensemble. Details are as in Figure 6.13.

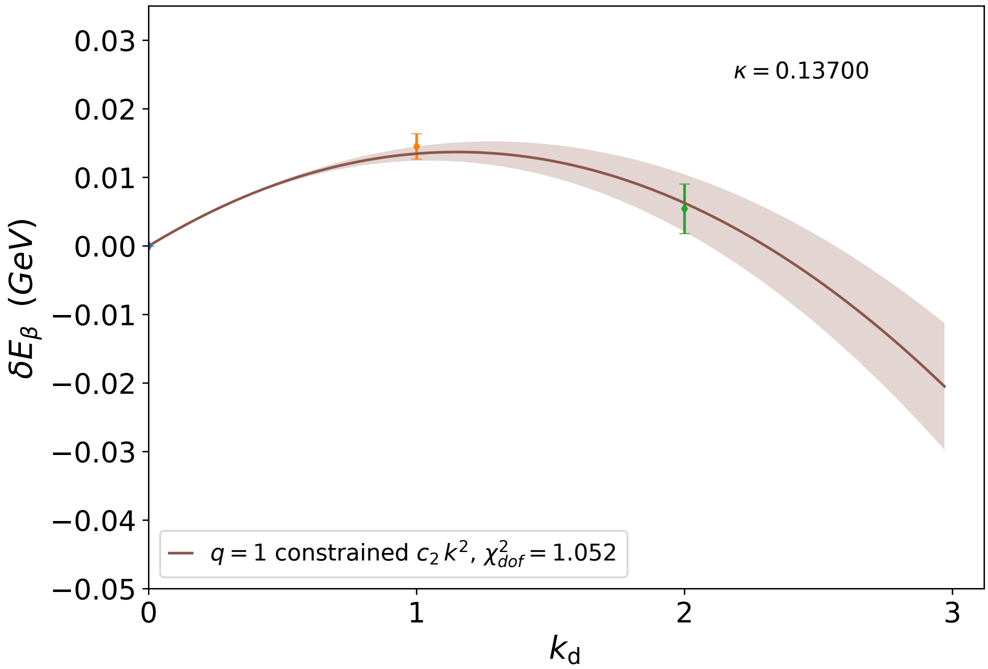

Figure 6.28. Constrained quadratic fit to the Σ^+ $E(B) - m$ energy shifts of Figure 6.25. The $\kappa_{ud} = 0.13700$ ensemble has a pion mass of $m_\pi = 702$ MeV. The hadronic Landau projection of Eq. (6.8) is used with only the $n = 1$ lowest eigenmode.

and for the lightest mass considered in Figure 6.27

$$\delta E(k_d = 1) < \delta E(k_d = 2)\,. \tag{6.17}$$

However this change in ordering is not concerning. The ordering is determined by a combination of the Landau level term $\propto |qe\,B|/2\,m$ and the magnetic polarisability term which contributes to the energy shift with an opposite sign. The change in ordering is monotonic as a function of pion mass, indicating a monotonic variation of the magnetic polarisability as a function of mass.

The fits to the energy shifts for the Σ^+ are of the same form as for the proton, they are the constrained quadratic fit of Eq. (6.14) to ensure a unitary charge Σ^+. These fits are shown in Figures 6.28 through 6.30 where good fit behaviour and $\chi^2_{dof} < 1.2$ are present. The resulting magnetic polarisability values from the quadratic term conversion of Eq. (4.15) are presented in Table 6.4. For the Σ^+, the magnetic polarisability has a clear quark-mass dependence as anticipated from the energy shifts.

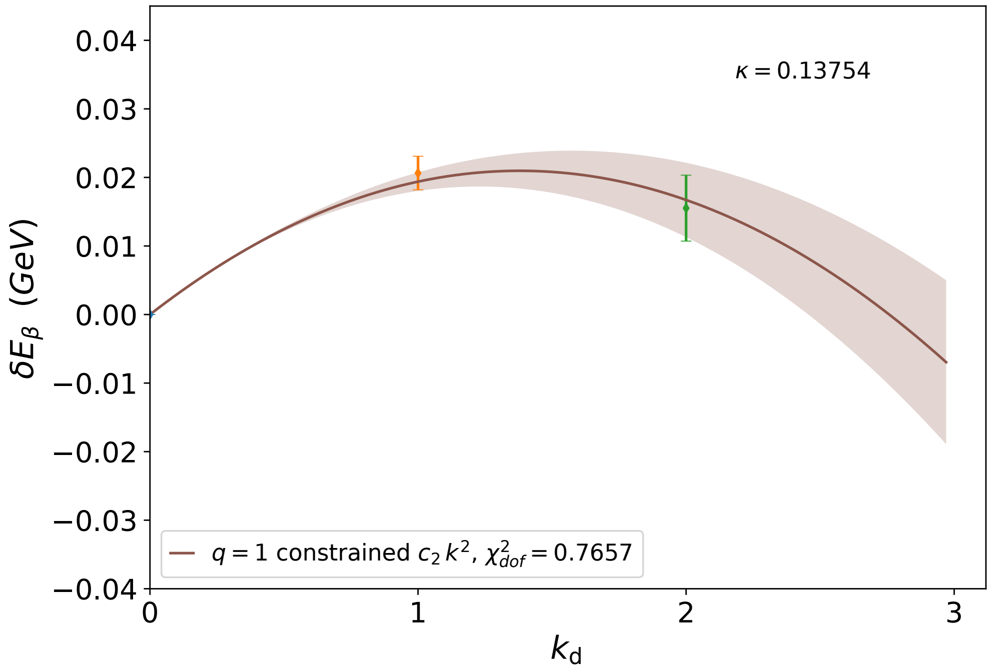

Figure 6.29. Constrained quadratic fit to the Σ^+ $E(B) - m$ energy shifts of Figure 6.26. The $\kappa_{ud} = 0.13754$ ensemble has a pion mass of $m_\pi = 411$ MeV. The hadronic Landau projection of Eq. (6.8) is used with only the $n = 1$ lowest eigenmode.

Table 6.4. Magnetic polarisability values for the Σ^+ at each quark mass. The numbers in parentheses describe statistical uncertainties.

m_π (MeV)	κ_{ud}	$\beta\,(\times 10^{-4})$ fm^3
702	0.13700	2.46(25)
411	0.13754	2.06(26)
296	0.13770	1.48(26)

As the Σ^+ is the octet hyperon which is closest in form to the proton, it may be illustrative to compare lattice magnetic polarisability values for these two particles. The values are most similar at the intermediate pion mass ensemble of $\kappa_{ud} = 0.13754$, corresponding to $m_\pi = 411$ MeV. This is perhaps in contrast to the expectation that they would be most similar when they are closest in mass on the $m_\pi = 702$ MeV ensemble. The difference between the Σ^+ and proton suggests that the magnetic polarisability also depends on hadron structure, rather than just the quark mass alone.

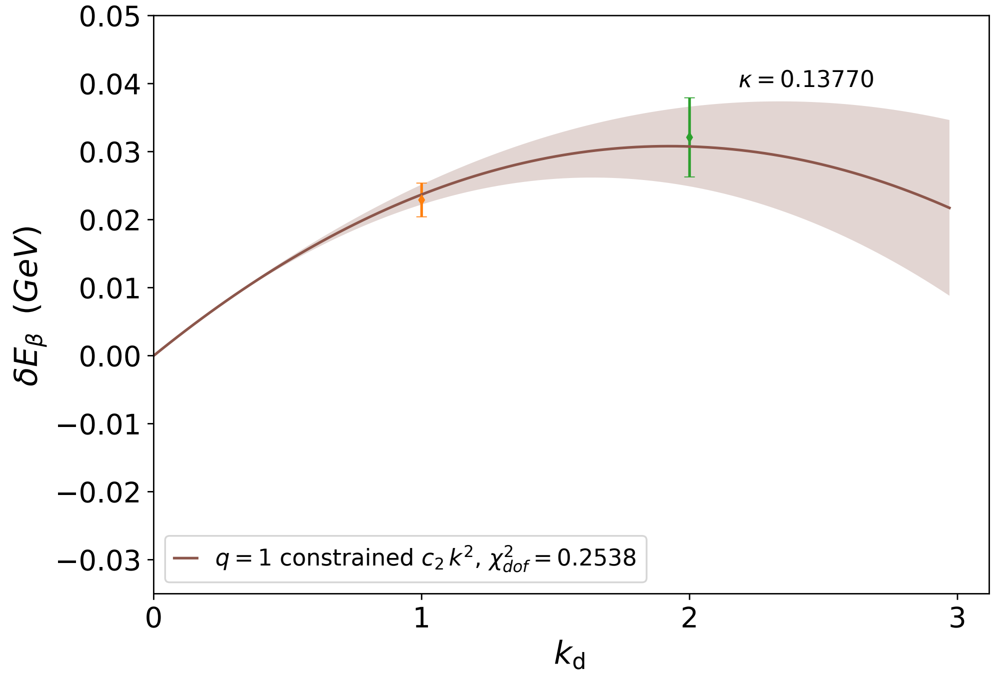

Figure 6.30. Constrained quadratic fit to the Σ^+ $E(B) - m$ energy shifts of Figure 6.27. The $\kappa_{ud} = 0.13770$ ensemble has a pion mass of $m_\pi = 296$ MeV. The hadronic Landau projection of Eq. (6.8) is used with only the $n = 1$ lowest eigenmode.

Ξ^0 baryon

Similar to the Σ^+, the Ξ^0 baryon closely resembles the neutron with quark content $(u\,s\,s)$. The down valence quarks in the neutron have been replaced with strange quarks.

The Ξ^0 is overall charge-less and hence a hadronic Landau projection is not appropriate. A standard Fourier projection used. The same $E(B) - M$ energy shift of Eq. (6.10) is considered for the Ξ^0 and indeed all hadrons considered in this chapter.

The Ξ^0 energy shift in Figures 6.31 through 6.33 appears to become more difficult to extract at heavier pion masses. This is contrary to expectations and likely purely to the differing number of correlation functions analysed. For the three ensembles, labelled $\kappa_{ud} = 0.13700,\ 0.13754,\ 0.13770$, the number of sources used was $\approx 3,\ 6,\ 3$ respectively. It should be noted that the statistical uncertainty on this latter, lightest mass ensemble is greater than that for the other two ensembles. This is evident in the differing scales of Figures 6.32 and 6.33.

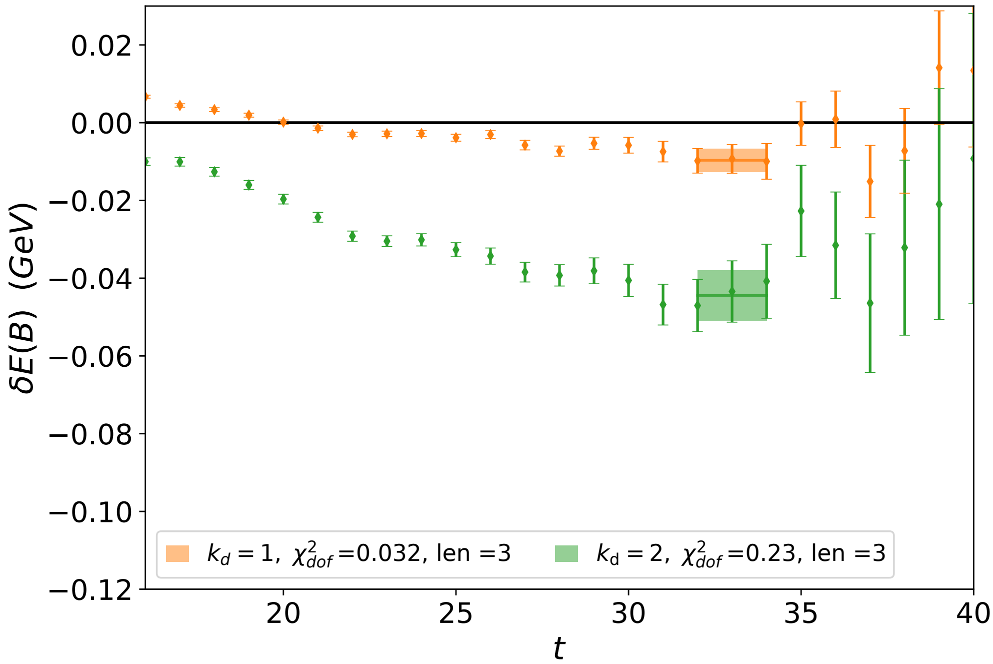

Figure 6.31. Ξ^0 effective energy shift for the $m_\pi = 702$ MeV ensemble. Details are as in Figure 6.13.

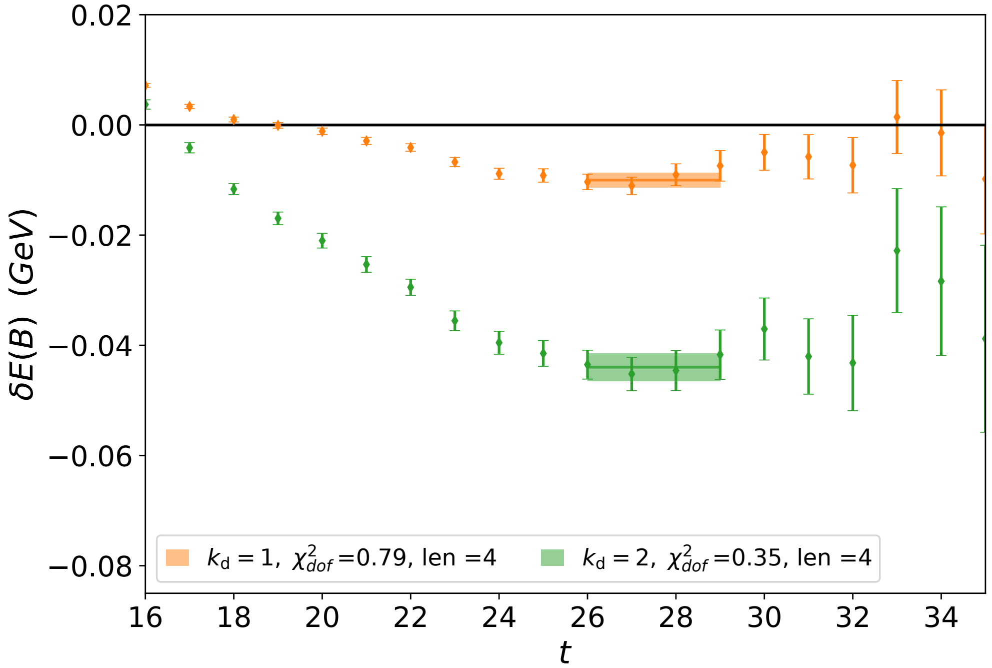

Figure 6.32. Ξ^0 effective energy shift for the $m_\pi = 411$ MeV ensemble. Details are as in Figure 6.13.

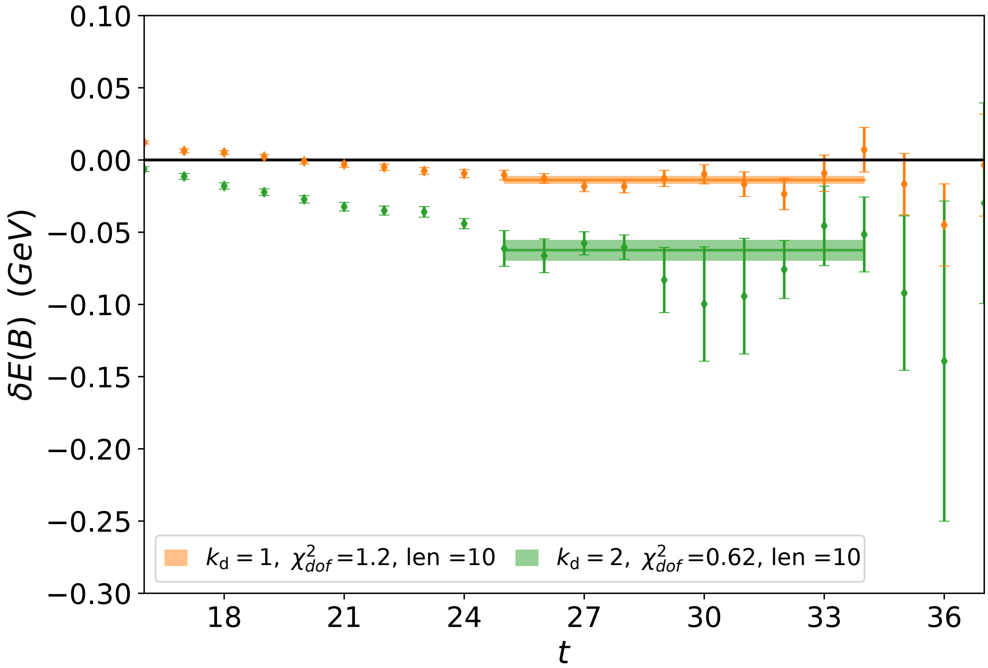

Figure 6.33. Ξ^0 effective energy shift for the $m_\pi = 296$ MeV ensemble. Details are as in Figure 6.13.

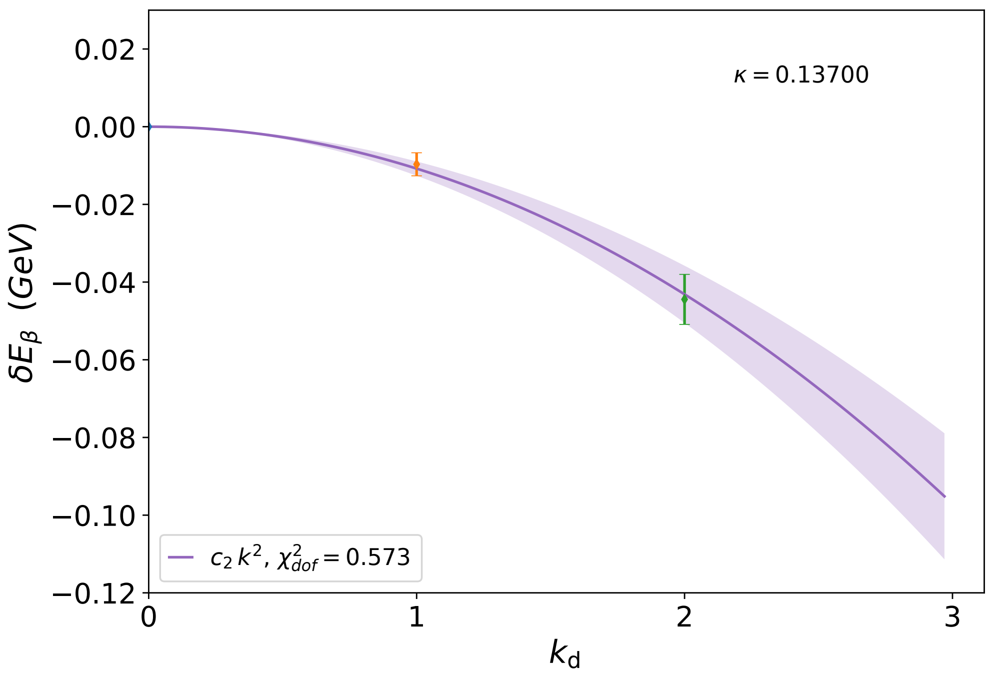

Figure 6.34. Quadratic only fit of the magnetic-field induced energy shift in Figure 6.31, to the magnetic-field quanta for the Ξ^0 on the $m_\pi = 702$ MeV ensemble.

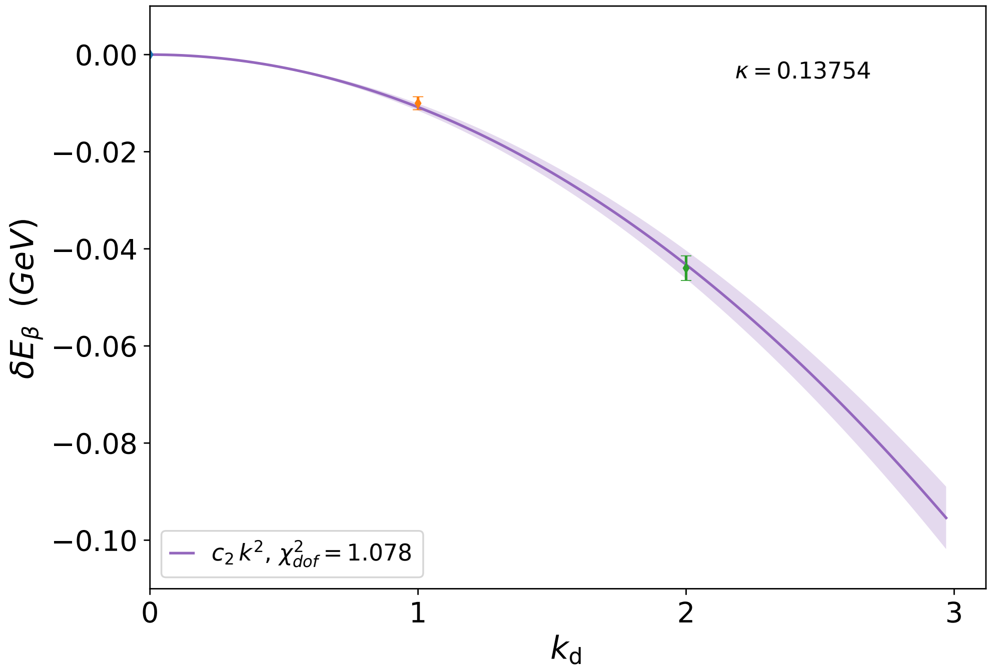

Figure 6.35. Quadratic only fit of the magnetic-field induced energy shift in Figure 6.32, to the magnetic-field quanta for the Ξ^0 on the $m_\pi = 411$ MeV ensemble.

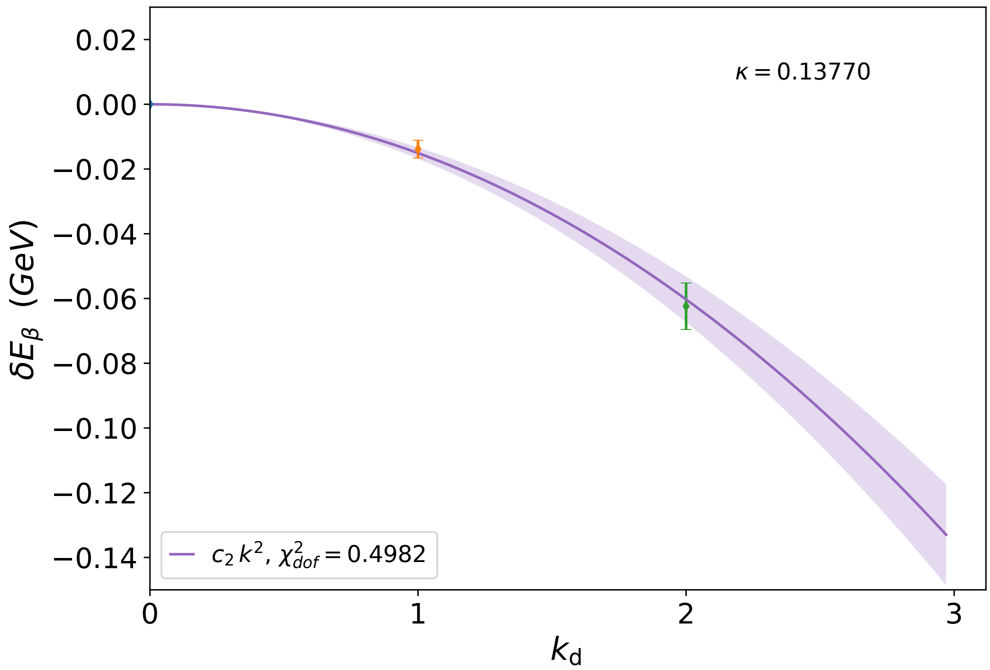

Figure 6.36. Quadratic only fit of the magnetic-field induced energy shift in Figure 6.33, to the magnetic-field quanta for the Ξ^0 on the $m_\pi = 296$ MeV ensemble.

Table 6.5. Magnetic polarisability values for the Ξ^0 at each quark mass. The numbers in parentheses describe statistical uncertainties.

m_π (MeV)	κ_{ud}	$\beta\,(\times 10^{-4})$ fm^3
702	0.13700	2.37(43)
411	0.13754	2.01(14)
296	0.13770	2.68(32)

Table 6.6. Lattice magnetic polarisability values for the baryons considered at each quark mass in units of $\times 10^4$ fm^3. The numbers in parentheses describe statistical uncertainties.

κ_{ud}	m_π (MeV)	β^p	β^{Σ^+}	β^n	β^{Ξ^0}
0.13700	702	1.90(19)	2.46(25)	1.91(12)	2.37(43)
0.13727	570	1.87(18)	–	1.61(10)	–
0.13754	411	1.98(21)	2.06(26)	1.53(29)	2.01(14)
0.13770	296	1.93(22)	1.48(26)	1.27(37)	2.68(32)

The quadratic fits in Figures 6.34 through 6.34 use the single quadratic fit function of Eq. (6.11). These all display good fit behaviour to the two field strengths considered and have a χ^2_{dof} less than our preferred limit of 1.2.

Magnetic polarisability values for the Ξ^0 are reported in Table 6.5 for the three gauge-field ensembles considered here. These values are not close to those of the neutron in Table 6.2, even at heavy up and down quark masses suggesting that the strange quark mass plays a significant role, perhaps changing the light up-quark contribution through an environmental effect. Future studies should examine individual quark sector contributions through the introduction of neutrally-charged quark flavours. This suggestion agrees with the behaviour seen for the Σ^+.

6.2.5. Lattice Magnetic Polarisability Summary

Table 6.6 summarises the magnetic polarisabilities for all the baryons considered at each quark mass. Through this table, it is easy to compare the magnetic polarisability of each baryon on each ensemble.

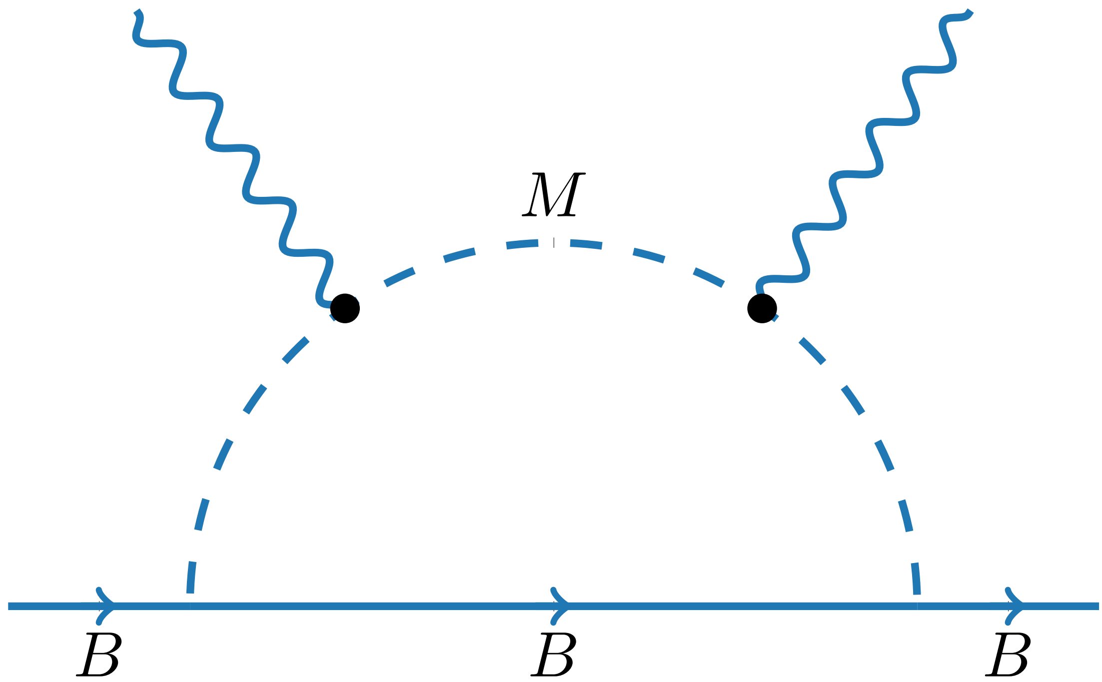

Figure 6.37. The leading order meson, M, loop contributions to the magnetic polarisability of the baryon B. These contributions have no baryon mass-splitting effects.

It is clear that the magnetic polarisability of the baryons considered are all of similar magnitude and sign but that the magnetic polarisabilities of the hyperons considered are not necessarily similar to their closest proton or neutron neighbour. It is interesting that the Σ^+ and neutron magnetic polarisability values both decrease as the physical up and down quark mass is increased while the proton and Ξ^0 magnetic polarisability is approximately constant across the range of pion masses considered.

6.3. Chiral effective field theory

Chiral effective field theory (χEFT) is the tool used to connect lattice QCD results at finite-volume and unphysical quark masses to the physical world. This analysis generalises that of Ref. [125] where extensions arise from the baryons considered herein.

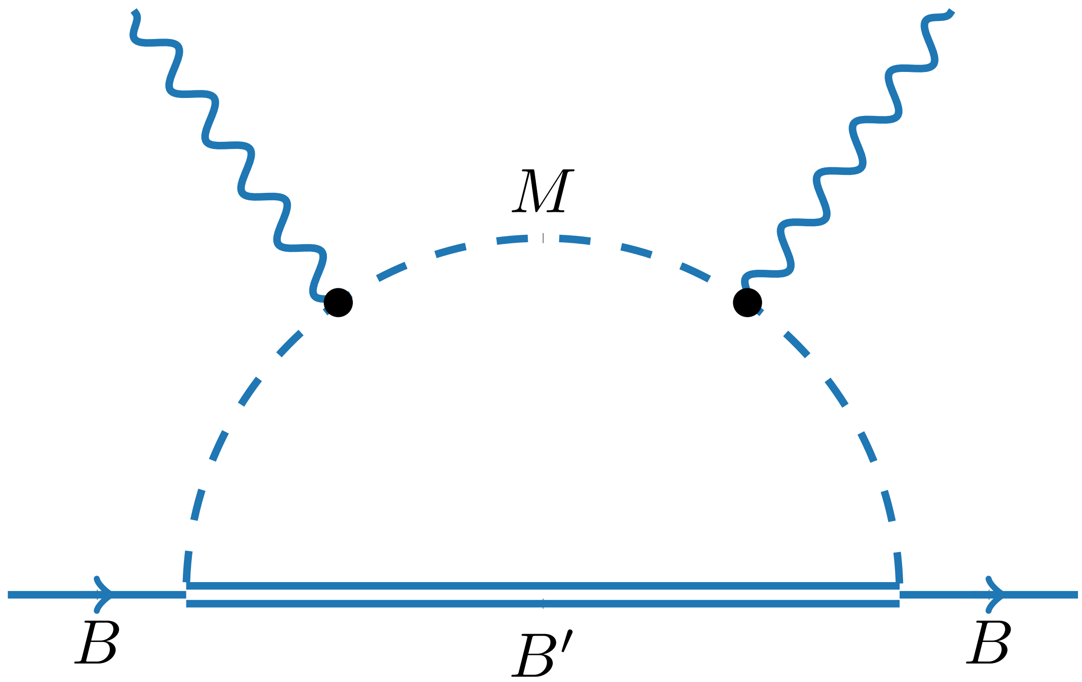

Figure 6.38. Leading-order meson, loop contributions to the magnetic polarisability of the baryon B; allowing transitions to nearby and strongly coupled octet or decuplet baryons, B' and octet-meson, M, pairs.

6.3.1. Formalism

The chiral expansion considered for the magnetic polarisability has the general form

$$\beta^{B}\left(m_\pi^2\right) = a_0\left(\Lambda\right) + a_2\left(\Lambda\right)\, m_\pi^2 + \sum_{M} \beta^{M\,B}\left(m_\pi^2, \Lambda\right) + \sum_{M,\,B'} \beta^{M\,B'}\left(m_\pi^2, \Lambda\right) + \mathcal{O}\left(m_\pi^3\right), \tag{6.18}$$

where $a_0\left(\Lambda\right)$ and $a_2\left(\Lambda\right)$ are the residual series coefficients [145] which are constrained by infinite volume corrected lattice QCD results and Λ is a renormalisation scale. The leading order loop contributions $\beta^{M\,B}\left(m_\pi^2, \Lambda\right)$ and $\beta^{M\,B'}\left(m_\pi^2, \Lambda\right)$ are shown in Figures 6.37 and 6.38 respectively. Here Figure 6.38 allows for transitions of the baryon B to strongly coupled baryons, B' which are nearby in energy, through a meson, M, loop. This is in contrast to Figure 6.37 which does not encounter baryon mass-splitting effects.

These leading-order loop contributions have integral forms [125] in the heavy-baryon limit [137] appropriate for a low energy expansion

$$\beta^{M\,B}\left(m_\pi^2, \Lambda\right) = \frac{e^2}{4\,\pi}\,\frac{1}{288\,\pi^3\,f_\pi^2}\,\chi_B \int d^3k\,\frac{\vec{k}^2\,u^2\left(k,\,\Lambda\right)}{\omega_{\vec{k},\,M}^6}, \tag{6.19}$$

$$\begin{aligned}\beta^{M\,B'}\left(m_\pi^2, \Lambda\right) =& \frac{e^2}{4\,\pi}\,\frac{1}{288\,\pi^3\,f_\pi^2}\,\chi_{B'} \int d^3k\,u^2\left(k,\,\Lambda\right) \\ &\times \frac{\omega_{\vec{k},\,M}^2\,\Delta\,\left(3\,\omega_{\vec{k},\,M} + \Delta\right) + \vec{k}^2\,\left(8\,\omega_{\vec{k},\,M}^2 + 9\,\omega_{\vec{k},\,M}\,\Delta + 3\,\Delta^2\right)}{8\,\omega_{\vec{k},\,M}^5\,\left(\omega_{\vec{k},\,M} + \Delta\right)^3},\end{aligned} \tag{6.20}$$

respectively. Here $\omega_{\vec{k},\,M} = \sqrt{\vec{k}^2 + m_M^2}$ is the energy carried by the meson M with mass m_M and three momenta $\vec{k}$, $f_\pi = 92.4$ MeV is the pion decay constant, χ_B and $\chi_{B'}$ are the $SU(3)$ flavour coupling coefficients for B and B' with the meson M and $u\left(k,\,\Lambda\right)$ is a dipole regulator

$$u\left(k,\,\Lambda\right) = \frac{1}{\left(1 + \vec{k}^2/\Lambda^2\right)^2}. \tag{6.21}$$

The dipole regulator ensures that only soft momenta flow through the degrees of freedom of the effective field theory.

The renormalised low-energy coefficients of the chiral expansion are formed from the residual series coefficients $a_0\left(\Lambda\right)$, $a_2\left(\Lambda\right)$ and the analytic Λ-dependent contributions of the loop integrals [139]. The full details of the renormalisation procedure are provided in the Appendix of Ref. [139].

The loop integral of Eq. (6.19) contains the leading non-analytic contribution proportional to $1/m_M$ while the loop integral of Eq. (6.20) accounts for transitions to nearby strongly coupled baryons B'. For a finite $B' - B$ mass splitting, $\Delta = m_{B'} - m_B$, this integral provides a non-analytic contribution proportional to $\left(-1/\Delta\right)\,\log\left(m_M/\Lambda\right)$ to the chiral expansion.

The standard full QCD coefficients, χ_B and $\chi_{B'}$ must be altered to account for the electroquenching of the lattice QCD calculations. As the background field is only present on the valence quarks of the lattice QCD simulation, the lattice results do not include the contribution of photon couplings to disconnected sea-quark loops of the vacuum. The full meson dressing of χEFT includes these disconnected sea-quark loops and it is

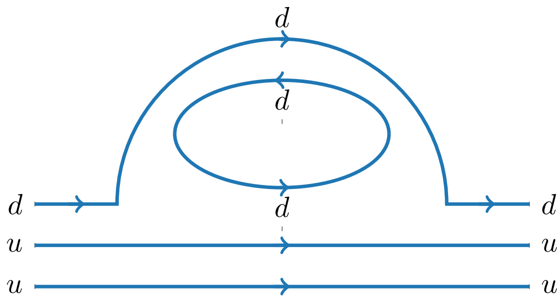

(a) The down quark loop diagram where the two photons can couple to valence-valence, sea-sea or valence-sea quarks.

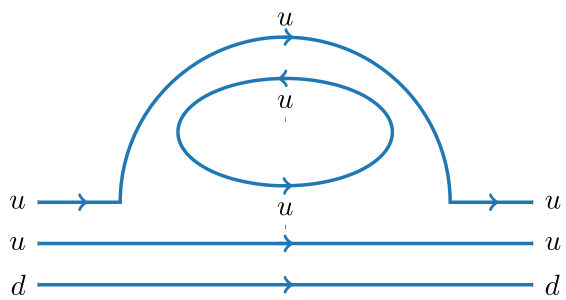

(b) The up quark loop diagram where the two photons can couple to valence-valence, sea-sea or valence-sea quarks.

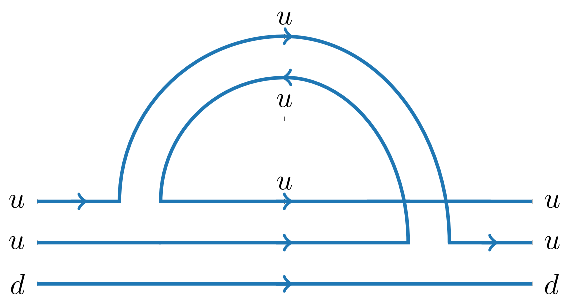

(c) The quark-flow diagram where the two photons can couple only to valence quarks.

Figure 6.39. Decomposition of the process $p \to p\,\pi^0$ into its possible one-loop quark-flow diagrams. The configuration of the two photon couplings to the valence and/or sea quarks determines the coefficients of partially quenched chiral perturbation theory.

thus necessary to model the corrections associated with their absence in the lattice QCD calculations.

Partially quenched chiral effective field theory

The loop coefficients for partially quenched chiral perturbation theory ($PQ\chi PT$) can be determined by considering the two photon couplings to the intermediate meson of the loop diagrams. By constructing quark flow diagrams, the loop diagram contribution is divided into "valence-valence", "valence-sea" or "sea-sea" contributions. These labels describe whether the two photons of Figures 6.37 and 6.38 couple to valence or sea quarks in the intermediate states available in these processes. Due to the electroquenched nature of the lattice QCD calculation, no valence-sea or sea-sea contributions are present in the lattice QCD results.

As an example; consider the proton with $p \to N\,\pi$. As there is no mass splitting between B and B', i.e. between p and N, this is an example of Figure 6.37. Further select the $p \to p\,\pi^0$ channel and write all possible quark-flow diagrams without attaching external photons to the meson, as shown in Figure 6.39. The quark-flow diagram of Figure 6.39c has only valence quarks, and hence contributes only to the valence-valence sector. The diagrams of Figures 6.39a and 6.39b contribute to all three sectors as the photon lines may be attached to the valence or sea-quark lines of the intermediate meson. The contributions to each of these sectors is proportional to the quark charges, i.e. for Figure 6.39b, the chiral coefficients of the leading non-analytic term of the chiral expansion are

$$\chi_{v-v} \propto q_u^2, \tag{6.22}$$

$$\chi_{v-s} \propto 2\, q_u\, q_{\overline{u}}, \tag{6.23}$$

$$\chi_{s-s} \propto q_{\overline{u}}^2, \tag{6.24}$$

where the factor of two on the valence-sea contribution reflects the two orderings of photon couplings available. The total contribution vanishes

$$\chi_t \propto \left(q_u^2 + 2\, q_u\, q_{\overline{u}} + q_{\overline{u}}^2\right) = \left(q_u + q_{\overline{u}}\right)^2 = 0. \tag{6.25}$$

By replacing the up or down quark sea-quark loops with a strange quark, the $SU(3)$ flavour couplings for the isolated disconnected sea-quark-loop flow can be obtained [177]. For the diagram in Figure 6.39b the $SU(3)$ flavour coupling is

$$\chi_{p\,\pi^0}^{diag-b} \propto \chi_{K^0\,\Sigma^+}^2 = 2\,(D-F)^2\,, \tag{6.26}$$

where $D + F = g_A = 1.267$ and the $SU(6)$ symmetry relation provides $F = \frac{2}{3}\,D$ [141,143]. The valence-sea and sea-sea contributions for Figure 6.39b are therefore

$$\chi_{v-s}^{diag-b} = 2\, q_u\, q_{\overline{u}}\, \chi_{K^0\,\Sigma^+}^2 = 4\, q_u\, q_{\overline{u}}\,(D-F)^2 \tag{6.27}$$

$$\chi_{s-s}^{diag-b} = q_{\overline{u}}^2\, \chi_{K^0\,\Sigma^+}^2 \qquad = 2\, q_{\overline{u}}^2\,(D-F)^2\,. \tag{6.28}$$

The full set of channels and contributions for the proton can be found in Tables B.1 and B.3. The valence-valence component can be found by subtracting the valence-sea and sea-sea contributions from the total contribution which is known from standard chiral perturbation theory.

Finite volume corrections

Due to the periodicity of the finite-volume lattice, only discrete momenta are possible. These obey the relation [11]

$$k_i = \frac{2\,\pi\,n_i}{L}, \tag{6.29}$$

where k_i is the momentum, n_i is the momentum quanta and $L = a\,N_s$ is the lattice size. The continuous meson loop integrals of Eqs. (6.19) and (6.20) are transformed into a sum over the discrete momenta available on the lattice. Hence, there is a finite-volume correction which is the difference between the loop sum and its corresponding loop integral. This difference should vanish for all integrals as $m_\pi\,L$ becomes large [178].

The loop $\to$ sum transformation takes the form

$$\int d^3k \to \frac{(2\,\pi)^3}{L^3} \sum_{k_x,\,k_y,\,k_z} . \tag{6.30}$$

The finite volume sums are thus

$$\beta^{M\,B}_{SUM}\left(m_\pi^2, \Lambda\right) = \frac{e^2}{4\,\pi}\,\frac{1}{288\,\pi^3\,f_\pi^2}\,\chi_B\,\frac{(2\,\pi)^3}{L^3} \sum_{k_x,\,k_y,\,k_z} \frac{\vec{k}^2\,u^2\left(\vec{k},\,\Lambda\right)}{\omega^6_{\vec{k},\,M}}, \tag{6.31}$$

$$\begin{aligned}\beta^{M\,B'}_{SUM}\left(m_\pi^2, \Lambda\right) =& \frac{e^2}{4\,\pi}\,\frac{1}{288\,\pi^3\,f_\pi^2}\,\chi_{B'}\,\frac{(2\,\pi)^3}{L^3} \sum_{k_x,\,k_y,\,k_z} u^2\left(\vec{k},\,\Lambda\right) \\ &\times \frac{\omega^2_{\vec{k},\,M}\,\Delta\left(3\,\omega_{\vec{k},\,M} + \Delta\right) + \vec{k}^2\left(8\,\omega^2_{\vec{k},\,M} + 9\,\omega_{\vec{k},\,M}\,\Delta + 3\,\Delta^2\right)}{8\,\omega^5_{\vec{k},\,M}\left(\omega_{\vec{k},\,M} + \Delta\right)^3}.\end{aligned} \tag{6.32}$$

To correct the lattice polarisability results, $\beta^{lat.}_{v-v}\,(m_\pi^2)$, which are finite-volume and have only valence-valence contributions to infinite volume $\beta^{FVC}_{v-v}\,(m_\pi^2)$, the process used is

$$\begin{aligned}\beta^{FVC}_{v-v}\left(m_\pi^2\right) = \beta^{lat.}_{v-v}\left(m_\pi^2\right) \\ &- \left(\sum_M \beta^{M\,B}_{SUM}\left(m_\pi^2, \Lambda^{FV}\right) + \sum_{M,\,B'} \beta^{M\,B'}_{SUM}\left(m_\pi^2, \Lambda^{FV}\right)\right) \\ &+ \left(\sum_M \beta^{M\,B}\left(m_\pi^2, \Lambda^{FV}\right) + \sum_{M,\,B'} \beta^{M\,B'}\left(m_\pi^2, \Lambda^{FV}\right)\right),\end{aligned} \tag{6.33}$$

where we note that the coefficients used in evaluating these integrals and sums reflect only valence-valence contributions. The regulator parameter dependence of the integral and sums used in calculating the finite-volume corrections has been made explicit by Λ^{FV}.

The finite-volume corrections should be independent of the the regulator parameter; this was examined in Ref. [179] where it was shown that choosing Λ^{FV} too small suppresses the infrared physics that the finite-volume corrections are attempting to describe and furthermore that the results saturate to a fixed result for large Λ^{FV}. As such we adopt the value $\Lambda^{FV} = 2.0$ GeV as in Ref. [179].

Extrapolation

In order to extrapolate to the physical regime where the pion has mass $m_\pi \approx 140$ MeV, the residual series coefficients $a_0\left(\Lambda\right)$ and $a_2\left(\Lambda\right)$ are constrained by fitting to the infinite-volume corrected lattice results

$$\beta^{FVC}_{v-v}\left(m_\pi^2\right) - \sum_{M} \beta^{M\,B}_{v-v}\left(m_\pi^2,\,\Lambda\right) - \sum_{M,\,B'} \beta^{M\,B'}_{v-v}\left(m_\pi^2,\,\Lambda\right) = a_0\left(\Lambda\right) + a_2\left(\Lambda\right)\,m_\pi^2, \quad (6.34)$$

where again $v - v$ denotes the electroquenched valence-valence only contributions of the loop integrals. The regulator parameter Λ is allowed to differ from the finite-volume value of Λ^{FV}.

The value used here is $\Lambda = 0.80$ GeV. This value is adopted in preparation for modelling of the missing disconnected sea-quark-loop contributions in the lattice QCD calculations [144–148]. $\Lambda = 0.80$ GeV models a pion cloud contribution to masses [145], magnetic moments [146], and charge radii [144], which enables the correction to the pion cloud encountered in unquenching to be modelled. This choice of regulator mass defines a baryon core contribution as the missing sea-quark contributions are added [149].

Once the residual series coefficients have been determined, the magnetic polarisability can be reconstructed at any value of m_π^2 using the chiral expansion of Eq. (6.18). In order to account for the valence-sea and sea-sea loop integral contributions when doing this extrapolation, the coefficients used are for the “total” process. The physical extrapolation is provided by setting $m_\pi = 0.140$ GeV.

In a similar manner, the fitted $a_0\left(\Lambda\right)$ and $a_2\left(\Lambda\right)$ values can be used to provide a target or expectation for future lattice QCD experiments by using the valence-valence

$\beta^{M,B}_{SUM}\left(m_\pi^2, \Lambda^{FV}\right)$ and $\beta^{M,B'}_{SUM}\left(m_\pi^2, \Lambda^{FV}\right)$ where we can adjust the lattice size. Such a use case is shown in Figures 6.41 and 6.42.

6.3.2. Results

The steps required for a chiral effective field theory for the magnetic polarisability are now clear. To summarise they are

1. Calculate magnetic polarisabilities at several values of the pion mass using lattice QCD,
2. Determine the valence-valence chiral coefficients by subtracting sea-quark-loop contributions from the "total" loop contributions,
3. Correct lattice results to infinite volume using Eq. (6.33) with the valence-valence coefficients,
4. Fit the residual series coefficients using Eq. (6.34),
5. Use the chiral expansion of Eq. (6.18) with "total" loop contributions.

Chiral expansions for the neutron, proton, Σ^+, and Ξ^0 are considered as lattice magnetic polarisabilities have been determined for all of these in the preceding sections.

All the $SU(3)$ flavour couplings required are detailed in Tables B.1 through B.5.

Neutron

The results of the separation of the loop contributions into total, valence-sea and sea-sea contributions for the neutron are shown in Table B.2 where the valence-valence can be found by subtracting the valence-sea and sea-sea from the total

$$\chi^2_{v-v} = \chi^2_t - \chi^2_{v-s} - \chi^2_{s-s}. \tag{6.35}$$

The chiral expansion, using a regulator parameter value of $\Lambda = 0.80$ GeV provides a magnetic polarisability of $\beta^n = 2.06(26) \times 10^{-4}$ fm^3 at the physical point. The numbers in parentheses here describe the statistical uncertainty. The systematic uncertainty in the higher order terms of the chiral expansion can be examined through variation of the regulator parameter Λ.

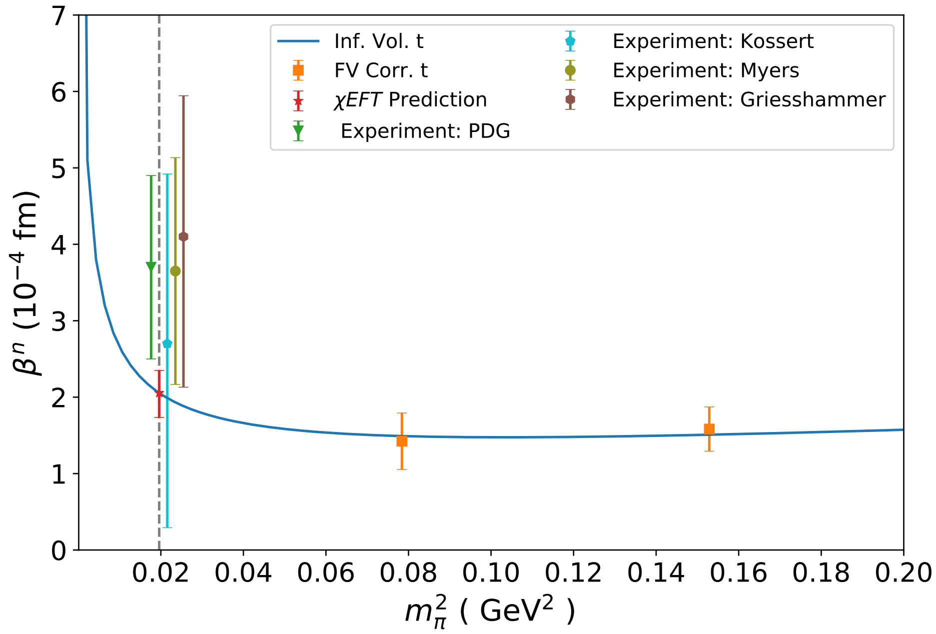

Figure 6.40. The magnetic polarisability of the neutron, β^n from our chiral effective field analysis (χEFT Prediction) and lattice results (FV Corr. t) of this chapter are compared with experimental measurements. The error bar at the physical point reflects systematic and statistical uncertainties added in quadrature. Experimental results from Kossert *et al.* [126, 127], the PDG [3], Myers *et al.* [129] and Griesshammer *et al.* [128] are offset for clarity.

To ensure a robust estimation of the systematic error associated with the choice of Λ, the regulator parameter is varied over the conservative range of $0.6 \leq \Lambda \leq 1.0$. This provides a systematic uncertainty of $\left(^{+15}_{-20}\right) \times 10^{-4}$ fm^3. The magnetic polarisability of the neutron predicted is thus

$$\beta^n = 2.06(26)\left(^{+15}_{-20}\right) \times 10^4 \text{ fm}^3.$$

This result is in very good agreement with the neutron magnetic polarisability value reported in Chapter 4 of $\beta^n = 2.05(25)(19) \times 10^{-4}$ fm^3 using the $U(1)$ Landau eigenmode projection technique. This agreement highlights the success of both the $U(1)$ Landau projection approach and the $SU(3) \times U(1)$ eigenmode quark projection technique. Good agreement is also seen with recent experimental measurements, as shown in Figure 6.40.

By using the fit coefficients $a_0(\Lambda)$, $a_2(\Lambda)$ and the sum forms of the integrals $\beta^{M,B}_{SUM}$, $\beta^{M,B'}_{SUM}$ predictions can be made for future lattice QCD calculations. The two figures

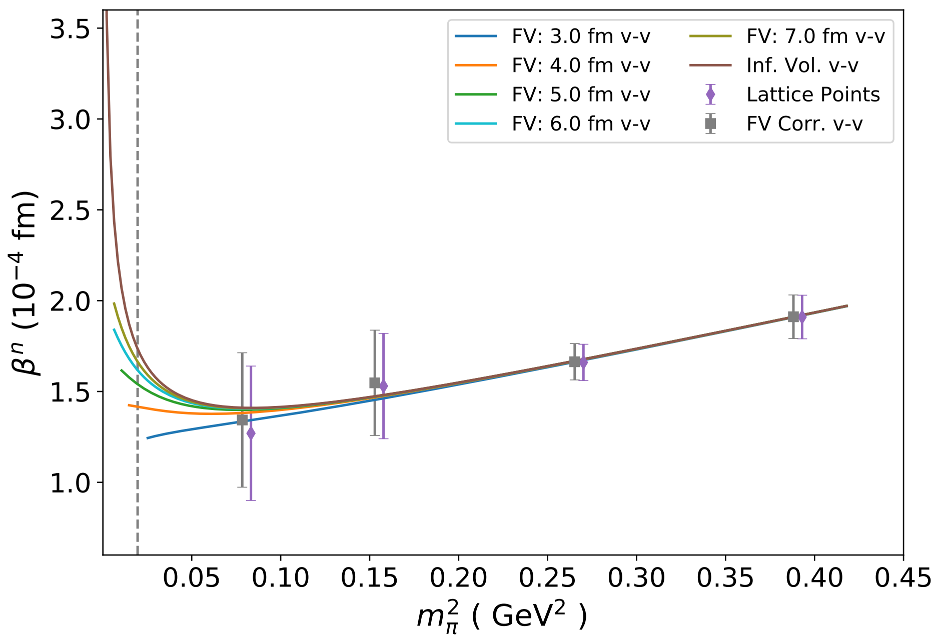

Figure 6.41. Finite volume extrapolations of β^n with valence-valence coefficients appropriate for electroquenched lattice QCD simulations. The infinite-volume case is also illustrated.

of Figures 6.41 and 6.42 show these predictions which are made for a range of lattice volumes, 3.0 fm $\leq L_s \leq$ 7.0 fm. Figure 6.41 uses the valence-valence form of the integral coefficient, these predictions are hence appropriate to a lattice QCD calculation which is electroquenched. In contrast, Figure 6.42 uses the full QCD coefficients and is appropriate for a simulation where the background field is present for the sea-quark-loops. A conservative $m_\pi L_s$ cut where masses are excluded if $m_\pi L_s \leq 2.4$ is applied to all finite-volume extrapolation plots. It is interesting to note that even extremely large lattice sizes such as $L_s = 7.0$ fm still differ from the infinite volume limit by $\sim 6\%$.

The lattice data points are also shown in Figures 6.41 and 6.42 where they are slightly offset such that the finite-volume corrected (FV Corr.) valence-valence (v-v), $\beta^{FVC}_{v-v}\,(m_\pi^2)$ of Eq. (6.34) or total (t) full QCD points, $\beta^{FVC}_t\,(m_\pi^2)$ are at the correct pion mass. These "total" (t) corrected points are given by

$$\begin{aligned}\beta^{FVC}_t\,(m_\pi^2) = \beta^{FVC}_{v-v}\,(m_\pi^2) &- \sum_M \left(\beta^{M\,B}_{v-v}\,(m_\pi^2,\,\Lambda) - \beta^{M\,B}_t\,(m_\pi^2,\,\Lambda)\right) \\ &- \sum_{M,\,B'} \left(\beta^{M\,B'}_{v-v}\,(m_\pi^2,\,\Lambda) - \beta^{M\,B'}_t\,(m_\pi^2,\,\Lambda)\right) \qquad (6.36)\end{aligned}$$

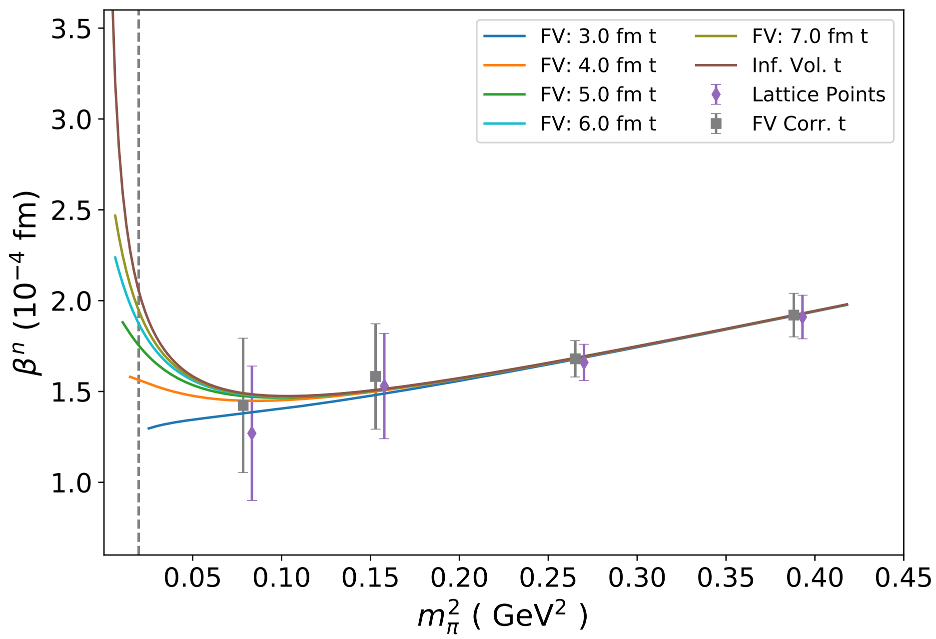

Figure 6.42. Finite volume extrapolations of β^n with total full QCD coefficients appropriate for fully dynamical background field lattice QCD simulations. The infinite-volume case relevant to experiment is also illustrated.

where $v - v$ or t denotes the integral coefficients χ_B, $\chi_{B'}$ used.

Comparing Figures 6.41 and 6.42, one observes the effect of the inclusion of sea-quark-loop contributions is similar in magnitude to the finite-volume corrections for the points calculated on the lattice.

Proton

The analysis for the proton proceeds in an identical manner to that of the neutron, excepting that the loop contributions are as in Table B.3. The chiral effective field theory analysis produces a physical-value prediction of

$$\beta^p = 2.79(22)\left(^{+13}_{-18}\right) \times 10^{-4}\ \mathrm{fm}^3,$$

where the numbers in parentheses are statistical and systematic errors respectively.

A comparison to a selection of recent experimental results is shown in Figure 6.43. Excellent agreement is observed between the result in this work and the experimental

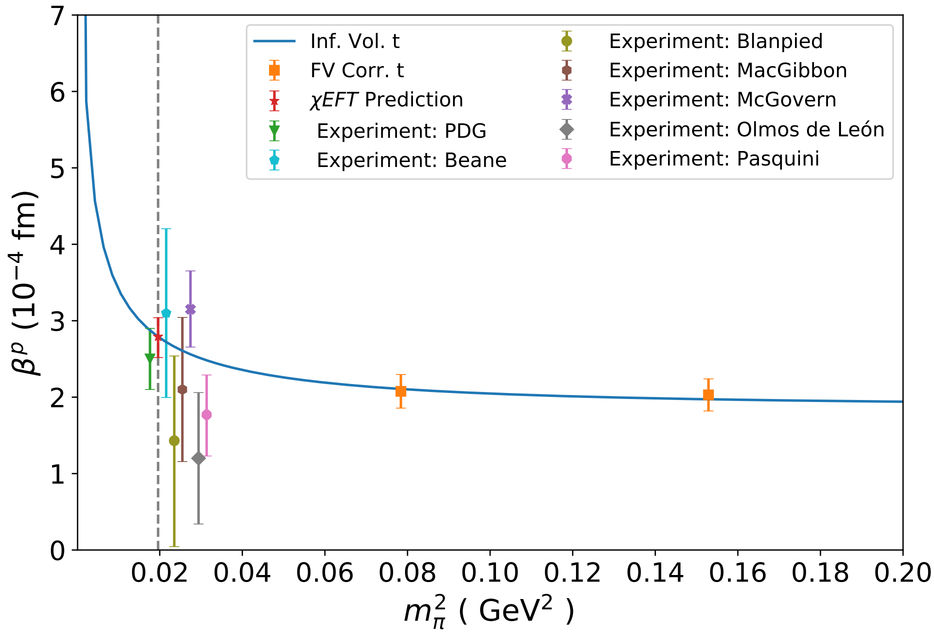

Figure 6.43. The magnetic polarisability of the proton, β^p, from the chiral effective field analysis herein (χEFT Prediction) and lattice results of this chapter (FV Corr. t) are compared with experimental measurements. The error bar at the physical point reflects systematic and statistical uncertainties added in quadrature. Experimental results from the PDG [3], McGovern *et al.* [180], Beane *et al.* [181], Blanpied *et al.* [182], Olmos de León *et al.* [183], MacGibbon *et al.* [184] and Pasquini *et al.* [185] are offset for clarity.

results. This agreement validates our current understanding of QCD through the quark projection technique and partially-quenched chiral effective field theory used herein.

In the same manner as the neutron, proton lattice QCD prediction plots are shown in Figures 6.44 and 6.45. Here the 7.0 fm result still differs from the infinite volume by $\sim 4\%$.

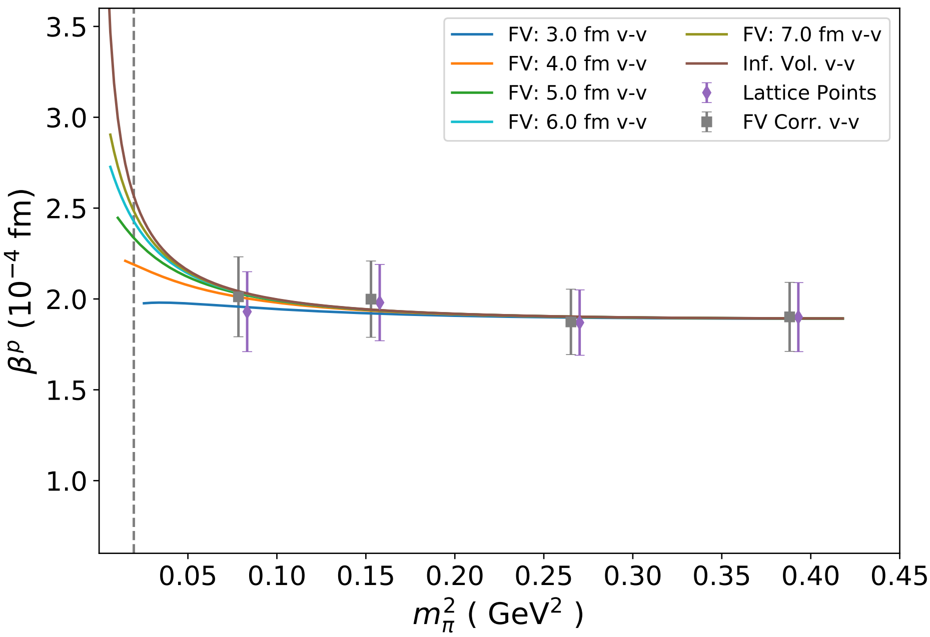

Figure 6.44. Finite volume extrapolations of β^p with valence-valence coefficients appropriate for electroquenched lattice QCD simulations. The infinite-volume case is also illustrated.

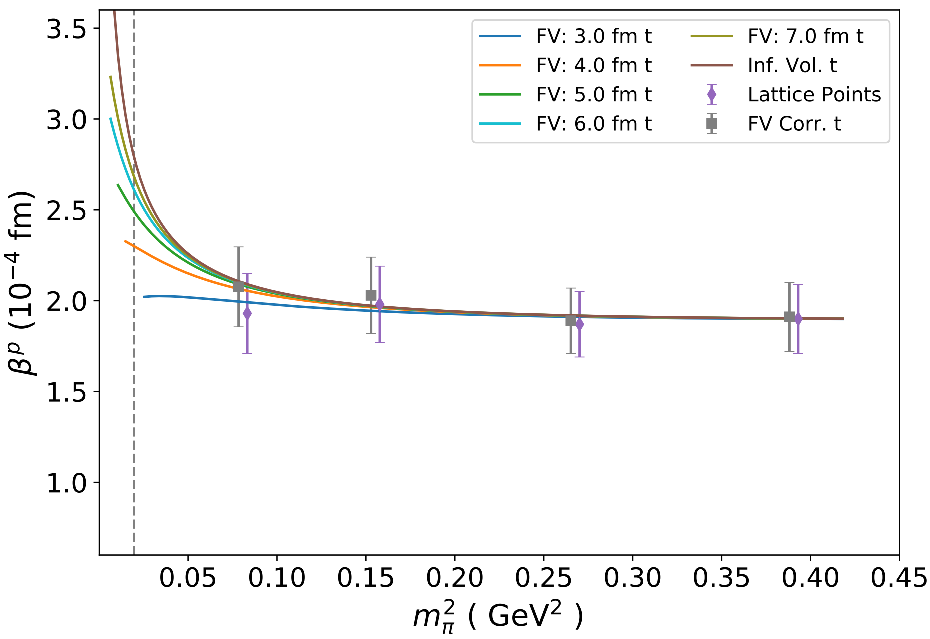

Figure 6.45. Finite volume extrapolations of β^p with total full QCD coefficients appropriate for fully dynamical background field lattice QCD simulations. The infinite-volume case relevant to experiment is also illustrated.

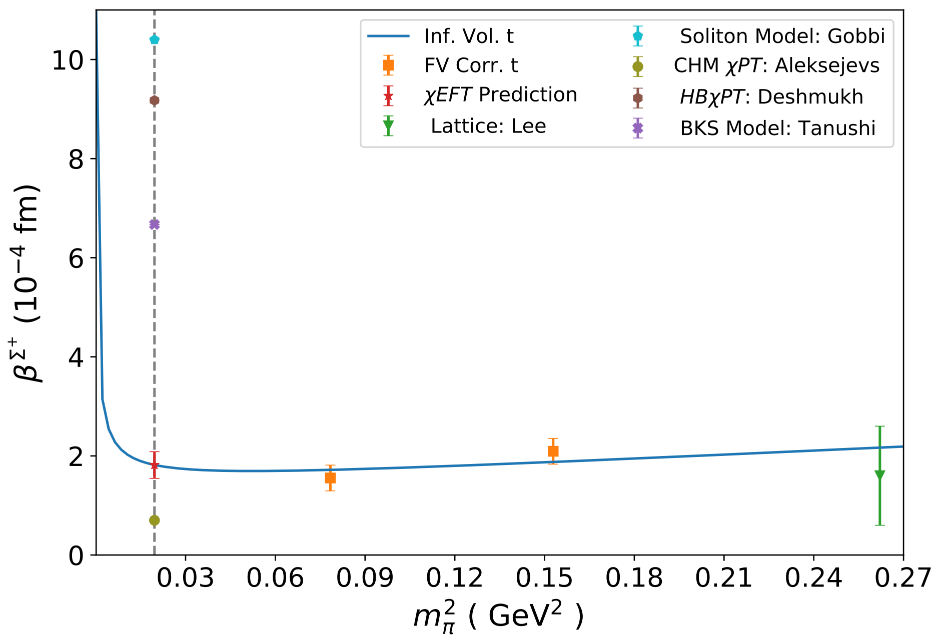

Figure 6.46. The magnetic polarisability of the Σ^+, β^{Σ^+}, from the chiral effective field analysis herein (χEFT Prediction) and lattice results of this chapter (FV Corr. t) are compared with a set of model approaches. The error bars on our physical value reflect systematic and statistical uncertainties added in quadrature. Results from Gobbi *et al.* [174], Aleksejevs *et al.* [172], Deshmukh *et al.* [173] and Tanushi *et al.* [175] are plotted without uncertainties at the physical point. A previous lattice calculation from Lee *et al.* [176] (Lattice: Lee) is shown at the appropriate pion mass.

Σ^+ Baryon

We continue with the analysis methods of the previous sections. The loop integral coefficients for each channel for the Σ^+ are presented in Table B.4 where we consider $M = \pi, \eta$ for the integral of Eq. (6.19) with $B = \Sigma$. For the integral with a finite mass splitting, $\Delta = M_{B'} - M_B$ of Eq. (6.20), we consider $M = K, \pi, \eta$ with $B' = N, \Xi, \Delta$ and Ξ^*.

The chiral effective field theory analysis herein predicts

$$\beta^{\Sigma^+} = 1.82(26) \left({}^{+7}_{-8}\right) \times 10^{-4} \text{ fm}^3, \tag{6.37}$$

at the physical point, a significant reduction from the proton's polarisability of $\beta^p = 2.79(22) \left({}^{+13}_{-18}\right) \times 10^{-4} \text{ fm}^3$.

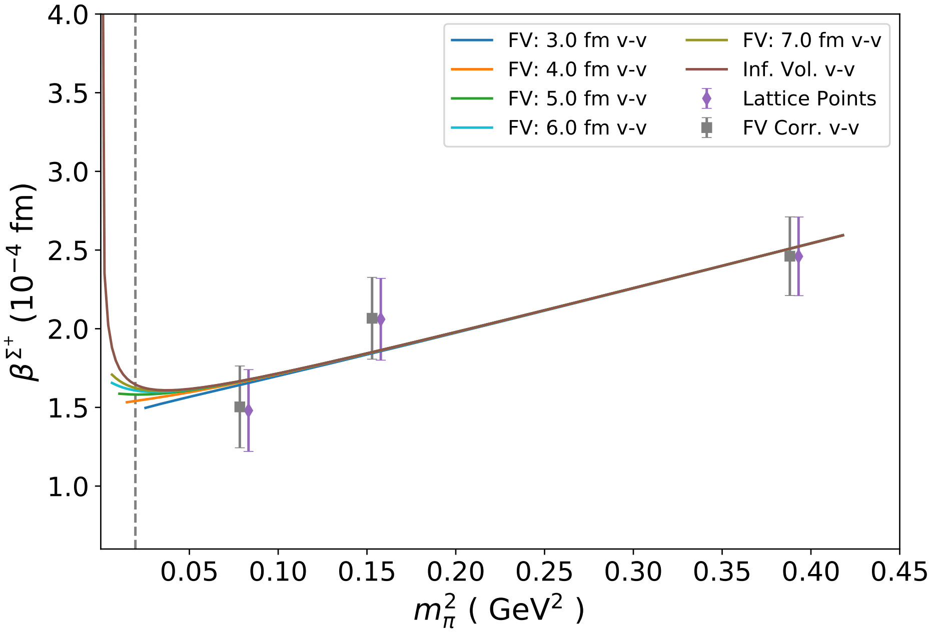

Figure 6.47. Finite volume extrapolations of β^{Σ^+} with valence-valence coefficients appropriate for electroquenched lattice QCD simulations. The infinite-volume case is also illustrated.

A comparison to a selection of model calculations at a physical pion mass and a non-physical mass lattice result is shown in Figure 6.46. The scatter in the model results is large but there is qualitative agreement with the value predicted by Aleksejevs *et al.* [172]. The previous lattice result by Lee *et al.* [176] also agrees.

Finite-volume predictions for both electroquenched and full QCD lattice simulations are shown in Figures 6.47 and 6.48 for a range of quark masses. It is interesting to note that a lattice of size $L_s = 7.0$ fm now gets within 2.5% of the infinite-volume results, compared to $\sim 6\%$ and $\sim 4\%$ for the neutron and proton respectively.

The result presented herein poses a challenge for both theoretical models and experimental measurements of the magnetic polarisability of the Σ^+.

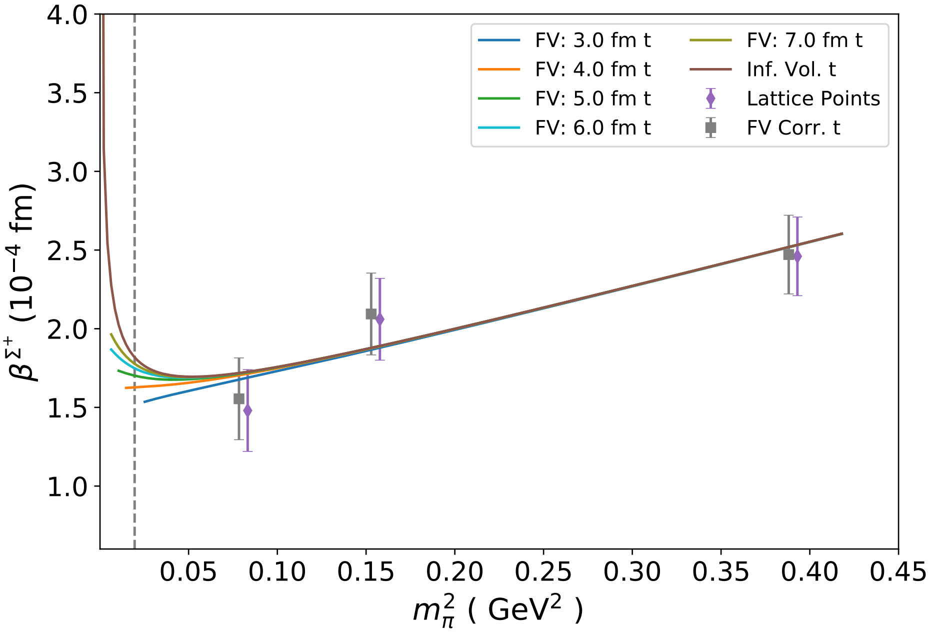

Figure 6.48. Finite volume extrapolations of β^{Σ^+} with total full QCD coefficients appropriate for fully dynamical background field lattice QCD simulations. The infinite-volume case relevant to experiment is also illustrated.

Ξ^0 Baryon

The chiral effective field theory analysis for the Ξ^0 is built upon the lattice QCD results of Table 6.5. We consider π, η and K-meson loop transitions to the Ξ, Σ, Ξ^-_{3S}, Ξ^*, Σ^* and Ω^- baryons. The Ξ^-_{3S} is an octet baryon with $J^P = \frac{1}{2}^+$ comprised of three valence strange quarks, encountered in partially quenched χPT.

The loop integral coefficients required are presented in Table B.5 and we henceforth follow the analysis procedure already discussed.

The chiral effective field theory prediction for the magnetic polarisability of the Ξ^0 at the physical point is

$$\beta^{\Xi^0} = 2.34(27)\left(^{+4}_{-5}\right) \times 10^{-4}\ \mathrm{fm}^3, \tag{6.38}$$

where the numbers in parentheses represent statistical and systematic errors respectively. This time, the polarisability is similar to the neutron with $\beta^n = 2.06(26)\left(^{+15}_{-20}\right) \times 10^4\ \mathrm{fm}^3$. Figure 6.49 shows a comparison of this result to recent model and lattice calculations. Qualitative agreement is seen with the Computational Hadronic Model (CHM) chiral

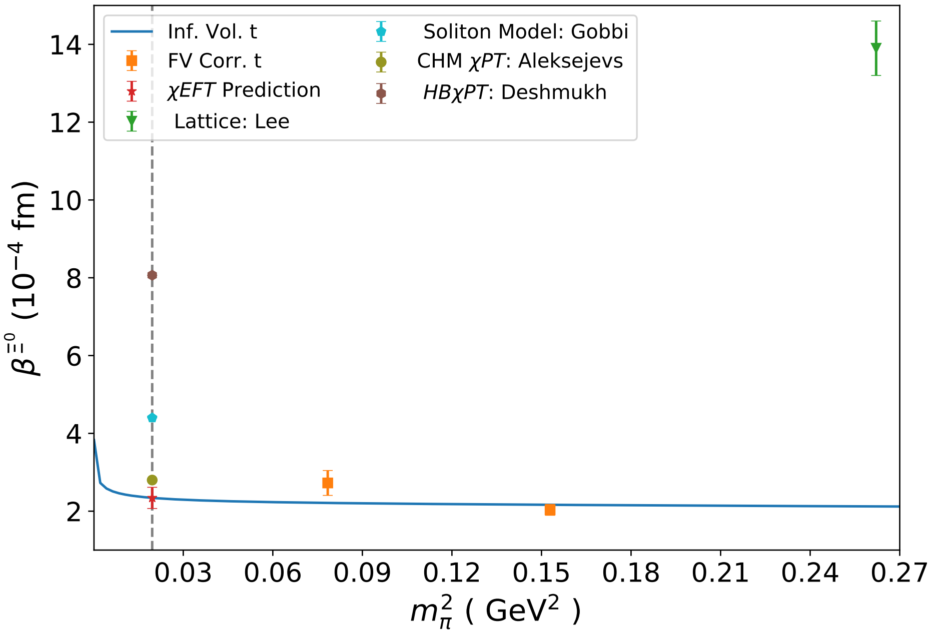

Figure 6.49. The magnetic polarisability of the Ξ^0, β^{Ξ^0}, from the chiral effective field analysis (χEFT Prediction) and lattice results of this chapter (FV Corr. t) are compared with a set of model approaches. The error bars on our physical value reflect systematic and statistical uncertainties added in quadrature. Results from Gobbi *et al.* [174], Aleksejevs *et al.* [172] and Deshmukh *et al.* [173] are plotted without uncertainties at the physical point. A previous lattice calculation from Lee *et al.* [176] (Lattice: Lee) is shown at the appropriate pion mass.

perturbation theory (χPT) of Ref. [172] as with the Σ^+. The lattice QCD result of Ref. [176] for the Ξ^0 does not agree with our result, in contrast to the Σ^+ where good agreement was observed. Clearly further progress in experimental and theoretical efforts is required in order to fully understand the magnetic polarisability of the Ξ^0.

Finite-volume predictions for the Ξ^0 at a range of pion masses to guide future lattice QCD work are presented in Figures 6.50 and 6.51. Here the lattice with side length $L_s = 7.0$ fm reproduces the infinite-volume result to within 1%. Considering this same difference for the neutron, proton and Σ^+ illustrates how weak coupling to the pion suppresses finite-volume effects.

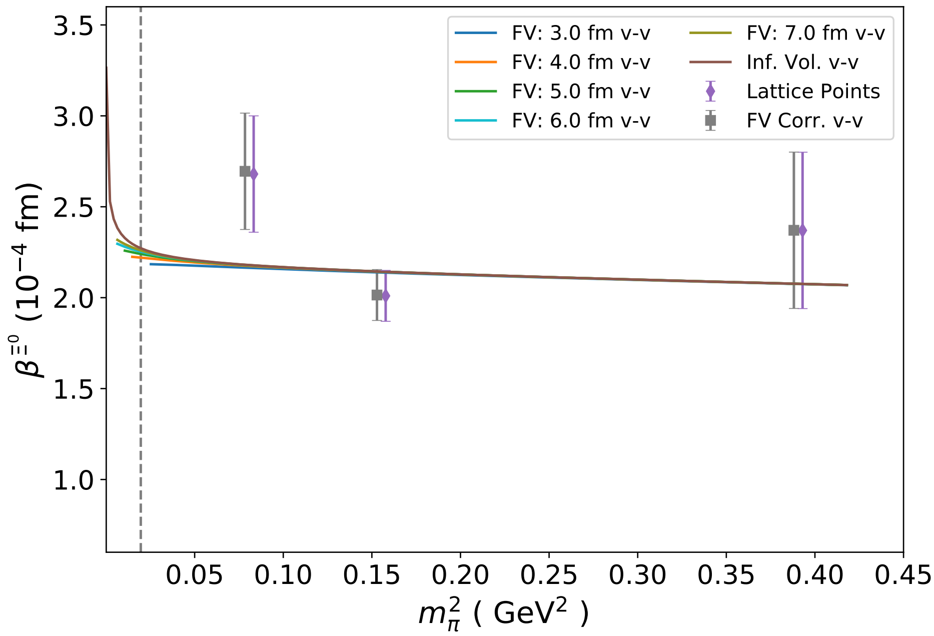

Figure 6.50. Finite volume extrapolations of β^{Ξ^0} with valence-valence coefficients appropriate for electroquenched lattice QCD simulations. The infinite-volume case is also illustrated.

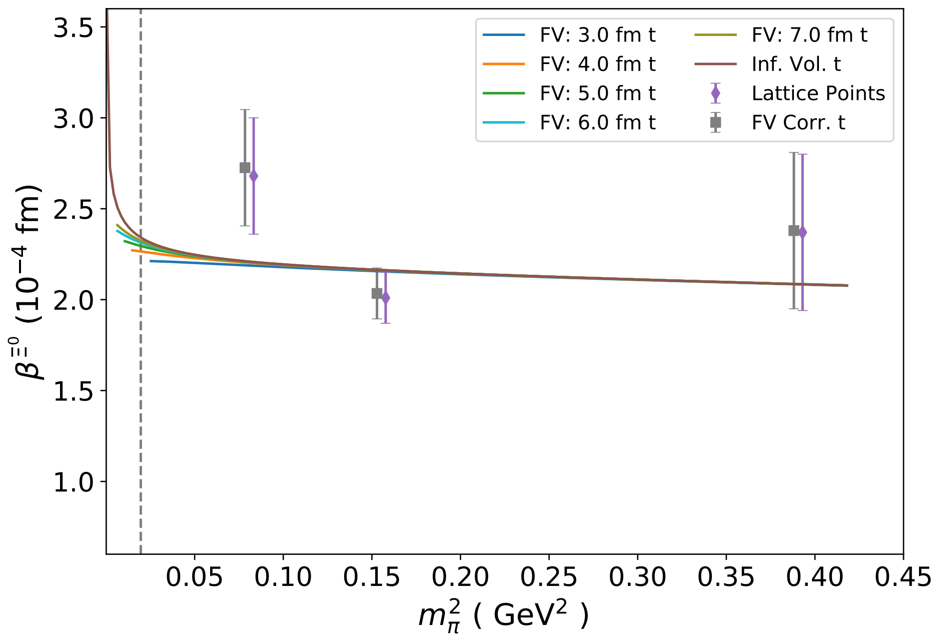

Figure 6.51. Finite volume extrapolations of β^{Ξ^0} with total full QCD coefficients appropriate for fully dynamical background field lattice QCD simulations. The infinite-volume case relevant to experiment is also illustrated.

Table 6.7. Predicted magnetic polarisability values for the octet baryons considered herein at the physical pion mass and each quark mass considered using total full QCD coefficients using the chiral effective field theory analysis of Section 6.3. The numbers in parentheses describe statistical and systematic uncertainties respectively.

κ_{ud}	m_π (MeV)	β^p	β^{Σ^+}	β^n	β^{Ξ^0}
0.13700	702	1.91(19)	2.47(25)	1.92(12)	2.38(43)
0.13727	570	1.89(18)	–	1.68(10)	–
0.13754	411	2.03(21)	2.09(26)	1.58(29)	2.03(14)
0.13770	296	2.08(22)	1.56(26)	1.42(37)	2.73(32)
Physical	140	2.79(22) $\left(^{+13}_{-18}\right)$	1.82(26) $\left(^{+7}_{-8}\right)$	2.06(26) $\left(^{+15}_{-20}\right)$	2.34(27) $\left(^{+4}_{-5}\right)$

6.4. Summary

A smeared source and the $SU(3) \times U(1)$ eigenmode projected quark sink which encapsulates both QCD and Landau level physics have been used to calculate baryon octet correlation functions in the presence of external magnetic fields. Correlation function ratios are used to form energy shifts from which the magnetic polarisability of the hadron can be extracted. A chiral effective field theory analysis is used to relate lattice QCD results to the physical regime.

The $SU(3) \times U(1)$ eigenmode projected quark sink is crucial in isolating the energy shifts required to extract the magnetic polarisability. A standard smeared or point sink does not produce correlation functions which couple only to the lowest-lying energy eigenstate in a background field. At the hadronic level, a Landau wave function projection onto the proton and Σ^+ two-point correlation functions assists in the isolation of these states. This is as these hadrons are charged, and hence experience hadronic Landau level physics in a uniform magnetic field. The combination of these techniques enables constant Euclidean-time plateau fits in the magnetic polarisability energy shift of the five baryons considered. This is the first time a single technique has been used to produce magnetic polarisability energy shift plateaus for all of these baryons.

Heavy-baryon chiral effective field theory and lattice QCD simulations at several pion masses have been used to connect to the physical regime. The resulting theoretical predictions for the magnetic polarisabilities along with the infinite-volume total full QCD corrected (FV Corr. t) lattice points are shown in Table 6.7. These corrected points

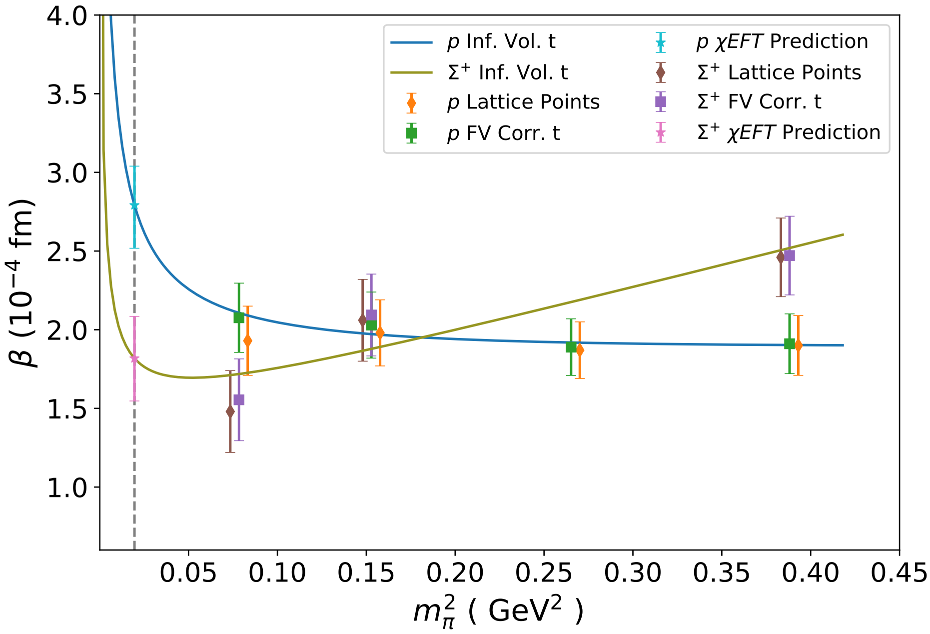

Figure 6.52. Comparisons of β^p and β^{Σ^+} with total full QCD coefficients at each quark mass and the extrapolated, physical point. FV Corr. t results of this chapter are at the correct m_π^2 value while lattice points are offset for clarity. The infinite-volume cases relevant to experiment is also illustrated.

form our best evidence for the quark mass dependence of the magnetic polarisability of each baryon in full QCD and may provide interesting tests for model builders.

Comparisons between the proton and Σ^+ where the singly represented down quark is changed to a strange quark and the neutron and Ξ^0 where the doubly represented down quarks are changed to strange quarks are presented in Figures 6.52 and 6.53. The physical predictions suggest that the change of the doubly represented down quark to a strange quark as we examine n and Ξ^0 has a smaller effect on the magnetic polarisability than changing the singly represented down quark in the proton to a strange quark in the Σ^+. This result informs the method by which the magnetic polarisability is manifest as the chiral limit is approached; i.e. the magnetic polarisability is largely determined by the singly represented quark. Examining the quark mass dependence of the magnetic polarisability paints a more complicated picture. There is clearly a complicated quark mass dependence visible in Figure 6.53 where despite the neutron and Ξ^0 extrapolated magnetic polarisabilities being similar, the largest difference at the three quark masses investigated is at the lightest pion mass considered.

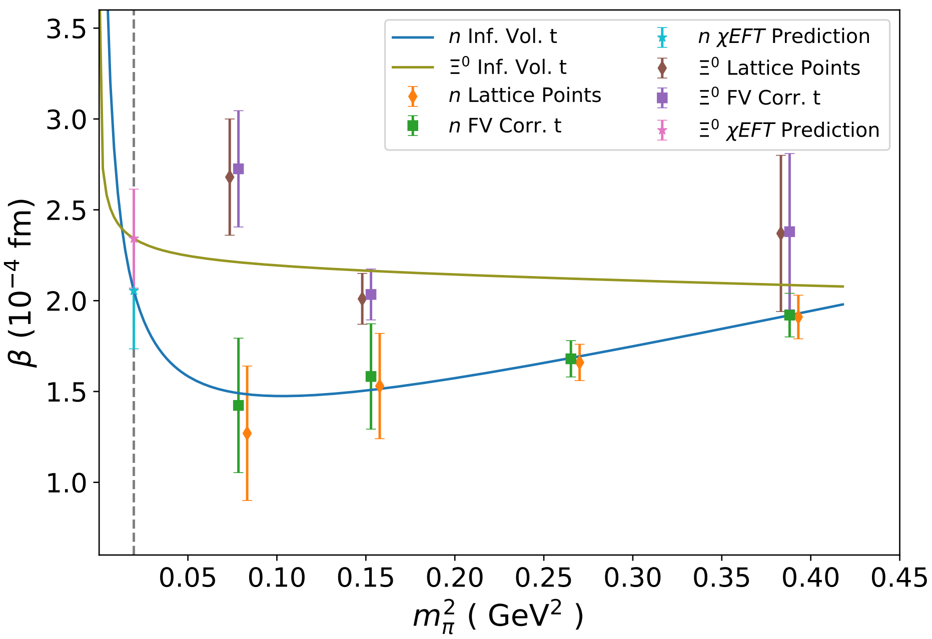

Figure 6.53. Comparisons of β^n and β^{Ξ^0} with total full QCD coefficients at each quark mass and the extrapolated, physical point. FV Corr. t results of this chapter are at the correct m_π^2 value while lattice points are offset for clarity. The infinite-volume cases relevant to experiment is also illustrated.

This quark mass dependence is a complicated challenge to model builders to provide insight into the physics which underlies these observations. Lattice QCD is well placed to examine the environmental sensitivity of the magnetic polarisability by considering baryons with neutral and charged quarks. It is trivial to construct a Σ^+ with neutrally charged up quarks and a charged strange quark and the opposite.

These predictions are founded upon *ab initio* lattice QCD simulations using effective-field theory techniques to account for the finite volume of the periodic lattice, disconnected sea-quark-loop contributions and an extrapolation to the light quark masses of nature.

The nucleon polarisability predictions are in good agreement with current experimental measurements and pose a challenge for greater experimental precision. An excellent review of recent results in nucleon polarisabilities is presented in Ref. [130]. There are few experimental results for hyperon magnetic polarisabilities and model calculations are similarly diverse in results. The chiral extrapolation performed herein agrees well with a subset of model approaches although further theoretical and experimental effort is needed in order to fully understand hyperon magnetic polarisabilities.

The lattice QCD simulation results presented in this chapter are electroquenched; they do not directly incorporate sea-quark-loop contributions from the magnetic field. Incorporating this effect would require a separate Monte Carlo simulation for each magnetic field strength considered and as such is prohibitively expensive. The relativistic energy shift used in Chapter 5 is another avenue for investigation; this would require improvements in lattice precision in order to successfully fit the $E(B) + M$ energy shift and hence construct the relativistic energy shift.

Chapter 7.

Pion polarisabilities

Pion electric (α_π) and magnetic (β_π) polarisabilities provide insight into the response of pion structure to an electric or magnetic field and can be experimentally determined using Compton scattering experiments. An example is the $\gamma\,\pi \to \gamma\,\pi$ process [186–189] where the polarisabilities describe the scattering angular distribution [189–193].

The pion polarisabilities have a long history of study in various theoretical frameworks. One of the most successful approaches used is chiral perturbation theory [165, 194, 195] where good agreement with experimental results is possible [165]. Alternate methods included the linear σ model [196] and dispersion sum rules [197–199]. Calculations using lattice QCD and the background field method exist [110, 111] and we will advance these using the novel techniques introduced in this thesis.

The introduction of the BFCC fermion action in Chapter 5 allows the magnetic polarisability of the pion to be calculated using Wilson-type fermions. Previous studies used the prohibitively expensive overlap action [110] and small volumes. In this chapter the same $2 + 1$ flavour dynamical gauge configurations provided by the PACS-CS collaboration [25] are considered. Calculations are performed at several non-zero pion masses in order to motivate a chiral extrapolation to the physical regime. Further developments in chiral effective field theory are required in order to enable extrapolations to the physical regime which incorporate finite-volume and sea-quark-loop corrections.

7.1. Interpolating operators

Recalling the meson octet of Figure 2.1, there are three pion species; the π^+, π^- and π^0. Here the π^+ and π^0 are considered and the π^- polarisability can be inferred from the π^+

results. The standard psuedoscalar meson interpolating operator

$$\chi = \overline{q}\,\gamma_5\,q \tag{7.1}$$

is used for each of these, where the quark content is varied appropriately. For the π^+, the annihilation operator is

$$\chi^{\pi^+} = \overline{d}\,\gamma_5\,u, \tag{7.2}$$

For the π^0 we consider the $\overline{u}u$ and $\overline{d}d$ contributions separately, defining

$$\chi^{\pi_u^0} = \overline{u}\,\gamma_5\,u \quad \text{and} \quad \chi^{\pi_d^0} = \overline{d}\,\gamma_5\,(d) \tag{7.3}$$

Due to the mass degeneracy of the lattice QCD simulation, these two neutral pion operators differ only by the external magnetic field strength experienced by the quarks. This degeneracy enables the π_u^0 and π_d^0 to be considered as magnetic field offset analogues of each other. The π^0 interpolating operator of Eq. (7.3) contains both the connected portion of the neutral pion correlator as shown in Figure 3.5a and the disconnected loops of Figure 3.5b. As the flavour-diagonal and flavour-crossed quark-disconnected loop contributions combine with relative signs, we focus on the connected contributions.

The same source smearings used in Chapter 6 are used here. In this way, QCD excited state effects are minimised. The $SU(3) \times U(1)$ eigenmode projection technique introduced in the previous chapter is used to provide a representation of quark level Landau effects. This is particularly necessary for the neutral pion as no hadronic level Landau wavefunction projection is appropriate. Such a hadronic projection is used for the π^+, where in accordance with Figure 6.6, only the first of the degenerate eigenmodes is used. The combination of these techniques, where appropriate, enable the formation of the energy shift plateaus crucial for extraction of the magnetic polarisability.

7.2. Magnetic polarisability

The formalism and techniques of Section 5.3.3 are used to obtain the magnetic polarisability from the two-point correlation functions discussed above. Results and fits are reported for both the charged and the neutral (π_d^0) pion.

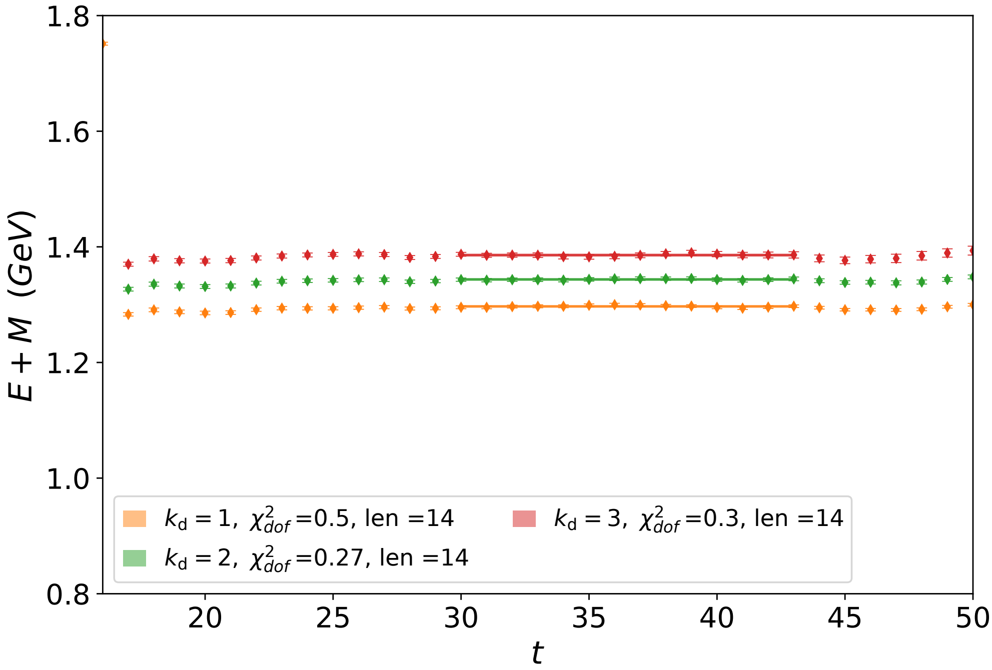

Figure 7.1. Charged pion effective energy shift $(E\,(B) + m_{\pi^+})$ from Eq. (5.24) on the $m_\pi =$ 702 MeV ensemble. The shaded regions illustrate the fit window selected. The three smallest field strengths are illustrated.

Recalling the relativistic form of the energy-field relation of Eq. (3.100), we consider the relativistic energy shift

$$E^2\,(B) = (E\,(B) + m_{\pi^+})\;(E\,(B) - m_{\pi^+}) = |qe\,B| - 4\,\pi\,m_\pi\,\beta_{\pi^+}\;|e\,B|^2 + \mathcal{O}\left(B^3\right), \quad (7.4)$$

where the lowest lying Landau level assumption has been made.

7.2.1. Charged pion

The charged pion takes advantage of the superior energy eigenstate isolation offered by the hadronic Landau eigenmode projection. This enables the long energy shift plateaus visible in Figures 7.1 through 7.8. It is particularly significant that it is possible to fit plateaus to the $(E\,(B) + m_{\pi^+})$ energy shift of Figure 7.7. This is the lightest mass considered, and the $(E\,(B) + m_{\pi^+})$ energy shift of Eq. (5.27) compounds correlated QCD fluctuations between the zero and non-zero magnetic field strength correlation functions.

The full range of $(E\,(B) + m_{\pi^+})$ and $(E\,(B) - m_{\pi^+})$ energy shift fits are presented here in order to showcase the effectiveness of the $SU(3) \times U(1)$ quark level eigenmode

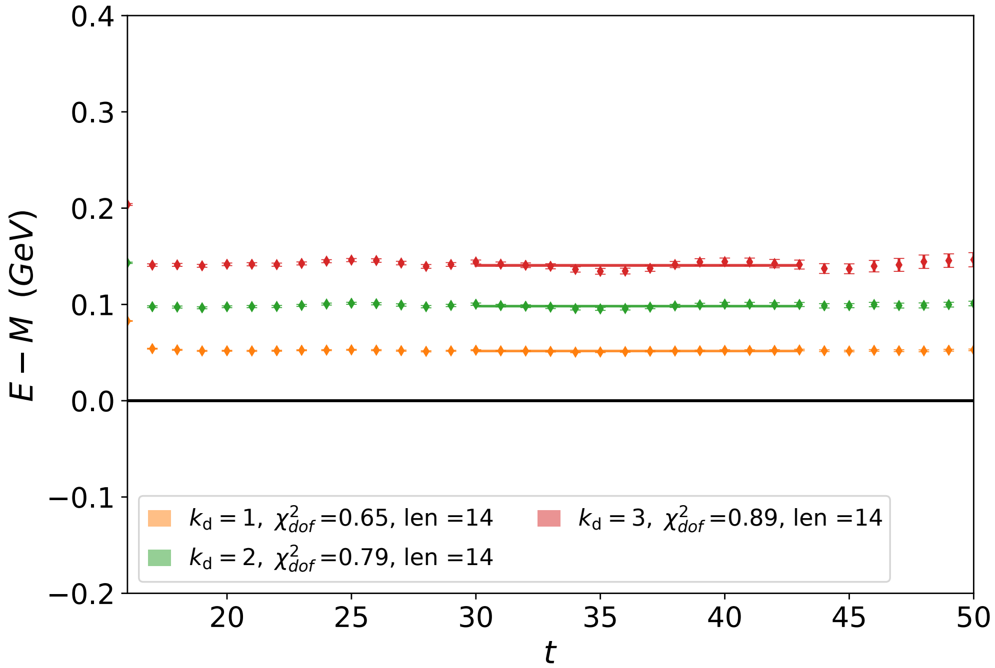

Figure 7.2. Charged pion effective energy shift $(E(B) - m_{\pi^+})$ from Eq. (5.25) on the $m_\pi =$ 702 MeV ensemble. The shaded regions illustrate the fit window selected. The three smallest field strengths are illustrated.

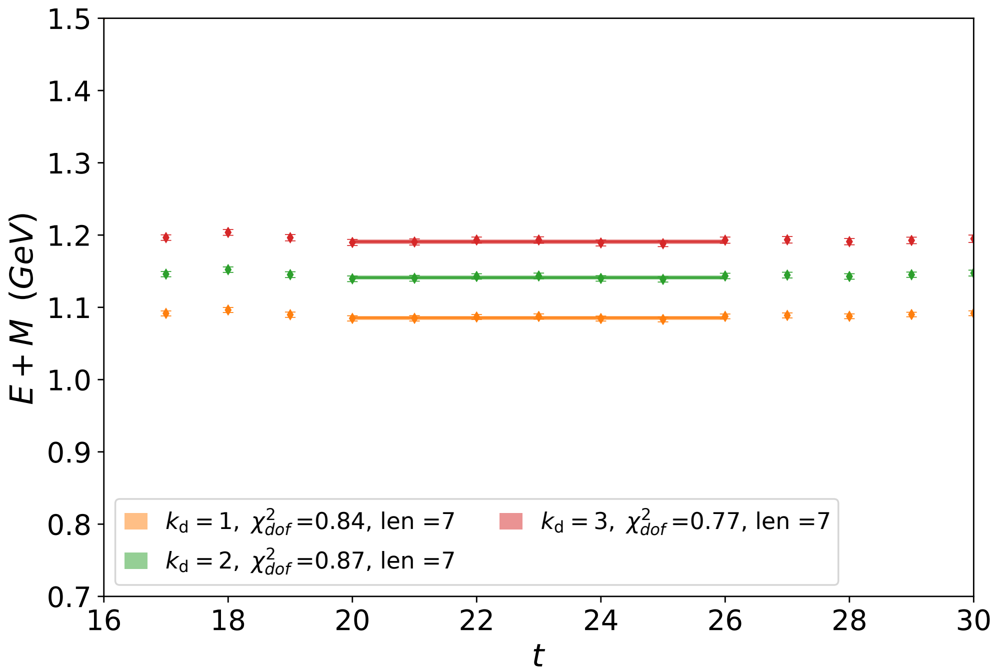

Figure 7.3. Charged pion effective energy shift $(E(B) + m_{\pi^+})$ on the $m_\pi = 570$ MeV ensemble. Details are as in the caption of Figure 7.1.

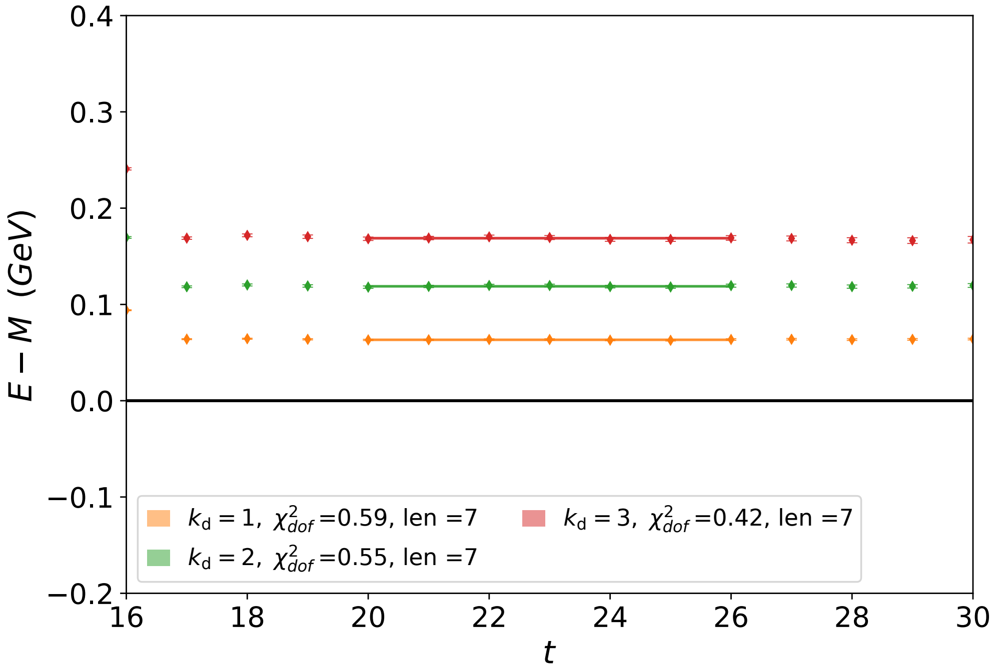

Figure 7.4. Charged pion effective energy shift $(E(B) - m_{\pi^+})$ on the $m_\pi = 570$ MeV ensemble. Details are as in the caption of Figure 7.2.

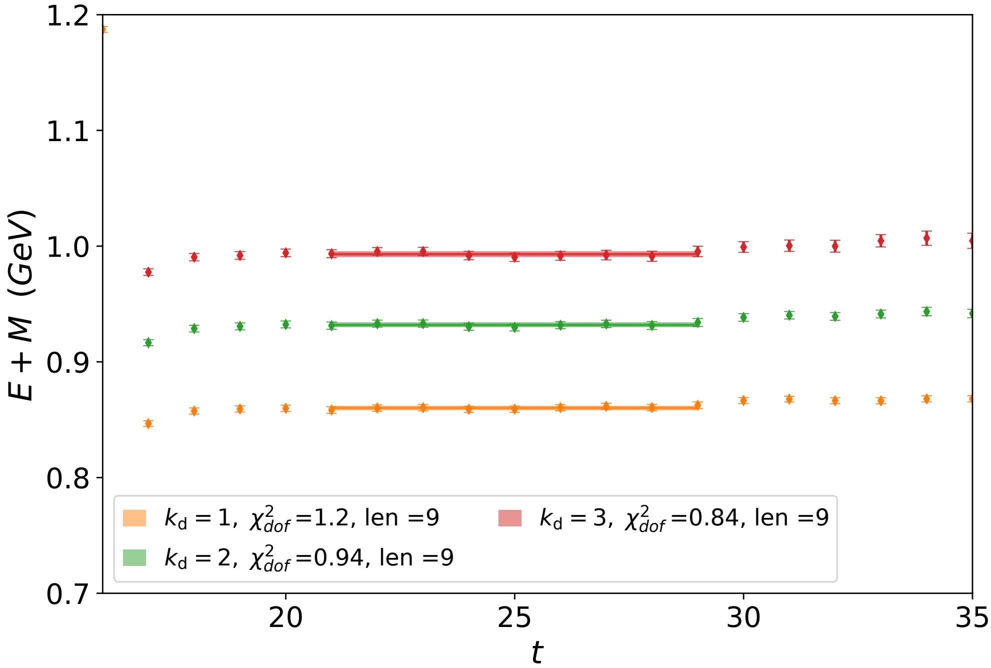

Figure 7.5. Charged pion effective energy shift $(E(B) + m_{\pi^+})$ on the $m_\pi = 411$ MeV ensemble. Details are as in the caption of Figure 7.1.

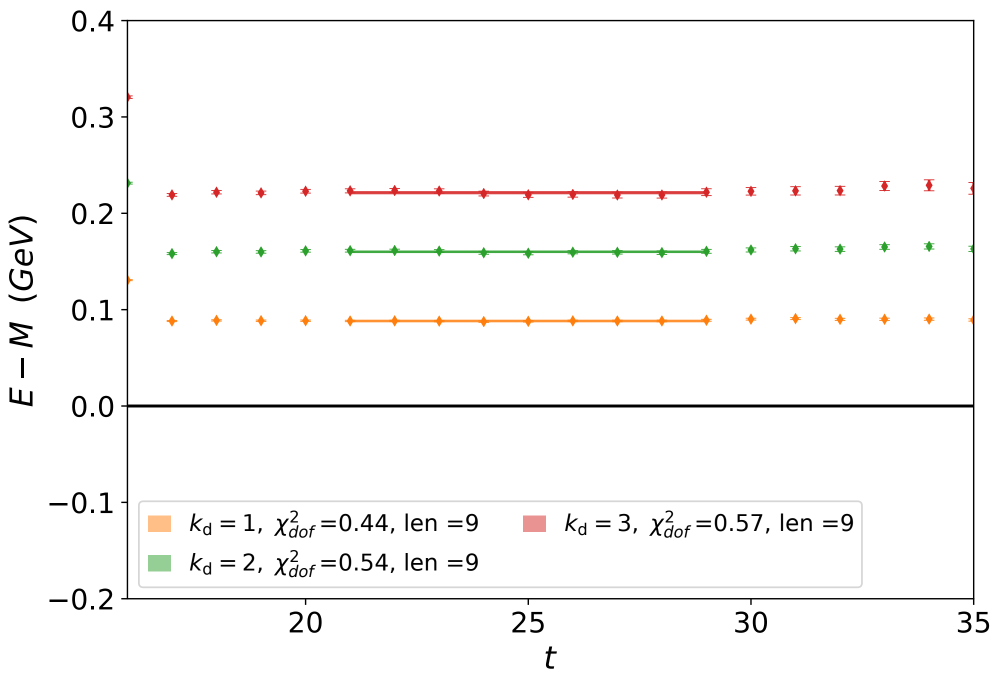

Figure 7.6. Charged pion effective energy shift $(E(B) - m_{\pi^+})$ on the $m_\pi = 411$ MeV ensemble. Details are as in the caption of Figure 7.2.

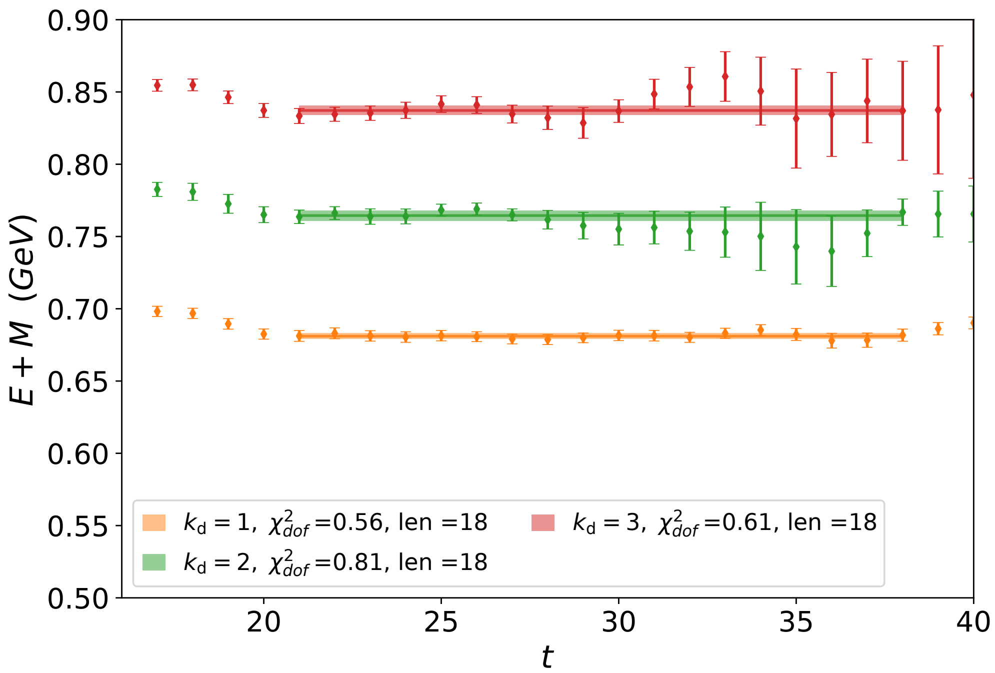

Figure 7.7. Charged pion effective energy shift $(E(B) + m_{\pi^+})$ on the $m_\pi = 296$ MeV ensemble. Details are as in the caption of Figure 7.1.

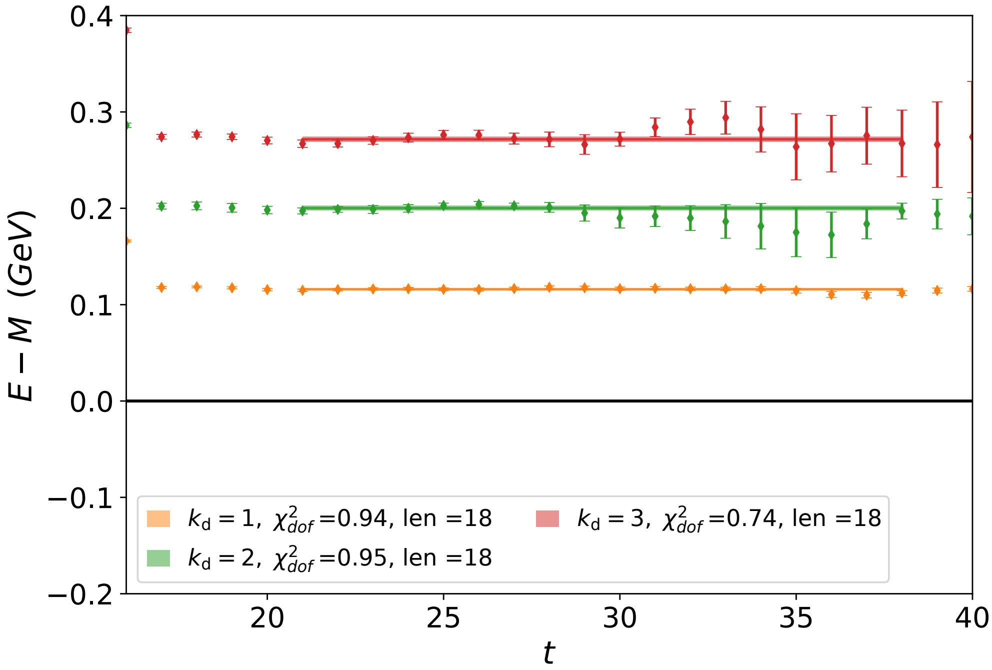

Figure 7.8. Charged pion effective energy shift $(E(B) - m_{\pi^+})$ on the $m_\pi = 296$ MeV ensemble. Details are as in the caption of Figure 7.2.

projection technique when combined with a hadronic Landau wavefunction projection. The isolation present in the energy shifts is a result of the detailed projection treatment of the effects of the background field at the quark level. These results represent a substantial improvement in our ability to fit constant Euclidean time plateau fits to these energy shifts.

The fit performed to the π^+ energy of Eq. (7.4) as a function of field strength could take the from

$$E^2(k_d) - m^2 = c_1\,k_d + c_2\,k_d^2, \tag{7.5}$$

where c_1 and c_2 are fit coefficients with units matching those of $E^2(B)$ as k_d is the unit-less minimal field quanta of Eq. (3.99). In the same manner as the proton and Σ^+ fits considered last chapter, this fit would allow the charge of the π^+ to differ from one. As such the $q = 1$ constrained energy shift is considered

$$E^2(B) - m^2 - |qe\,B| = -4\,\pi\,m_\pi\,\beta_\pi\,|e\,B|^2 + \mathcal{O}\left(B^3\right), \tag{7.6}$$

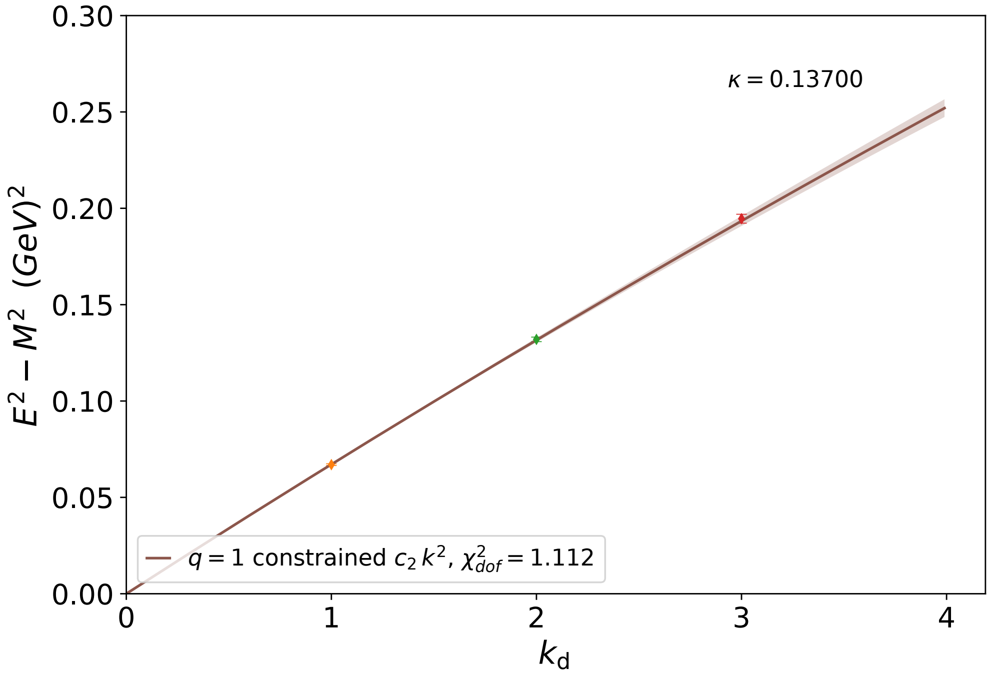

Figure 7.9. Constrained quadratic fit to the $m_\pi = 702$ MeV $\left(E^2\,(B) - m^2_{\pi^+}\right)$ energy shift formed from Figures 7.1 and 7.2. The shaded region indicates the $1\,\sigma$ statistical uncertainty through the Jackknife method.

and the appropriate fit function is

$$E^2\,(k_d) - m^2 - |qe\,B| = c_2\,k_d^2. \tag{7.7}$$

This fit function is used for each of the four relativistic energy shifts formed from the energy shifts of Figures 7.1 through 7.8 and the resulting fits for each of the four masses considered are shown in Figures 7.9 through 7.12. Each of these fits describes the data well with a χ^2_{dof} beneath our limit of $\chi^2_{dof} \leq 1.2$ and close to one.

The resulting magnetic polarisability values are shown in Table 7.1. These values are not in agreement with the current experimental value of $\beta_{\pi^+} = -2.0 \pm 0.6 \pm 0.7 \times 10^{-4}$ fm^3 [3] (where the standard $\alpha_\pi = -\beta_\pi$ assumption has been made) but this is not unexpected. The lattice calculations are performed with the standard limitations of

- Heavier than physical pion (quark) mass,
- Finite volume,

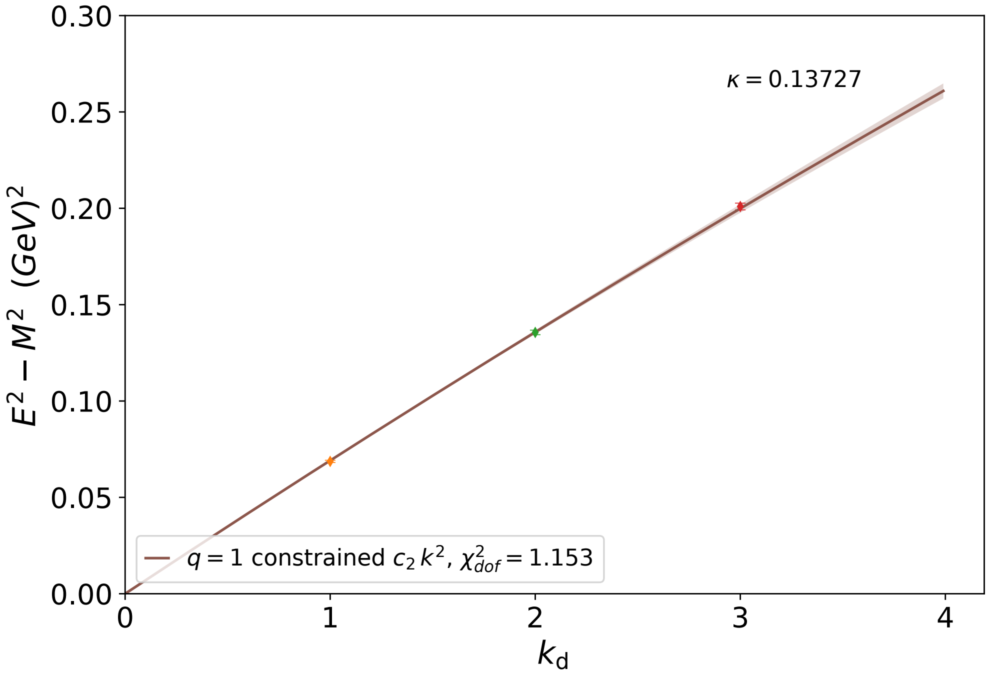

Figure 7.10. Constrained quadratic fit to the $m_\pi = 570$ MeV $\left(E^2\left(B\right) - m^2_{\pi+}\right)$ energy shift formed from Figures 7.3 and 7.4. Details as in Figure 7.9.

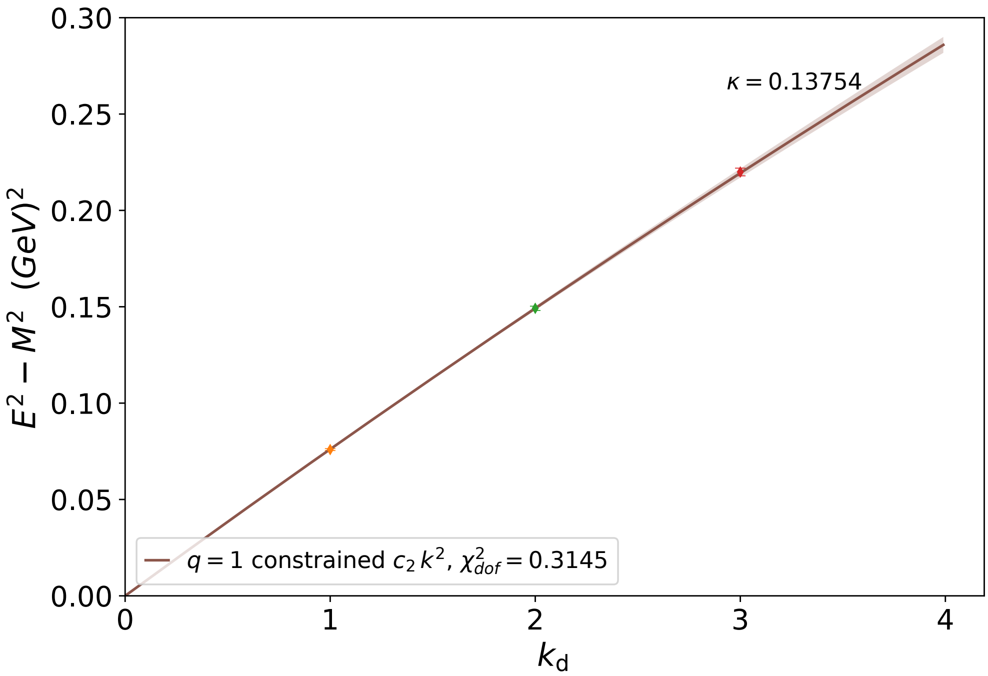

Figure 7.11. Constrained quadratic fit to the $m_\pi = 411$ MeV $\left(E^2\left(B\right) - m^2_{\pi+}\right)$ energy shift formed from Figures 7.5 and 7.6. Details as in Figure 7.9.

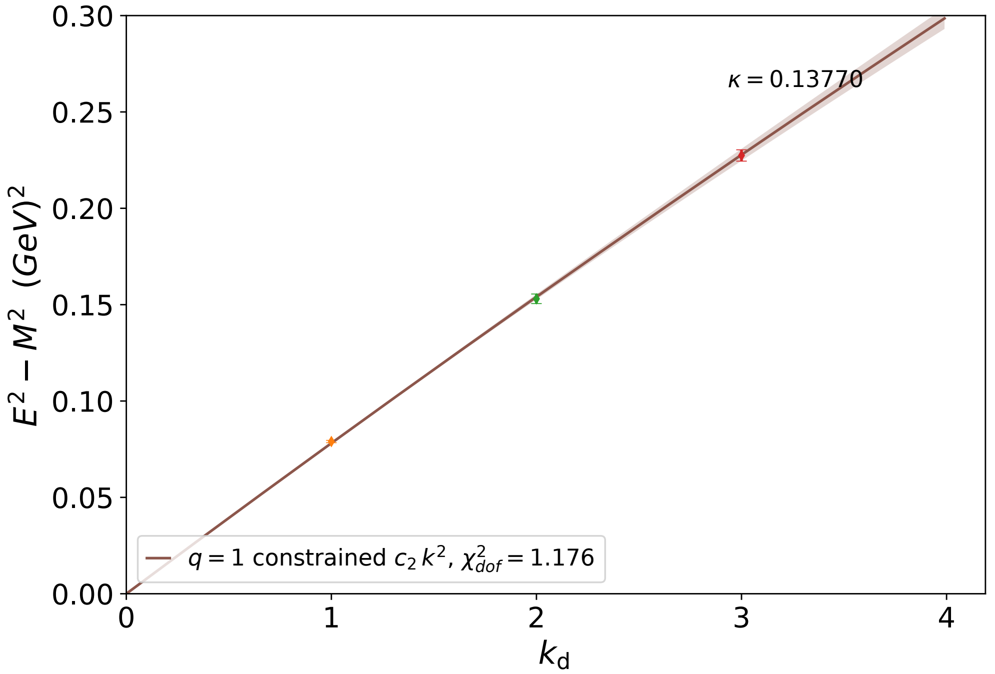

Figure 7.12. Constrained quadratic fit to the $m_\pi = 296$ MeV $E^2(B) - m^2_{\pi^+}$ energy shift formed from Figures 7.7 and 7.8. Details as in Figure 7.9.

Table 7.1. Magnetic polarisability values for the charged pion π^+ at each quark mass. The numbers in parentheses describe statistical uncertainties.

m_π (MeV)	κ_{ud}	β ($\times 10^{-4}$) fm^3
702	0.13700	0.255(56)
570	0.13727	0.275(54)
411	0.13754	0.355(62)
296	0.13770	0.35(11)

- Electro-quenching effects - the "sea" quarks do not experience the background magnetic field.

All of these may have a significant effect on the magnetic polarisability value. The chiral effective field theory calculations of Chapters 4 and 6 shown in Figures 4.14 and 6.42 for the neutron show a strong dependence of the magnetic polarisability on the volume considered. Previous lattice QCD calculations [200, 201] of the closely related electric polarisability have shown a potential sign crossing for α_{π^+} as a function of pion mass so the pion mass may also have a strong effect on the magnetic polarisability as we approach the physical regime. These results will serve as valuable input to a chiral effective field theory analysis incorporating finite-volume effects and accounting for sea-quark contributions.

7.2.2. Neutral pion

In considering the neutral pion in lattice QCD one usually focuses on the connected contribution of Figure 3.5a. The increased expense of computing the disconnected diagram of Figure 3.5b, combined with the cancellation of terms for the pion, make the disconnected contribution particularly challenging.

The magnetic polarisability of the neutral pion is difficult to extract experimentally [202] but the combination $(\alpha + \beta)_{\pi^0}$ has been extracted [197, 203] with reasonable success. The difference combination, $(\alpha - \beta)_{\pi^0}$ is more difficult. There also exists calculations in different theoretical models [164], with a two-loop chiral perturbation theory calculation being particularly notable [204].

Earlier lattice QCD simulations have been performed in order to investigate the magnetic polarisability of the neutral pion, β_{π^0} [110, 111]. These results use only the aforementioned connected diagrams and have only qualitative agreement with both the experimental results and the chiral perturbation theory results of Refs. [164] and [204].

We fit using the fit process and method of Section 5.3.3 where here the fit function is

$$E^2\left(k_d\right) - m^2 = c_2\, k_d^2, \tag{7.8}$$

requiring the $\left(E\left(B\right) + m_{\pi^0}\right)$ and $\left(E\left(B\right) - m_{\pi^0}\right)$ energy shifts.

The $\left(E\left(k_d = 3\right) + m_{\pi^0}\right)$ energy shift for the largest field strength considered is too noisy to accurately fit on each of the four ensembles considered. As such only the two lowest field strengths are used when extracting the magnetic polarisability for the neutral pion. These energy shifts are displayed in Figures 7.13 through 7.20 where it obvious that the $\left(E\left(B\right) + m_{\pi^0}\right)$ energy shift is substantially harder to determine than $\left(E\left(B\right) - m_{\pi^0}\right)$. This is due to the compounding rather than cancellation of correlated QCD fluctuations in the ratios of Eqs. (5.24) and (5.25). This is particularly obvious in Figure 7.19 which is the lightest mass ensemble considered.

It is possible to fit a single quadratic to the B dependence of the $E^2\left(B\right) - m^2_{\pi^0_d}$ energy shift on each of the four ensembles considered. The success of the quadratic only fit for

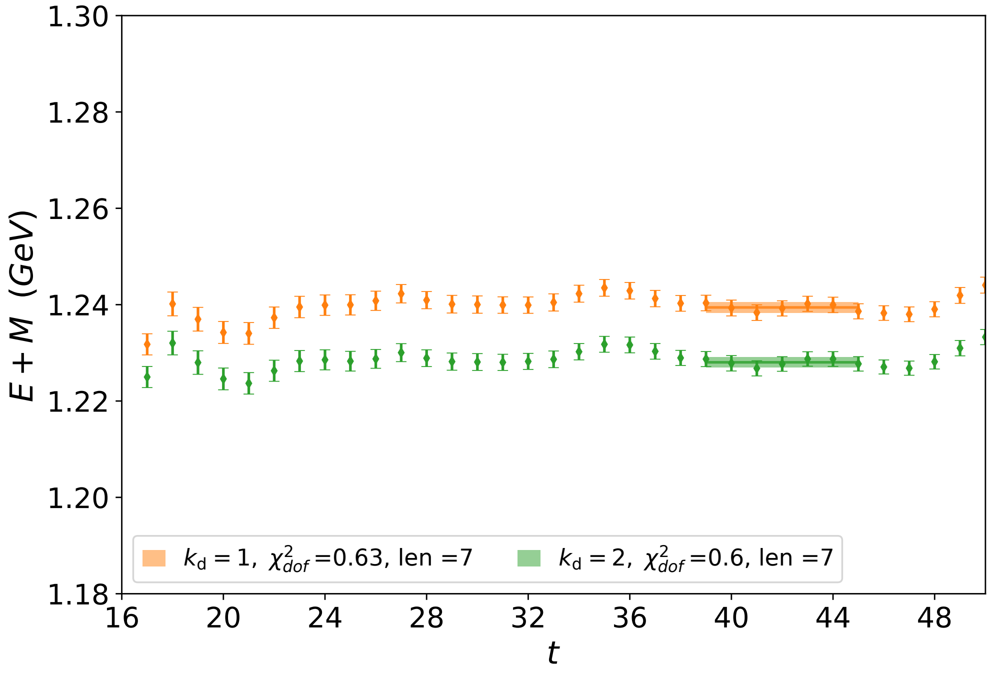

Figure 7.13. Neutral pion effective energy shift $\left(E\,(B) + m_{\pi^0_d}\right)$ on the $m_\pi = 702$ MeV ensemble. Details are as in the caption of Figure 7.1.

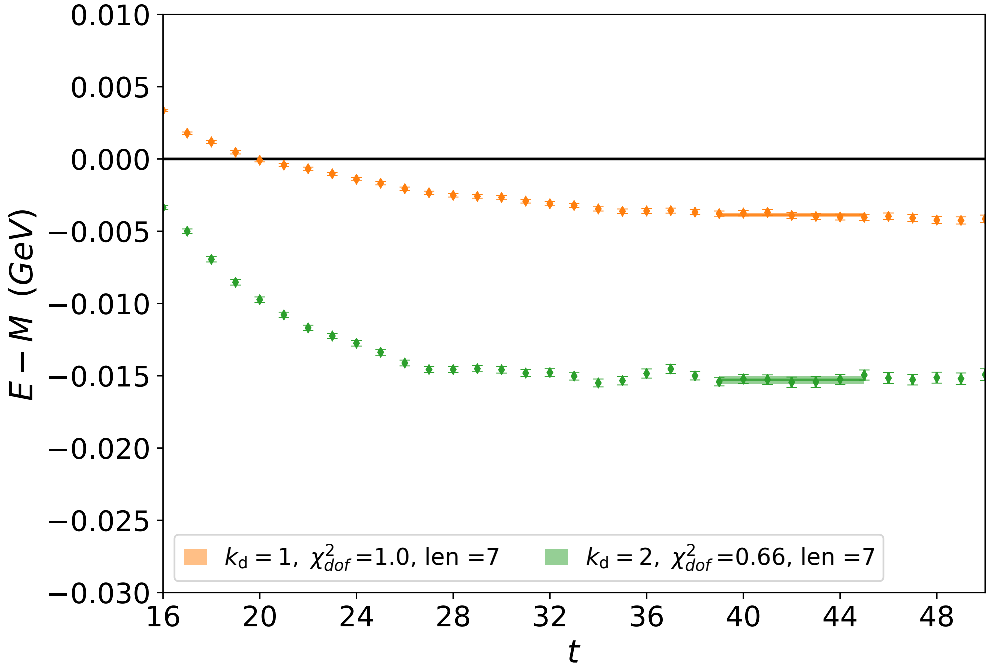

Figure 7.14. Neutral pion effective energy shift $\left(E\,(B) - m_{\pi^0_d}\right)$ on the $m_\pi = 702$ MeV ensemble. Details are as in the caption of Figure 7.2.

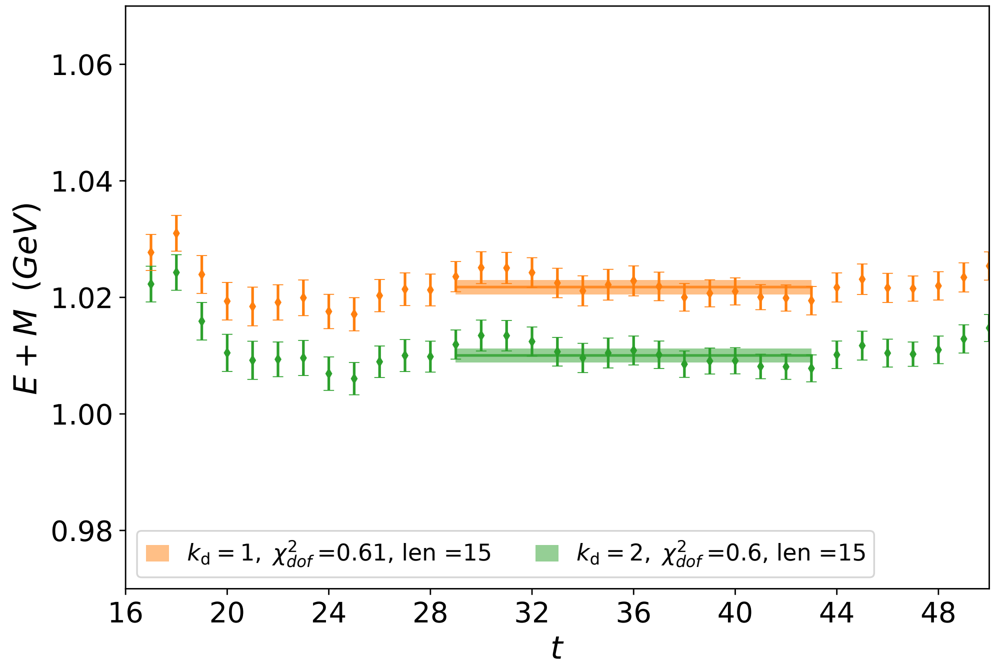

Figure 7.15. Neutral pion effective energy shift $\left(E\left(B\right)+m_{\pi_d^0}\right)$ on the $m_\pi = 570$ MeV ensemble. Details are as in the caption of Figure 7.1.

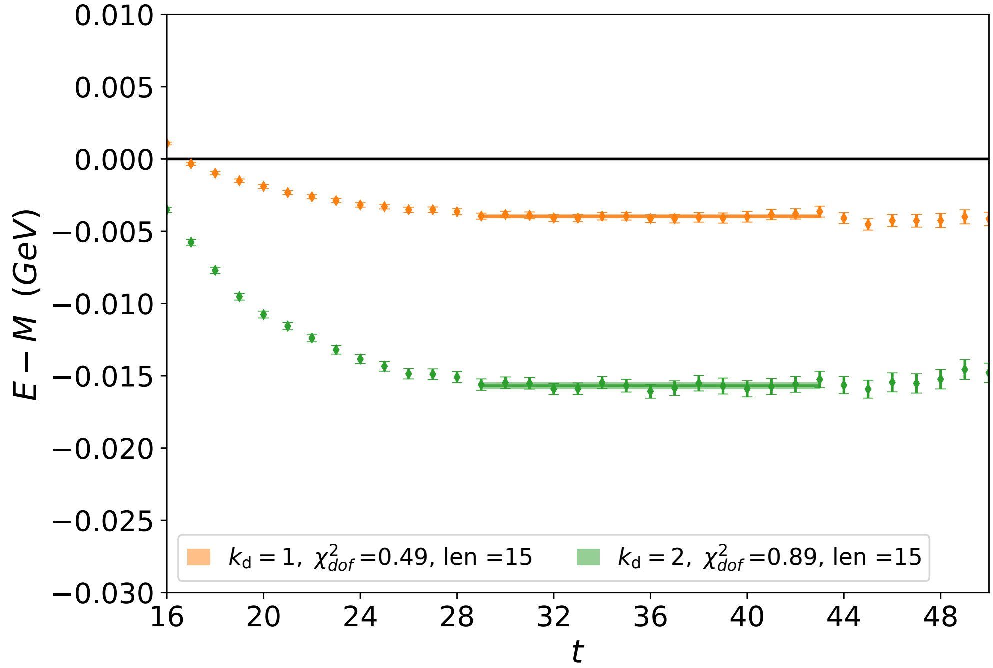

Figure 7.16. Neutral pion effective energy shift $\left(E\left(B\right)-m_{\pi_d^0}\right)$ on the $m_\pi = 570$ MeV ensemble. Details are as in the caption of Figure 7.2.

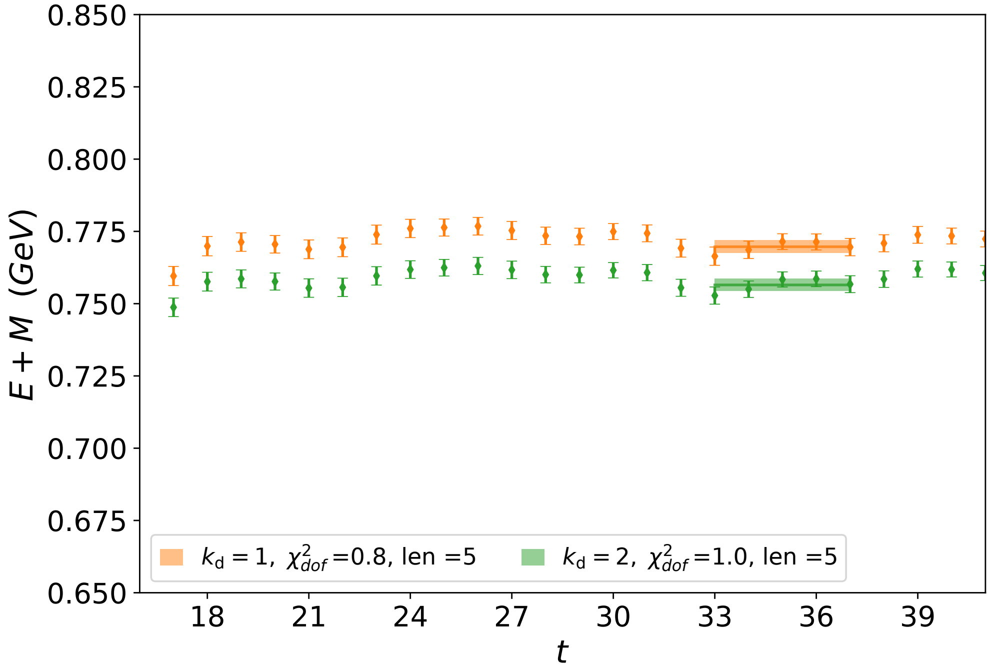

Figure 7.17. Neutral pion effective energy shift $\left(E(B) + m_{\pi^0_d}\right)$ on the $m_\pi = 411$ MeV ensemble. Details are as in the caption of Figure 7.1.

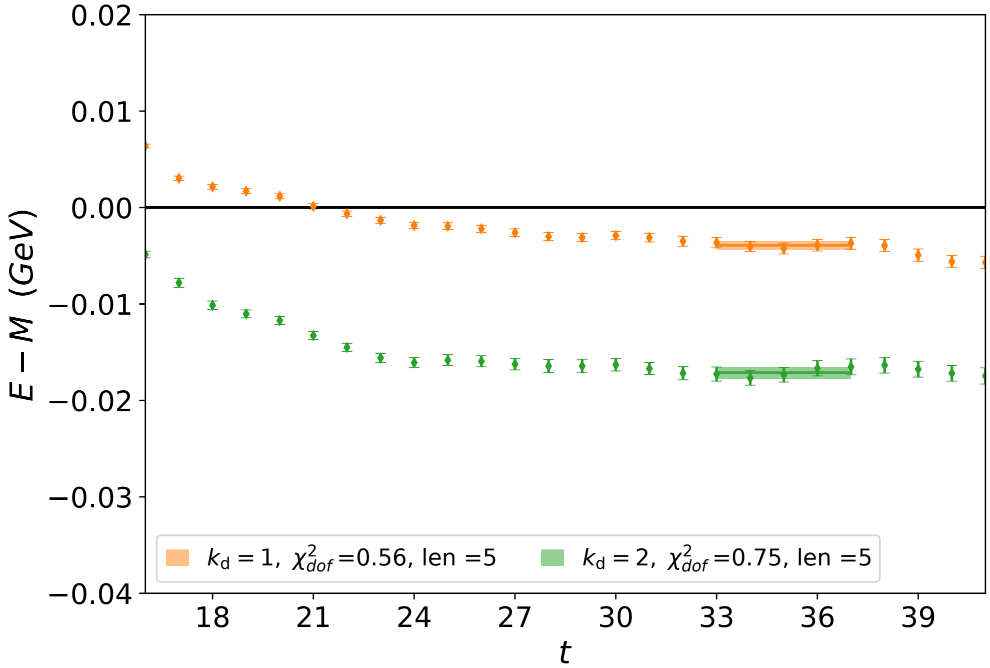

Figure 7.18. Neutral pion effective energy shift $\left(E(B) - m_{\pi^0_d}\right)$ on the $m_\pi = 411$ MeV ensemble. Details are as in the caption of Figure 7.2.

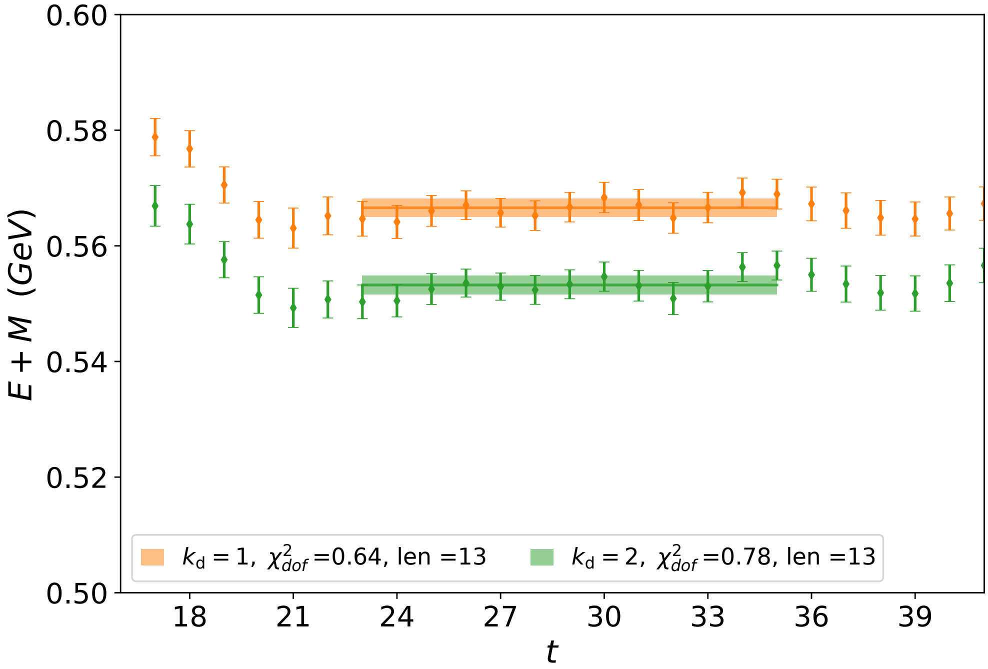

Figure 7.19. Neutral pion effective energy shift $\left(E\left(B\right)+m_{\pi_d^0}\right)$ on the $m_\pi = 296$ MeV ensemble. Details are as in the caption of Figure 7.1.

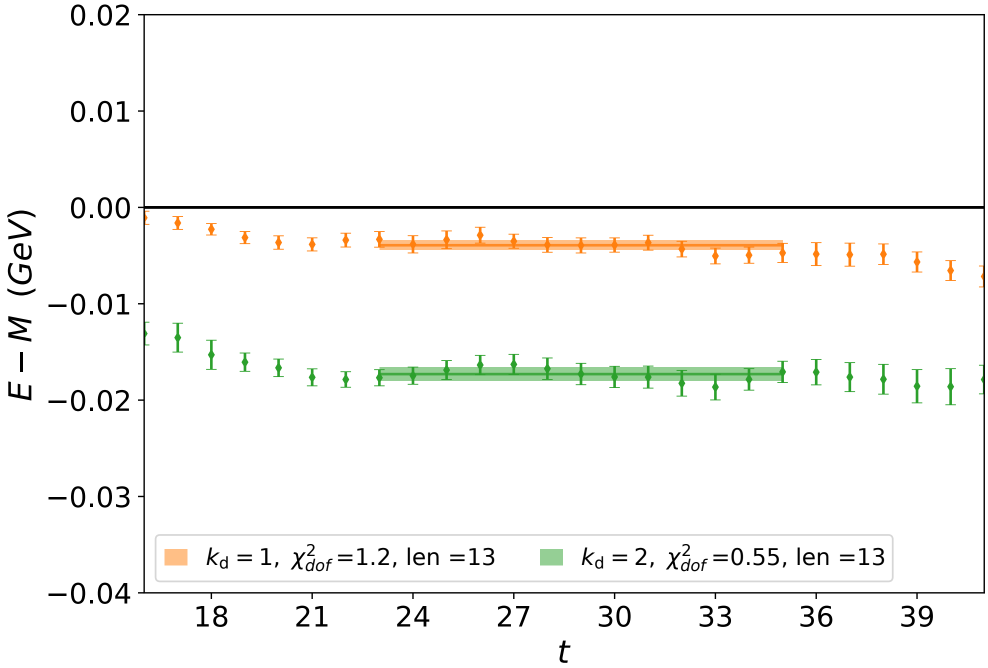

Figure 7.20. Neutral pion effective energy shift $\left(E\left(B\right)-m_{\pi_d^0}\right)$ on the $m_\pi = 296$ MeV ensemble. Details are as in the caption of Figure 7.2.

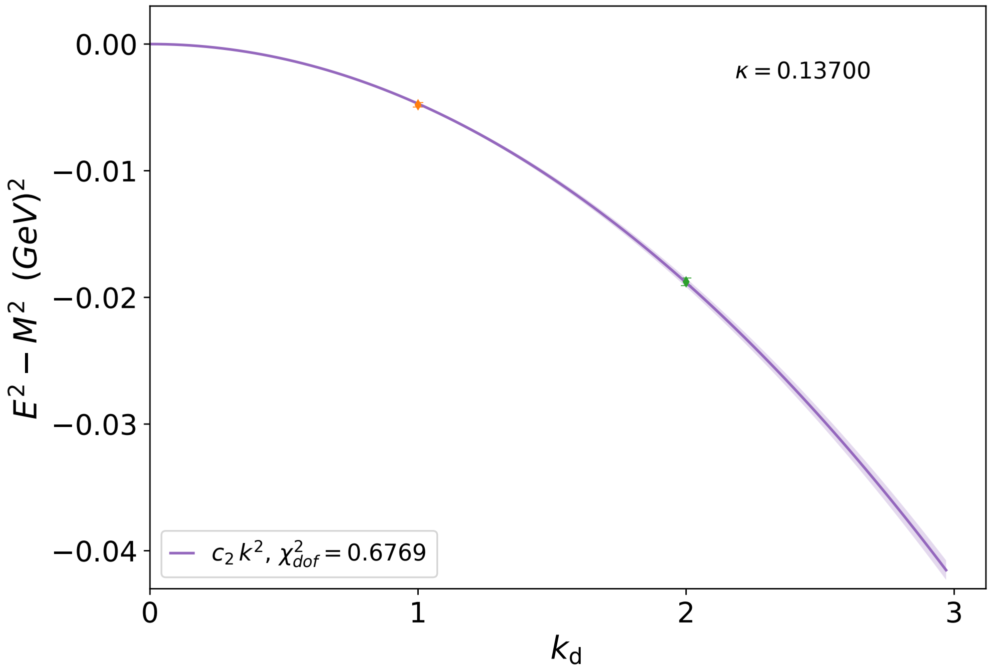

Figure 7.21. Quadratic only fit to the π_d^0 $m_\pi = 702$ MeV $\left(E^2\,(B) - m^2_{\pi_d^0}\right)$ energy shift formed from Figures 7.13 and 7.14. Details as in Figure 7.9.

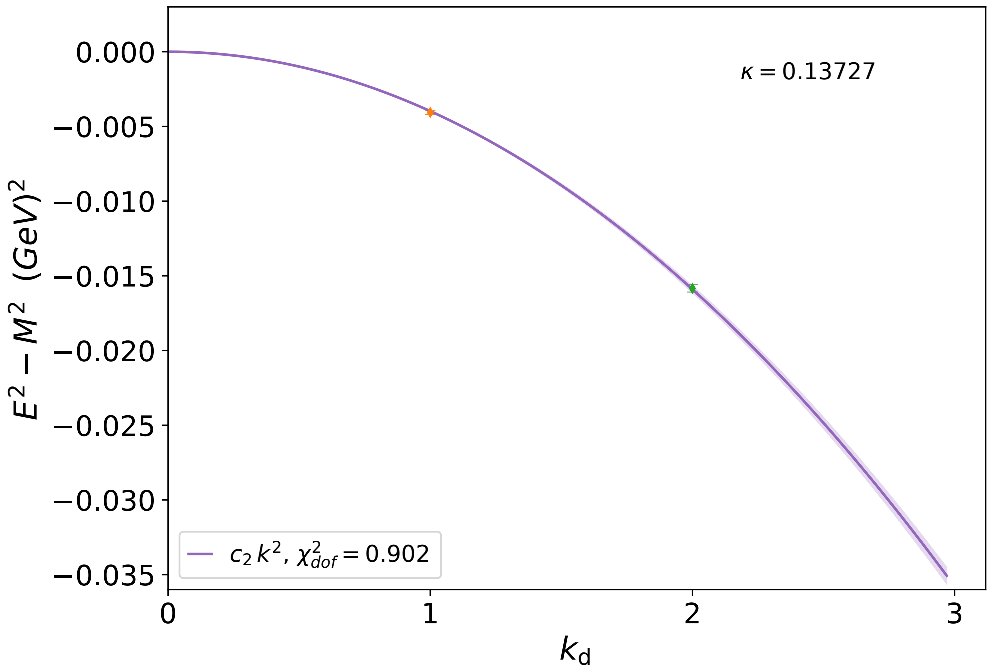

Figure 7.22. Quadratic only fit to the π_d^0 $m_\pi = 570$ MeV $\left(E^2\,(B) - m^2_{\pi_d^0}\right)$ energy shift formed from Figures 7.15 and 7.16. Details as in Figure 7.9.

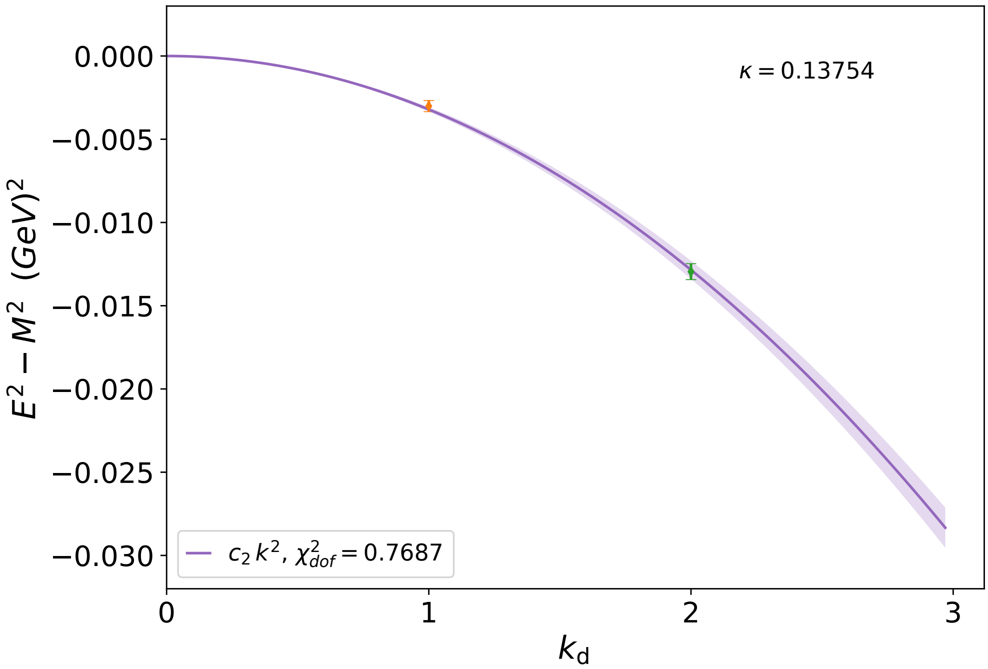

Figure 7.23. Quadratic only fit to the π^0_d $m_\pi = 411$ MeV $\left(E^2\,(B) - m^2_{\pi^0_d}\right)$ energy shift formed from Figures 7.17 and 7.18. Details as in Figure 7.9.

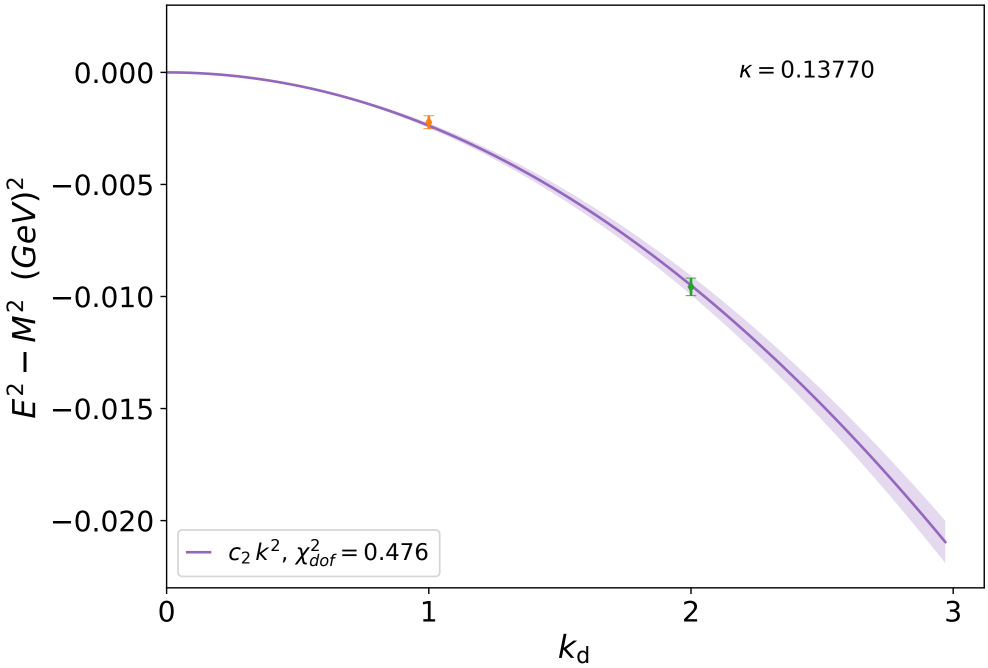

Figure 7.24. Quadratic only fit to the π^0_d $m_\pi = 296$ MeV $\left(E^2\,(B) - m^2_{\pi^0_d}\right)$ energy shift formed from Figures 7.19 and 7.20. Details as in Figure 7.9.

Table 7.2. Magnetic polarisability values for the neutral pion π^0 at each quark mass. The numbers in parentheses describe statistical uncertainties.

m_π (MeV)	κ_{ud}	$\beta^{\pi^0_d}$ ($\times 10^{-4}$) fm^3	β^{π^0} ($\times 10^{-4}$) fm^3
702	0.13700	0.900(17)	2.25(5)
570	0.13727	0.872(16)	2.18(4)
411	0.13754	0.766(33)	1.92(9)
296	0.13770	0.754(35)	1.89(9)

these highly precise pion correlation function energy shifts suggests that higher order contributions in B are negligible. Each of the fits in Figures 7.21 through 7.24 fit the data well,and have good χ^2_{dof} values. These χ^2_{dof} values are less than our limit of 1.2 and are also substantially larger than zero.

The magnetic polarisability is extracted from the quadratic fit coefficient using the relation of Eq. (5.32). The resulting magnetic polarisability values are reported in Table 7.2 in their physical units of $\times 10^{-4}$ fm^3. Although these results are from the $\overline{d}d$ pion correlation, we can relate these results to the full neutral pion correlator as the $\overline{u}u$ pion is simply the $\overline{d}d$ pion in a field of twice the magnitude,

$$E^2_{\pi^0_u}(B/2) = E^2_{\pi^0_d}(B) \tag{7.9}$$

Considering the $\overline{d}d$ and $\overline{u}u$ relativistic energy shifts

$$E^2_{\pi^0_d}(B) - m^2_{\pi^0} = -4\,\pi\, m_\pi\, \beta_{\pi^0_d}\, |B|^2 + \mathcal{O}\left(B^3\right), \tag{7.10}$$

and

$$E^2_{\pi^0_u}(B) - m^2_{\pi^0} = -4\,\pi\, m_\pi\, \beta_{\pi^0_u}\, |B|^2 + \mathcal{O}\left(B^3\right), \tag{7.11}$$

where we have allowed the $\overline{u}u$ and $\overline{d}d$ pions to have differing magnetic polarisabilities allows us to write

$$\begin{aligned} E^2_{\pi^0_u}\left(\frac{B}{2}\right) - m^2_{\pi^0} &= -4\,\pi\, m_\pi\, \beta_{\pi^0_u}\left|\frac{B}{2}\right|^2 + \mathcal{O}\left(B^3\right) \\ &= -4\,\pi\, m_\pi\, \beta_{\pi^0_u}\,\frac{1}{4}\,|B|^2 + \mathcal{O}\left(B^3\right) \end{aligned} \tag{7.12}$$

Hence

$$E^2_{\pi^0_d}(B) - m^2_{\pi^0} = -4\,\pi\,m_\pi\,\beta_{\pi^0_d}\,|B|^2 + \mathcal{O}\left(B^3\right)$$
$$= -4\,\pi\,m_\pi\,\beta_{\pi^0_u}\,\frac{1}{4}\,|B|^2 + \mathcal{O}\left(B^3\right), \qquad (7.13)$$

where we have used Eqs. (7.9) and (7.12). Thus

$$\frac{1}{4}\,\beta_{\pi^0_u} = \beta_{\pi^0_d}$$
$$\implies \beta_{\pi^0_u} = 4\,\beta_{\pi^0_d}. \qquad (7.14)$$

The magnetic polarisability of the full neutral pion is then the average of the $\overline{u}u$ and $\overline{d}d$ polarisabilities

$$\beta_{\pi^0} = \frac{1}{2}\,\left(\beta_{\pi^0_d} + \beta_{\pi^0_u}\right)$$
$$= \frac{1}{2}\,\left(\beta_{\pi^0_d} + 4\,\beta_{\pi^0_d}\right) = \frac{5}{2}\,\beta_{\pi^0_d}. \qquad (7.15)$$

This value is also reported in Table 7.2.

There is only a small amount of variation in the resulting magnetic polarisability values as a function of pion mass. This is in contrast to the neutron. The $\beta_{\pi^0_d}$ sit in between the one-loop and two-loop results of Ref. [164]. The full neutral pion results, using Eq. (7.15) are in good agreement with a number of the theoretical and experimental approaches [202]. However it must be noted that we consider only the connected parts of the neutral pion correlator here.

It is interesting that the π^0_d magnetic polarisability values in Chapter 5 do not agree at the $1\,\sigma$ level with the values found in this chapter on the same ensembles. This is because the results in Chapter 5 used a point sink rather than the $SU(3) \times U(1)$ eigenmode projected sink used in this chapter which better captures the physics associated with an external magnetic field. The plateau isolation using the eigenmode projected sink is much better than that using a point sink.

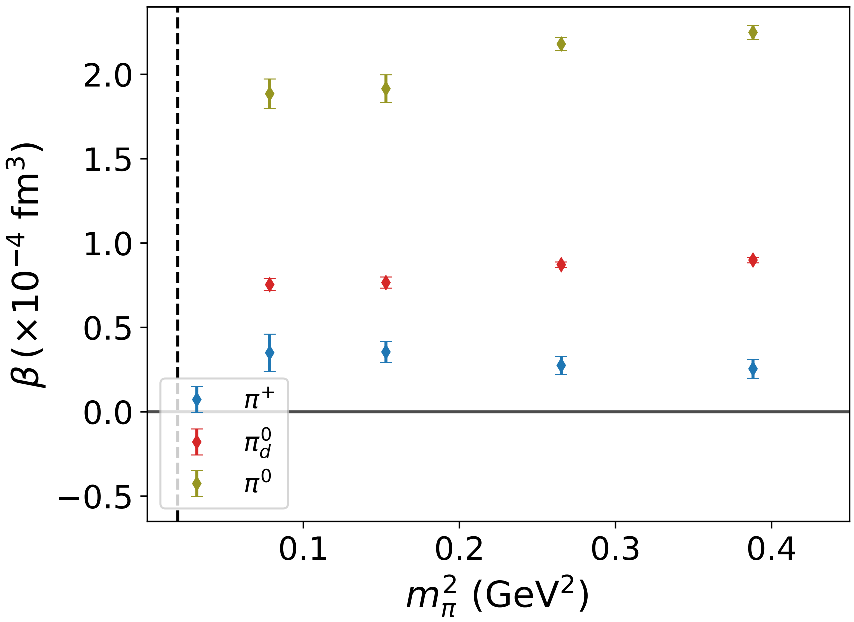

Figure 7.25. Magnetic polarisability of the pion as a function of m_π^2.

7.3. Summary

The neutral and charged pion magnetic polarisabilities have been calculated using lattice QCD. These calculations are the first systematic study of pion magnetic polarisabilities across a range of pion masses which used a fermion action free of contaminating magnetic-field dependent mass-renormalisation effects. This fundamental step forward in our understanding of this important property is made possible by the use of the $SU(3) \times U(1)$ eigenmode quark-projection technique, Landau-wavefunction hadronic-projection technique and the background-field-corrected clover fermion action. A comparison between the charged π^+, neutral pion π^0_d and neutral pion π^0 results is presented in Figure 7.25 as a function of pion mass where the precision granted by the $SU(3) \times U(1)$ eigenmode projection technique and pion correlation functions is clear.

The charged pion magnetic polarisability differs quite substantially from its physical value of $\beta^{\mathrm{phys}}{}_{\pi^+} = -2.0 \mp 0.6 \mp 0.7 \times 10^{-4}\ \mathrm{fm}^3$ (derived under the standard assumption that $\alpha_{\pi^+} + \beta_{\pi^+} = 0$) [3]. Existing chiral perturbation theory work [165] is not straightforwardly applicable to the results considered herein [179, 205] necessitating the development of improved chiral effective field theory methods. To connect the results herein to experiment, one could formulate chiral effective-field theory in a finite-volume to determine the finite-volume corrections. Similarly, corrections due to the electroquenched nature of our calculation can be addressed using the methods of partially quenched chiral effective field theory.

Further investigation using lattice QCD could focus on doing the full neutral pion correlator

$$\chi_{\pi^0} = \frac{1}{\sqrt{2}} \left(\overline{u}\,(x)\ \gamma_5\, u\,(x) - \overline{d}\,(x)\ \gamma_5\, d\,(x)\right), \tag{7.16}$$

including the disconnected loop of Figure 3.5b. The full correlation function requires the x to x loop propagator. The standard method to calculate this is the same as for all-to-all propagators, via stochastic estimation of inverse matrix elements. An introductory discussion can be found in Refs. [170] and [171] and an application in Ref. [206].

Similarly the background field could be extended to the "sea" quarks of the simulation at gauge field generation time. This requires a separate set of gauge fields for each field strength and as such is prohibitively expensive as correlations are lost.

Chapter 8.

Conclusions & Future Work

This thesis presents details of work performed to calculate the magnetic polarisabilities of hadrons using numerical simulations of lattice Quantum Chromodynamics (QCD) with the background field method. In Chapter 2, the basic properties of octet mesons and baryons and the decuplet baryons are touched upon and the path integral approach to QCD considered.

Chapter 3 details the methodology for lattice QCD calculations of observables. The lattice spacing and finite-volume are responsible for unphysical lattice artefacts which are controlled using a variety of improved methods. The methods used herein are discussed in detail ahead of their implementation in Chapter 5.

The magnetic polarisability of the neutron is calculated in Chapter 4. We demonstrate how the inclusion of Landau level physics at the quark level through the $U(1)$ Landau-eigenmode quark-propagator-projection technique enables the production of the effective energy shifts required to calculate the magnetic polarisability. These effective energy shifts plateau early and are easily fit. Higher order contributions in the energy-field relation were taken into account when fitting the effective energy shifts as a function of external magnetic-field strength and found to be negligible in comparison to existing statistical uncertainties. A chiral effective field theory analysis, incorporating finite-volume and sea-quark-loop effects is used to predict the magnetic polarisability of the physical neutron to be $\beta^n = 2.05(25)(19) \times 10^{-3}$ fm^3 where the numbers in parantheses represent statistical and systematic errors respectively. This prediction is in agreement with a number of experimental measurements.

In Chapter 5, a field-dependent additive quark-mass renormalisation is examined. This lattice artefact is introduced when a background magnetic field is used with a fermion action containing the Wilson term. This problem is shown in the free-field limit. We then demonstrate how a tree-level clover term removes the additive mass renormalisation due to the Wilson term in this limit. In the transition to full QCD, the clover coefficient is renormalised away from the tree-level value. We show how this prevents the cancellation of the Wilson and clover field-dependent quark mass renormalisations. By separating the QCD and the analytically known background field contributions to the clover term, the field-dependent mass renormalisation due to the Wilson term is removed. Free of this issue, the magnetic polarisability of the neutral pion is investigated using a point sink and the relativistic magnetic-polarisability energy shift.

Inspired by the success of the $U(1)$ Landau eigenmode projection method, in Chapter 6, we consider the eigenmodes of the $SU(3) \times U(1)$ lattice Laplacian. These eigenmodes are used to project the quark propagator. Neutron, proton, Σ^+ and Ξ^0 effective energy shifts are calculated. The effective energy shifts for each of these baryons plateau, such that is possible to find constant Euclidean time fits. For the charged baryons, a lattice Landau-eigenmode projection is utilised at the hadronic level. This takes the place of the Fourier projection to definite momenta and is crucial in isolating the lowest-lying Landau level energy eigenstate of the baryon. From the determined energy shifts, fits as a function of field strength are performed and the magnetic polarisability of each of these baryons determined. The chiral effective field theory analysis of Chapter 4 is extended to account for the baryons considered herein and predictions of the magnetic polarisability of the neutron, proton, Σ^+ and Ξ^0 at the physical point are made. These predictions are the first calculations using lattice QCD and the background field method combined with an extrapolation which accounts for finite-volume effects and sea-quark-loop contributions. The hyperon magnetic polarisabilities in particular, serve to guide future experimental and theoretical efforts to understand the underlying dynamics.

Finally, we return to the pion. Using the techniques assembled in the preceding chapters, the magnetic polarisabilities of the charged and neutral pions are calculated. This calculation is the first systematic calculation using Wilson fermions free of magnetic-field dependent quark-mass renormalisation across a range of pion masses. This is a fundamental step forward in our understanding of pion polarisabilities which is made possible by the use of the $SU(3) \times U(1)$ quark-propagator projection technique. The energy eigenstate isolation present in the effective energy shifts required for the relativistic energy shift is directly due to the consideration of Landau physics at both the quark and the hadronic level. The neutral pion magnetic polarisability results presented herein agree well with chiral perturbation studies and both neutral and charged pion polarisabilities at all pion masses considered are provided to motivate future chiral extrapolations to the physical regime addressing finite-volume and sea-quark contributions.

Overall the calculations performed in this thesis have been successful. A unified method for isolating the lowest-lying energy eigenstate for both charged and neutral hadrons in a background magnetic field has been developed. This, along with the removal of the field-dependent additive-mass renormalisation due to the Wilson term has enabled the first systematic study of octet baryon and pion magnetic polarisabilities using lattice QCD across a range of pion masses. The range of pion masses enables a chiral effective field theory analysis to produce physical predictions for the magnetic polarisabilities of the neutron, proton, Σ^+ and Ξ^0.

In the future, we see a number of avenues for improvement and further development of these calculations. One such avenue is the inclusion of disconnected contributions in the neutral-pion correlation function; as the down and up quarks in an external magnetic field are no longer degenerate, these contributions have the potential to be substantial. The hyperon polarisability calculations hint at an environmental sensitivity of the magnetic polarisability contributions; this sensitivity could be further examined and understood by considering partially charged baryons. Here only the singly-represented or doubly-represented quarks would experience the external magnetic field rather than all three quarks. Simulations over a range of lattice volumes to fully account for finite-volume effects and calculations at lighter pion masses are also desirable. Research aimed at understanding the structure of hadronic excitations can also benefit from the techniques developed herein. Using an eigenmode projected quark propagator and the variational method one may be able to determine magnetic moments and polarisabilities of excited states.

Appendix A.

Gamma Matrices

Drawing from Ref. [15] a brief discussion of the Pauli, gamma and Gell-Mann matrices follows.

A.1. Pauli Matrices

The Pauli spin-matrices satisfy

$$\begin{aligned} \sigma_j \, \sigma_k = \delta_{j\,k} + i \, \epsilon_{j\,k\,l} \, \sigma_l, \\ \sigma_1 \, \sigma_2 \, \sigma_3 = i, \end{aligned}$$

for $j,\ k,\ l = 1, 2, 3$ and are

$$\sigma_1 = \begin{pmatrix} 0 & 1 \\ 1 & 0 \end{pmatrix}, \quad \sigma_2 = \begin{pmatrix} 0 & -i \\ i & 0 \end{pmatrix}, \quad \sigma_3 = \begin{pmatrix} 1 & 0 \\ 0 & -1 \end{pmatrix}. \tag{A.1}$$

The Pauli matrices are often written as $\vec{\sigma} = \sigma_{1,\,2,\,3}$.

A.2. Gamma Matrices

The gamma matrices satisfy the anti-commutator relation

$$\{\gamma_\mu,\ \gamma_\nu\} = 2\,\delta_{\mu\,\nu}. \tag{A.2}$$

A $2 \otimes 2$ block notation is usually used to represent the gamma matrices; here the gamma matrices in the Dirac representation are

$$\gamma^0 = \begin{pmatrix} \mathbb{I} & 0 \\ 0 & -\mathbb{I} \end{pmatrix}, \quad \vec{\gamma} = \begin{pmatrix} 0 & \vec{\sigma} \\ -\vec{\sigma} & 0 \end{pmatrix}. \tag{A.3}$$

The last gamma matrix, γ_5 is

$$\gamma_5 = i\,\gamma_1\,\gamma_2\,\gamma_3\,\gamma^0 = \gamma_5^\dagger = \begin{pmatrix} 0 & \mathbb{I} \\ \mathbb{I} & 0 \end{pmatrix} \tag{A.4}$$

In the Pauli representation, the gamma matrices are Hermitian

$$\gamma_4 = \begin{pmatrix} \mathbb{I} & 0 \\ 0 & -\mathbb{I} \end{pmatrix}, \quad \vec{\gamma} = \begin{pmatrix} 0 & -i\,\vec{\sigma} \\ i\,\vec{\sigma} & 0 \end{pmatrix}, \tag{A.5}$$

and γ_5 is

$$\gamma_5 = \gamma_1\,\gamma_2\,\gamma_3\,\gamma^0 = \gamma_5^\dagger = -\begin{pmatrix} 0 & \mathbb{I} \\ \mathbb{I} & 0 \end{pmatrix} \tag{A.6}$$

This is also known as the Sakurai representation of the gamma matrices [207] and is the form used in calculating the correlation functions of this thesis.

A.3. Gell-Mann matrices

The eight 3×3 Gell-Mann matrices are [9]

$$
\begin{aligned}
t_1 &= \begin{pmatrix} 0 & 1 & 0 \\ 1 & 0 & 0 \\ 0 & 0 & 0 \end{pmatrix} \quad t_2 = \begin{pmatrix} 0 & -1 & 0 \\ 1 & 0 & 0 \\ 0 & 0 & 0 \end{pmatrix} \quad t_3 = \begin{pmatrix} 1 & 0 & 0 \\ 0 & -1 & 0 \\ 0 & 0 & 0 \end{pmatrix} \\
t_4 &= \begin{pmatrix} 0 & 0 & 1 \\ 0 & 0 & 0 \\ 1 & 0 & 0 \end{pmatrix} \quad t_5 = \begin{pmatrix} 0 & 0 & -1 \\ 0 & 0 & 0 \\ 1 & 0 & 0 \end{pmatrix} \quad t_6 = \begin{pmatrix} 0 & 0 & 0 \\ 0 & 0 & 1 \\ 0 & 1 & 0 \end{pmatrix} \\
t_7 &= \begin{pmatrix} 0 & 0 & 0 \\ 0 & 0 & -1 \\ 0 & 1 & 0 \end{pmatrix} \quad t_8 = \begin{pmatrix} \frac{1}{\sqrt{3}} & 0 & 0 \\ 0 & \frac{1}{\sqrt{3}} & 0 \\ 0 & 0 & \frac{-2}{\sqrt{3}} \end{pmatrix}
\end{aligned} \tag{A.7}
$$

A.4. Useful Identities

A number of useful identities are presented.

$$
\not{a}\,\not{b} = a \cdot b - i\,\sigma^{\mu\nu}\,a^{\mu}\,b^{\nu} \tag{A.8}
$$

$$
\sigma^{\mu\nu} = -\sigma^{\nu\mu} \tag{A.9}
$$

The inverse of linear combinations of gamma matrices is $(a, b_\mu) \in \mathbb{R}$ is [11]

$$
\left(a\,\mathbb{I} + i \sum_{\mu=1}^{4} \gamma^{\mu}\,b_{\mu} \right)^{-1} = \frac{a\,\mathbb{I} - i\sum_{\mu=1}^{4} \gamma^{\mu}\,b_{\mu}}{a^2 + \sum_{\mu=1}^{4} b_{\mu}^2} \tag{A.10}
$$

Appendix B.

Lattice Appendix

B.1. Link variable gauge transformation

The gluon fields are represented by link variables which are parallel transport operators

$$U_\mu(x) = P\ \exp\left[-i\,g\int_x^{x+a\,\hat{\mu}} dz_\mu A_\mu(z)\right].$$

We now apply the gauge transformation property of A_μ of Eq. (2.9) to this to obtain

$$U_\mu(x) \stackrel{\Omega}{\to} P\ \exp\left[-i\,g\int_x^{x+a\,\hat{\mu}} \left(dz_\mu \Omega\,(z)\ A_\mu(z)\,\Omega^\dagger\,(z) + \frac{i}{g}\ (\partial_\mu\,\Omega\,(z))\ \Omega^\dagger\,(z)\right)\right]. \tag{B.1}$$

A path ordered exponential of a function $\mathfrak{a}(t)$ may be written

$$P\left[-\int_0^t dt'\mathfrak{a}(t')\right] = \lim_{N\to\infty}\left[\mathrm{e}^{\mathfrak{a}(t_1)\,\Delta\,t}\,\mathrm{e}^{\mathfrak{a}t_2\,\Delta\,t}\ \ldots\ \mathrm{e}^{\mathfrak{a}t_N\,\Delta\,t}\right], \tag{B.2}$$

where $t_1 = 0$, $t_N = t$ and $i = 1, \ldots, N$ such that the integral range is partitioned into equal slices of length $\Delta\,t = \frac{t_N - t_1}{N} = \frac{t}{N}$.

Also useful is the relation

$$\begin{aligned}
\exp\left[i\,g\,\Omega\,(x)\ A_\mu(x)\,\Omega^\dagger\,(x)\right] &= \sum_{k=0}^{\infty}\frac{\left(i\,g\,\Omega\,(x)\ A_\mu(x)\,\Omega^\dagger\,(x)\right)^k}{k!}\\
&= \sum_{k=0}^{\infty}\Omega\,(x)\ \frac{\left(i\,g\,A_\mu(x)\right)^k}{k!}\,\Omega^\dagger\,(x)\\
&= \Omega\,(x)\ \mathrm{e}^{i\,g\,A_\mu(x)}\,\Omega^\dagger\,(x)\,,
\end{aligned} \tag{B.3}$$

Now using Eqs. ($B.2$) and ($B.3$); Eq. ($B.1$) can be written

$$U_\mu(x) \xrightarrow{\Omega} \lim_{N\to\infty} \Omega\,(z_1)\; \mathrm{e}^{i\,g\,A_\mu(z_1)}\, \Omega^\dagger\,(z_1)\; \mathrm{e}^{(\partial_\mu\,\Omega(z_1))\,\Omega^\dagger(z_1)\,\Delta\,z}$$
$$\times\Omega\,(z_2)\; \mathrm{e}^{i\,g\,A_\mu(z_2)}\, \Omega^\dagger\,(z_2)\; \mathrm{e}^{(\partial_\mu\,\Omega(z_2))\,\Omega^\dagger(z_2)\,\Delta\,z} \times \ldots$$
$$\times\Omega\,(z_N)\; \mathrm{e}^{i\,g\,A_\mu(z_N)}\, \Omega^\dagger\,(z_N)\; \mathrm{e}^{(\partial_\mu\,\Omega(z_N))\,\Omega^\dagger(z_N)\,\Delta\,z} \tag{B.4}$$

where here $z_1 = x$ and $z_N = x + a\,\hat{\mu}$ for $\Delta\,z = \frac{a}{N}$.

We now use the definition of the parallel transport operator for $\exp\left[(\partial_\mu\,\Omega\,(z_i))\;\Omega^\dagger\,(z_i)\;\Delta\,z\right]$ over the path $\Delta\,z$

$$\Omega^\dagger\,(z_i)\;\mathrm{e}^{\left(\partial_\mu\,\Omega^\dagger(z_i)\right)\Omega^\dagger(z_i)\,\Delta\,z} = \Omega^\dagger\,(z_{i+1})\,,$$

which neatly eliminates all the internal gauge transformations in Eq. ($B.4$). This then reduces to

$$U_\mu(x) \xrightarrow{\Omega} \Omega\,(x)\;U_\mu(x)\,\Omega^\dagger\,(x + a\,\hat{\mu})\,, \tag{B.5}$$

which is the desired gauge transformation property of U_μ.

B.2. The plaquette

The plaquette has form

$$P_{\mu\nu}(x) = U_\mu(x)\,U_\nu(x + a\,\hat{\mu})\,U_\mu^\dagger(x + a\,\hat{\mu})\,U_\nu^\dagger(x). \tag{B.6}$$

Each of these terms can be written as, i.e.

$$U_\nu\,(x + a\,\hat{\mu}) = \exp\left(-i\,g\,a\;\,A_\nu\,(x + a\,\hat{\mu})\right), \tag{B.7}$$

and hence the Baker-Campbell-Hausdorff identity [208]

$$\exp(A)\exp(B) = \exp\left(A + B + \frac{1}{2}\,[A, B] + \cdots\right), \tag{B.8}$$

may be used. A and B are arbitrary matrices and the dots indicate higher powers of matrices which are omitted here. Applying Eq. ($B.8$) to Eq. ($B.6$) with the expansion of

Eq. ($B.7$) gives

$$
\begin{aligned}
P_{\mu\nu}(x) = \exp\Bigg(& -i\,g\,a\;A_\mu(x) - i\,g\,a\;A_\nu\left(x + a\,\hat{\mu}\right) - \frac{1}{2}\,g^2\,a^2\;\left[A_\mu(x), A_\nu\left(x + a\,\hat{\mu}\right)\right] \\
& + i\,g\,a\;A_\mu\left(x + a\,\hat{\nu}\right) + i\,g\,a\;A_\nu(x) - \frac{1}{2}\,g^2\,a^2\;\left[A_\mu\left(x + a\,\hat{\nu}\right), A_\nu(x)\right] \\
& + \frac{1}{2}\,g^2\,a^2\;\left[A_\mu(x), A_\mu\left(x + a\,\hat{\nu}\right)\right] + \frac{1}{2}\,g^2\,a^2\;\left[A_\mu(x), A_\nu(x)\right] \\
& + \frac{1}{2}\,g^2\,a^2\;\left[A_\nu\left(x + a\,\hat{\mu}\right), A_\mu\left(x + a\,\hat{\nu}\right)\right] + \frac{1}{2}\,g^2\,a^2\;\left[A_\nu\left(x + a\,\hat{\mu}\right), A_\nu(x)\right] + \mathcal{O}\left(a^3\right)\Bigg)\,.
\end{aligned}
\tag{B.9}
$$

Now perform a Taylor expansion for gauge fields with shifted arguments, i.e. $A_\nu\left(x + a\,\hat{\mu}\right)$; we set [11]

$$
A_\nu\left(x + a\,\hat{\mu}\right) = A_\nu(x) + a\,\partial_\mu\,A_\nu(x) + \mathcal{O}\left(a^2\right). \tag{B.10}
$$

Consider now the non-commutator terms only of Eq. ($B.9$) (omitting the exponential for the moment)

$$
\begin{aligned}
& - i\,g\,a\;A_\mu(x) - i\,g\,a\;A_\nu\left(x + a\,\hat{\mu}\right) + i\,g\,a\;A_\mu\left(x + a\,\hat{\nu}\right) + i\,g\,a\;A_\nu(x) \\
& = i\,g\,a\;\left(-A_\mu(x) - A_\nu(x) - a\,\partial_\mu\,A_\nu(x) + A_\mu(x) + a\,\partial_\nu\,A_\mu(x) + A_\nu(x) + \mathcal{O}\left(a^2\right)\right) \\
& = i\,g\,a^{\,2}\;\left(\partial_\nu A_\mu(x) - \partial_\mu A_\nu(x)\right) + \mathcal{O}\left(a^3\right).
\end{aligned}
\tag{B.11}
$$

The five commutators of Eq. ($B.9$) with shifted gauge fields, give respectively

$$
\begin{aligned}
\left[A_\mu(x), A_\nu\left(x + a\,\hat{\mu}\right)\right] &= \left[A_\mu(x), A_\nu(x)\right] + a\;\left[A_\mu(x), \partial_\mu A_\nu(x)\right] + \mathcal{O}\left(a^2\right) \\
\left[A_\mu\left(x + a\,\hat{\nu}\right), A_\nu(x)\right] &= \left[A_\mu(x), A_\nu(x)\right] + a\;\left[\partial_\nu A_\mu(x), A_\nu(x)\right] + \mathcal{O}\left(a^2\right) \\
\left[A_\mu(x), A_\mu\left(x + a\,\hat{\nu}\right)\right] &= \left[A_\mu(x), A_\mu(x)\right] + a\;\left[A_\mu(x), \partial_\nu A_\mu(x)\right] + \mathcal{O}\left(a^2\right) \\
\left[A_\nu\left(x + a\,\hat{\mu}\right), A_\mu\left(x + a\,\hat{\nu}\right)\right] &= \left[A_\nu(x), A_\mu(x)\right] + a\;\left[\partial_\mu A_\nu(x), A_\mu(x)\right] + a\;\left[A_\nu(x), \partial_\nu A_\mu(x)\right] + \mathcal{O}\left(a^2\right) \\
\left[A_\nu\left(x + a\,\hat{\mu}\right), A_\nu(x)\right] &= \left[A_\nu(x), A_\nu(x)\right] + a\;\left[\partial_\mu A_\nu(x), A_\nu(x)\right] + \mathcal{O}\left(a^2\right).
\end{aligned}
\tag{B.12}
$$

Noting that A_μ, A_ν are Hermitian and the (continuum) definition of the field strength tensor

$$
G_{\mu\nu}(x) = \partial_\mu A_\nu(x) - \partial_\nu A_\mu(x) + i\,g\;\left[A_\mu(x), A_\nu(x)\right], \tag{B.13}
$$

and reassemble and substitute all these back into Eq. (B.11), keeping only terms up to (and including) $\mathcal{O}\left(a^2\right)$.

$$\begin{aligned}
P_{\mu\nu}(x) &= \exp\left(-i\,g\,a^{\,2}\,\left(\partial_\nu A_\mu(x) - \partial_\mu A_\mu(x)\right) + 2\,\frac{1}{2}\,g^2\,a^2\,\left[A_\nu(x), A_\mu(x)\right] + \mathcal{O}\left(a^3\right)\right) \\
&= \exp\left(-i\,g\,a^{\,2}\,\left(\partial_\nu A_\mu(x) - \partial_\mu A_\mu(x) - i\,g\,\left[A_\nu(x), A_\mu(x)\right]\right) + \mathcal{O}\left(a^3\right)\right) \\
&= \exp\left(i\,g\,a^{\,2}\,G_{\mu\nu}(x) + \mathcal{O}\left(a^3\right)\right). \qquad \text{(B.14)}
\end{aligned}$$

B.3. Naive Fermion Action

Using the following expansions about x for the gauge links and fermion fields

$$U_\mu(x) \simeq 1 - i\,g\,a\,A_\mu(x) + \mathcal{O}\left(a^2\right) \qquad \text{(B.15)}$$

$$U_\mu\left(x + a\,\hat{\mu}\right) \simeq 1 - i\,g\,a\,A_\mu(x) + \mathcal{O}\left(a^2\right) \qquad \text{(B.16)}$$

$$\psi\left(x + a\,\hat{\mu}\right) \simeq \psi(x) + a\,\partial_\mu\,\psi(x) + \mathcal{O}\left(a^2\right) \qquad \text{(B.17)}$$

$$\psi\left(x - a\,\hat{\mu}\right) \simeq \psi(x) - a\,\partial_\mu\,\psi(x) + \mathcal{O}\left(a^2\right) \qquad \text{(B.18)}$$

where the second line uses Eq. (B.10); the covariant finite difference derivative operator of Eq. (3.8) can be written

$$\begin{aligned}
\nabla_\mu(x)\,\psi(x) &= \frac{1}{2\,a}\,\Big[\left(1 - i\,g\,a\,A_\mu(x) + \mathcal{O}\left(a^2\right)\right)\,\left(\psi(x) + a\,\partial_\mu\,\psi(x) + \mathcal{O}\left(a^2\right)\right) \\
&\qquad - \left(1 + i\,g\,a\,A_\mu(x) + \mathcal{O}\left(a^2\right)\right)\,\left(\psi(x) - a\,\partial_\mu\,\psi(x) + \mathcal{O}\left(a^2\right)\right)\Big] \\
&= \frac{1}{2\,a}\,\Big[\psi(x) + a\,\partial_\mu\,\psi(x) - i\,g\,a\,A_\mu(x)\psi(x) - i\,g\,a^{\,2}\,A_\mu(x)\,\partial_\mu\,\psi(x) + \mathcal{O}\left(a^2\right) \\
&\qquad - \left(\psi(x) - a\,\partial_\mu\,\psi(x) + i\,g\,a\,A_\mu(x)\psi(x) - i\,g\,a^{\,2}\,A_\mu(x)\,\partial_\mu\,\psi(x) + \mathcal{O}\left(a^2\right)\right)\Big] \\
&= \left(\partial_\mu - igA_\mu(x) + \mathcal{O}\left(a^2\right)\right)\,\psi(x). \qquad \text{(B.19)}
\end{aligned}$$

This is the continuum covariant derivative operator in the limit $a \to 0$.

B.3.1. Wilson Fermion Action

The additional Wilson term in momentum space is shown in Eq. (3.25) and is

$$\begin{aligned}
D^W(p) &= \frac{i}{a}\sum_{\mu=1}^{4} 1-\cos(p_\mu) \\
&= \frac{i}{a}\sum_{\mu=1}^{4}\left(1-\frac{1}{2}\left(\mathrm{e}^{i\,p_\mu}+\mathrm{e}^{-i\,p_\mu}\right)\right) \\
2\,D^W(p) &= \frac{i}{a}\sum_{\mu=1}^{4}\left(2-\mathrm{e}^{i\,p_\mu}-\mathrm{e}^{-i\,p_\mu}\right) \\
&= \frac{i}{a}\sum_{\mu=1}^{4}\left(2-\mathrm{e}^{i\,p\,\cdot\,(x+a\,\hat{\mu})}-\mathrm{e}^{i\,p\,\cdot\,(x-a\,\hat{\mu})}\right). \qquad \text{(B.20)}
\end{aligned}$$

Taking the Fourier transformation as in Eq. (3.21) yields

$$\begin{aligned}
2\,D^W(n,m) &= \frac{1}{|\Lambda|}\sum_{p\in\widetilde{\Lambda}} \mathrm{e}^{i\,p\,\cdot\,n}\,2\,D^W(p)\,\mathrm{e}^{-i\,p\,\cdot\,m} \\
&= \frac{1}{|\Lambda|}\sum_{p\in\widetilde{\Lambda}} \mathrm{e}^{i\,p\,\cdot\,n}\sum_{\mu=1}^{4}\left(2-\mathrm{e}^{i\,p\,\cdot\,(x+a\,\hat{\mu})}-\mathrm{e}^{i\,p\,\cdot\,(x-a\,\hat{\mu})}\right)\mathrm{e}^{-i\,p\,\cdot\,m} \\
&= \frac{1}{|\Lambda|}\frac{1}{a}\sum_{p\in\widetilde{\Lambda}}\sum_{\mu=1}^{4}\left(2\,\mathrm{e}^{-i\,p\,\cdot\,(m-n)}-\mathrm{e}^{i\,p\,\cdot\,n}\left(\mathrm{e}^{-i\,p\,\cdot\,(m-(x+a\,\hat{\mu}))}-\mathrm{e}^{-i\,p\,\cdot\,(m-(x-a\,\hat{\mu}))}\right)\right) \\
&= \frac{1}{a}\sum_{\mu=1}^{4}\left(\delta\,(m-n)-\delta_{x+a\,\hat{\mu},m}-\delta_{x-a\,\hat{\mu},m}\right), \qquad \text{(B.21)}
\end{aligned}$$

where $\widetilde{\Lambda}$ is the total available momenta. The Wilson term in position space is hence

$$D^W(x,y) = -a\sum_{\mu=1}^{4}\frac{1}{2\,a^2}\left(U_\mu(x)\,\delta_{x+a\,\hat{\mu},y}-2\,\delta_{x,y}+U_\mu^\dagger(x-a\,\hat{\mu})\,\delta_{x-a\,\hat{\mu},y}\right), \qquad \text{(B.22)}$$

where the gauge links U_μ are necessary to maintain gauge invariance.

Errors

Considering the Wilson term of Eq. (3.28), write

$$\frac{1}{2\,\epsilon}\left(f\left(x+\epsilon\right)-2\,f(x)+f\left(x-\epsilon\right)\right). \tag{B.23}$$

Now Taylor expand $f\left(x+\epsilon\right)$ and $f\left(x-\epsilon\right)$ as

$$\begin{aligned} f\left(x+\epsilon\right) &= f(x)+\epsilon\,f'(x)+\frac{\epsilon^2}{2}\,f''(x)+\mathcal{O}\left(\epsilon^3\right) \\ f\left(x-\epsilon\right) &= f(x)-\epsilon\,f'(x)+\frac{\epsilon^2}{2}\,f''(x)+\mathcal{O}\left(\epsilon^3\right) \end{aligned}$$

and so

$$\frac{1}{2\,\epsilon}\left(f\left(x+\epsilon\right)-2\,f(x)+f\left(x-\epsilon\right)\right)=f''(x)+\mathcal{O}\left(\epsilon\right), \tag{B.24}$$

which has $\mathcal{O}\left(\epsilon\right)$ errors.

B.4. Baryon Wick contractions

The wick contractions for a baryon operator as in Eq. (3.51) are explicitly shown below. Consider $\mathcal{B}\left(x,\Phi\right)\overline{\mathcal{B}}\left(x,\Phi\right)$ from Eqs. (3.45) and (3.46), suppressing location, colour and spin structure write

$$\mathcal{B}\,\overline{\mathcal{B}}\propto\overline{\psi}_{f'}\,\overline{\psi}_{g'}\,\overline{\psi}_{h'}\,\psi_f\,\psi_g\,\psi_h. \tag{B.25}$$

Consider now the Wick contractions here

$$
\begin{aligned}
&\overline{\psi}_{f'}\,\overline{\psi}_{g'}\,\overline{\psi}_{h'}\,\psi_f\,\psi_g\,\psi_h \propto \delta^{f}_{f'}\,\delta^{g}_{g'}\,\delta^{h}_{h'} \\
&\overline{\psi}_{f'}\,\overline{\psi}_{g'}\,\overline{\psi}_{h'}\,\psi_f\,\psi_g\,\psi_h \propto \delta^{f}_{f'}\,\delta^{h}_{g'}\,\delta^{g}_{h'} \\
&\overline{\psi}_{f'}\,\overline{\psi}_{g'}\,\overline{\psi}_{h'}\,\psi_f\,\psi_g\,\psi_h \propto \delta^{g}_{f'}\,\delta^{f}_{g'}\,\delta^{h}_{h'} \\
&\overline{\psi}_{f'}\,\overline{\psi}_{g'}\,\overline{\psi}_{h'}\,\psi_f\,\psi_g\,\psi_h \propto \delta^{g}_{f'}\,\delta^{h}_{g'}\,\delta^{f}_{h'} \\
&\overline{\psi}_{f'}\,\overline{\psi}_{g'}\,\overline{\psi}_{h'}\,\psi_f\,\psi_g\,\psi_h \propto \delta^{h}_{f'}\,\delta^{g}_{g'}\,\delta^{f}_{h'} \\
&\overline{\psi}_{f'}\,\overline{\psi}_{g'}\,\overline{\psi}_{h'}\,\psi_f\,\psi_g\,\psi_h \propto \delta^{h}_{f'}\,\delta^{f}_{g'}\,\delta^{g}_{h'} .
\end{aligned}
\tag{B.26}
$$

What is immediately clear from Eq. (*B*.26) is that only contractions between quark fields of the same flavour produce a non-zero contribution. In practice this limits the number of contractions required. For example the neutron operator of Eq. (3.49) has only two contributing Wick contractions.

B.5. Baryon correlation function spin structure

The baryon two-point correlation function described in Section 3.4.2 is a 4×4 complex matrix in Dirac spinor space. In particular we want to show that the positive parity signal is in the $(1,1)$ and $(2,2)$ components of the correlation function Eq. (3.67)

$$
G\left(\vec{p}\,,t\right) = \sum_{\alpha,\tilde{p},s} \mathrm{e}^{-E_\alpha\, t} \sum_{\vec{x}} \mathrm{e}^{-i\,\vec{p}\,\cdot\,\vec{x}}\, Z^{\alpha}_{N_{1/2+}}\, \overline{Z'}^{\alpha}_{N_{1/2+}} \left(\frac{\gamma\cdot p + M^{\alpha}_{B+}}{2\,E^{\alpha}_{B+}} \right). \tag{B.27}
$$

For the zero-momentum correlation function $\left(\vec{p} = \vec{0}\right)$, then

$$
\gamma\cdot p = \gamma_4\cdot p_4 = \gamma_4\, M_{B^+}, \tag{B.28}
$$

and so

$$G\left(\vec{p},t\right) \propto \frac{\gamma_4\, M_{B^+} + M_{B^+}}{2\, M_{B^+}}. \tag{B.29}$$

Using the definition of γ_4 in Eq. (A.5) it is easy to see that the $(1,1)$ and $(2,2)$ components give

$$G\left(\vec{p},t\right) \propto \frac{2\, M_{B^+}}{2\, M_{B^+}} = 1 \neq 0 \tag{B.30}$$

while all other indices produce $G\left(\vec{p},t\right) \propto 0$. In particular components $(3,3)$ and $(4,4)$ result in

$$G\left(\vec{p},t\right) \propto \frac{-M_{B^+} + M_{B^+}}{2\, M_{B^+}} = 0. \tag{B.31}$$

The positive parity components of the correlation function are hence only in the $(1,1)$ and $(2,2)$ components. For completeness, a similar argument for the negative parity baryon can be found in Ref. [12].

B.6. Least squares fitting

Fits in this thesis are performed via a linear least squares minimisation procedure [31]. The χ^2 per degree of freedom

$$\chi^2 = \sum_{i=1}^{N_t} \sum_{j=1}^{N_t} \left(y(t_i) - T(t_i)\right) \mathcal{C}^{-1}(t_i,t_j) \left(y(t_j) - T(t_j)\right), \tag{B.32}$$

is minimised. Here $y(t_i)$ is the dependent variable at t_i, the theoretical fitted value is $T(t_i)$, $\mathcal{C}^{-1}(t_i,t_j)$ is the covariance matrix and N_t is the total number of data points being fitted to. The covariance matrix is estimated via the jackknife method [74, 209]

$$\begin{aligned}\mathcal{C}(t_i,t_j) &= \frac{N_c-1}{N_c} \sum_{m=1}^{Nc} \left(\overline{y_m}(t_i) - \overline{\overline{y}}(t_i)\right) \left(\overline{y_m}(t_j) - \overline{\overline{y}}(t_j)\right) \\ &= \frac{N_c-1}{N_c} \sum_{m=1}^{N_c} \overline{y_m}(t_i)\, \overline{y_m}(t_j) - \overline{\overline{y}}(t_i)\, \overline{\overline{y}}(t_j),\end{aligned} \tag{B.33}$$

where N_c is the number of data points being averaged at each N_t, $\overline{y_m}(t_i)$ is the jackknife ensemble average of the system at t_i after the m_{th} data point has been removed and $\overline{\overline{y}}(t_i)$ is the average of all the jackknife ensemble averages, given by

$$\overline{\overline{y}}(t_i) = \frac{1}{N_c} \sum_{m=1}^{N_c} \overline{y_m}(t_i). \tag{B.34}$$

B.7. Magnetic section of clover term

As the field $A_\nu(x) = 0$ for all x in the *middle* of the lattice, the clover plaquette term of Eq. (3.38) simplifies to

$$\begin{aligned} \mathcal{C}_{\mu\nu}(x) &= U_\mu(x)\, U_\mu^\dagger(x + a\,\hat{\nu}) + U_\mu^\dagger(x + a\,\hat{\nu} - a\,\hat{\mu})\; U_\mu(x - a\,\hat{\mu}) \\ &+ U_\mu^\dagger(x - a\,\hat{\mu})\; U_\mu(x - a\,\hat{\mu} - a\,\hat{\nu}) + U_\mu(x - a\,\hat{\nu})\; U_\mu^\dagger(x). \end{aligned} \tag{B.35}$$

This may be written in a form which is clearer for the potential $A_x = -B\,\hat{y}$ as

$$\begin{aligned} \mathcal{C}_{12}(x,\, y) &= U_\mu(x,\, y)\, U_\mu^\dagger(x,\, y + a) + U_\mu^\dagger(x + a,\, y)\; U_\mu(x - a,\, y) \\ &+ U_\mu^\dagger(x - a,\, y)\; U_\mu(x - a,\, y - a) + U_\mu(x,\, y - a)\; U_\mu^\dagger(x,\, y), \end{aligned} \tag{B.36}$$

where

$$U_\mu(x,\, y) = \mathrm{e}^{-i\,a\,qe\,B\,y}. \tag{B.37}$$

The clover plaquette then becomes

$$\begin{aligned} \mathcal{C}_{\mu\nu}(x,\, y) &= \mathrm{e}^{-i\,a\,qe\,B\,y}\,\mathrm{e}^{i\,a\,qe\,B\,(y+a)} + \mathrm{e}^{i\,a\,qe\,B\,(y+a)}\,\mathrm{e}^{-i\,a\,qe\,B\,y} \\ &+ \mathrm{e}^{i\,a\,qe\,B\,y}\,\mathrm{e}^{-i\,a\,qe\,B\,(y-a)} + \mathrm{e}^{-i\,a\,qe\,B\,(y-a)}\,\mathrm{e}^{-i\,a\,qe\,B\,y} \\ &= 4\,\mathrm{e}^{i\,a^2\,qe\,B + \mathcal{O}\left(a^3\right)}, \end{aligned} \tag{B.38}$$

where the Baker-Campbell-Hausdorff identity [208] has been used in the last line.

The clover fermion definition of the field strength tensor is given by

$$F_{\mu\nu}(x) = \frac{1}{8\,i}\,\frac{1}{qe\,a^2}\left(\mathcal{C}_{\mu\nu}(x) - \mathcal{C}_{\mu\nu}^\dagger(x)\,\frac{1}{3}\,\mathrm{Tr}\left(\mathcal{C}_{\mu\nu}(x) - \mathcal{C}_{\mu\nu}^\dagger(x)\right)\right). \tag{B.39}$$

Thus the magnetic section of the clover term is

$$\begin{aligned} F_{12} &= \frac{1}{8\,i}\,\frac{1}{qe\,a^2}\,\left(C_{12} - C_{12}^\dagger\right) \\ &= \frac{1}{8\,i}\,\frac{1}{qe\,a^2}\,\left(4\,\mathrm{e}^{i\,a^2\,qe\,B+\mathcal{O}\left(a^3\right)} - 4\,\mathrm{e}^{-i\,a^2\,qe\,B+\mathcal{O}\left(a^3\right)}\right) \\ &= \frac{1}{2\,i}\,\frac{1}{qe\,a^2}\,\left(\sin\left(a^2\,qe\,B\right)\right), \end{aligned} \tag{B.40}$$

as in Eq. (5.13).

B.8. Chiral effective field theory coefficients

The partially quenched chiral effective field theory discussed in Section 6.3 requires separating the loop diagram contribution into valence-valence, valence-sea, sea-sea and of course the sum or total contribution. This is done in Table B.2 for the neutron, Table B.3 and Tables B.4 and B.5 for the Σ^+ and the Ξ^0 respectively. These contributions were determined using the process outlined in Section 6.3.1.

B.8.1. Numerical coupling coefficient values

The $SU(3)$ flavour coupling coefficient numerical values for each of these contributions are derived by considering the appropriate chiral Lagrangian. These numerical values can be found in Table B.1 [125, 173, 177, 210].

The coefficients of the processes in Refs. [173] and [210] may be related to those in Table B.1 by squaring then multiplying by $\frac{4}{3}$. An example is the $\Sigma^{*\,0}\,\pi^+$ coupling. In the above referenced works it is

$$\begin{aligned} \chi_{\Sigma^{*\,0}\,\pi^+\,\Sigma^-} &= -\frac{1}{\sqrt{6}}\,\mathcal{C}, \\ \chi^2_{\Sigma^{*\,0}\,\pi^+\,\Sigma^-} &= \frac{1}{6}\,\mathcal{C}^2, \end{aligned} \tag{B.41}$$

which clearly matches $\chi^2_{\pi^+\,\Sigma^{*\,0}} = \frac{2}{9}\,\mathcal{C}^2$ if multiplied by $\frac{4}{3}$.

Table B.1. $SU(3)$ flavour coupling coefficients for the chiral effective field theory analysis. The header row indicates the intermediate baryon species in the meson-baryon loop dressing. Through conservation of quark flavour, one can identify the baryon which is being dressed.

Σ^*		Δ		Σ		Λ		N		Ξ^*		Ξ		Ω	
$\chi^2_{K^+\,\Sigma^{*\,-}}$	$\frac{4}{9}\,\mathcal{C}^2$	$\chi^2_{\pi^-\,\Delta^+}$	$\frac{4}{9}\,\mathcal{C}^2$	$\chi^2_{K^+\,\Sigma^-}$	$2\,(D-F)^2$	$\chi^2_{K^0\,\Lambda}$	$\frac{1}{3}\,(D+3\,F)^2$	$\chi^2_{\pi^+\,n}$	$2\,(D+F)^2$	$\chi^2_{K^+\,\Xi^{*\,0}}$	$\frac{4}{9}\,\mathcal{C}^2$	$\chi^2_{K^+\,\Xi^0}$	$2\,(D+F)^2$	$\chi^2_{K^+\,\Omega^-}$	$\frac{4}{3}\,\mathcal{C}^2$
$\chi^2_{K^0\,\Sigma^{*\,0}}$	$\frac{2}{9}\,\mathcal{C}^2$	$\chi^2_{\pi^+\,\Delta^-}$	$\frac{4}{3}\,\mathcal{C}^2$	$\chi^2_{K^0\,\Sigma^0}$	$(D-F)^2$	$\chi^2_{K^+\,\Lambda}$	$\frac{1}{3}\,(D+3\,F)^2$	$\chi^2_{\pi^-\,p}$	$2\,(D+F)^2$	$\chi^2_{\pi^+\,\Xi^{*\,-}}$	$\frac{4}{9}\,\mathcal{C}^2$	$\chi^2_{\pi^+\,\Xi^-}$	$2\,(D-F)^2$		
$\chi^2_{K^-\,\Sigma^{*\,+}}$	$\frac{4}{9}\,\mathcal{C}^2$	$\chi^2_{\pi^+\,\Delta^0}$	$\frac{4}{9}\,\mathcal{C}^2$	$\chi^2_{K^+\,\Sigma^0}$	$(D-F)^2$	$\chi^2_{\pi^+\,\Lambda}$	$\frac{4}{3}\,D^2$	$\chi^2_{\overline{K}^0\,p}$	$2\,(D-F)^2$						
$\chi^2_{K^+\,\Sigma^{*\,0}}$	$\frac{2}{9}\,\mathcal{C}^2$	$\chi^2_{\pi^-\,\Delta^{++}}$	$\frac{4}{3}\,\mathcal{C}^2$	$\chi^2_{K^0\,\Sigma^+}$	$2\,(D-F)^2$	$\chi^2_{\overline{K}^0\,\Lambda}$	$\frac{1}{3}\,(D-3\,F)^2$								
$\chi^2_{K^0\,\Sigma^{*\,+}}$	$\frac{4}{9}\,\mathcal{C}^2$	$\chi^2_{\pi^0\,\Delta^+}$	0	$\chi^2_{\pi^+\,\Sigma^0}$	$2\,F$										
$\chi^2_{\pi^+\,\Sigma^{*\,0}}$	$\frac{2}{9}\,\mathcal{C}^2$	$\chi^2_{K^-\,\Delta^{++}}$	$\frac{4}{3}\,\mathcal{C}^2$	$\chi^2_{K^-\,\Sigma^+}$	$2\,(D+F)^2$										
$\chi^2_{\overline{K}^0\,\Sigma^{*\,0}}$	$\frac{2}{9}\,\mathcal{C}^2$	$\chi^2_{\overline{K}^0\,\Delta^+}$	$\frac{4}{9}\,\mathcal{C}^2$	$\chi^2_{\overline{K}^0\,\Sigma^0}$	$(D+F)^2$										

Table B.2. Chiral coefficients for the leading-order loop integral contributions for the neutron.

Process	Total	Valence-sea	Sea-sea
$n \to N\,\pi$			
$n \to n\,\pi^0$	0	$\frac{3}{6}\,\left(2\,q_u\,q_{\overline{u}}\,\chi^2_{K^+\,\Sigma^-} + 2\,q_d\,q_{\overline{d}}\,\left(\chi^2_{K^0\,\Sigma^0} + \chi^2_{K^0\,\Lambda}\right)\right)$	$\frac{3}{6}\,\left(q^2_{\overline{u}}\,\chi^2_{K^+\,\Sigma^-} + q^2_{\overline{d}}\,\left(\chi^2_{K^0\,\Sigma^0} + \chi^2_{K^0\,\Lambda}\right)\right)$
$n \to n\,\eta$	0	$\frac{1}{6}\,\left(2\,q_u\,q_{\overline{u}}\,\chi^2_{K^+\,\Sigma^-} + 2\,q_d\,q_{\overline{d}}\,\left(\chi^2_{K^0\,\Sigma^0} + \chi^2_{K^0\,\Lambda}\right)\right)$	$\frac{1}{6}\,\left(q^2_{\overline{u}}\,\chi^2_{K^+\,\Sigma^-} + q^2_{\overline{d}}\,\left(\chi^2_{K^0\,\Sigma^0} + \chi^2_{K^0\,\Lambda}\right)\right)$
$n \to n\,\eta'$	0	$\frac{2}{6}\,\left(2\,q_u\,q_{\overline{u}}\,\chi^2_{K^+\,\Sigma^-} + 2\,q_d\,q_{\overline{d}}\,\left(\chi^2_{K^0\,\Sigma^0} + \chi^2_{K^0\,\Lambda}\right)\right)$	$\frac{2}{6}\,\left(q^2_{\overline{u}}\,\chi^2_{K^+\,\Sigma^-} + q^2_{\overline{d}}\,\left(\chi^2_{K^0\,\Sigma^0} + \chi^2_{K^0\,\Lambda}\right)\right)$
$n \to p\,\pi^-$	$\chi^2_{\pi^-\,p}$	$2\,q_d\,q_{\overline{u}}\,\left(\chi^2_{K^0\,\Sigma^0} + \chi^2_{K^0\,\Lambda}\right)$	$q^2_{\overline{u}}\,\left(\chi^2_{K^0\,\Sigma^0} + \chi^2_{K^0\,\Lambda}\right)$
$n \to n^-\,\pi^+$	0	$2\,q_u\,q_{\overline{d}}\,\chi^2_{K^+\,\Sigma^-}$	$q^2_{\overline{d}}\,\chi^2_{K^+\,\Sigma^-}$
$n \to \Sigma\,K$			
$n \to (\Sigma^0,\,\Lambda)\;K^0$	0	$2\,q_d\,q_{\overline{s}}\,\left(\chi^2_{K^0\,\Sigma^0} + \chi^2_{K^0\,\Lambda}\right)$	$q^2_{\overline{s}}\,\left(\chi^2_{K^0\,\Sigma^0} + \chi^2_{K^0\,\Lambda}\right)$
$n \to \Sigma^-\,K^-$	$\chi^2_{K^+\,\Sigma^-}$	$2\,q_u\,q_{\overline{s}}\,\chi^2_{K^+\,\Sigma^-}$	$q^2_{\overline{s}}\,\chi^2_{K^+\,\Sigma^-}$
$n \to \Delta\,\pi$			
$n \to \Delta^0\,\pi^0$	0	$\frac{3}{6}\,\left(2\,q_u\,q_{\overline{u}}\,\chi^2_{K^+\,\Sigma^*-} + 2\,q_d\,q_{\overline{d}}\,\chi^2_{K^0\,\Sigma^*0}\right)$	$\frac{3}{6}\,\left(q^2_{\overline{u}}\,\chi^2_{K^+\,\Sigma^*-} + q^2_{\overline{d}}\,\chi^2_{K^0\,\Sigma^*0}\right)$
$n \to \Delta^0\,\eta$	0	$\frac{1}{6}\,\left(2\,q_u\,q_{\overline{u}}\,\chi^2_{K^+\,\Sigma^*-} + 2\,q_d\,q_{\overline{d}}\,\chi^2_{K^0\,\Sigma^*0}\right)$	$\frac{1}{6}\,\left(q^2_{\overline{u}}\,\chi^2_{K^+\,\Sigma^*-} + q^2_{\overline{d}}\,\chi^2_{K^0\,\Sigma^*0}\right)$
$n \to \Delta^0\,\eta'$	0	$\frac{2}{6}\,\left(2\,q_u\,q_{\overline{u}}\,\chi^2_{K^+\,\Sigma^*-} + 2\,q_d\,q_{\overline{d}}\,\chi^2_{K^0\,\Sigma^*0}\right)$	$\frac{2}{6}\,\left(q^2_{\overline{u}}\,\chi^2_{K^+\,\Sigma^*-} + q^2_{\overline{d}}\,\chi^2_{K^0\,\Sigma^*0}\right)$
$n \to \Delta^+\,\pi^-$	$\chi^2_{\pi^-\,\Delta^+}$	$2\,q_d\,q_{\overline{u}}\,\chi^2_{K^0\,\Sigma^*0}$	$q^2_{\overline{u}}\,\chi^2_{K^0\,\Sigma^*0}$
$n \to \Delta^-\,\pi^+$	$\chi^2_{\pi^+\,\Delta^-}$	$2\,q_u\,q_{\overline{d}}\,\chi^2_{K^+\,\Sigma^*-}$	$q^2_{\overline{d}}\,\chi^2_{K^+\,\Sigma^*-}$
$n \to \Sigma^*\,K$			
$n \to \Sigma^{*0}\,K^0$	0	$2\,q_d\,q_{\overline{s}}\,\chi^2_{K^0\,\Sigma^*0}$	$q^2_{\overline{s}}\,\chi^2_{K^0\,\Sigma^*0}$
$n \to \Sigma^{*-}\,K^+$	$\chi^2_{K^+\,\Sigma^*-}$	$2\,q_u\,q_{\overline{s}}\,\chi^2_{K^+\,\Sigma^*-}$	$q^2_{\overline{s}}\,\chi^2_{K^+\,\Sigma^*-}$

Table B.3. Chiral coefficients for the leading-order loop integral contributions for the proton.

Process	Total	Valence-sea	Sea-sea
$p \to N\,\pi$			
$p \to p\,\pi^0$	0	$\frac{3}{6}\left(2\,q_u\,q_{\overline{u}}\left(\chi^2_{K^+\,\Sigma^0} + \chi^2_{K^+\,\Lambda}\right) + 2\,q_d\,q_{\overline{d}}\,\chi^2_{K^0\,\Sigma^+}\right)$	$\frac{3}{6}\left(q^2_{\overline{u}}\left(\chi^2_{K^+\,\Sigma^0} + \chi^2_{K^+\,\Lambda}\right) + q^2_{\overline{d}}\,\chi^2_{K^0\,\Sigma^+}\right)$
$p \to p\,\eta$	0	$\frac{1}{6}\left(2\,q_u\,q_{\overline{u}}\left(\chi^2_{K^+\,\Sigma^0} + \chi^2_{K^+\,\Lambda}\right) + 2\,q_d\,q_{\overline{d}}\,\chi^2_{K^0\,\Sigma^+}\right)$	$\frac{1}{6}\left(q^2_{\overline{u}}\left(\chi^2_{K^+\,\Sigma^0} + \chi^2_{K^+\,\Lambda}\right) + q^2_{\overline{d}}\,\chi^2_{K^0\,\Sigma^+}\right)$
$p \to p\,\eta'$	0	$\frac{2}{6}\left(2\,q_u\,q_{\overline{u}}\left(\chi^2_{K^+\,\Sigma^0} + \chi^2_{K^+\,\Lambda}\right) + 2\,q_d\,q_{\overline{d}}\,\chi^2_{K^0\,\Sigma^+}\right)$	$\frac{2}{6}\left(q^2_{\overline{u}}\left(\chi^2_{K^+\,\Sigma^0} + \chi^2_{K^+\,\Lambda}\right) + q^2_{\overline{d}}\,\chi^2_{K^0\,\Sigma^+}\right)$
$p \to n\,\pi^+$	$\chi^2_{\pi^+\,n}$	$2\,q_u\,q_{\overline{d}}\left(\chi^2_{K^+\,\Sigma^0} + \chi^2_{K^+\,\Lambda}\right)$	$q^2_{\overline{d}}\left(\chi^2_{K^+\,\Sigma^0} + \chi^2_{K^+\,\Lambda}\right)$
$p \to p^{++}\,\pi^-$	0	$2\,q_d\,q_{\overline{u}}\,\chi^2_{K^0\,\Sigma^+}$	$q^2_{\overline{u}}\,\chi^2_{K^0\,\Sigma^+}$
$p \to \Sigma\,K$			
$p \to (\Sigma^0, \Lambda)\ K^+$	$\chi^2_{K^+\,\Sigma^0} + \chi^2_{K^+\,\Lambda}$	$2\,q_u\,q_{\overline{s}}\left(\chi^2_{K^+\,\Sigma^0} + \chi^2_{K^+\,\Lambda}\right)$	$q^2_{\overline{s}}\left(\chi^2_{K^+\,\Sigma^0} + \chi^2_{K^+\,\Lambda}\right)$
$p \to \Sigma^+\,K^0$	0	$2\,q_d\,q_{\overline{s}}\,\chi^2_{K^0\,\Sigma^+}$	$q^2_{\overline{s}}\,\chi^2_{K^0\,\Sigma^+}$
$p \to \Delta\,\pi$			
$p \to \Delta^0\,\pi^+$	$\chi^2_{\pi^+\,\Delta^0}$	$2\,q_u\,q_{\overline{d}}\,\chi^2_{K^+\,\Sigma^{*\,0}}$	$q^2_{\overline{d}}\,\chi^2_{K^+\,\Sigma^{*\,0}}$
$p \to \Delta^{++}\,\pi^-$	$\chi^2_{\pi^-\,\Delta^{++}}$	$2\,q_d\,q_{\overline{u}}\,\chi^2_{K^0\,\Sigma^{*\,+}}$	$q^2_{\overline{u}}\,\chi^2_{K^0\,\Sigma^{*\,+}}$
$p \to \Delta^+\,\pi^0$	0	$\frac{3}{6}\left(2\,q_u\,q_{\overline{u}}\,\chi^2_{K^+\,\Sigma^{*\,0}} + 2\,q_d\,q_{\overline{d}}\,\chi^2_{K^0\,\Sigma^{*\,+}}\right)$	$\frac{3}{6}\left(q^2_{\overline{u}}\,\chi^2_{K^+\,\Sigma^{*\,0}} + q^2_{\overline{d}}\,\chi^2_{K^0\,\Sigma^{*\,+}}\right)$
$p \to \Delta^+\,\eta$	0	$\frac{1}{6}\left(2\,q_u\,q_{\overline{u}}\,\chi^2_{K^+\,\Sigma^{*\,0}} + 2\,q_d\,q_{\overline{d}}\,\chi^2_{K^0\,\Sigma^{*\,+}}\right)$	$\frac{1}{6}\left(q^2_{\overline{u}}\,\chi^2_{K^+\,\Sigma^{*\,0}} + q^2_{\overline{d}}\,\chi^2_{K^0\,\Sigma^{*\,+}}\right)$
$p \to \Delta^+\,\eta'$	0	$\frac{2}{6}\left(2\,q_u\,q_{\overline{u}}\,\chi^2_{K^+\,\Sigma^{*\,0}} + 2\,q_d\,q_{\overline{d}}\,\chi^2_{K^0\,\Sigma^{*\,+}}\right)$	$\frac{2}{6}\left(q^2_{\overline{u}}\,\chi^2_{K^+\,\Sigma^{*\,0}} + q^2_{\overline{d}}\,\chi^2_{K^0\,\Sigma^{*\,+}}\right)$
$p \to \Sigma^*\,K$			
$p \to \Sigma^{*\,0}\,K^+$	$\chi^2_{K^+\,\Sigma^{*\,0}}$	$2\,q_u\,q_{\overline{s}}\,\chi^2_{K^+\,\Sigma^{*\,0}}$	$q^2_{\overline{s}}\,\chi^2_{K^+\,\Sigma^{*\,0}}$
$p \to \Sigma^{*\,+}\,K^0$	0	$2\,q_d\,q_{\overline{s}}\,\chi^2_{K^0\,\Sigma^{*\,+}}$	$q^2_{\overline{s}}\,\chi^2_{K^0\,\Sigma^{*\,+}}$

Table B.4. Chiral coefficients for the leading-order loop integral contributions for the Σ^+.

Process	Total	Valence-sea	Sea-sea
$\Sigma^+ \to \Sigma\,\pi$			
$\Sigma^+ \to (\Sigma^0, \Lambda)\ \pi^+$	$\chi^2_{\pi^+\,\Sigma^0} + \chi^2_{\pi^+\,\Lambda}$	$2\,q_u\,q_{\overline{d}}\ \left(\chi^2_{\pi^+\,\Sigma^0} + \chi^2_{\pi^+\,\Lambda}\right)$	$q^2_{\overline{d}}\ \left(\chi^2_{\pi^+\,\Sigma^0} + \chi^2_{\pi^+\,\Lambda}\right)$
$\Sigma^+ \to \Sigma^+\,\pi^0$	0	$\frac{3}{6}\,2\,q_u\,q_{\overline{u}}\ \left(\chi^2_{\pi^+\,\Sigma^0} + \chi^2_{\pi^+\,\Lambda}\right)$	$\frac{3}{6}\,q^2_{\overline{u}}\ \left(\chi^2_{\pi^+\,\Sigma^0} + \chi^2_{\pi^+\,\Lambda}\right)$
$\Sigma^+ \to \Sigma^+\,\eta$	0	$\frac{1}{6}\,2\,q_u\,q_{\overline{u}}\ \left(\chi^2_{\pi^+\,\Sigma^0} + \chi^2_{\pi^+\,\Lambda}\right)$	$\frac{1}{6}\,q^2_{\overline{u}}\ \left(\chi^2_{\pi^+\,\Sigma^0} + \chi^2_{\pi^+\,\Lambda}\right)$
$\Sigma^+ \to \Sigma^+\,\eta'$	0	$\frac{2}{6}\,2\,q_u\,q_{\overline{u}}\ \left(\chi^2_{\pi^+\,\Sigma^0} + \chi^2_{\pi^+\,\Lambda}\right)$	$\frac{2}{6}\,q^2_{\overline{u}}\ \left(\chi^2_{\pi^+\,\Sigma^0} + \chi^2_{\pi^+\,\Lambda}\right)$
$\Sigma^+ \to N\,K$			
$\Sigma^+ \to p\,\overline{K}^0$	0	$2\,q_s\,q_{\overline{d}}\,\chi^2_{\overline{K}^0\,p}$	$q^2_{\overline{d}}\chi^2_{\overline{K}^0\,p}$
$\Sigma^+ \to p^{++}\,K^-$	0	$2\,q_s\,q_{\overline{u}}\,\chi^2_{\overline{K}^0\,p}$	$q^2_{\overline{u}}\chi^2_{\overline{K}^0\,p}$
$\Sigma^+ \to \Xi\,K$			
$\Sigma^+ \to \Xi^0\,K^+$	$\chi^2_{K^+\,\Xi^0}$	$2\,q_u\,q_{\overline{s}}\ \left(\chi^2_{\pi^+\,\Sigma^0} + \chi^2_{\pi^+\,\Lambda}\right)$	$q^2_{\overline{s}}\ \left(\chi^2_{\pi^+\,\Sigma^0} + \chi^2_{\pi^+\,\Lambda}\right)$
$\Sigma^+ \to \Sigma^*\,\pi$			
$\Sigma^+ \to \Sigma^{*\,0}\,\pi^+$	$\chi^2_{\pi^+\,\Sigma^{*\,0}}$	$2\,q_u\,q_{\overline{d}}\,\chi^2_{\pi^+\,\Sigma^{*\,0}}$	$q^2_{\overline{d}}\,\chi^2_{\pi^+\,\Sigma^{*\,0}}$
$\Sigma^+ \to \Sigma^{*\,+}\,\pi^0$	0	$\frac{3}{6}\,2\,q_u\,q_{\overline{u}}\,\chi^2_{\pi^+\,\Sigma^{*\,0}}$	$\frac{3}{6}\,q^2_{\overline{u}}\,\chi^2_{\pi^+\,\Sigma^{*\,0}}$
$\Sigma^+ \to \Sigma^{*\,+}\,\eta$	0	$\frac{1}{6}\,2\,q_u\,q_{\overline{u}}\,\chi^2_{\pi^+\,\Sigma^{*\,0}}$	$\frac{1}{6}\,q^2_{\overline{u}}\,\chi^2_{\pi^+\,\Sigma^{*\,0}}$
$\Sigma^+ \to \Sigma^{*\,+}\,\eta'$	0	$\frac{2}{6}\,2\,q_u\,q_{\overline{u}}\,\chi^2_{\pi^+\,\Sigma^{*\,0}}$	$\frac{2}{6}\,q^2_{\overline{u}}\,\chi^2_{\pi^+\,\Sigma^{*\,0}}$
$\Sigma^+ \to \Delta\,K$			
$\Sigma^+ \to \Delta^{++}\,K^-$	$\chi^2_{K^-\,\Delta^{++}}$	$2\,q_s\,q_{\overline{u}}\,\chi^2_{\overline{K}^0\,\Delta^+}$	$q^2_{\overline{u}}\,\chi^2_{\overline{K}^0\,\Delta^+}$
$\Sigma^+ \to \Delta^+\,\overline{K}^0$	0	$2\,q_s\,q_{\overline{d}}\,\chi^2_{\overline{K}^0\,\Delta^+}$	$q^2_{\overline{d}}\,\chi^2_{\overline{K}^0\,\Delta^+}$
$\Sigma^+ \to \Xi^*\,K$			
$\Sigma^+ \to \Xi^{*\,0}\,K^+$	$\chi^2_{K^+\,\Xi^{*\,0}}$	$2\,q_u\,q_{\overline{s}}\,\chi^2_{\pi^+\,\Sigma^{*\,0}}$	$q^2_{\overline{s}}\,\chi^2_{\pi^+\,\Sigma^{*\,0}}$

Table B.5. Chiral coefficients for the leading-order loop integral contributions for the Ξ^0.

Process	Total	Valence-sea	Sea-sea
$\Xi^0 \to \Xi\,\pi$			
$\Xi^0 \to \Xi^-\,\pi^+$	$\chi^2_{\pi^+\,\Xi^-}$	$2\,q_u\,q_{\overline{d}}\,\chi^2_{\pi^+\,\Xi^-}$	$q^2_{\overline{d}}\,\chi^2_{\pi^+\,\Xi^-}$
$\Xi^0 \to \Xi^0\,\pi^0$	0	$\frac{3}{6}\,2\,q_u\,q_{\overline{u}}\,\chi^2_{\pi^+\,\Xi^-}$	$\frac{3}{6}\,q^2_{\overline{u}}\,\chi^2_{\pi^+\,\Xi^-}$
$\Xi^0 \to \Xi^0\,\eta$	0	$\frac{1}{6}\,2\,q_u\,q_{\overline{u}}\,\chi^2_{\pi^+\,\Xi^-}$	$\frac{1}{6}\,q^2_{\overline{u}}\,\chi^2_{\pi^+\,\Xi^-}$
$\Xi^0 \to \Xi^0\,\eta'$	0	$\frac{2}{6}\,2\,q_u\,q_{\overline{u}}\,\chi^2_{\pi^+\,\Xi^-}$	$\frac{2}{6}\,q^2_{\overline{u}}\,\chi^2_{\pi^+\,\Xi^-}$
$\Xi^0 \to \Sigma\,K$			
$\Xi^0 \to \Sigma^+\,K^-$	$\chi^2_{K^-\,\Sigma^+}$	$2\,q_s\,q_{\overline{u}}\,\left(\chi^2_{\overline{K}^0\,\Sigma^0} + \chi^2_{\overline{K}^0\,\Lambda}\right)$	$q^2_{\overline{u}}\,\left(\chi^2_{\overline{K}^0\,\Sigma^0} + \chi^2_{\overline{K}^0\,\Lambda}\right)$
$\Xi^0 \to (\Sigma^0,\Lambda)\,\overline{K}^0$	0	$2\,q_s\,q_{\overline{d}}\,\left(\chi^2_{\overline{K}^0\,\Sigma^0} + \chi^2_{\overline{K}^0\,\Lambda}\right)$	$q^2_{\overline{d}}\,\left(\chi^2_{\overline{K}^0\,\Sigma^0} + \chi^2_{\overline{K}^0\,\Lambda}\right)$
$\Xi^0 \to \Xi^-_{3S}\,K$			
$\Xi^0 \to \Xi^-_{3S}\,K^+$	0	$2\,q_u q_{\overline{s}}\,\chi^2_{\pi^+\,\Xi^-}$	$q^2_{\overline{s}}\,\chi^2_{\pi^+\,\Xi^-}$
$\Xi^0 \to \Xi^*\,\pi$			
$\Xi^0 \to \Xi^{*\,-}\,\pi^+$	$\chi^2_{\pi^+\,\Xi^{*\,-}}$	$2\,q_u\,q_{\overline{d}}\,\chi^2_{\pi^+\,\Xi^{*\,-}}$	$q^2_{\overline{d}}\,\chi^2_{\pi^+\,\Xi^{*\,-}}$
$\Xi^0 \to \Xi^{*\,0}\,\pi^0$	0	$\frac{3}{6}\,2\,q_u\,q_{\overline{u}}\,\chi^2_{\pi^+\,\Xi^{*\,-}}$	$\frac{3}{6}\,q^2_{\overline{u}}\,\chi^2_{\pi^+\,\Xi^{*\,-}}$
$\Xi^0 \to \Xi^{*\,0}\,\eta$	0	$\frac{1}{6}\,2\,q_u\,q_{\overline{u}}\,\chi^2_{\pi^+\,\Xi^{*\,-}}$	$\frac{1}{6}\,q^2_{\overline{u}}\,\chi^2_{\pi^+\,\Xi^{*\,-}}$
$\Xi^0 \to \Xi^{*\,0}\,\eta'$	0	$\frac{2}{6}\,2\,q_u\,q_{\overline{u}}\,\chi^2_{\pi^+\,\Xi^{*\,-}}$	$\frac{2}{6}\,q^2_{\overline{u}}\,\chi^2_{\pi^+\,\Xi^{*\,-}}$
$\Xi^0 \to \Sigma^*\,K$			
$\Xi^0 \to \Sigma^{*\,0}\,\overline{K}^0$	0	$2\,q_s\,q_{\overline{d}}\,\chi^2_{\overline{K}^0\,\Sigma^{*\,0}}$	$q^2_{\overline{d}}\,\chi^2_{\overline{K}^0\,\Sigma^{*\,0}}$
$\Xi^0 \to \Sigma^{*\,+}\,K^-$	$\chi^2_{K^-\,\Sigma^{*\,+}}$	$2\,q_s\,q_{\overline{u}}\,\chi^2_{\overline{K}^0\,\Sigma^{*\,0}}$	$q^2_{\overline{u}}\,\chi^2_{\overline{K}^0\,\Sigma^{*\,0}}$
$\Xi^0 \to \Omega\,K$			
$\Xi^0 \to \Omega^-\,K^+$	$\chi^2_{K^+\,\Omega^-}$	$2\,q_u\,q_{\overline{s}}\,\chi^2_{\pi^+\,\Xi^{*\,-}}$	$q^2_{\overline{s}}\,\chi^2_{\pi^+\,\Xi^{*\,-}}$

Table B.6. Zero-field baryon effective masses used to determine the magnetic polarisability in the relation of Eq. (4.15).

Baryon	κ	m_π (GeV)	Source smearing sweeps	Mass (GeV)	Fit window	χ^2_{dof}
Nucleon	0.13700	0.702	150	1.407(7)	19-27	0.43
	0.13727	0.570	175	1.284(8)	19-24	0.95
	0.13754	0.411	300	1.133(3)	18-33	1.05
	0.13770	0.296	350	1.072(11)	19-24	0.66
Ξ^0	0.13700	0.702	150	1.468(4)	22-34	1.10
	0.13754	0.411	300	1.351(6)	22-32	0.87
	0.13770	0.296	250	1.331(5)	21-34	0.88
Λ	0.13700	0.702	150	1.430(4)	19-34	1.11
	0.13754	0.411	300	1.228(6)	22-32	0.94
	0.13770	0.296	250	1.183(5)	20-30	0.97
Σ^+	0.13700	0.702	150	1.438(4)	19-35	1.10
	0.13754	0.411	300	1.276(7)	23-32	1.14
	0.13770	0.296	250	1.238(5)	18-26	0.91

B.9. Baryon masses

The baryon masses used for the determination of the magnetic polarisability β in the fit-polarisability ratio of Eq. (4.15) are determined from the zero-field effective mass of the appropriate correlation function. These masses are presented in Table B.6 for each baryon considered in Chapters 4 and 6.

Appendix C.

Landau levels

A charged scalar particle in a uniform magnetic field will have an associated Landau energy proportional to its charge. In the non-relativistic limit, the Landau energy spectrum is equivalent to that of a harmonic oscillator, $E_n = \left(n + \frac{1}{2}\right)\,\omega$ where ω is the classical cyclotron frequency; $\omega = |qe\,B|$. Here the magnetic field is oriented along the $\hat{z}$-direction and the particle has charge qe.

C.1. Continuum, infinite volume formulation

The relativistic form of the Landau levels can be derived [109] by considering the Dirac equation for a point-like particle with charge qe which has been modified by a minimal (classical) electromagnetic coupling

$$\partial_\mu \to \partial_\mu - i\,qe, A_\mu \tag{C.1}$$

The Dirac equation is then

$$\left(i\,\not{\partial} + qe\,\not{A} - m\right)\,\psi(x) = 0. \tag{C.2}$$

By splitting γ^μ into γ^0, γ^i and rearranging this can be rewritten

$$i\,\gamma^0\,\frac{\partial\,\psi}{\partial\,t} = \left(\gamma^i\,\hat{p}_i - qe\,\gamma^i\,A_i - qe\,\gamma^0\,A_0 + m\right)\psi. \tag{C.3}$$

In the Dirac representation of the gamma matrices define

$$\beta\left(=\gamma^0\right)=\begin{pmatrix} I & 0 \\ 0 & -I \end{pmatrix}, \quad \vec{\alpha}\left(=\gamma^0\,\gamma^i\right)=\begin{pmatrix} 0 & \vec{\sigma} \\ \vec{\sigma} & 0 \end{pmatrix}. \tag{C.4}$$

Multiply both sides by γ^0

$$i\,\frac{\partial\,\psi}{\partial\,t}=\left(\vec{\alpha}\cdot\vec{\hat{p}}-qe\,\vec{\alpha}\cdot\vec{A}-qe\,A_0+\beta\,m\right)\psi. \tag{C.5}$$

Separating $\psi\to\psi=\begin{pmatrix}\phi\\ \chi\end{pmatrix}$, we form the coupled equations

$$\begin{aligned} i\,\frac{\partial\,\phi}{\partial\,t} &= \vec{\sigma}\cdot\left(\vec{\hat{p}}-qe\,\vec{A}\right)\,\chi+\left(-qe\,A_0+m\right)\,\phi \\ i\,\frac{\partial\,\chi}{\partial\,t} &= \vec{\sigma}\cdot\left(\vec{\hat{p}}-qe\,\vec{A}\right)\,\phi+\left(-qe\,A_0-m\right)\,\chi \end{aligned} \tag{C.6}$$

The choice made for the electromagnetic potential is the same as that for the background field method; $A^0=A^x=A^y=0$, $A^z=Bx$ is chosen in order to give a constant magnetic field $\vec{B}$ in the $\hat{z}$ direction. Taking a stationary solution of energy E, $\psi=e^{-i\,E\,t}\begin{pmatrix}\phi\\ \chi\end{pmatrix}$ Eq. (C.6) becomes

$$\begin{aligned} \left(-E-m\right)\,\phi &= \vec{\sigma}\cdot\left(\vec{\hat{p}}-qe\,\vec{A}\right)\chi \\ \left(-E+m\right)\,\chi &= \vec{\sigma}\cdot\left(\vec{\hat{p}}-qe\,\vec{A}\right)\phi. \end{aligned}$$

Combining these allows χ to be eliminated and an equation for ϕ obtained

$$\begin{aligned} \left(E^2-m^2\right)\,\phi &= \left[\vec{\sigma}\cdot\left(\vec{\hat{p}}-qe\,\vec{A}\right)\right]^2\,\phi \\ &= \left[\left(\vec{\hat{p}}-qe\,\vec{A}\right)^2-qe\,\vec{\sigma}\cdot\vec{B}\right]\,\phi \\ &= \left[\vec{\hat{p}}^2+(qe)^2\,B^2\,x^2-qe\,B\,\left(\sigma_z+2\,x\,p_y\right)\right]\,\phi \\ &= \left[\vec{\hat{p}}^2+\left(qe\,B\,x-p_y\right)^2+qe\,B\,\sigma_z\right]\,\phi. \end{aligned} \tag{C.7}$$

Eq. (C.7) is the Hamiltonian of a harmonic oscillator. All of p_y, p_z and σ_z commute with the right hand side and so the particle can be constrained to the $x-y$ plane by setting $p_z = 0$ for simplicity. We seek solutions of the form

$$\phi(x) = e^{i\,p_y\,y}\, f(x) \tag{C.8}$$

for $f(x)$ satisfying

$$\left[-\frac{d^2}{dx^2} + (qe\,B\,x - p_y)^2 - qe\,B\,\sigma_z\right] f(x) = \left(E^2 - m^2\right)\, f(x). \tag{C.9}$$

Auxiliary variables ω, a are defined for $qe\,B > 0$

$$\begin{aligned} \omega &= \sqrt{qe\,B}\,\left(x - \frac{p_y}{qe\,B}\right) \\ a &= \frac{E^2 - m^2}{qe\,B}, \end{aligned}$$

which enables Eq. (C.9) to be written as

$$\left(-\frac{d^2}{d\omega^2} + \omega^2 - \sigma_z\right)\, f = a\, f. \tag{C.10}$$

If f is an eigenvector of σ_z with corresponding eigenvalues $\alpha = \pm 1$ then

$$\begin{aligned} f &= \begin{pmatrix} f_1 \\ 0 \end{pmatrix}, \text{ for } \alpha = 1 \\ f &= \begin{pmatrix} 0 \\ f_{-1} \end{pmatrix} \text{ for } \alpha = -1, \end{aligned}$$

then f_α satisfies

$$\left(\frac{d^2}{d\omega^2} - \omega^2 - \sigma_z\right)\, f_\alpha(\omega) = -\,(a + \alpha)\, f_\alpha(w), \quad \alpha = \pm 1.$$

This has a solution which is expressed in terms of a Hermite polynomial $H_n(\omega)$

$$f_\alpha = c\,e^{-\omega^2/2}\, H_n(\omega), \tag{C.11}$$

if $a + \alpha = 2\,n + 1$ for $n = 0, 1, 2, \ldots$. The energy levels are then

$$
\begin{aligned}
E^2 &= m^2 + qe\,B\ (2\,n + 1 - \alpha) \\
E &= m\,\sqrt{1 + \frac{qe\,B}{m^2}\ (2\,n + 1 - \alpha)}.
\end{aligned}
$$

Using a small x expansion of $\sqrt{1+x}$ with $x = \frac{qe\,B}{m^2}\ (2\,n + 1 - \alpha)$

$$
\sqrt{1+x} = 1 + \frac{1}{2} - \frac{x^2}{8} + \frac{x^3}{16} + \mathcal{O}\left(x^4\right); \tag{C.12}
$$

the energy expansion is

$$
\begin{aligned}
E = m &+ \frac{qe\,B}{2\,m}\ (2\,n + 1) - \alpha\,\frac{qe\,B}{2\,m} - \frac{(qe\,B)^2}{8\,m^3}\,(2\,n + 1 - \alpha)^2 \\
&+ \frac{(qe\,B)^3}{8\,m^5}\,(2\,n + 1 - \alpha)^3 + \mathcal{O}\left(\frac{(qe\,B)^4}{m^7}\right).
\end{aligned} \tag{C.13}
$$

The second term is the energy due to the Landau levels while the first is the mass of the particle. The third term is due to the magnetic moment as it is proportional to α, the eigenvalue of σ_z which appears in the spin operator. Higher order terms can be safely ignored for $qe\,B \ll m$. We have shown that the Landau levels for a particle of charge qe and mass m in a magnetic field B are given by

$$
E_{\text{Landau}} = \frac{qe\,B}{2m}\,(2\,n + 1) \ \text{ for } n = 0, 1, 2, 3 \ldots. \tag{C.14}
$$

C.2. Discretised, finite volume formulation

Consider a second order equation for a Dirac spinor ψ

$$
\left(\not{D}\,\not{D} - m^2\right)\,\psi = 0, \tag{C.15}
$$

where $\not{D} = \gamma^\mu D_\mu = \gamma^\mu \left(\partial_\mu + iqe\, A_\mu\right)$ as in Eq. (C.1). Next using a useful identity from Appendix A.4 this can be written as

$$\left(\not{D}\,\not{D} - m^2\right)\,\psi = \Bigg(D\cdot D - \frac{i}{2}\left(\left(\partial_\mu + iqe\,A_\mu\right)\,\sigma^{\mu\nu}\,\left(\partial_\nu + iqe\,A_\nu\right)\right.$$
$$\left. + \left(\partial_\nu + iqe\,A_\nu\right)\,\sigma^{\nu\mu}\,\left(\partial_\mu + iqe\,A_\mu\right)\right) - m^2\Bigg)\,\psi. \tag{C.16}$$

Consider

$$\begin{aligned}
&\left(\partial_\mu + iqe\,A_\mu\right)\,\sigma^{\mu\nu}\,\left(\partial_\nu + iqe\,A_\nu\right)\,\psi \\
&= \sigma^{\mu\nu}\,\left(\partial_\mu + iqe\,A_\mu\right)\,\left(\partial_\nu + iqe\,A_\nu\right)\,\psi \\
&= \sigma^{\mu\nu}\,\left(\left(\partial_\mu\partial_\nu\right)\,\psi + \left(\partial_\mu\,iqe\,A_\nu\right)\,\psi + iqe\,A_\nu\,\partial_\mu\,\psi + iqe\,A_\mu\,\partial_\nu\,\psi - q^2e^2\,A_\mu\,A_\nu\,\psi\right).
\end{aligned} \tag{C.17}$$

Similarly use Eq. (A.9) to write

$$\begin{aligned}
&\left(\partial_\nu + iqe\,A_\nu\right)\,\sigma^{\nu\mu}\,\left(\partial_\mu + iqe\,A_\mu\right)\,\psi \\
&= -\sigma^{\mu\nu}\,\left(\left(\partial_\nu\partial_\mu\right)\,\psi + \left(\partial_\nu\,iqe\,A_\mu\right)\,\psi + iqe\,A_\mu\,\partial_\nu\,\psi + iqe\,A_\nu\,\partial_\mu\,\psi - q^2e^2\,A_\nu\,A_\mu\,\psi\right).
\end{aligned} \tag{C.18}$$

Using these; Eq. (C.16) can now be simplified to

$$\begin{aligned}
\left(\not{D}\,\not{D} - m^2\right)\,\psi &= \left(D\cdot D - \frac{i}{2}\,\sigma^{\mu\nu}\,\left(\left(\partial_\mu\,iqe\,A_\nu\right) - \left(\partial_\nu\,iqe\,A_\mu\right)\right) - m^2\right)\,\psi \\
&= \left(D^2 + \frac{qe}{2}\,\sigma^{\mu\nu}\,F_{\mu\nu} - m^2\right)\,\psi,
\end{aligned} \tag{C.19}$$

as $F_{\mu\nu} = \partial_\mu\,A_\nu - \partial_\nu\,A_\mu$. With a constant background magnetic field $\vec{B} = \vec{\nabla}\times\vec{A}$ (and in an appropriate spinor representation), Eq. (C.19) can be written

$$\left(D^2 + qe\begin{bmatrix}\vec{\sigma}\cdot\vec{B} & 0 \\ 0 & \vec{\sigma}\cdot\vec{B}\end{bmatrix} + m^2\right)\,\psi = 0. \tag{C.20}$$

For $\vec{B} = B\,\hat{z}$ and spin-polarisation factor $\alpha = \pm 1$ the equation for each spinor component ψ_τ is

$$\left(D^2 + \alpha\,qe\,B + m^2\right)\,\psi_\tau = 0, \tag{C.21}$$

where $\alpha = (-1)^{(\tau-1)}$. The eigen-energies are a function of the mass, m, field strength, B, spin-polarisation, α, and momentum in the $\hat{z}$ direction, p_z and are given by [109]

$$E^2(B) = m^2 = |qe\,B|\;(2\,n + 1 - \alpha) + p_z^2, \tag{C.22}$$

where n is an integer describing the quantised energy level; the relativistic Landau energy.

The important point is that the eigenmode basis of the operator $(D^2 + \alpha\,qe\,B + m^2)$ is independent of the two constant terms $(\alpha\,qe\,B,\, m^2)$ and depends only on the covariant Laplacian operator $D^2 = D^\mu D_\mu$. This is in contrast to the eigen-energies which depend on the spin-coupling term.

The Landau modes on a discrete lattice for a charged Dirac particle in a uniform magnetic field oriented along the z axis, $\vec{B} = B\hat{z}$ correspond to the eigenmodes of the two-dimensional U(1) gauge-covariant lattice Laplacian

$$\Delta_{\vec{x},\vec{x}'} = 4\,\delta_{\vec{x},\vec{x}'} - \sum_{\mu=1,2} U_\mu^B\,(\vec{x})\;\delta_{\vec{x}+\hat{\mu},\vec{x}'} + U_\mu^{B\dagger}\,(\vec{x}-\hat{\mu})\;\delta_{\vec{x}-\hat{\mu},\vec{x}'}\,, \tag{C.23}$$

where $U_\mu^B\,(\vec{x})$ is the same U(1) gauge link as used in the full lattice QCD calculation and discussed in Section 3.6.1. In contrast to the infinite degeneracy of the infinite volume the lattice Landau modes exhibit a finite degeneracy dependent on the product $qe\,B$ of the charge and magnetic-field strength. The lowest Landau level on the lattice, in particular has a degeneracy equal to the magnetic flux quanta $|k|$ defined in Eq. (3.99).

Bibliography

[1] ATLAS collaboration, G. Aad et al., *Observation of a new particle in the search for the Standard Model Higgs boson with the ATLAS detector at the LHC*, *Phys. Lett. B* **716** (2012) 1–29, [arXiv:1207.7214]. 1

[2] CMS collaboration, S. Chatrchyan et al., *Observation of a New Boson at a Mass of 125 GeV with the CMS Experiment at the LHC*, *Phys. Lett. B* **716** (2012) 30–61, [arXiv:1207.7235]. 1

[3] Particle Data Group collaboration, M. Tanabashi, K. Hagiwara, K. Hikasa, K. Nakamura, Y. Sumino, F. Takahashi et al., *Review of particle physics*, *Phys. Rev. D* **98** (Aug, 2018) 030001. 1, 2.1.1, 2.1, 2.2, 2.3, 2.4, 4.15, 6.2.4, 6.40, 6.43, 7.2.1, 7.3

[4] L. Okun, *The theory of weak interaction*, in *The theory of weak interaction*, pp. 845–866, 1962. 2.1

[5] M. Kaku, *Quantum Field Theory: A Modern Introduction*. Oxford University Press, 1993. 2.1

[6] G. 't Hooft, *Dimensional regularization and the renormalization group*, *Nucl. Phys.* **B61** (1973) 455–468. 2.1

[7] D. Griffiths, *Introduction to elementary particles*. 2008. 2.1.1

[8] D. B. Newell, F. Cabiati, J. Fischer, K. Fujii, S. G. Karshenboim, H. S. Margolis et al., *The CODATA 2017 values of h, e, k, and n_a for the revision of the si*, *Metrologia* **55** (jan, 2018) L13–L16. 2.1.1

[9] M. Gell-Mann, *The eightfold way: A theory of strong interaction symmetry*, (1961) . 2.1.1, A.3

[10] Y. Ne'eman, *Derivation of strong interactions from a gauge invariance*, *Nucl.Phys.* **26** (1961) 222–229. 2.1.1

[11] C. Gattringer and C. B. Lang, *Quantum chromodynamics on the lattice*, Lect. Notes Phys. **788** (2010) 1–343. 2.2, 2.2.1, 3, 3.4.1, 3.4.3, 3.4.4, 3.6.2, 5.2.1, 6.3.1, A.4, B.2

[12] B. G. Lasscock, *Baryon spectroscopy from lattice QCD*. PhD thesis, University of Adelaide, School of Chemistry and Physics, Centre for the Subatomic Structure of Matter, 2006. 2.2, 3.4.2, B.5

[13] F. M. Stokes, *On the Structure of Nucleon Excited States in Lattice QCD*. PhD thesis, Faculty of Sciences, University of Adelaide, Australia, 2018. 2.2, 3.1

[14] A. J. Chambers, *Hadron Structure and the Feynman-Hellmann Theorem in Lattice Quantum Chromodynamics*. PhD thesis, Faculty of Sciences, School of Physical Sciences, Department of Physics, University of Adelaide, Australia, 2018. 2.2

[15] I. Montvay and G. Munster, *Quantum fields on a lattice*. Cambridge Monographs on Mathematical Physics. Cambridge University Press, 1997, 10.1017/CBO9780511470783. 2.2.1, 3, 3.4.3, A

[16] F. Mandl, *Statistical Physics*. Manchester Physics Series. 2nd ed. 2.2.1

[17] J. Smit, *Introduction to quantum fields on a lattice: A robust mate*, *Cambridge Lect. Notes Phys.* **15** (2002) 1–271. 2.2.1, 3

[18] S. O. Bilson-Thompson, *Investigation of Topology, Instantons, and the Nahm Transform in Lattice QCD using Highly Improved Operators*. PhD thesis, Department of Physics and Mathematical Physics, University of Adelaide, Australia, 4, 2002. 3.2

[19] F. D. R. Bonnet, *Improved Actions in Lattice QCD*. PhD thesis, Special Research Centre for the Subatomic Structure of Matter (CSSM) and Department of Physics and Mathematical Physics, University of Adelaide, 5005, Australia, 5, 2002. 3.2

[20] K. G. Wilson, *Confinement of Quarks*, Phys. Rev. **D10** (1974) 2445–2459. 3.2, 3.3.1

[21] K. Symanzik, *Continuum Limit and Improved Action in Lattice Theories. 1. Principles and phi**4 Theory*, Nucl. Phys. **B226** (1983) 187–204. 3.2

[22] K. Symanzik, *Continuum Limit and Improved Action in Lattice Theories. 2. O(N) Nonlinear Sigma Model in Perturbation Theory*, Nucl. Phys. **B226** (1983) 205–227. 3.2

[23] Y. Iwasaki, *Renormalization Group Analysis of Lattice Theories and Improved Lattice Action. II. Four-dimensional non-Abelian SU(N) gauge model*, arXiv:1111.7054. 3.2

[24] K. G. Wilson, *Monte Carlo Calculations for the Lattice Gauge Theory*, *NATO Sci. Ser. B* **59** (1980) 363–402. 3.2

[25] PACS-CS collaboration, S. Aoki et al., *2+1 Flavor Lattice QCD toward the Physical Point*, *Phys. Rev.* **D79** (2009) 034503, [arXiv:0807.1661]. 3.2, 3.2, 3.4.3, 3.7, 3.12, 3.7, 3.1, 4.2.2, 5.2.2, 5.2.3, 7

[26] P. H. Ginsparg and K. G. Wilson, *A Remnant of Chiral Symmetry on the Lattice*, *Phys. Rev.* **D25** (1982) 2649. 3.3.1, 3.3.1, 5

[27] H. Neuberger, *Exactly massless quarks on the lattice*, *Phys. Lett.* **B417** (1998) 141–144, [hep-lat/9707022]. 3.3.1, 3.3.1, 5

[28] J. Kogut and L. Susskind, *Hamiltonian formulation of wilson's lattice gauge theories*, *Phys. Rev. D* **11** (Jan, 1975) 395–408. 3.3.1

[29] L. Susskind, *Lattice fermions*, *Phys. Rev. D* **16** (Nov, 1977) 3031–3039. 3.3.1

[30] T. Blum, C. E. Detar, S. A. Gottlieb, K. Rummukainen, U. M. Heller, J. E. Hetrick et al., *Improving flavor symmetry in the Kogut-Susskind hadron spectrum*, *Phys. Rev.* **D55** (1997) R1133–R1137, [hep-lat/9609036]. 3.3.1

[31] W. H. Press, S. A. Teukolsky, W. T. Vetterling and B. P. Flannery, *Numerical Recipes in Fortran 77: the Art of Scientific Computing. Second Edition*, vol. 1. Cambridge University Press, 2006. 3.3.1, 3.4.4, B.6

[32] H. B. Nielsen and M. Ninomiya, *No Go Theorem for Regularizing Chiral Fermions*, *Phys. Lett.* **105B** (1981) 219–223. 3.3.1

[33] H. B. Nielsen and M. Ninomiya, *Absence of neutrinos on a lattice. 1. proof by homotopy theory*, . 3.3.1

[34] H. B. Nielsen and M. Ninomiya, *Absence of neutrinos on a lattice. 2. intuitive topological proof*, *Nucl.Phys.B* **193** (1981) 173–194. 3.3.1

[35] A. L. Kiratidis, *Multi-particle baryon spectroscopy in lattice quantum chromodynamics.*, Master's thesis, Special Research Centre for the Subatomic Structure of Matter, Department of Physics, School of Physical Sciences,

University of Adelaide, Australia, 2012. 3.3.1

[36] D. B. Kaplan, *A Method for simulating chiral fermions on the lattice*, *Phys. Lett. B* **288** (1992) 342–347, [hep-lat/9206013]. 3.3.1

[37] Y. Shamir, *Chiral fermions from lattice boundaries*, *Nucl. Phys. B* **406** (1993) 90–106, [hep-lat/9303005]. 3.3.1

[38] A. Borici, *Truncated overlap fermions*, *Nucl. Phys. B Proc. Suppl.* **83** (2000) 771–773, [hep-lat/9909057]. 3.3.1

[39] R. C. Brower, H. Neff and K. Orginos, *Mobius fermions: Improved domain wall chiral fermions*, *Nucl. Phys. B Proc. Suppl.* **140** (2005) 686–688, [hep-lat/0409118]. 3.3.1

[40] R. C. Brower, H. Neff and K. Orginos, *The Möbius domain wall fermion algorithm*, *Comput. Phys. Commun.* **220** (2017) 1–19, [arXiv:1206.5214]. 3.3.1

[41] B. Sheikholeslami and R. Wohlert, *Improved Continuum Limit Lattice Action for QCD with Wilson Fermions*, *Nucl. Phys.* **B259** (1985) 572. 3.3.1

[42] D. B. Leinweber, R. M. Woloshyn and T. Draper, *Electromagnetic structure of octet baryons*, *Phys. Rev.* **D43** (1991) 1659–1678. 3.4

[43] J. N. Hedditch, *Meson properties from lattice QCD*. PhD thesis, Adelaide U., 2006. 3.4, 3.4.2

[44] B. Lasscock, J. Hedditch, W. Kamleh, D. Leinweber, W. Melnitchouk, A. Williams et al., *Even parity excitations of the nucleon in lattice qcd*, *Phys.Rev.D* **76** (2007) 054510, [arXiv:0705.0861]. 3.4.2, 3.4.2

[45] B. Lasscock, D. B. Leinweber, W. Melnitchouk, A. W. Thomas, A. G. Williams, R. D. Young et al., *Spin 3/2 pentaquark resonance signature in lattice qcd*, *Phys.Rev.D* **72** (2005) 074507, [hep-lat/0504015]. 3.4.2, 3.4.3

[46] M. S. Mahbub, A. O. Cais, W. Kamleh, B. G. Lasscock, D. B. Leinweber and A. G. Williams, *Isolating Excited States of the Nucleon in Lattice QCD*, *Phys. Rev.* **D80** (2009) 054507, [arXiv:0905.3616]. 3.4.3, 4.1.2

[47] M. S. Mahbub, W. Kamleh, D. B. Leinweber and A. G. Williams, *Searching for low-lying multi-particle thresholds in lattice spectroscopy*, *Annals Phys.* **342** (2014) 270–282, [arXiv:1310.6803]. 3.4.3

[48] S. Schaefer, R. Sommer and F. Virotta, *Investigating the critical slowing down of QCD simulations*, *PoS* **LAT2009** (2009) 032, [arXiv:0910.1465]. 3.4.3

[49] ALPHA collaboration, S. Schaefer, R. Sommer and F. Virotta, *Critical slowing down and error analysis in lattice QCD simulations*, *Nucl. Phys. B* **845** (2011) 93–119, [arXiv:1009.5228]. 3.4.3

[50] M. Luscher, *Topology, the Wilson flow and the HMC algorithm*, *PoS* **LATTICE2010** (2010) 015, [arXiv:1009.5877]. 3.4.3

[51] M. Luscher and S. Schaefer, *Lattice QCD without topology barriers*, *JHEP* **07** (2011) 036, [arXiv:1105.4749]. 3.4.3

[52] M. Luscher and S. Schaefer, *Lattice QCD with open boundary conditions and twisted-mass reweighting*, *Comput. Phys. Commun.* **184** (2013) 519–528, [arXiv:1206.2809]. 3.4.3

[53] H.-W. Lin and S. D. Cohen, *Lattice QCD beyond ground states*, in *4th International Workshop on Numerical Analysis and Lattice QCD New Haven, CT, May 1-3, 2007*, 2007. arXiv:0709.1902. 3.4.4

[54] G. P. Lepage, B. Clark, C. T. H. Davies, K. Hornbostel, P. B. Mackenzie, C. Morningstar et al., *Constrained curve fitting*, *Nucl. Phys. Proc. Suppl.* **106** (2002) 12–20, [hep-lat/0110175]. 3.4.4

[55] J. Dragos, R. Horsley, W. Kamleh, D. B. Leinweber, Y. Nakamura, P. E. L. Rakow et al., *Nucleon matrix elements using the variational method in lattice qcd*, *Phys.Rev.D* **94** (2016) 074505, [arXiv:1606.03195]. 3.4.4, 3.4.4

[56] C. Michael, *Adjoint Sources in Lattice Gauge Theory*, *Nucl. Phys.* **B259** (1985) 58–76. 3.4.4

[57] M. Luscher and U. Wolff, *How to calculate the elastic scattering matrix in two-dimensional quantum field theories by numerical simulation*, *Nucl.Phys.B* **339** (1990) 222–252. 3.4.4

[58] UKQCD Collaboration collaboration, C. R. Allton, C. T. Sachrajda, R. M. Baxter, S. P. Booth, K. C. Bowler, S. Collins et al., *Gauge-invariant smearing and matrix correlators using wilson fermions at $\beta = 6.2$*, *Phys. Rev. D* **47** (Jun, 1993) 5128–5137. 3.4.4

[59] T. Burch, C. Gattringer, L. Ya. Glozman, C. Hagen, D. Hierl, C. B. Lang et al.,

Excited hadrons on the lattice: Baryons, Phys. Rev. **D74** (2006) 014504, [hep-lat/0604019]. 3.4.4

[60] W. Melnitchouk, S. O. Bilson-Thompson, F. D. R. Bonnet, J. N. Hedditch, F. X. Lee, D. B. Leinweber et al., *Excited baryons in lattice QCD*, Phys. Rev. **D67** (2003) 114506, [hep-lat/0202022]. 3.4.4

[61] B. Blossier, M. Della Morte, G. von Hippel, T. Mendes and R. Sommer, *On the generalized eigenvalue method for energies and matrix elements in lattice field theory*, JHEP **04** (2009) 094, [arXiv:0902.1265]. 3.4.4

[62] F. M. Stokes, W. Kamleh and D. B. Leinweber, *Opposite-parity contaminations in lattice nucleon form factors*, Phys.Rev.D **99** (2019) 074506, [arXiv:1809.11002]. 3.4.4

[63] C. Alexandrou, T. Leontiou, C. N. Papanicolas and E. Stiliaris, *Novel analysis method for excited states in lattice QCD: The nucleon case*, Phys. Rev. **D91** (2015) 014506, [arXiv:1411.6765]. 3.4.4

[64] C. Alexandrou, C. N. Papanicolas and E. Stiliaris, *A Novel method for the determination of hadron excited states in Lattice QCD applied to the nucleon*, PoS **LATTICE2008** (2008) 099, [arXiv:0810.3982]. 3.4.4

[65] C. Alexandrou, J. Berlin, M. Dalla Brida, J. Finkenrath, T. Leontiou and M. Wagner, *Lattice QCD investigation of the structure of the $a_0(980)$ meson*, Phys. Rev. **D97** (2018) 034506, [arXiv:1711.09815]. 3.4.4

[66] S. Gusken, *A Study of smearing techniques for hadron correlation functions*, Nucl. Phys. Proc. Suppl. **17** (1990) 361–364. 3.5, 3.5

[67] M. Della Morte, B. Jaeger, T. Rae and H. Wittig, *Improved interpolating fields for hadrons at non-zero momentum*, Eur. Phys. J. **A48** (2012) 139, [arXiv:1208.0189]. 3.5

[68] D. S. Roberts, W. Kamleh, D. B. Leinweber, M. S. Mahbub and B. J. Menadue, *Accessing High Momentum States In Lattice QCD*, Phys. Rev. **D86** (2012) 074504, [arXiv:1206.5891]. 3.5

[69] G. S. Bali, B. Lang, B. U. Musch and A. Schäfer, *Novel quark smearing for hadrons with high momenta in lattice QCD*, Phys. Rev. **D93** (2016) 094515, [arXiv:1602.05525]. 3.5

[70] Hadron Spectrum collaboration, M. Peardon, J. Bulava, J. Foley, C. Morningstar, J. Dudek, R. G. Edwards et al., *A Novel quark-field creation operator construction for hadronic physics in lattice QCD*, *Phys. Rev.* **D80** (2009) 054506, [arXiv:0905.2160]. 3.5, 6.1.1

[71] M. Wurtz, R. Lewis and R. M. Woloshyn, *Free-form smearing for bottomonium and B meson spectroscopy*, *Phys. Rev.* **D92** (2015) 054504, [arXiv:1505.04410]. 3.5

[72] UKQCD collaboration, C. R. Allton et al., *Gauge invariant smearing and matrix correlators using Wilson fermions at Beta = 6.2*, *Phys. Rev.* **D47** (1993) 5128–5137, [hep-lat/9303009]. 3.5, 4

[73] G. P. Lepage and P. B. Mackenzie, *On the viability of lattice perturbation theory*, *Phys. Rev.* **D48** (1993) 2250–2264, [hep-lat/9209022]. 3.5

[74] S. Boinepalli, *Electromagnetic properties of baryons from lattice QCD*. PhD thesis, Department of Physics, University of Adelaide, Australia, Centre for the Subatomic Structure of Matter, 2006. 3.5, B.6

[75] J. Hoek, M. Teper and J. Waterhouse, *Topological Fluctuations and Susceptibility in SU(3) Lattice Gauge Theory*, *Nucl. Phys.* **B288** (1987) 589–627. 3.5.1

[76] G. S. Bali and K. Schilling, *Static quark - anti-quark potential: Scaling behavior and finite size effects in SU(3) lattice gauge theory*, *Phys. Rev.* **D46** (1992) 2636–2646. 3.5.1

[77] G. S. Bali, K. Schilling and C. Schlichter, *Observing long color flux tubes in SU(2) lattice gauge theory*, *Phys. Rev.* **D51** (1995) 5165–5198, [hep-lat/9409005]. 3.5.1

[78] P. J. Moran and D. B. Leinweber, *Over-improved stout-link smearing*, *Phys. Rev.* **D77** (2008) 094501, [arXiv:0801.1165]. 3.5.1

[79] S. D. Thomas, W. Kamleh and D. B. Leinweber, *Instanton contributions to the low-lying hadron mass spectrum*, *Phys. Rev.* **D92** (2015) 094515, [arXiv:1410.7105]. 3.5.1

[80] S. Basak, I. Sato, S. Wallace, R. Edwards, D. Richards, G. T. Fleming et al., *Combining quark and link smearing to improve extended baryon operators*, *PoS* **LAT2005** (2006) 076, [hep-lat/0509179]. 3.5.1

[81] J. M. Bulava et al., *Excited State Nucleon Spectrum with Two Flavors of*

Dynamical Fermions, Phys. Rev. **D79** (2009) 034505, [arXiv:0901.0027]. 3.5.1

[82] C. Morningstar and M. J. Peardon, *Analytic smearing of SU(3) link variables in lattice QCD*, Phys. Rev. **D69** (2004) 054501, [hep-lat/0311018]. 3.5.1

[83] G. Lepage, *Flavor symmetry restoration and symanzik improvement for staggered quarks*, Phys.Rev.D **59** (1999) 074502, [hep-lat/9809157]. 3.5.1

[84] MILC collaboration, K. Orginos and D. Toussaint, *Testing improved actions for dynamical kogut-susskind quarks*, Phys.Rev.D **59** (1999) 014501, [hep-lat/9805009]. 3.5.1

[85] MILC collaboration, K. Orginos, D. Toussaint and R. Sugar, *Variants of fattening and flavor symmetry restoration*, Phys.Rev.D **60** (1999) 054503, [hep-lat/9903032]. 3.5.1

[86] CSSM Lattice collaboration, J. M. Zanotti, S. O. Bilson-Thompson, F. Bonnet, P. Coddington, D. Leinweber, A. G. Williams et al., *Hadron masses from novel fat link fermion actions*, Phys.Rev.D **65** (2002) 074507, [hep-lat/0110216]. 3.5.1

[87] J. M. Zanotti, D. B. Leinweber, W. Melnitchouk, A. G. Williams and J. B. Zhang, *Hadron properties with FLIC fermions*, Lect. Notes Phys. **663** (2005) 199–225, [hep-lat/0407039]. 3.5.1

[88] J. Smit and J. C. Vink, *Remnants of the Index Theorem on the Lattice*, Nucl. Phys. **B286** (1987) 485–508. 3.6

[89] M. Burkardt, D. B. Leinweber and X.-m. Jin, *Background field formalism in quantum systems*, Phys. Lett. **B385** (1996) 52–56, [hep-ph/9604450]. 3.6, 3.6.2, 4

[90] J.-W. Lee and B. C. Tiburzi, *Reconciling the lattice background field method with nonrelativistic QED: Spinor case*, Phys. Rev. **D90** (2014) 074036, [arXiv:1407.8159]. 3.6, 3.6.2

[91] G. Martinelli, G. Parisi, R. Petronzio and F. Rapuano, *The Proton and Neutron Magnetic Moments in Lattice QCD*, Phys. Lett. **B116** (1982) 434–436. 3.6, 3.6.2, 4

[92] C. W. Bernard, T. Draper, K. Olynyk and M. Rushton, *Lattice QCD Calculation of Some Baryon Magnetic Moments*, Phys. Rev. Lett. **49** (1982) 1076. 3.6, 3.6.1, 3.6.1, 3.6.2, 4

[93] H. R. Fiebig, W. Wilcox and R. M. Woloshyn, *A Study of Hadron Electric Polarizability in Quenched Lattice QCD*, Nucl. Phys. **B324** (1989) 47–66. 3.6, 3.7

[94] J. C. Christensen, W. Wilcox, F. X. Lee and L.-m. Zhou, *Electric polarizability of neutral hadrons from lattice QCD*, Phys. Rev. **D72** (2005) 034503, [hep-lat/0408024]. 3.6

[95] W. Freeman, A. Alexandru, M. Lujan and F. X. Lee, *Sea quark contributions to the electric polarizability of hadrons*, Phys. Rev. **D90** (2014) 054507, [arXiv:1407.2687]. 3.6, 3.7

[96] W. Detmold, B. C. Tiburzi and A. Walker-Loud, *Extracting Electric Polarizabilities from Lattice QCD*, Phys. Rev. **D79** (2009) 094505, [arXiv:0904.1586]. 3.6

[97] E. Shintani, S. Aoki, N. Ishizuka, K. Kanaya, Y. Kikukawa, Y. Kuramashi et al., *Neutron electric dipole moment with external electric field method in lattice QCD*, Phys. Rev. **D75** (2007) 034507, [hep-lat/0611032]. 3.6

[98] E. Shintani, S. Aoki and Y. Kuramashi, *Full QCD calculation of neutron electric dipole moment with the external electric field method*, Phys. Rev. **D78** (2008) 014503, [arXiv:0803.0797]. 3.6

[99] F. X. Lee, R. Kelly, L. Zhou and W. Wilcox, *Baryon magnetic moments in the background field method*, Phys. Lett. **B627** (2005) 71–76, [hep-lat/0509067]. 3.6

[100] C. Aubin, K. Orginos, V. Pascalutsa and M. Vanderhaeghen, *Magnetic Moments of Delta and Omega- Baryons with Dynamical Clover Fermions*, Phys. Rev. **D79** (2009) 051502, [arXiv:0811.2440]. 3.6

[101] T. Primer, W. Kamleh, D. Leinweber and M. Burkardt, *Magnetic properties of the nucleon in a uniform background field*, Phys. Rev. **D89** (2014) 034508, [arXiv:1307.1509]. 3.6, 3.6.1, 3.6.2, 4.1.2, 4.2.3, 6.2.3

[102] A. Parreno, M. J. Savage, B. C. Tiburzi, J. Wilhelm, E. Chang, W. Detmold et al., *Octet baryon magnetic moments from lattice QCD: Approaching experiment from a three-flavor symmetric point*, Phys. Rev. **D95** (2017) 114513, [arXiv:1609.03985]. 3.6

[103] D. S. Roberts, P. O. Bowman, W. Kamleh and D. B. Leinweber, *Wave Functions of the Proton Ground State in the Presence of a Uniform Background Magnetic*

Field in Lattice QCD, Phys. Rev. **D83** (2011) 094504, [arXiv:1011.1975]. 3.6

[104] NPLQCD collaboration, E. Chang, W. Detmold, K. Orginos, A. Parreno, M. J. Savage, B. C. Tiburzi et al., *Magnetic structure of light nuclei from lattice QCD*, Phys. Rev. **D92** (2015) 114502, [arXiv:1506.05518]. 3.6, 3.6.2, 3.7, 4

[105] F. Bruckmann, G. Endrodi, M. Giordano, S. D. Katz, T. G. Kovacs, F. Pittler et al., *Landau levels in QCD*, Phys. Rev. **D96** (2017) 074506, [arXiv:1705.10210]. 3.6, 4.1.2, 4.1.2, 5.2, 6, 6.1.1

[106] S. Borsanyi et al., *Ab initio calculation of the neutron-proton mass difference*, Science **347** (2015) 1452–1455, [arXiv:1406.4088]. 3.6

[107] J. Maxwell, *A dynamical theory of the electromagnetic field*, Phil. Trans. Roy. Soc. Lond. **155** (1865) 459–512. 3.6.1

[108] G. 't Hooft, *A Property of Electric and Magnetic Flux in Nonabelian Gauge Theories*, Nucl. Phys. **B153** (1979) 141–160. 3.6.1

[109] C. Itzykson and J. B. Zuber, *Quantum Field Theory*. International Series in Pure and Applied Physics. McGraw-Hill , New York, 1980. 3.6.2, C.1, C.2

[110] E. V. Luschevskaya, O. E. Solovjeva and O. V. Teryaev, *Magnetic polarizability of pion*, Phys. Lett. **B761** (2016) 393–398, [arXiv:1511.09316]. 3.6.2, 7, 7.2.2

[111] G. S. Bali, B. B. Brandt, G. Endrodi and B. Glaessle, *Meson masses in electromagnetic fields with Wilson fermions*, Phys. Rev. **D97** (2018) 034505, [arXiv:1707.05600]. 3.6.2, 4.3.2, 5, 5.2.1, 5.3.2, 5.3.2, 7, 7.2.2

[112] R. Bignell, W. Kamleh and D. Leinweber, *Pion in a uniform background magnetic field with clover fermions*, Phys. Rev. D **100** (Dec, 2019) 114518, [arXiv:1910.14244]. 3.6.2

[113] B. C. Tiburzi and S. O. Vayl, *Method to extract charged hadron properties from lattice QCD in magnetic fields*, Phys. Rev. **D87** (2013) 054507, [arXiv:1210.4464]. 3.6.2, 4, 4.1.2, 6.1.3

[114] R. Sommer, *A New way to set the energy scale in lattice gauge theories and its applications to the static force and alpha-s in SU(2) Yang-Mills theory*, Nucl. Phys. **B411** (1994) 839–854, [hep-lat/9310022]. 3.7

[115] B. J. Menadue, W. Kamleh, D. B. Leinweber and M. S. Mahbub, *Isolating the*

$\Lambda(1405)$ *in Lattice QCD*, Phys. Rev. Lett. **108** (2012) 112001, [arXiv:1109.6716]. 3.7

[116] B. J. Menadue, *A Study of the $\Lambda(1405)$ in Lattice QCD*. PhD thesis, School of Physical Sciences : Physics, University of Adelaide, Australia, 2018. 3.7, 3.7

[117] M. Gell-Mann, R. J. Oakes and B. Renner, *Behavior of current divergences under SU(3) x SU(3)*, Phys. Rev. **175** (1968) 2195–2199. 3.7, 5.2, 5.2.1

[118] C. W. Bernard and M. F. Golterman, *Partially quenched gauge theories and an application to staggered fermions*, Phys. Rev. D **49** (1994) 486–494, [hep-lat/9306005]. 3.7

[119] S. R. Sharpe and N. Shoresh, *Physical results from unphysical simulations*, Phys. Rev. D **62** (2000) 094503, [hep-lat/0006017]. 3.7

[120] S. Prelovsek, C. Dawson, T. Izubuchi, K. Orginos and A. Soni, *Scalar meson in dynamical and partially quenched two-flavor QCD: Lattice results and chiral loops*, Phys. Rev. D **70** (2004) 094503, [hep-lat/0407037]. 3.7

[121] C. Bernard and M. Golterman, *On the foundations of partially quenched chiral perturbation theory*, Phys. Rev. D **88** (2013) 014004, [arXiv:1304.1948]. 3.7

[122] Acharya, Neramballi Ripunjay, *Disconnected Contributions to Hadronic Processes*. PhD thesis, Rheinische Friedrich-Wilhelms-Universität Bonn, Jan., 2020. 3.7

[123] J. Finkenrath, F. Knechtli and B. Leder, *One flavor mass reweighting in lattice QCD*, Nucl. Phys. B **877** (2013) 441–456, [arXiv:1306.3962]. 3.7

[124] B. Leder, J. Finkenrath and F. Knechtli, *One flavor mass reweighting: foundations*, PoS **LATTICE2013** (2014) 035, [arXiv:1401.1079]. 3.7

[125] J. M. M. Hall, D. B. Leinweber and R. D. Young, *Finite-volume and partial quenching effects in the magnetic polarizability of the neutron*, Phys. Rev. **D89** (2014) 054511, [arXiv:1312.5781]. 3.7, 4.3, 4.3.1, 4.3.1, 5.4, 6.3, 6.3.1, B.8.1

[126] K. Kossert et al., *Neutron polarizabilities investigated by quasifree Compton scattering from the deuteron*, Phys. Rev. Lett. **88** (2002) 162301, [nucl-ex/0201015]. 4, 4.15, 6.40

[127] K. Kossert et al., *Quasifree Compton scattering and the polarizabilities of the neutron*, Eur. Phys. J. **A16** (2003) 259–273, [nucl-ex/0210020]. 4, 4.15, 6.40

[128] H. W. Griesshammer, J. A. McGovern, D. R. Phillips and G. Feldman, *Using effective field theory to analyse low-energy Compton scattering data from protons and light nuclei*, Prog. Part. Nucl. Phys. **67** (2012) 841–897, [arXiv:1203.6834]. 4, 4.15, 6.40

[129] COMPTON@MAX-LAB collaboration, L. S. Myers et al., *Measurement of Compton Scattering from the Deuteron and an Improved Extraction of the Neutron Electromagnetic Polarizabilities*, Phys. Rev. Lett. **113** (2014) 262506, [arXiv:1409.3705]. 4, 4.15, 6.40

[130] F. Hagelstein, *Nucleon Polarizabilities and Compton Scattering as a Playground for Chiral Perturbation Theory*, arXiv:2006.16124. 4, 6.4

[131] G. Parisi, *The Strategy for Computing the Hadronic Mass Spectrum*, Phys. Rept. **103** (1984) 203–211. 4, 6.1.3

[132] R. Bignell, D. Leinweber, W. Kamleh and M. Burkardt, *Nucleon Magnetic Properties from Lattice QCD with the Background Field Method*, *PoS* **INPC2016** (2017) 287, [arXiv:1704.08435]. 4.1.2, 5.2

[133] C. T. H. Davies, G. G. Batrouni, G. R. Katz, A. S. Kronfeld, G. P. Lepage, K. G. Wilson et al., *Fourier Acceleration in Lattice Gauge Theories. 1. Landau Gauge Fixing*, Phys. Rev. **D37** (1988) 1581. 4.1.2

[134] F. D. R. Bonnet, P. O. Bowman, D. B. Leinweber, A. G. Williams and D. G. Richards, *Discretization errors in Landau gauge on the lattice*, Austral. J. Phys. **52** (1999) 939–948, [hep-lat/9905006]. 4.1.2

[135] M. G. Beckett, B. Joo, C. M. Maynard, D. Pleiter, O. Tatebe and T. Yoshie, *Building the International Lattice Data Grid*, Comput. Phys. Commun. **182** (2011) 1208–1214, [arXiv:0910.1692]. 4.2.2

[136] T. J. Primer, *Magnetic Properties of the Nucleon in a Uniform Background Field*. PhD thesis, School of Chemistry and Physics, Discipline of Physics, University of Adelaide, 5005, Australia, 6, 2013. 4.2.3, 6.2.3

[137] E. E. Jenkins and A. V. Manohar, *Baryon chiral perturbation theory using a heavy fermion Lagrangian*, Phys. Lett. **B255** (1991) 558–562. 4.3.1, 6.3.1

[138] V. Lensky and V. Pascalutsa, *Predictive powers of chiral perturbation theory in Compton scattering off protons*, Eur. Phys. J. **C65** (2010) 195–209,

[arXiv:0907.0451]. 4.3.1

[139] R. D. Young, D. B. Leinweber and A. W. Thomas, *Convergence of chiral effective field theory*, *Prog. Part. Nucl. Phys.* **50** (2003) 399–417, [hep-lat/0212031]. 4.3.1, 6.3.1

[140] W. Detmold, B. C. Tiburzi and A. Walker-Loud, *Electromagnetic and spin polarisabilities in lattice QCD*, *Phys. Rev.* **D73** (2006) 114505, [hep-lat/0603026]. 4.3.1

[141] E. E. Jenkins, *Baryon masses in chiral perturbation theory*, *Nucl.Phys.B* **368** (1992) 190–203. 4.3.1, 6.3.1

[142] F. Gursey and L. Radicati, *Spin and unitary spin independence of strong interactions*, *Phys. Rev. Lett.* **13** (1964) 173–175. 4.3.1

[143] R. F. Lebed, *Determination of su(6) clebsch-gordan coefficients and baryon mass and electromagnetic moment relations*, *Phys.Rev.D* **51** (1995) 5039–5052, [hep-ph/9411204]. 4.3.1, 6.3.1

[144] P. Wang, D. B. Leinweber, A. W. Thomas and R. D. Young, *Chiral extrapolation of octet-baryon charge radii*, *Phys. Rev.* **D79** (2009) 094001, [arXiv:0810.1021]. 4.3.1, 6.3.1

[145] R. D. Young, D. B. Leinweber, A. W. Thomas and S. V. Wright, *Chiral analysis of quenched baryon masses*, *Phys. Rev.* **D66** (2002) 094507, [hep-lat/0205017]. 4.3.1, 6.3.1, 6.3.1

[146] D. B. Leinweber, S. Boinepalli, I. C. Cloet, A. W. Thomas, A. G. Williams, R. D. Young et al., *Precise determination of the strangeness magnetic moment of the nucleon*, *Phys. Rev. Lett.* **94** (2005) 212001, [hep-lat/0406002]. 4.3.1, 6.3.1

[147] D. B. Leinweber, S. Boinepalli, A. W. Thomas, P. Wang, A. G. Williams, R. D. Young et al., *Strange electric form-factor of the proton*, *Phys. Rev. Lett.* **97** (2006) 022001, [hep-lat/0601025]. 4.3.1, 6.3.1

[148] P. Wang, D. B. Leinweber, A. W. Thomas and R. D. Young, *Strange magnetic form factor of the proton at $Q^{**}2 = 0.23$- $GeV^{**}2$*, *Phys. Rev.* **C79** (2009) 065202, [arXiv:0807.0944]. 4.3.1, 6.3.1

[149] P. Wang, D. B. Leinweber and A. W. Thomas, *Strange magnetic form factor of the nucleon in a chiral effective model at next to leading order*, *Phys. Rev.* **D89**

(2014) 033008, [arXiv:1312.3375]. 4.3.1, 6.3.1

[150] B. B. Brandt, G. Bali, G. Endrödi and B. Glässle, *QCD spectroscopy and quark mass renormalisation in external magnetic fields with Wilson fermions*, *PoS* **LATTICE2015** (2016) 265, [arXiv:1510.03899]. 5, 5

[151] E. V. Luschevskaya, O. E. Solovjeva, O. A. Kochetkov and O. V. Teryaev, *Magnetic polarizabilities of light mesons in $SU(3)$ lattice gauge theory*, *Nucl. Phys.* **B898** (2015) 627–643, [arXiv:1411.4284]. 5

[152] R. Horsley et al., *QED effects in the pseudoscalar meson sector*, *JHEP* **04** (2016) 093, [arXiv:1509.00799]. 5.1.1

[153] J. Gasser and H. Leutwyler, *Quark Masses*, *Phys. Rept.* **87** (1982) 77–169. 5.2

[154] L. Giusti and M. Luscher, *Chiral symmetry breaking and the Banks-Casher relation in lattice QCD with Wilson quarks*, *JHEP* **03** (2009) 013, [arXiv:0812.3638]. 5.2.1

[155] K. Cichy, E. Garcia-Ramos and K. Jansen, *Chiral condensate from the twisted mass Dirac operator spectrum*, *JHEP* **10** (2013) 175, [arXiv:1303.1954]. 5.2.1

[156] Flavour Lattice Averaging Group collaboration, S. Aoki et al., *FLAG Review 2019: Flavour Lattice Averaging Group (FLAG)*, *Eur. Phys. J. C* **80** (2020) 113, [arXiv:1902.08191]. 5.2.1

[157] M. D'Elia and F. Negro, *Chiral Properties of Strong Interactions in a Magnetic Background*, *Phys. Rev.* **D83** (2011) 114028, [arXiv:1103.2080]. 5.2.1

[158] G. S. Bali, F. Bruckmann, G. Endrodi, Z. Fodor, S. D. Katz, S. Krieg et al., *The QCD phase diagram for external magnetic fields*, *JHEP* **02** (2012) 044, [arXiv:1111.4956]. 5.2.1

[159] JLQCD, CP-PACS collaboration, S. Aoki et al., *Nonperturbative $O(a)$ improvement of the Wilson quark action with the RG-improved gauge action using the Schrodinger functional method*, *Phys. Rev.* **D73** (2006) 034501, [hep-lat/0508031]. 5.2.2

[160] S. R. Sharpe, *Quenched chiral logarithms*, *Phys. Rev. D* **46** (1992) 3146–3168, [hep-lat/9205020]. 5.3.2

[161] C. W. Bernard and M. F. Golterman, *Chiral perturbation theory for the quenched*

approximation of QCD, Phys. Rev. D **46** (1992) 853–857, [hep-lat/9204007]. 5.3.2

[162] M. Chernodub, *Superconductivity of qcd vacuum in strong magnetic field*, Phys.Rev.D **82** (2010) 085011, [arXiv:1008.1055]. 5.4

[163] M. Chernodub, *Spontaneous electromagnetic superconductivity of vacuum in strong magnetic field: evidence from the nambu–jona-lasinio model*, Phys.Rev.Lett. **106** (2011) 142003, [arXiv:1101.0117]. 5.4

[164] S. Bellucci, J. Gasser and M. E. Sainio, *Low-energy photon-photon collisions to two loop order*, Nucl. Phys. **B423** (1994) 80–122, [hep-ph/9401206]. 5.4, 7.2.2, 7.2.2

[165] J. Gasser, M. A. Ivanov and M. E. Sainio, *Revisiting gamma gamma —> pi+ pi- at low energies*, Nucl. Phys. **B745** (2006) 84–108, [hep-ph/0602234]. 5.4, 7, 7.3

[166] G. Endrődi, *QCD in magnetic fields: from Hofstadter's butterfly to the phase diagram*, PoS **LATTICE2014** (2014) 018, [arXiv:1410.8028]. 6

[167] R. Bignell, W. Kamleh and D. Leinweber, *Magnetic polarizability of the nucleon using a Laplacian mode projection*, Phys. Rev. D **101** (2020) 094502, [arXiv:2002.07915]. 6.1.1

[168] J. Bulava, K. Juge, C. Morningstar, M. Peardon and C. Wong, *Two-particle Correlation Functions with Distilled Propagators*, PoS **LAT2009** (2009) 097, [arXiv:0911.2044]. 6.1.1

[169] C. Egerer, D. Richards and F. Winter, *Controlling excited-state contributions with distillation in lattice QCD calculations of nucleon isovector charges g_S^{u-d}, g_A^{u-d}, g_T^{u-d}*, Phys. Rev. D **99** (2019) 034506, [arXiv:1810.09991]. 6.1.1

[170] S.-J. Dong and K.-F. Liu, *Stochastic estimation with Z(2) noise*, Phys. Lett. **B328** (1994) 130–136, [hep-lat/9308015]. 6.1.1, 7.3

[171] J. Foley, K. Jimmy Juge, A. O'Cais, M. Peardon, S. M. Ryan and J.-I. Skullerud, *Practical all-to-all propagators for lattice QCD*, Comput. Phys. Commun. **172** (2005) 145–162, [hep-lat/0505023]. 6.1.1, 7.3

[172] A. Aleksejevs and S. Barkanova, *Dynamical polarizabilities of su(3) octet of baryons*, J.Phys.G **38** (2011) 035004, [arXiv:1010.3457]. 6.2.4, 6.46, 6.3.2, 6.49, 6.3.2

[173] A. Deshmukh and B. C. Tiburzi, *Octet baryons in large magnetic fields*, *Phys.Rev.D* **97** (2018) 014006, [arXiv:1709.04997]. 6.2.4, 6.46, 6.49, B.8.1

[174] C. Gobbi, C. L. Schat and N. N. Scoccola, *Hyperon polarizabilities in the bound state soliton model*, *Nucl.Phys.A* **598** (1996) 318–334, [hep-ph/9509211]. 6.2.4, 6.46, 6.49

[175] Y. Tanushi, S. Saito and M. Uehara, *One loop calculations of hyperon polarizabilities under the large n(c) consistency condition*, *Phys.Rev.C* **61** (2000) 055204, [nucl-th/9911071]. 6.2.4, 6.46

[176] F. X. Lee, L. Zhou, W. Wilcox and J. C. Christensen, *Magnetic polarizability of hadrons from lattice qcd in the background field method*, *Phys.Rev.D* **73** (2006) 034503, [hep-lat/0509065]. 6.2.4, 6.46, 6.3.2, 6.49, 6.3.2

[177] D. B. Leinweber, *Quark contributions to baryon magnetic moments in full, quenched and partially quenched qcd*, *Phys.Rev.D* **69** (2004) 014005, [hep-lat/0211017]. 6.3.1, B.8.1

[178] S. R. Beane, *Nucleon masses and magnetic moments in a finite volume*, *Phys. Rev.* **D70** (2004) 034507, [hep-lat/0403015]. 6.3.1

[179] J. M. M. Hall, D. B. Leinweber and R. D. Young, *Power Counting Regime of Chiral Effective Field Theory and Beyond*, *Phys. Rev.* **D82** (2010) 034010, [arXiv:1002.4924]. 6.3.1, 7.3

[180] J. A. McGovern, D. R. Phillips and H. W. Griesshammer, *Compton scattering from the proton in an effective field theory with explicit Delta degrees of freedom*, *Eur. Phys. J.* **A49** (2013) 12, [arXiv:1210.4104]. 6.43

[181] S. R. Beane, M. Malheiro, J. A. McGovern, D. R. Phillips and U. van Kolck, *Nucleon polarizabilities from low-energy Compton scattering*, *Phys. Lett.* **B567** (2003) 200–206, [nucl-th/0209002]. 6.43

[182] G. Blanpied et al., *N —> delta transition and proton polarizabilities from measurements of p (gamma polarized, gamma), p (gamma polarized, pi0), and p (gamma polarized, pi+)*, *Phys. Rev.* **C64** (2001) 025203. 6.43

[183] V. O. de León et al., *Low-energy Compton scattering and the polarizabilities of the proton*, *Eur. Phys. J.* **A10** (2001) 207–215. 6.43

[184] B. E. MacGibbon, G. Garino, M. A. Lucas, A. M. Nathan, G. Feldman and

B. Dolbilkin, *Measurement of the electric and magnetic polarizabilities of the proton*, Phys. Rev. **C52** (1995) 2097–2109, [nucl-ex/9507001]. 6.43

[185] B. Pasquini, P. Pedroni and S. Sconfietti, *Proton scalar dipole polarizabilities from real Compton scattering data, using fixed-t subtracted dispersion relations and the bootstrap method*, arXiv:1903.07952. 6.43

[186] Y. Antipov et al., *Measurement of pi- meson polarizability in pion compton effect*, Phys.Lett.B **121** (1983) 445–448. 7

[187] COMPASS collaboration, C. Adolph et al., *Measurement of the charged-pion polarizability*, Phys. Rev. Lett. **114** (2015) 062002, [arXiv:1405.6377]. 7

[188] L. V. Fil'kov and V. L. Kashevarov, *Dipole Polarizabilities of $\pi^{\pm}$-Mesons*, Int. J. Mod. Phys. Conf. Ser. **47** (2018) 1860092, [arXiv:1806.06852]. 7

[189] M. Moinester and S. Scherer, *Compton Scattering off Pions and Electromagnetic Polarizabilities*, Int. J. Mod. Phys. **A34** (2019) 1930008, [arXiv:1905.05640]. 7

[190] B. R. Holstein, *Pion polarizability and chiral symmetry*, Comments Nucl.Part.Phys. **19** (1990) 221–238. 7

[191] M. A. Moinester and V. Steiner, *Pion and kaon polarizabilities and radiative transitions*, hep-ex/9801008. 7

[192] S. Scherer, *Real and virtual Compton scattering at low-energies*, Czech. J. Phys. **49** (1999) 1307–1345, [nucl-th/9901056]. 7

[193] J. Ahrens et al., *Measurement of the pi+ meson polarizabilities via the gamma $p \to$ gamma pi+ n reaction*, Eur. Phys. J. **A23** (2005) 113–127, [nucl-ex/0407011]. 7

[194] A. V. Manohar, *Chiral perturbation theory*, in *QCD and high-energy hadronic interactions. Proceedings, Hadronic Session of the 28th Rencontres de Moriond, Moriond Particle Physics Meeting, Les Arcs, France, March 20-27, 1993*, pp. 177–186, 1993. hep-ph/9305298. 7

[195] U. Burgi, *Charged pion pair production and pion polarizabilities to two loops*, Nucl. Phys. **B479** (1996) 392–426, [hep-ph/9602429]. 7

[196] V. Bernard, B. Hiller and W. Weise, *Pion Electromagnetic Polarizability and Chiral Models*, Phys. Lett. **B205** (1988) 16–21. 7

[197] L. V. Fil'kov and V. L. Kashevarov, *Compton scattering on the charged pion and*

the process gamma gamma —> pi0 pi0, Eur. Phys. J. **A5** (1999) 285–292, [nucl-th/9810074]. 7, 7.2.2

[198] L. V. Fil'kov and V. L. Kashevarov, *Dipole and quadrupole polarizabilities of the pion*, in *Proceedings, 6th International Workshop on the Physics of Excited Nucleons (NSTAR 2007): Bonn, Germany, September 5-8, 2007*, 2008. arXiv:0802.0965. 7

[199] R. Garcia-Martin and B. Moussallam, *MO analysis of the high statistics Belle results on $\gamma\gamma \to \pi^+\pi^-, \pi^0\pi^0$ with chiral constraints*, Eur. Phys. J. **C70** (2010) 155–175, [arXiv:1006.5373]. 7

[200] M. Lujan, A. Alexandru, W. Freeman and F. Lee, *Finite volume effects on the electric polarizability of neutral hadrons in lattice qcd*, Phys.Rev.D **94** (2016) 074506, [arXiv:1606.07928]. 7.2.1

[201] A. Alexandru, M. Lujan, W. Freeman and F. Lee, *Pion electric polarizability from lattice qcd*, in *Pion electric polarizability from lattice QCD*, vol. 1701, p. 040002, 2016. arXiv:1501.06516. DOI. 7.2.1

[202] L. V. Fil'kov and V. L. Kashevarov, *Determination of pi0 meson quadrupole polarizabilities from the process gamma gamma —> pi0 pi0*, Phys. Rev. **C72** (2005) 035211, [nucl-th/0505058]. 7.2.2, 7.2.2

[203] A. E. Kaloshin, V. M. Persikov and V. V. Serebryakov, *First estimates of the (alpha + Beta)**pi from two photon experiments*, Phys. Atom. Nucl. **57** (1994) 2207–2208, [hep-ph/9402220]. 7.2.2

[204] J. Gasser, M. A. Ivanov and M. E. Sainio, *Low-energy photon-photon collisions to two loops revisited*, Nucl. Phys. **B728** (2005) 31–54, [hep-ph/0506265]. 7.2.2

[205] C. Bernard, S. Hashimoto, D. B. Leinweber, P. Lepage, E. Pallante, S. R. Sharpe et al., *Panel discussion on chiral extrapolation of physical observables*, Nucl. Phys. Proc. Suppl. **119** (2003) 170–184, [hep-lat/0209086]. 7.3

[206] A. L. Kiratidis, *Spectroscopy with Multi-Hadron Interpolating Operators in Lattice Quantum Chromodynamics*. PhD thesis, Special Research Centre for the Subatomic Structure of Matter, Department of Physics, School of Physical Sciences, University of Adelaide, Australia, 2016. 7.3

[207] J. J. Sakurai, *Advanced quantum mechanics*. Addison-Wesley, Redwood City,

Calif., 1967. A.2

[208] R. Achilles and A. Bonfiglioli, *The early proofs of the theorem of Campbell, Baker, Hausdorff, and Dynkin*, *Archive for History of Exact Sciences* **66** (May, 2012) 295–358. B.2, B.7

[209] B. Efron, *Computers and the theory of statistics: Thinking the unthinkable*, *SIAM Review* **21** (1979) 460–480. B.6

[210] P. E. Shanahan, *Strangeness and Charge Symmetry Violation in Nucleon Structure*. PhD thesis, Faculty of Sciences, School of Physical Sciences, Department of Physics, University of Adelaide, Australia, 2015. B.8.1